STUDIES ON SUPPRESSION OF FLUX CREEP AND SCALING OF VORTEX LIQUID RESISTIVITY IN RARE EARTH MODIFIED (Bi,Pb)-2212 SUPERCONDUCTORS

Thesis Submitted to the

UNIVERSITY OF KERALA

for the Award of the Degree of

DOCTOR OF PHILOSOPHY

in

PHYSICS

By

VINU. S

Applied Superconductivity and Ceramics Group
Materials and Minerals Division

NATIONAL INSTITUTE FOR INTERDISCIPLINARY SCIENCE AND TECHNOLOGY (NIIST)
Council of Scientific and Industrial Research (CSIR)
Trivandrum - 695 019, India

2011

DECLARATION

      I, **VINU. S** hereby declare that the work presented in the Ph. D. thesis entitled **"*Studies on suppression of flux creep and scaling of vortex liquid resistivity in rare earth modified (Bi,Pb)-2212 superconductors*"** is an independent research work carried out by me for the award of degree of ***Doctor of Philosophy in Physics*** of the University of Kerala, under the guidance of **Dr. U. Syamaprasad**, Chief Scientist and Head, Applied Superconductivity and Ceramics Group, National Institute for Interdisciplinary Science and Technology (NIIST), CSIR, Trivandrum-695019. I further declare that this thesis or any part of it has not been submitted anywhere else for any other degree, diploma or other similar title.

VINU. S

Trivandrum,
02-09-2011.

NATIONAL INSTITUTE FOR INTERDISCIPLINARY SCIENCE AND TECHNOLOGY (NIIST)

(Formerly Regional Research Laboratory, Thiruvananthapuram)

Council of Scientific & Industrial Research
Industrial Estate PO, Trivandrum – 695 019, Kerala, INDIA

Tel : 91-471-2515 373 / 2515 233; Fax : +91-471-2491 712 / 2490 186
E-mail : syamcsir@gmail.com; syam@niist.res.in

ISO 9001 REGISTERED

Dr. U. SYAMAPRASAD
Chief Scientist and Head
Applied Superconductivity and Ceramics Group

02-09-2011

CERTIFICATE

Certified that the work embodied in the thesis entitled, **"*Suppression of flux creep and scaling of vortex liquid resistivity in rare earth modified (Bi, Pb)-2212 superconductors*"** is an authentic record of the research work carried out by **Mr. S. VINU,** Applied Superconductivity and Ceramic Group, National Institute for Interdisciplinary Science and Technology (NIIST), CSIR, Trivandrum, under my supervision and guidance in partial fulfillment of the requirement for the award of degree of *Doctor of Philosophy in Physics* of the *University of Kerala*. It is further certified that no part of this thesis has been presented previously anywhere else for the award of any other degree.

U. Syamaprasad
(Research Guide)

Dedicated to

the loving memory of my sweet mother

Acknowledgements

*Above all, I bow my head before the **God,** the Most Beneficent and Merciful for giving me the opportunity, good health and strength to accomplish my ambition of carrying out research in the field of superconductivity. I also express my sincere gratitude to **Saint Jude**, for all his blessings and also giving confidence in undertaking this Ph. D. work.*

*I wish to express my deep sense of gratitude to my research supervisor **Dr. V. Syamaprasad,** Chief Scientist and Head, Applied Superconductivity and Ceramics Group, National Institute for Interdisciplinary Science and Technology, Trivandrum, India for his valuable guidance, timely motivations, continuous encouragement and support throughout the period of my Ph.D. work. Words are insufficient to express my thanks to him for giving me such a wonderful opportunity for being his student. Without his ardent and expert direction this work would not have been completed.*

*Next, I would like to thank **Dr. Suresh Das**, Director, NIIST (CSIR), Trivandrum, India; **Dr. B. C. Pai** and **Dr. T. K. Chandrashekar**, former Directors, **Mr. Harikrishna Bhatt**, Chairman, APC, for providing all the necessary facilities to carry out this work and for their creative suggestions and encouragement.*

*I would be grateful to **Most. Rev. Fr. Premkumar., M. S. W.,** the correspondent, Malankara Catholic College (MCC), Mariagiri, K. K. Dist, India for his valuable help, inspirations, keen interest and advice which were highly motivating.*

*I take this chance to express my gratitude to **Mr. P. Guruwsamy**, Technical Officer, NIIST (CSIR), Trivandrum, India, for his encouragement, suggestions and sincere support during the entire period of the work.*

*I express my sincere thanks to **Dr. K. G. K. Warrier**, **Dr. Peter Koshy**, **Dr. P. Prabhakar Rao**, **Dr. Ananthakumar**, and **Dr. V. M. Sreekumar**, NIIST (CSIR), Trivandrum, India for their help during this work. I also express my heartfelt thanks to **Mr. M. Chandran, Mr. S. G. K. Pillai** and **Mr. Robert Philip** for extending different instrumental facilities.*

*I owe my sincere gratitude to my colleagues **Dr. P. M. Sarun** and **R. Shabna** for their sincere help, creative suggestions and the warmth of deep friendship during the entire course of this work. I wish to express*

i

PREFACE

*So far, the Nobel Prize in Physics has been awarded five times for research in superconductivity to a total of ten physicists: in **1913** to Heike Kamerlingh Onnes for discovering the phenomenon of superconductivity; in **1972** to John Bardeen, Leon Neil Cooper and Robert Schrieffer for their microscopic explanation of superconductivity, the BCS theory; in **1973** to Brian David Josephson for predicting the Josephson effect; in **1987** to Johannes Georg Bednorz and Karl Alex Muller for discovering ceramic 'high temperature superconductors'; and in **2003** to Alexei Abrikosov, Vitali Ginzburg, and Anthony James Legget for the prediction of the Abrikosov vortex lattice, for the Ginzburg–Landau theory and for achievements in the theory of superfluidity and superconductivity and this itself will tell the importance of this fascinating field and the search and research for good conductors, for practical applications.*

After the discovery of superconductivity, it took almost 50 years until this fascinating phenomenon was understood microscopically, when in 1957 Bardeen, Cooper and Schrieffer established their BCS theory. But long before this, there were powerful phenomenological theories capable to explain most of the electromagnetic and thermodynamic observations on superconductors and these are very useful even today. The London theory of Fritz and Heinz London from 1935 is particularly useful for the description of the high T_c superconductors. The Ginzburg–Landau theory of 1951 is quite universal; it contains the London theory as a particular limit and predicts that superconductors can be of type-I with positive energy of the wall between normal conducting and superconducting domains or of type-II with negative wall energy, pointing to an instability.

The penetration of vortices into type-II superconductors was predicted first by Abrikosov when he found a two-dimensional periodic solution of the Ginzburg–Landau (GL) equations. Abrikosov correctly interpreted this solution as a periodic arrangement of flux lines, the flux-line lattice (FLL). Each flux line or fluxon, vortex line carries one quantum of magnetic flux $\phi = h/2e = 2.07 \times 10^{-15}$ Tm^2, which is caused by the super-currents circulating in this vortex and the magnetic field peaks at the vortex positions. The vortex core is a tube in which the superconductivity is weakened; the position of the vortex is defined by the line at which the

superconducting order parameter vanishes. For well separated or isolated vortices, the radius of the tube of magnetic flux equals the magnetic penetration depth λ, and the core radius is somewhat larger than the superconducting coherence length ξ. The periodic solution exists when the GL parameter $\kappa = \lambda/\xi$ exceeds the value $1/\sqrt{2}$ (this condition defines type-II superconductors) and when the applied magnetic field $B_a = \mu_0 H_a$ ranges between the lower critical field $B_{c1} = \mu_0 H_{c1} \approx \phi_0 \ln(\sqrt{2}k)/(4\pi\lambda^2)$, where $B = 0$, and the upper critical field $B_{c2} = \mu_0 H_{c2} = \phi_0/(2\pi\xi^2)$, where $B = B_a = B_{c2}$. For $|B_a| < B_{c1}$, the superconductor is in the Meissner state, which expels all magnetic flux and forces $B \equiv 0$ inside the superconductor except in a thin surface layer of thickness λ. With increasing applied magnetic field, the spacing of the vortices decreases and the average flux density $\overline{B}$ increases; one has $\overline{B} = 2\phi_0(\sqrt{3}a^2)$ for the triangular FLL. The flux tubes then overlap such that the periodic induction $B(x, y)$ is nearly constant, with only a small relative variation about its average $\overline{B}$. With further increase of $\overline{B}$ the vortex cores also begin to overlap such that the amplitude of the order parameter decreases until it vanishes when $\overline{B}$ reaches B_{c2}, where the superconductivity disappears.

The GL theory also yields the magnetization curves of the ideal vortex lattice and the elastic properties of the vortex lattice, which turn out to be highly non-local (dispersive). The effects of vortex pinning and the melting of the vortex lattice into a vortex liquid, occurring in high T_c superconductors may be calculated by treating the vortex lattice as an elastic medium. The magnetic dc and ac properties of superconductors with realistic shapes (e.g., rectangular platelets and films, thick strips, thin disks and rings, and thick disks or short cylinders) can be computed from the London theory or from the Maxwell equations using appropriate constitutive laws for the electric field $E(J, B)$ (generated by moving vortices) as a function of the current density J (driving the vortices) and induction B or vortex density B/ϕ_0.

The discovery of high temperature superconductors (HTS) by Bednorz and Muller in 1987 has marked tremendous advance in the field of superconductivity as it has contributed enormous scientific and industrial benefits worldwide in the fields such as energy, electronics, communication, medicine and transportation. In particular, the cuprate based HTS has had an enduring fascination for the condensed matter physics community not only due to their high T_c values but also for their scientific significance. Despite considerable research, there is no

recognized theory for HTS materials and by what routes, the Mott insulators accomplish the miraculous transformation into superconductors with the addition of electrons or holes are the big problem that, to date has not been solved. This reflects the lack of a formal understanding of strongly correlated metal oxides but also reflects the experimental subtleties of this system with its marked tendency for disorder, compositional complexity and anisotropic properties.

Even though there are a large number of high T_c superconducting materials known today, Bi -based superconductors have attracted researchers due to their widespread applications. The material has not only high transition temperature (T_c), but also has extremely high critical magnetic field (B_{c2}). It is less susceptible to degradation as a result of oxygen loss and less sensitive to attack by water and carbon dioxide compared to any other HTS and its lower melting point being in the range 800–900 $°C$. The main advantage of Bi -based system is its layered structure, which can be progressively deformed to induce a high degree of texturing, thereby enhancing the superconducting properties. Among the Bi -based systems, $Bi-2212$ ($Bi_2Sr_2Ca_1Cu_2O_{8+\delta}$) is considered to be the best candidate for fabrication of long length wires and tapes with moderate current carrying capabilities. Moreover, the superconducting transition temperature of $Bi-2212$ is strongly related to the carrier concentration in the CuO_2 planes. The hole carrier density of the CuO_2 plane in $Bi-2212$ can be altered by changing the oxygen stoichiometry or by cationic substitution of divalent Ca/Sr in the active layers of $Bi-2212$ by suitable cations. Hence, the properties of $Bi-2212$ superconductor can be tailored for specific applications.

The structural, superconducting and flux pinning properties of HTS can also be improved by doping and the modified materials are most suitable for the application at higher temperatures and magnetic fields fields. Doping can also be used as a powerful method to explore the mechanism of high temperature superconductivity. There exist a large number of reports on rare earth (RE) doping on HTS. The role of RE substitution on the superconducting properties of $Bi-2212$ superconductor has been studied since, it is an efficient tool to understand the underlying mechanism of high T_c superconductors. In Bi -based superconductors, large scale RE doping is possible only in $Bi-2201$ and $Bi-2212$. In $Bi-2223$ higher amounts of RE doping is not possible. Most of the existing RE doping studies in $Bi-2212$ are at Ca site and in Pb free samples and the results show that for RE

*doped samples, the T_c value decreases and only there is a marginal improvement in self-field J_C. Again there is no information available on in-field J_C and flux pinning properties. But RE doping in Pb substituted $Bi - 2212$ $[(Bi, Pb) - 2212]$ at its Sr site has shown a tremendous enhancement in T_c, self- and in-field J_C values and flux pinning properties. Hence for the present work, I have choosen the superconductor $(Bi, Pb) - 2212$ and the REs (i) Lutitium (Lu), (ii) Holium (Ho), (iii) Dysprosium (Dy), (iv) Terbium (Tb), (v) Gadolinium (Gd), (vi) Europium (Eu), (vii) Cerium (Ce), (viii) Neodymium (Nd) and (ix) Lanthanum (La) as the dopants and the site Sr for substitution. The program of my doctoral thesis was (**i**) to explore the influence of RE substitution at the Sr site on the superconducting properties of $(Bi, Pb) - 2212$, (**ii**) to find the impact of dopant level and processing condition on the superconducting and flux pinning properties, (**iii**) to enhance our knowledge and understanding on the doping dependent evolution of HTS, (**iv**) to suppress the flux creep and to enhance the flux pinning properties, (**v**) to evaluate the theory and different mechanisms of flux pinning (**vi**) to analyze the effect of refining the microstructure by fine tuning of sintering temperature, (**vii**) to search the novel effect of out-of-plane (disorder outside the CuO_2 plane) disorder, (**viii**) to explore the significance of different lattice sites for substitution, (**ix**) to study the $E - J$ characteristics and n-index, (**x**) to determine and analyze the temperature and magnetic field dependent activation energy, (**xi**) to compare the conventional Arrhenius model with the newly modified vortex-glass model, (**xii**) to analyze the thermally activated flux flow $(TAFF)$ resistivity and (**xiii**) to scale the vortex liquid resistivity close to the vortex-glass to liquid transition regime for RE modified $(Bi, Pb) - 2212$ superconductors.*

*The dissertation is organized into eight chapters. The introductory chapter (**chapter 1**) begins with a brief overview on high temperature superconductivity, superconducting materials, structural arrangement, underlying theories, applications and the specialties of Bi-based superconductors. The details of the experimental and analytical techniques in general are outlined in **chapter 2** while the specific methods used are also described in the respective chapters.*

*In **chapter 3,** the influence of rare earth $(Lu, Ho, Dy$ and $Tb)$ substitution on the superconducting properties of $(Bi, Pb) - 2212$ system is discussed in detail. The structural and superconducting properties are studied for different RE concentrations in the range*

$0 < x < 0.5$ *and the results are compared with the RE -free $(Bi, Pb) - 2212$ superconductor.*
The REs are chosen on the basis of ionic size and valence criteria and a variety of analytical
tools like XRD, SEM, EDAX, $R - T$ and J_C measurements are employed for the
determination of structural and transport properties. The superconducting properties such as
T_c and J_C are highly enhanced and this increase is explained by the dual effect of the decrease
in the hole concentration (P) in CuO_2 planes from the over-doped to an optimally-doped state
and the improvement of coupling between the CuO_2 layers which is achieved by RE
substitution. Beyond the optimum levels, the T_c gets reduced and an under-doped condition is
attained due to reduced hole density, which triggers a metal to insulator transition in
$(Bi, Pb) - 2212$ system.

    *In **chapter 4,** the suppression of flux creep and flux pinning properties of RE $(Lu, Ho,$*
Dy, Tb, Gd and $Eu)$ substituted $(Bi, Pb) - 2212$ system is discussed in detail and the results
are compared with the RE -free $(Bi, Pb) - 2212$ system. The enhancement of flux pinning
properties is evident from the improved $J_C(B)$ and normalized $J_C(B)$ characteristics. Among
the RE substituted samples, the $J_C(B)$ characteristics are found to be much better for Eu
substituted samples and the maximum values of bulk pinning force densities $(F_{P\max})$ of the RE
- substituted samples are found to shift towards higher fields and temperature and this means
that the irreversibility line (IL) of the RE substituted samples shift towards higher fields and
temperatures. Also, $n > 15$ and $J < J_g$ shows a glass-state for flux-lines, indicating their
improved flux-pinning ability due to the creation of point defects by the substituted RE atoms.
The improved U_C values also support this. A correlation between $n - indices$ and J_C of RE
substituted $(Bi, Pb) - 2212$ superconductor is also observed. The
$J_C(B), F_P(B), E - J, U(J) - J$ characteristics are highly improved for RE substituted
$(Bi, Pb) - 2212$ superconductors. Also enhanced U_C and n values at applied fields under
transport current flow show that the RE modified material is a promising candidate for
magnetic applications. The pinning analysis clearly demonstrates that the substitution of RE in
$(Bi, Pb) - 2212$ superconductor significantly enhances its flux pinning strength at a relatively

high temperature of 64 K by the introduction of point defects, which also contribute to the J_C of the RE substituted $(Bi, Pb) - 2212$ superconductor.

*In **chapter 5,** the effect of refinement of microstructure on the flux pinning properties of RE $(Ho, Dy, Gd \text{ and } La)$ substituted $(Bi, Pb) - 2212$ system is discussed in detail. The effect of sintering temperature on the RE substituted $(Bi, Pb) - 2212$ superconductors is investigated systematically. The microstructural variations are highly temperature-sensitive. The T_c value is found to be invariant with the sintering temperature for the same RE content. The J_C value of RE substituted samples depends mainly on the RE used and the enormous increase of self-field J_C of the samples (with same RE content) heat treated at higher sintering temperatures is due to the formation of the refined microstructure. While the formation of disrupted grains with decreased texturing reduces the self-field J_C of the samples heat treated above or below the optimum sintering temperature (T_{opt}). The investigation of the microstructural and flux pinning properties of RE substituted $(Bi, Pb) - 2212$ superconductors prepared at different temperatures ranging from 846 to 860 $^{\circ}C$ point towards the importance of fine tuning of heat treatment temperature in the preparation of RE substituted $(Bi, Pb) - 2212$ superconductors to tailor their properties depending on different applications. For instance, the RE substituted samples prepared at comparatively lower sintering temperatures (846 – 850 $^{\circ}C$) are useful for magnetic field applications due to their better flux pinning properties. Whereas, the samples prepared at higher sintering temperatures (854 – 860 $^{\circ}C$) are useful for self-field applications due to their enhanced self-field current carrying capacity.*

*In **chapter 6,** the novel effects of disorder at various out-of-plane lattice sites on the superconducting and flux pinning properties of RE substituted $(Bi, Pb) - 2212$ system is analyzed in detail. It is found that the self-field J_C and $J_C(B)$ characteristics of RE substituted samples are highly sensitive to the dopant site. The enhancement of flux pinning properties are evident from the improved $J_C(B)$ characteristics and the Dew-Hughes pinning analysis shows that for all samples, the peak position of F_P at h = 0.33 ± 0.03 which further shows that the main pinning mechanism is due to point defects aroused out of the substitution of RE atoms at the respective cationic sites. Among the RE substituted samples, SrRE shows the best $J_C(B)$ performance and the least self-field J_C, while CaRE shows the least $J_C(B)$*

performance and the best self-field J_C. These results show that the irreversibility line of the RE substituted samples [especially SrRE] gets shifted towards higher magnetic fields and temperatures, and the flux pinning strength sensitively depends on the site in which RE is substituted. The enhancement of superconducting and flux pinning properties are discussed based on the variation of out-of-plane disorder, changes in the chemical as well as electronic inhomogeneities due to the doping of RE atoms in the $(Bi, Pb) - 2212$ system.

*In **chapter 7,** the thermally activated flux flow $(TAFF)$ resistivity of RE $(RE = Lu, Ho, Eu, La \ and \ Ce)$ substituted $(Bi, Pb) - 2212$ superconductor has been discussed in detail with the help of two theoretical methods [(i) Arrhenius method and (ii) modified vortex-glass model]. The analysis of the resistivity data using the Arrhenius plot show that with decreasing temperature, the activation energy $U_0(B)$ initially shows a plateau region and subsequently changes to a divergent behavior which indicates the crossover from the Arrhenius to the vortex-glass regime. By using the modified vortex-glass model, the equations for ρ and $U_0(B,T)$ are obtained and the outcome of the analyses using these equations are in good agreement with the experimental data. In addition, the scaling analysis is shown to be applicable for the whole vortex-liquid regime of the RE substituted samples and thus it is concluded that the analysis of TAFF behavior in any high T_c superconductor using the modified vortex-glass model is highly advantageous over the Arrhenius method. Again, among the RE substituted samples, SrRE shows the best in-field performance and hence the flux flow resistivity is very much suppressed for this sample while CaRE shows the least. Thus it is concluded that for magnetic field applications defects created at the Sr site is more influential than defects at Bi or Ca sites. The highly enhanced temperature and magnetic field dependent activation energy at applied fields under transport current flow suggests that the RE modified $(Bi, Pb) - 2212$ superconducting materials are the promising candidates for magnetic applications. Finally, **chapter 8** summarizes the major conclusions drawn out from the work and the scope for future work.*

.

CONTENTS

1. Overview on high temperature superconductors

2. Synthesis and Characterization

3.   Influence of rare earth substitution on the superconducting properties of (Bi, Pb)-2212 system

4. Suppression of flux creep and flux pinning properties of rare earth (Lu, Ho, Dy, Tb, Gd and Eu) substituted (Bi, Pb)-2212

List of Abbreviations

Symbol		Description
BCS	:	Bardeen Cooper Schreiffer
BSCCO	:	Bismuth strontium calcium copper oxide
DOS	:	Density of states
EDAX	:	Energy dispersive X-ray analysis
GPIB	:	General purpose interface board
HTS	:	High temperature superconductor
LTS	:	Low temperature superconductor
MIT	:	Metal to insulator transition
NMR	:	Nuclear Magnetic Resonance
PC	:	Personal computer
PDF	:	Powder diffraction file
RE	:	Rare earth
RRR	:	Residual resistivity ratio
RVB	:	Resonance valence band theory
SEM	:	Scanning electron microscope
TAFF	:	Thermally activated flux flow
XRD	:	X-ray diffraction
YBCO	:	Yttrium barium copper oxide
IL	:	Irreversibility line
LN_2	:	Liquid nitrogen
MRI	:	Magnetic resonance imaging
SQUID	:	Superconducting quantum interference device
VRH	:	Variable range hopping

List of symbols

Symbol		Description
$\overset{\circ}{\text{A}}$	:	Angstrom
A	:	Absorption coefficient of the material
mA	:	milli Ampere
$\Delta(0)$	:	BCS band gap
$\alpha,\ \beta,\ \gamma$	:	Angles of a unit cell
T_c	:	Critical temperature
$T_{c\max}$	:	Maximum value of T_c
T_m	:	Melting temperature
T_g	:	Glass transition temperature
ΔT_c	:	Transition width
κ	:	Ginzburg Landau parameter
kV	:	kilo volt
λ_{L}	:	Penetration depth
L	:	Total length of flux line per unit volume
Ω	:	ohm (unit of resistance)
ϕ_0	:	Magnetic flux quanta
η	:	Efficiency factor
$\psi(\text{r})$	:	Wave function
ρ	:	Resistivity
ρ_{ab}	:	In-plane resistivity
ρ_{c}	:	Out-of-plane resistivity
ρ_n	:	Normal state resistivity
ρ_0	:	Characteristic resistivity
$\rho_{300\ K}$	:	Resistivity at 300 K
θ	:	Angle of diffraction

Symbol		Description
θ_c	:	Critical angle
ξ	:	Coherence length
a, b, c	:	Lattice parameters
a_0	:	Inter-atomic distance
B	:	Magnetic induction
C and $C^{\dagger}$	:	Creation and annihilation operator
F	:	Lotgering index
F_x	:	Volume percentage of phase x
F_P	:	Flux pinning force
$F_{P\max}$	:	Flux pinning force density
f_P	:	Pinning force per unit length of pinned flux line
h, k, l	:	Reciprocal lattices
l	:	Spacing between pinning centers
I_{total}	:	Integrated peak intensity of all phases
I_x	:	Integrated peak intensity of phase x
I_{hkl}	:	integrated intensity of hkl planes
k_B	:	Boltzmann constant
K	:	Temperature in Kelvin scale
n_s^*	:	Density of superelectrons
t	:	Transfer parameter
v	:	velocity of *TAFF*
v_c	:	Critical velocity of *TAFF*
A, p, q	:	Dew-Hughes pinning parameters
P	:	Hole carrier concentration per Cu atom
Pa	:	Pascal
B_{irr}	:	Irreversibility magnetic field

Symbol		Description
C_i	:	Weight percentage of investigated element
C_s	:	Weight percentage of standard element
$2D$	:	Two dimension
$3D$	:	Three dimension
d	:	Interplanar spacing
s	:	Critical exponent
E	:	Electric field
E_0	:	Critical electric field
H_C	:	Critical magnetic field
H_{C1}	:	Upper critical field
H_{C2}	:	Lower critical field
T	:	Tesla
I_{00l}	:	Intersity of $00l$ plane
I_i	:	Peak intensity of investigated element
I_S	:	Peak intensity of standard element
J	:	Current density
J_C	:	Critical current density
J_g	:	Current density for vortex glass to liquid transition
k_+ / k_-	:	Wave vector
n	:	Order of reflection
$N_S(E, \theta)$	:	Density of state function
$\sigma^2(r, x)$	:	Variance of ionic radii
nm	:	Nanometer
I_r	:	Intensity ratio of randomized powder
I_a	:	Intensity ratio of textured pellet
r	:	Position vector
R	:	Resistance

Symbol		Description
U_C	:	Pinning energy
$U(J)$	:	Pinning potential barrier
U_0	:	Current independent pinning energy
$U_0(B)$	:	Magnetic field dependent activation energy
$U_0(B,T)$	:	Temperature and magnetic field dependent activation energy
$Vol.\%$	:	Volume percentage
$wt.\%$	:	Weight percentage
ΔW	:	Work done in moving unit length of flux line
$G(H,T)$	:	Gibbs function per unit volume of the superconductor
ΔG	:	Change in Gibbs function
S_V	:	Surface area per unit volume

Chapter 1

CHAPTER 1

Overview on high temperature superconductivity

1.1. Introduction

In 1908, Professor Heike Kamerlingh Onnes initiated the field of low temperature physics by liquefying helium in his laboratory at Leiden (Holland). Three years later, he found that at 4.2 K, the dc resistance of mercury dropped to zero [Figure 1.1(a) and 1.1(b)]. With that finding the field of ***superconductivity*** was born [Onnes (1911)]. A perfect superconductor is a material that exhibits two characteristics properties, namely zero electrical resistance and perfect diamagnetism, when it is cooled below a particular temperature T_c, called the critical temperature. A considerable amount of time went by before physicists become aware of the second distinguishing characteristic of a superconductor (namely, its perfect diamagnetism). In 1933, Walter Meissner and Robert Ochsenfeld [Meissner et al. (1933)] found that when a superconductor material is cooled below its transition temperature in a magnetic field, an electric current is established on its surface which create an equal and opposite magnetic field to the one that is being applied and results in a net zero magnetic field inside the superconductor. As a result, the flux inside the superconductor is expelled in magnetic fields below a certain threshold value [Figure 1.2(a) and 1.2(b)]. The phenomenon came to be known as ***Meissner effect***, and laid the foundation for the thermodynamic treatment of superconductivity.

The detailed research by Kamerlingh Onnes, Meissner and Ochsenfeld showed that the normal or superconducting state of a material is determined by the temperature, applied magnetic field and the current flowing through the superconductor. Thus, for the occurrence of superconductivity in a material, the temperature must be below the critical temperature (T_c), the external magnetic field must be below the critical field (H_C) and the current density through the material must be below the critical current density (J_C). The three parameters $T_c(H,J)$, $H_C(T,J)$ and $J_C(H,T)$ define a critical surface as illustrated in figure 1.2 (c) and inside the surface the material is in superconducting state and outside the surface the material is in normal state.
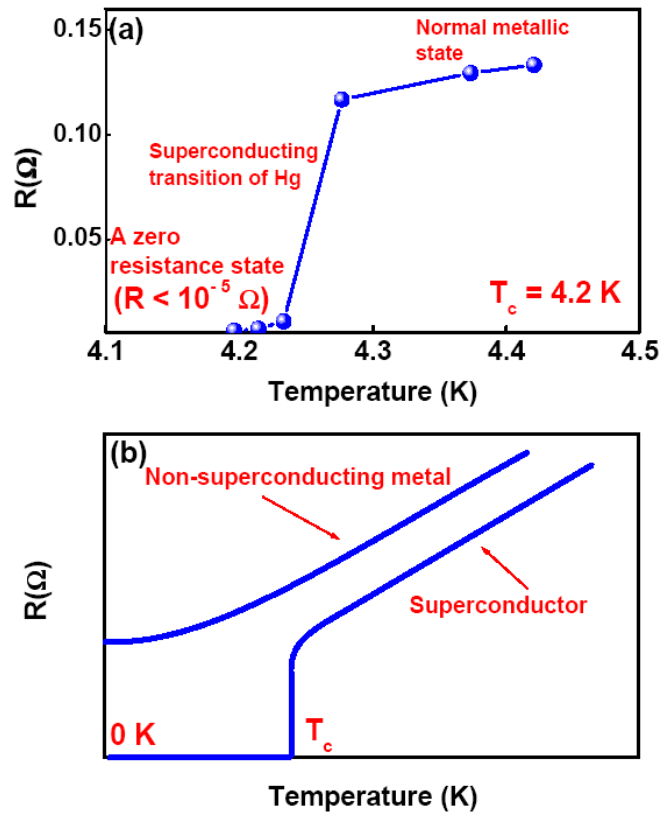
Figure 1.1: (a) $R-T$ plot of mercury obtained by Kamerlingh Onnes and (b) the variation of resistance with temperature for a normal conductor and a superconductor.

The usefulness of a superconductor for technological applications depends on its ability to carry high current density without resistive loss at the working field (H) and temperature (T). There are two limits to the J_C in practical superconductors: (i) the intrinsic J_C is limited by the upper critical field (H_{C2}) and the irreversibility field (H_{irr}), and (ii) the extrinsic J_C is limited by the factors like grain connectivity, grain orientation (anisotropy) and flux pinning. Hence the main focuss of research in this area has been to develop superconductors with high values of T_c, H_C and J_C envisioned to realize superconducting materials for practical applications with reduced operation cost.
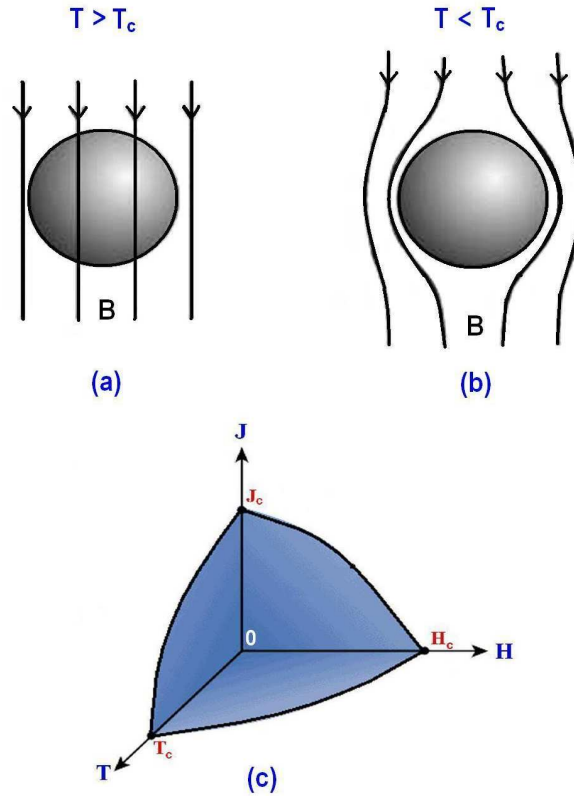
Figure 1.2: (a) and (b) Illustration of the Meissner effect and (c) the three dimensional critical surface of a superconductor.

1.2. Theoretical background

Though superconductivity is discovered in 1911, it took a long time to get a successful microscopic explanation for its occurrence. In 1934, Gorter and Gasimer proposed the first model called two-fluid model to describe superconductivity. After the discovery of Meissner effect, the London equations proposed by London brothers [London et al. (1935)] explained the behaviour of a superconductor in magnetic fields. Also London brothers proved that the field inside a superconductor in the Meissner state decays exponentially with distance from the surface. This defines the London penetration depth [London et al. (1935)], λ_L, being defined as $H(\lambda_L) = (1/e) H(0)$, where $H(0)$ is the field at the surface of the superconductor. In 1950 Ginzberg and Landau [Ginzburg Ginzburg V L, "Nobel Lecture" (2004)] explained the normal to superconducting transition using the Landau theory of phase transitions. Landau theory takes
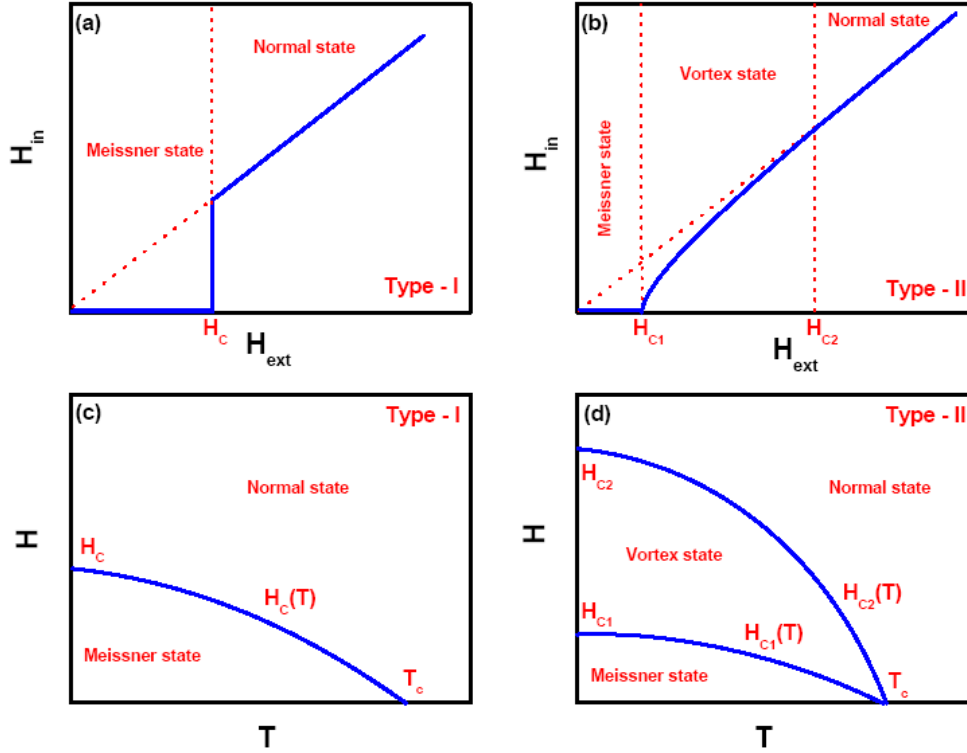
Figure 1.3: (a) and (b) Variation of internal magnetic field with external field for type I and type II superconductors and (c) and (d) show the $H - T$ phase diagram of type I and type II superconductors.

electrodynamic, quantum mechanic and thermodynamic properties into account and expresses the degree of superconductivity in a material as a complex order parameter described by the density of super-electrons n_s^* and a phase θ at position r, as $\psi(r) = n_s^*(r)e^{i\theta(r)}$. Using this expression in an expansion of Gibbs free energy near T_c, (where the order parameter is small), gives the two GL-equations which define two fundamental length scales characterizing the superconducting state. They are the penetration depth (λ_L), which has already been mentioned, and the coherence length, ξ, which characterizes the spatial variation of $\psi(r)$ and in an ordinary superconductor, it can be up to a few micrometers in length.

In 1957, Abrikosov [Abrikosov (1957)] successfully predicted the vortex structure in superconductors by applying GL-theory, which provides an immense understanding of the magnetic properties of superconductors. Thus, all the superconductors were divided into two classes, type I and type II, based on the ratio of fundamental superconductivity parameters λ_L to

ξ. This ratio, $\kappa = \lambda_L / \xi$, is called the ***Ginzburg – Landau parameter***. If $\kappa < 0.707$, the superconductor is type I. If $\kappa > 0.707$, the superconductor is type II. The more fundamental characteristic distinction for type I and type II superconductors is the sign of the interface energy between the normal and superconducting domains. Type I has a positive interface energy, and type II has negative interface energy. Type I superconductors expel an external magnetic field from their interior, up to a thermodynamic critical field H_C. For external fields above H_C the superconductor turns into normal material and allows the external fields to penetrate into the interior of the superconductor. For fields $< H_C$ (Meissner state) type I superconductor acts as a perfect diamagnet so that $\chi = -1$ and $M = -H$ and for fields $> H_C$ (normal state) $\chi = 0$ and $M = 0$. Figure 1.3 (a) shows the variations of internal field with external field for a type I superconductor.

The negative interface energy allows the type II superconductor to occupy as much interfacial area as possible and hence, the type II superconductors have two critical fields H_{C1} and H_{C2} [Figure 1.3 (b)]. Below the lower critical field H_{C1}, a type II superconductor behaves as that of a type I superconductor and expels any magnetic field from its interior. For fields above the value of H_{C1}, the external magnetic field starts to penetrate into the interior of the type II superconductor in the form of quantized flux vortices. These quantized flux vortices are known as fluxons and each fluxon is a tube of radius of the order of London penetration depth λ_L in which superconducting screening currents circulate around a small non superconducting core of radius ξ. The flux carried by a single fluxon is $\Phi_0 = h/2e = 2 \times 10^{-15} \, Wb$ [Abrikosov (2004)]. As the external field increases, more and more flux vortices are created at the surface of the superconductor and are penetrated into the interior, and they arrange themselves in a regular lattice. This state, called the mixed state or vortex state is important for the practical applications. As the field increases further, the flux vortices fill the superconducting matrix and thus reduce the superconducting area. At a particular high field, called the upper critical field H_{C2}, the entire superconducting area is filled by vortices and the superconductor turns into a normal material. For fields $< H_{C1}$ (Meissner state) type II superconductor acts as a perfect diamagnet so that $\chi = -1$ and $M = -H$, for fields $> H_{C1}$ and $< H_{C2}$ (mixed or vortex state) magnetic field penetrates in the form of quantized vortices so that $0 > \chi > -1$ and

$0 > M > -H$ and for fields $> H_{C2}$ (normal state) $\chi = 0$ and $M = 0$. Figure 1.3 (b) shows the variations of internal field with external field for a type II superconductor. Figure 1.3 (c) and (d) show schematic $H - T$ phase diagrams for type I and type II superconductors, respectively. The H_{C1} is of the order of $10–100$ mT for most of the type II superconductors, while they have very high H_{C2} values of several tesla. This property allows the type II superconductors to remain superconducting in high fields, which is advantageous in many applications such as magnetic levitation and transformers. Thus, the GL-theory is a very efficient tool to analyze the physical properties of a superconductor, but it does not give a microscopic explanation to what happens inside the material as it becomes superconducting.

A microscopic quantum theory of superconductivity was first published in 1957 by Bardeen, Cooper and Schreiffer, and is known as the **BCS** theory [[a]Bardeen et al. (1957), [b]Bardeen et al. (1957)], which explains the fascinating properties of superconductors. According to **BCS** theory, the pairing of electrons (Cooper pairs) via the exchange of atomic vibrations (phonons) is the reason for the occurrence of superconductivity. The pairing of electrons is in momentum space rather than in real space. In the superconducting state some of the electrons in the material form pairs known as Cooper pairs (super-electron pairs) and condensate into an energy state. An electron-phonon interaction, mediates the pairing of electrons. As a negatively charged electron moves through a lattice of positive ions, it locally distorts the neighborhood lattice and creates an area of greater positive charge density around it. Another electron passing nearby in the lattice is then attracted to this charge distortion and forms the Cooper pair. The electrons are thus indirectly attracted to each other and form a Cooper pair (Figure 1.4) through the lattice (phonon) interaction. The coherent superposition of these Cooper pairs into a condensate creates an energy gap in the excitation spectrum. In the superconducting state this gap prevents the scattering of electrons and produces zero electrical resistance. In a simplified picture, superconductivity is created by two paired electrons (Cooper pair) having wave vectors of opposite sign, K_+ and K_- but being equal in magnitude $|K_+| = |K_-|$. Their total wave vector will then be ~ 0, which corresponds to an infinite wavelength. The wavelength is much larger than the distance between the atoms in a crystal, which means that the Cooper pair will not be scattered by the lattice and thus it does not experience any resistance as it flows through the material. The coherent superposition of these Cooper pairs into a condensate creates an energy gap in the excitation spectrum which prevents the scattering of electrons and infinite

conductivity is maintained in superconducting state. The binding energy of Cooper pairs was estimated to be $\Delta(0) = 1.75 k_B T_c$ at zero kelvin [Bardeen et al. (1957)], where $\Delta(0)$ is the superconducting energy gap.
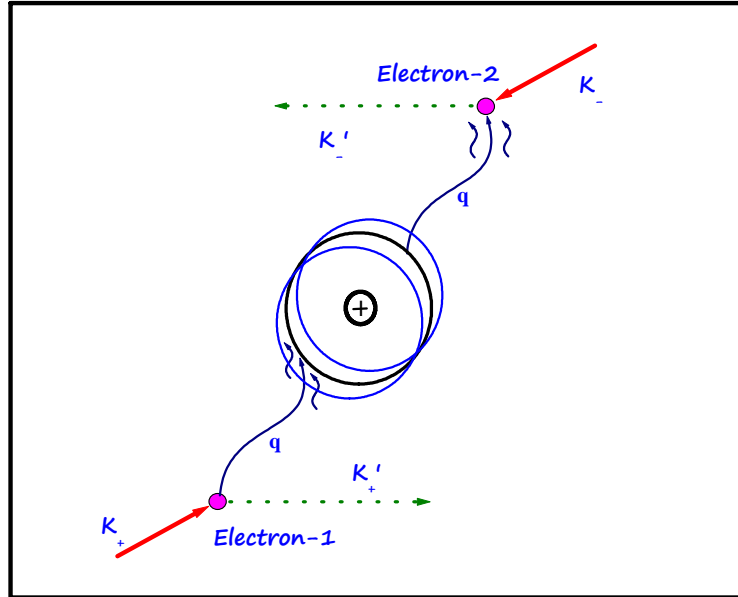
Figure 1.4: The phonon mediated electron-electron interaction to form the Cooper pair. The electron-1 modifies the vibration of positive ion, which in turn interacts with electron-2 and the net result is the attractive interaction between the two electrons.

     The **BCS** theory successfully explained the superconductivity in low T_c materials, but it failed to satisfactorily explain the superconductivity in high T_c cuprates [Lee et al. (2006)]. For example, the occurrence of T_c values higher than 40 K could not be explained by **BCS** theory. Also the experimentally determined energy gap of **HTS** was found to be twice as that calculated using **BCS** theory. Hence for **HTS** materials more specific superconductivity theories have been developed, and most important one is the Resonating Valance Band (RVB) theory [Anderson (1987)]. Also there emerged a set of new theories which have been forwarded with **BCS** type mechanism such as phonon coupling, polaron mediated interactions, mediation through excitons, plasmons, spin fluctuations etc. In the year 2000, Pan et al [Pan et al. (2000)] proposed that high temperature superconductivity involves fluctuations of the magnetic spins of atomic nuclei, rather than phonon mediated mechanism of classical low temperature

superconductors (LTS). Using Low temperature STM studies on HTS materials, they observed that high T_c superconductivity originated from strong interaction of electrons moving through copper oxide layers. However, till now no successful theory could be formulated for HTS materials due to the lack of direct evidence.

1. 3 Superconducting materials

Mercury (Hg) is the first material observed to be superconducting in 1911. Now, nearly after one century of the discovery of the phenomenon, thousands of materials including elemental metals, alloys, binary and multicomponent compounds of metals, ceramics, doped fullerenes and organic molecules are found to be superconducting with transition temperatures ranging from a milli kelvin to ~ 150 K [Geballe (2001), Phillips (2000)]. Many materials which are non-superconducting under normal conditions become superconducting under pressure, upon irradiation or charge doping and some materials in the form of thin film.

Table 1.1 gives some of the superconducting materials of various classes/families. Among the simple elemental superconductors Li has the highest T_c of 20 K under high pressure while Nb has the highest T_c of 9.25 K under normal conditions. Highly conducting ordinary metallic materials like Cu, Ag and Au are non-superconductors even to the lowest temperature studied. Al is superconducting and has a T_c of 1.18 K in bulk and 3.6 K in the form of thin film. Inter-metallic materials with the A15 crystal structure such as *V3Si, Nb3Sn, Nb3Ga* and *Nb3Ge* have higher transition temperatures than the elemental superconductors. Of these A15 superconductors, *Nb3Ge* has a T_c of 23.2 K and this was the highest T_c for a superconductor for many decades, before the mid 80's. All these simple elemental, alloy and intermetallic superconductors that have T_c at or below 23 K are known as the low temperature superconductors (LTS) and are well explained by the BCS theory of superconductivity.

The discovery of superconductivity in copper oxide systems was a breakthrough in superconductivity research. In 1986 Bednorz and Müller from the IBM laboratory in Ruschlikon near Zurich reported the existence of superconductivity in $La-Ba-Cu-O$ system at a surprisingly high T_c of ~ 30 K, [Bednorz et al. (1986)] initiating the era of high T_c superconductivity (HTS). The discovery of superconductivity in the mixed $Y-Ba-Cu-O$

compound system with T_c above 90 K, higher than the boiling temperature of liquid nitrogen (77 K) was another milestone in the search for new **HTS** materials [Wu et al. (1987)]. Today, different cuprate compounds have been found and that display the superconducting properties at relatively high temperatures. The highest reliable T_c ever measured up to now was in the **$HgBa_2Ca_2Cu_3O_8$** system ($T_c = 164$ K) under 30 GPa pressure [Gao et al. (1994)].

In March 2001, a new type of superconductor, MgB_2 was discovered and it is having a T_c of 39 K [Nagamatsu et al. (2001)]. It has a layered structure but not as anisotropic as the cuprates and has two band gaps open up below T_c [Liu et al. (2001), Szabo et al. (2001)], implying that there are two types of super-electrons in the material. It is presumed that this can cause creation of vortices carrying an arbitrary fraction of a magnetic flux quantum [Babaev et al. (2002)]. Recently, in 2008, iron based superconductor, **$LaFeAsF_xO_{1-x}$** $\left(x = 0.11\right)$ was discovered having a T_c of 26 K [Kamihara et al. (2008)], which was raised to 50 – 55 K by replacing La by different rare earths. These iron based superconductors have very high H_{C2} values of the order of 300 T [Jia et al. (2008)]. However, arsenic toxicity and the necessity of inert atmosphere, high pressure and temperature are the main challenges to be addressed for the development of these materials into practical conductors [An R Z, Wei L, Jie Y, Wei Y, Li S X, Cai L Z, et al. (2008)].

Table 1.1: Superconducting materials under various classifications

[Jrome et al. (1980), Saito et al. (1991), Poole et al. (1995), Hott et al. (2005), Buzea et al. (2001), Buzea et al. (2005), Kamihara et al. (2008), An et al. (2008), Ishiguro et al. (1998), Jia et al. (2008), Yamamoto et al. (2008), Yi et al. (2008)].

Type/class	Example	$T_c\left(K\right)$
Elements	Hg	4.2
	Nb	9.2
	Li (under pressure)	20
	B (under pressure)	11
	W (thin film)	5.5
	Pd (irradiated)	3.2

Amophous materials	$U_{85.7}Fe_{14.3}$	1.0
	$Th_{80}Co_{20}$	3.8
Alloys	VTi	7.0
	NbTi	9.0
A15 type (A3B)	Nb_3Sn	18.0
	Nb_3Ge	23.2
Laves phase (AB2)	ZrV_2	9.6
	$LaOs_2$	8.9
Chevrel phase (ABxMo6S8)	$PbMo_6S_8$	12.6
	$Sn_{1.2}Mo_6S_8$	14.2
Heavy electron systems	UPd_2Al_3	2.0
	$CeCu_2Si_3$	0.6
Magnetic material	$ErRh_4B_4$	10
Doped Fullerenes	Cs_3C_{60}	47.4
	$Rb_{2.7}Tl_{2.2}C_{60}$	45
Borides	MgB_2	39
	ZrB_{12}	5.82
	YRh_4B_4	11.3
Borocarbides	YPd_2B_2C	23
Oxides	$Ba_{0.6}K_{0.4}BiO_3$	30
	$LiTi_2O_4$	13.7
Cuprates	$YBa_2Cu_3O_7$	92
	$Bi_2Sr_2Ca_1Cu_2O_8$	80
	$Bi_2Sr_2Ca_2Cu_3O_{10}$	110
	$Hg_2Sr_2Ca_2Cu_3O_{10}$	135
Oxypnictides	$SmO_{0.9}F_{0.1}FeAs$	55
	$NdO_{0.82}F_{0.18}FeAs$	51

1.3.1   Crystal structure

The important structural element of all high T_c superconductors is the set of n CuO_2 planes separated by the charge reservoirs. Materials such as $La_{2-x}Sr_xCuO_4$ and $Nd_{2-x}Sr_xCuO_4$

contain one plane per unit cell and are referred to as single layered compounds. The most commonly studied $Bi-2212$ and $Y-123$ systems are double-layered systems with $n=2$ planes per unit cell. The electron transport and processes responsible for superconductivity at high T_c are believed to be the intimately connected CuO_2 planes.

Several families of cuprates can be synthesized with $n=1,2,3$ and within each family, the transition temperature increases with number of CuO_2 layers. Also, the cuprates are characterized by superconducting CuO_2 planes separated by non-metallic interlayer acting as charge reservoirs for the CuO_2 planes. It has an orthorhombic or tetragonal lattice structure, with an elongated *c*-axis while *a*- and *b*-axes are of comparable or same length. The general chemical formula of high T_c superconductors can be empirically represented as $A_mE_2Ca_{n-1}Cu_nO_{2n+m+2+y}$, where *A = Bi/Pb/Tl/Hg/Au/Cu/ Ca/B/Al/Ga, E = Ba or Sr,* and *m* and *n* are integers and *0 < y< 1* [Yamauchi et al. (2000)].
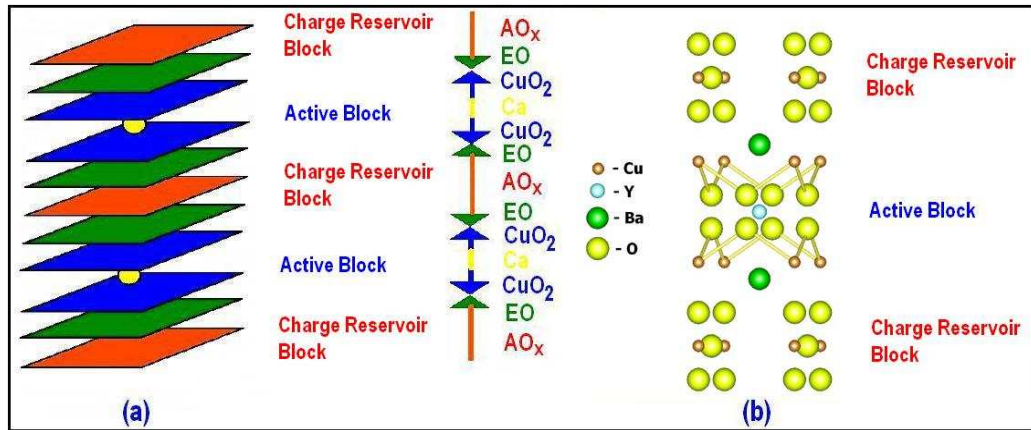
Figure 1.5: (a) General crystal structure of cuprate based high temperature superconductor and (b) shows the crystal structure of $YBa_2Cu_3O_{7-\delta}$ **superconductor.**

The choice of E depends on the active layers $\left(AO_x\right)$ involved, since it has to provide necessary spatial adjustment of CuO_2 to the AO_x layers. These active layers and $\left(CuO_2/Ca_{n-1}/CuO_2\right)$ stacks are separated by charge reservoir stack, $EO/\left(AO_x\right)_m/EO$ as shown in figure 1.5 (a). Superconductivity in **HTS** is believed to have its origin from different superconductive

interactions existing in the CuO_2 layers [Orenstein et al. (2000)]. Strongest of all these interactions is the intralayer coupling within each CuO_2 layer. Interlayer coupling, the superconductive interactions between CuO_2 layers within a given $\left(CuO_2 / Ca_{n-1} / CuO_2 \right)$ stack, is weaker than intralayer coupling. The weakest of all is the Josephson's coupling, which exists between different $\left(CuO_2 / Ca_{n-1} / CuO_2 \right)$ stacks across the insulating interlayer. For example, figure 1.5 (b) showing the $YBa_2Cu_3O_{7-\delta}$ structure, one can clearly see stacks of the simple cubic perovskite. On inspecting the structure, one plane at a time, one finds that the orthorhombic $Y-123$ structure consists of layers such as, *CuO, BaO, CuO2, Y, CuO2, BaO* and *CuO,* beginning at the bottom and proceeding upwards. Thus, in $YBa_2Cu_3O_{7-\delta}$ superconductor, $\left(CuO_2 / Y / CuO_2 \right)$ and *BaO* layers act as CuO_2 stack and active layer, respectively.

1.3.2   Important properties

The layered structure, non stoichiometry and anisotropic properties are certain common features of high temperature cuprate based superconductors. All cuprate based **HTS**s have CuO_2 sheets with or without apical oxygen atoms. The mobile charge carriers in the cuprates are in the CuO_2 planes and the superconductivity is believed to take place in these planes. These CuO_2 planes are separated each other by intervening $Cu-O$ chains in 123 and 214 cuprates. The   layer   containing   other   materials   or   metal   oxide   layers $\left(Ba-O, \; Bi-O, \; Tl-O \; and \; Hg-O \right)$ in other cuprates serve as the charge carrier reservoirs. The presence of other elements and the spacing between the CuO_2 planes also change the value of T_c.

If the crystal contains an element with variable valancy, then any change in the number of ions of that element can be compensated by changes in the ion charge. This maintains the charge balance but alters the stoichiometry. Elements with variable valancy mostly occur in transition elements and in rare earths. The non stoichiometric compounds can have formulae that do not have simple integer ratios of atoms. They usually exhibit a range of compositions.

The oxygen stoichiometry and ordering also plays a crucial role in determining the structure and properties of cuprates. In 123 systems the dependence of the structure and properties on oxygen content has been well studied, because the oxygen stoichiometry is easily

varied between 6 and 7 due to the loosely bound oxygen atoms in the $Cu-O$ chains. For example in $YBa_2Cu_3O_{7-\delta}$, when $0 \leq \delta \leq 0.25$, the structure is orthorhombic $(c = 3b)$ and $T_c = 90\ K$. When $0.3 \leq \delta \leq 0.4$, the structure is still orthorhombic, but $c \neq 3b$, and $T_c = 50-60\ K$. When $\delta = 1.0$, the structure is tetragonal and the material is non superconducting. In the case of $BSCCO$ system, excess oxygen in the $Bi-O$ layers (one oxygen for every four or five unit cells) leads to incommensurate modulation.

Finally the **HTS** materials are highly anisotropic in many of their properties such as resistivity, critical current and upper critical field [Hagen et al. (1988), Worthigton et al. (1987)]. This is thought to arise from the quasi two-dimensional nature of the conducting CuO_2 planes [Goodenough et al. (1990), Raveau et al. (1990)]. In $Bi-2212$ crystals, the normal state conductivity parallel to the CuO_2 planes is typically 10^5 times higher than that in the perpendicular direction, making them the most anisotropic of all known superconductors. The anisotropic parameter η is 1 for *NbTi* and Nb_3Sn, 2 to 3 for MgB_2, 5 to 7 for *YBCO* and 50 to 200 for *BSCCO*. The large anisotropic nature of *BSCCO*, restricts its application at very low temperatures and low self-field uses such as power cables, even though $H_{C2}\ (at\ 77\ K)$ exceeds 10 T. The anisotropy in critical current density (J_C) is one of the important factors to be considered for practical applications such as the fabrication of superconducting magnets and for other field based applications. In addition to this, the investigation of anisotropy in **HTS** materials will provide very useful information on the dominant pinning mechanism operating in these materials.

1.3.3   The Bi$_2$Sr$_2$Ca$_{n-1}$Cu$_n$O$_{2n+4+\delta}$ system

The Bi-based high T_c cuprate superconducting materials can be represented by the homologue series having general formula $Bi_2Sr_2Ca_{n-1}Cu_nO_{2n+4+\delta}$ that contain either, $n = 1,\ 2\ or\ 3\ CuO_2$ layers per unit cell. Primitive unit cells of single-layer, bilayer, and trilayer Bi-based superconductors differ only in the number $(n-1)$ of $CuO_2/Ca/CuO_2$ slabs packed along the c-axis; upon insertion of one or two slabs, the c-axis parameter of the crystallographic cells increases from 24.6 to 30.6 and 37.1 Å [Tarascon et al. (1998)]. All the members in the series are superconductors with different T_c values. The $Bi_2Sr_2Cu_1O_{6+\delta}$ superconductor (n = 1)

has a T_c around ~ 10 K. $Bi_2Sr_2Ca_1Cu_2O_{8+\delta}$ (n=2) and $Bi_2Sr_2Ca_2Cu_3O_{10+\delta}$ (n = 3) have $T_c s$ of ~ 80 K and 110 K, respectively [Maeda et al. (1988)]. The compounds with higher value (n = 4 and 5) also exist in multiphase mixture of bulk or thin films having a T_c of 90 K and 50 K, respectively.

1.3.3.1. Bi-2201 system

The $Bi_2Sr_2Cu_1O_{6+\delta}$ system is usually referred to as $Bi-2201$ and it has a T_c of ~ 10 K. Its structure contains a CuO_2 layer at its centre surrounded by a $Sr-O$ layer and then a $Bi-O$ layer on each side. The equilibrium phase is over doped with holes and is a semiconductor. This phase is orthorhombic (*Amaa*) with cell parameters; a = 5.36 $\overset{\circ}{A}$, b = 5.37 $\overset{\circ}{A}$ and c = 24.37 $\overset{\circ}{A}$. The number of formula units per cell is $Z = 4$. The superconducting Raveau phase is reported to have a wide range of solid solubility and pseudo tetragonal crystal symmetry. $Bi-2201$ has the simplest prototype structure due to the presence of single octahedrally coordinated $Cu-O$ planes with no intervening Ca layer like other Bi-based superconductors.

1.3.3.2. Bi-2212 system

The $Bi_2Sr_2Ca_1Cu_2O_{8+\delta}$ ($Bi-2212$) is the most important and extensively studied high T_c phase (Figure 1.6). The crystal structure of $Bi-2212$ is composed of three building blocks other than two CuO_2 planes: (1) Bi_2O_2 block, (2) $Sr-O$ block, and (3) Ca block. These three blocks are charge reservoirs and, at the same time, sources of disorder which result in the structural supermodulation of the $Bi-O$ layers. The excess oxygen atoms are located in or near the Bi_2O_2 block which acts as the hole dopant. Bi^{3+} ions tend to replace the Sr^{2+} ions in the $Sr-O$ block (sometimes called site mixing). The Ca^{2+} ions in the plane sandwiched by two CuO_2 planes can easily be replaced by rare-earth ions with relatively smaller ionic radii. Bi^{3+} and RE^{3+} substituted for Sr^{2+} and Ca^{2+} decrease the hole density in the CuO_2 layer. Ca adopts eight co-ordinates. There is no oxygen at this level. Therefore, Cu has only five nearest neighbours in square pyramidal co-ordination rather than elongated octahedral co-ordination of $Bi-2201$. The structure may be described with the orthorhombic Amaa group with cell

parameters being $a = 5.414 \overset{\circ}{A}$, $b = 5.418 \overset{\circ}{A}$ and $c = 30.89 \overset{\circ}{A}$, with $Z = 4$. The detailed structural parameter of $Bi_2Sr_2Ca_1Cu_2O_{8+\delta}$ is given in **table** 1.2.
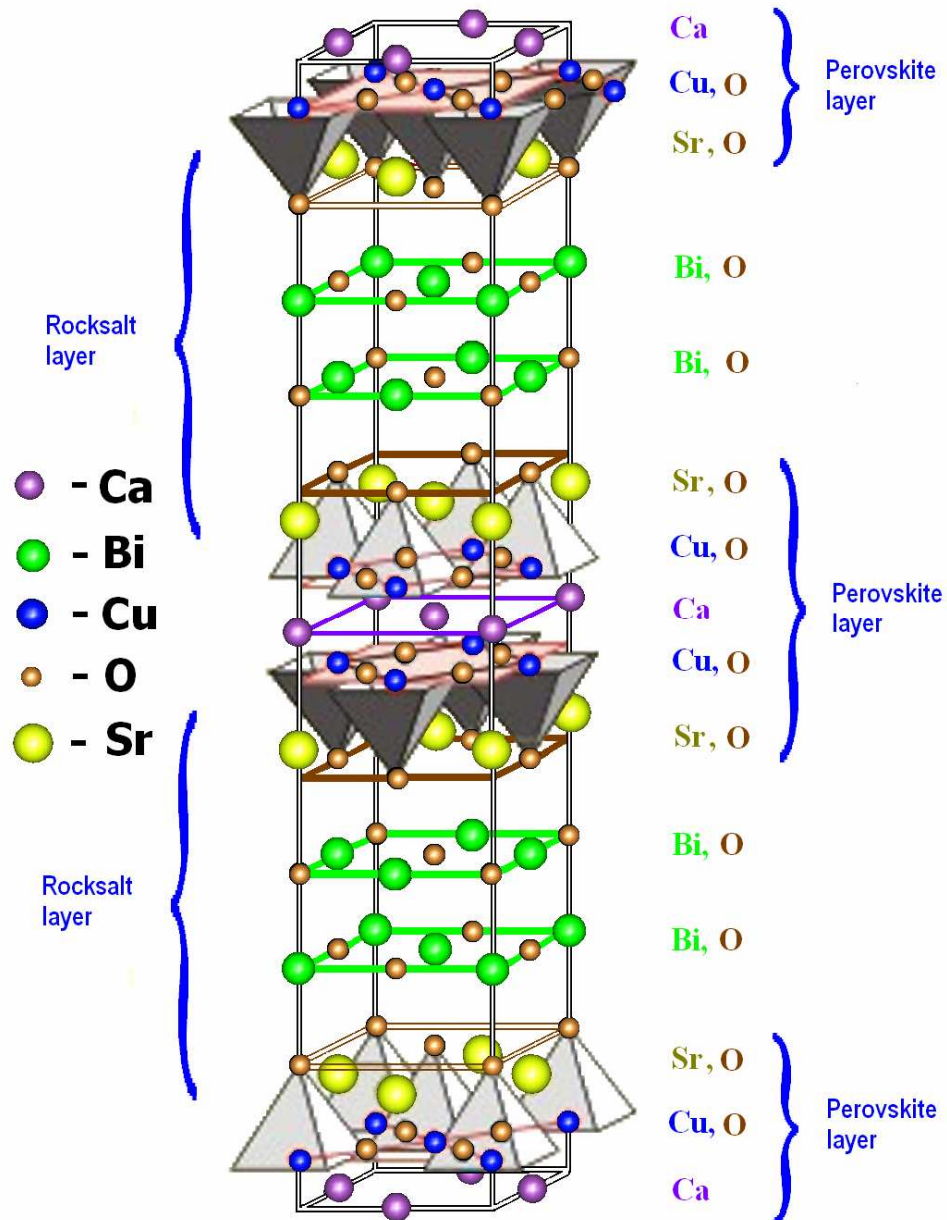
Figure 1.6: Crystal structure of $Bi-2212$ high temperature superconductor.

Table 1.2: Structural parameters of Bi$_2$Sr$_2$CaCu$_2$O$_{8+\delta}$ obtained by Rietveld Refinement [Sunshine et al. (1988)].

Cell parameter	a = 5.415 Å	b = 5.419 Å	c = 30.90 Å	V = 906.7 Å^3	
Atom	Position	x	y	z	Occupancy
Bi(1)	8i	0.00	0.00	0.1989	1.0
Sr	8i	0.00	0.50	0.1091	1.0
Ca	4b	0.00	0.50	0.0000	0.8
Bi(2)	4b	0.00	0.50	0.0000	0.2
Cu	8i	0.00	0.00	0.0543	1.0
O(1)	16j	0.25	0.25	0.0510	1.0
O(2)	8i	0.00	0.50	0.1980	1.0
O(3)	8i	0.00	0.00	0.1200	1.0

1.3.3.3. Bi-2223 system

The $Bi_2Sr_2Ca_2Cu_3O_{10+\delta}$, referred to as $Bi-2223$, shows the highest T_c of 110 K among Bi-based superconductors. Its structure consists of additional CuO_2 and Ca layers, inserted with $CuO_2 / Ca / CuO_2$ block of $Bi-2212$ yielding $CuO_2 / Ca / CuO_2 / Ca / CuO_2$ club sandwich. The other Cu atoms are in square pyramid co-ordination while inner Cu atoms are in square plane co-ordination. These layers are separated by insulating layers with a rock salt structure. These rock salt layers lead to a distance of 1.2 nm, the coherence length between the blocks. Hence, anisotropy is large (>30), pinning is weak and transport properties are very sensitive to magnetic fields. The space group assigned to this phase is *Amaa* with a $= 5.39$ Å, b $= 5.41$ Å, c $= 37.1$ Å, and $Z = 4$.

1. 4 Physics behind the HTS materials

The CuO_2 layers are believed to be the location of the mobile charge carriers in the cuprate *HTS* compounds [Orenstein et al. (2000)]. This is in agreement with band structure calculations [Figure 1.7 (a)]. There are several chemical, structural and electronic aspects of the copper oxide superconductors that distinguish them from other oxides. In copper oxide, the difference in energy between the oxygen and metal orbital is very small, and produce electronic

energy bands. Also, oxygen is highly involved in the conduction process as in the case of copper, which is a rare situation in conducting oxides.
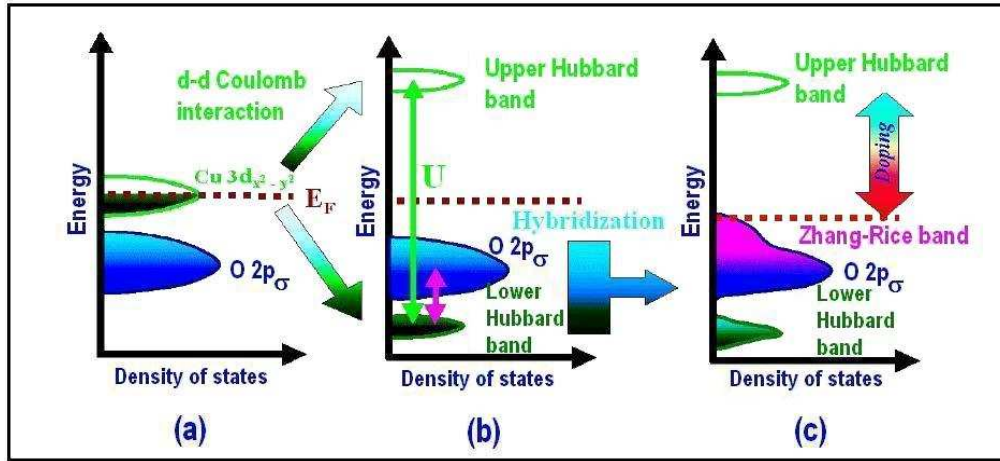
Figure 1.7: Schematics of the electronic energy states involved in the charge transport in *HTS* (a) in an independent electron model, (b) including on-site Coulomb repulsion of the $Cu\ 3d_{x^2-y^2}$ states and (c) hybridization of oxygen $O\ 2p_\sigma$ states and the lower Hubbard $Cu\ 3d_{x^2-y^2}$ band.

The electronic configuration for Cu atom is $1s^2 2s^2 2p^6 3s^2 3p^6 4s^2 3d^9$: nine of the ten available d-orbital energy states are filled. The shape of the $Cu-O$ co-ordination polyhedra are such that there are four near in-plane oxygen neighbors and one or two distant apical oxygen. This makes the energies of the orbital towards the apices because of lower repulsion from the oxygen orbital. The result is that the nine electron configuration has a single unpaired electron in the $Cu\ 3d_{x^2-y^2}$ orbital [Figure 1.8]. That is the deformation of the oxygen octahedra which surround each Cu ion make the $3d_{x^2-y^2}$ orbital, the only unoccupied $Cu\ 3d$ orbital and it accommodate the single hole.

This copper $3d_{x^2-y^2}$ state hybridizes with the $O\ 2p_\sigma$ orbital of the surrounding four oxygen atoms. Due to the strong Coulomb repulsion for adding another hole at a Cu site, these holes cannot move to neighboring Cu sites. This Coulomb correlation effect prevents a metallic behavior and turns the stoichiometric *HTS* compounds into insulators [Figure 1.7 (b)].
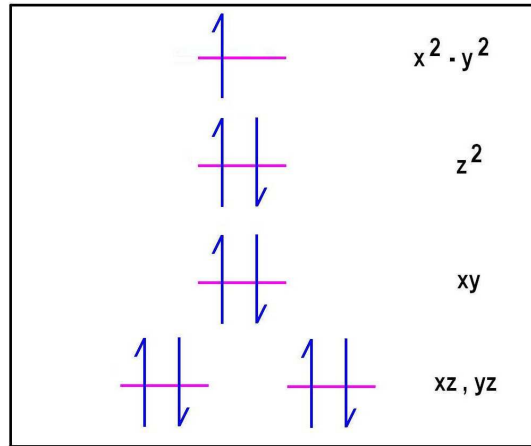
Figure 1.8: The d-electron configuration for Cu^{2+}.

Actually, the metal-insulator transition of copper oxides is more complicated than this classical Mott scenario. The gap for electronic excitations here is not determined by the mutual Coulomb repulsion of copper $3d_{x^2-y^2}$ holes, but, by the energy required to transfer a charge from an oxygen ion to the copper ion since the highest occupied electronic states are derived from oxygen $O\ 2p_\sigma$ orbital with only a small admixture of Cu character [Figure 1.7 (c)]. Hence, undoped copper oxides are not Mott-Hubbard insulators but Charge-Transfer insulators. Virtual charge fluctuations generate a super-exchange interaction, which favours antiparallel alignment of neighbouring spins. The result is long-range anti-ferromagnetic order up to rather high Néel temperatures T_N. What is special about copper oxides in the big zoo of conducting oxides is that they are composed of CuO_2 layers which form 2-dimensional spin-1/2 Heisenberg anti-ferromagnetic subsystems that are subject to particularly strong quantum spin fluctuations. This is the starting point for many theoretical descriptions of the HTS in cuprate compounds such as the Resonating Valence Bond (RVB) [Anderson (1987)] or the Quantum Critical Point (QCP) scenario. In the RVB picture, the anti-ferromagnetic lattice is perceived as a network of spin singlets made up of pairs of antiparallel Cu spins of the anti-ferromagnetic lattice. The ground state of the anti-ferromagnetic lattice is in this view a resonating superposition of such configurations of valence bonds in close analogy to the chemical picture of resonating double

bonds in benzene. Putting an additional oxygen hole on a certain lattice site compensates the corresponding *Cu* spin by means of a singlet formation and leaves somewhere an unpaired spin of the related broken valence bond. The same holds true for the removal of a *Cu* hole (along with its spin). The many-body ground state of such a system with broken valence bonds is suggested to be a liquid-like state made up of the remaining resonating valence bonds and the decoupled charges (holons) and unpaired spins (spinons) as independent degrees of freedom.

The single-band Hubbard model and its variations have become the most common framework used for making theoretical analyses and predictions about the cuprates [Hubbard (1963)]. They are tight-binding models, which says that each electron is modeled as being bound to a specific discrete site, as opposed existing in a state with more continuous degrees of freedom. In its original formulation, the Hubbard model only allows electrons to move directly to immediately adjacent sites (called nearest neighbour hopping, controlled by the transfer parameter t), but extensions to the model can also include next-nearest neighbour hopping (parameterized as t'), or even greater hops (t'') etc. Among the biggest successes of this model is its ability to produce a normal state Fermi surface consistent with experimental measurement. As a result, such measurements are routinely parameterized in terms of the hopping parameters of the model. The Hubbard model consists of a simple two-part Hamiltonian intended to describe a system of strongly interacting particles, such as the electrons in a Mott insulator. The particles are assumed to be on a lattice with up to two present at each site. The Hubbard Hamiltonian is:

$$H = H_{hop} + H_{\text{int}} \tag{1.1}$$

where, H_{hop}, the energy required by the particles to hop from one site to another. This form is originally written by Gutzwiller [Gutzwiller (1963)] in which, the kinetic energy term H_{hop} is given in momentum space terms. The second term (H_{int}) represents the energy required for two particles to occupy the same lattice site, and is referred to as the interaction term. Shortly after Gutzwiller wrote it in this form, the first term of the Hamiltonian was rewritten in real space terms by Hubbard [Hubbard (1963)]:

$$H_{real-space} = \sum_{x,y,\sigma} t_{x,y} c_{x,\sigma}^{\dagger} c_{y,\sigma} + \sum_{x} U_x n_{x,\uparrow} n_{x,\downarrow} \qquad (1.2)$$

where, c and $c^{\dagger}$ are creation and annihilation operators, respectively, t is the kinetic energy (or transfer) term, and $\sigma \in \{\uparrow, \downarrow\}$. While x and y can refer to any sites in the lattice, the matrix element $t_{x,y}$ is non-zero only when they are nearest neighbours. Despite its simple form, with suitable choices of t and U, the Hubbard model can be shown to exhibit a range of properties including magnetic order such as antiferromagnetism. As $U \to 0$ for non-zero t in equation (1.2), the system approaches a non-interacting state, with plane wave solutions. At the other extreme, as U becomes large with respect to t, the energy required for two particles to occupy the same site becomes large and the system is referred to as strongly correlated. In the half filled Hubbard model, the number of electrons becomes same as lattice sites. By increasing $U \to t$, the model describes a transition from metal to Mott insulator (a Mott transition), since the increasing Coulomb repulsion at a particular site, prevents electron transport from site to site. This brings us closer to a plausible model of the normal state CuO_2 plane in the cuprate based superconductors.

Although the Hubbard model can display many properties of Mott insulators, it does not offer any direct insights into the cuprates. For that, a model was needed, that represented the behaviour of electrons and holes in the CuO_2 plane. Emery proposed [Emery (1987)] a three-band Hamiltonian that accounted for the various energy contributions of electrons and holes in the copper and oxygen orbitals, and of those hopping between them. Zhang and Rice were able to simplify this construction significantly by introducing the object now known as the Zhang-Rice singlet state [Zhang et al. (1988)]. It was known experimentally that holes in the CuO_2 plane actually lie on oxygen sites. In the half-filled $(U - t)$ Hubbard model, each copper atom can be regarded as having a $3d_{x^2-y^2}$ hole, since it has a $3d_{x^2-y^2}$ state with only one electron in it. This hole is depicted in as having spin $\downarrow$ in figure 1.9. Zhang and Rice argued that once the material is hole doped, any hole on the surrounding oxygen atoms can form a lower energy state by hybridizing with the central copper hole to form a singlet state. These singlets would then be free to travel around the crystal, hopping from site to site, always centred around one copper atom. Because the motion is centered on the copper atoms, the system can be described with a

one-band model that disregards the oxygen sites. The result is a theoretical justification for the validity of using the $t-J$ model, as originally proposed by Anderson [Anderson (1987)], to represent the in-plane electronic structure of the cuprates. This model is constructed by taking the $U \rightarrow t$ limit of the Hubbard model, and introducing an antiferromagnetic interaction term:

$$H_{\text{int}(t-J)} = J \sum_{\langle i,j \rangle} \left(S_i.S_j - \frac{1}{4} n_i n_j \right)$$

(1.3)
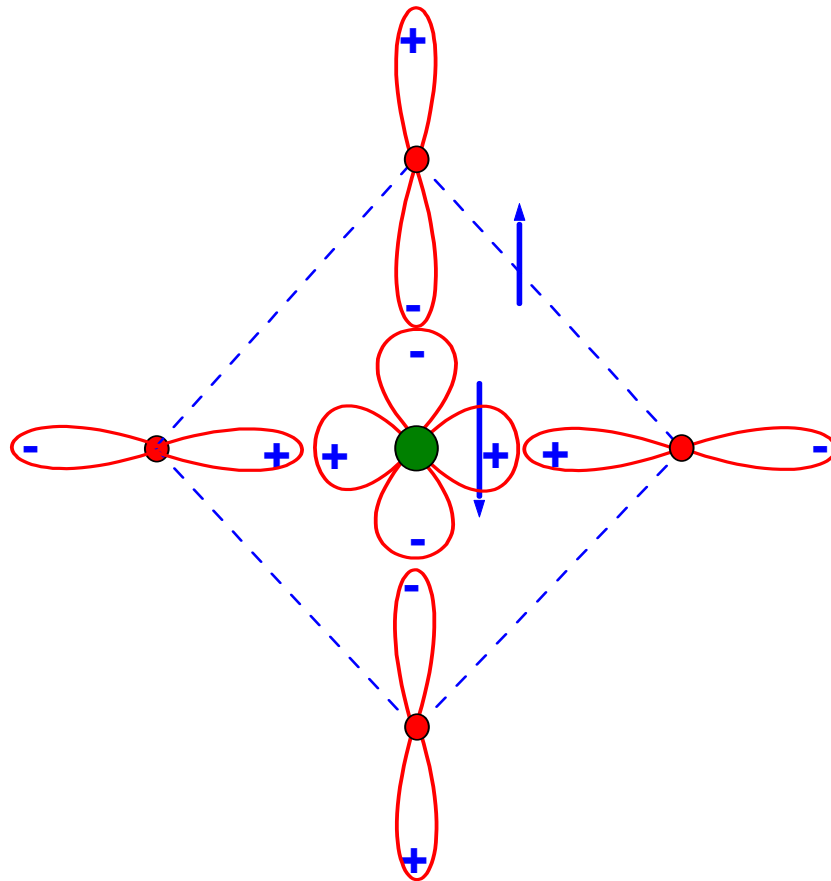
Figure 1.9: The Zhang-Rice singlet. Four oxygen atoms (red) surround a central copper atom (olive). A down-arrow represents the spin of the hole present on any copper site, and an up-arrow represents the spin of a dopant-induced hole on the oxygen site.

where $\langle i, j \rangle$ are nearest-neighbour pairs, S_i and S_j are spin $1/2$ operators. The antiferromagnetic interaction energy J is equal to $4t^2/U$ because of the possibility of a virtual spin-flipping process involving a hop to an adjacent occupied site and back. This model produces an antiferromagnetic ground state (in the $U \rightarrow t$ or undoped limit), since the energy of the system can be lowered by ensuring that neighboring electrons have oppositely aligned spins.

Numerical studies of the two-dimensional $t - J$ model suggest that at optimal values of the parameter $J/t \left(\sim 0.3 - 0.4 \right)$ the holes form bound pairs with effective attractive force acting between them. These pairs can then be expected to condense at low temperatures, leading to superconductivity [Dagotto (1994)]. In this picture, the formation of the pairs does not immediately require that they condense into a single ground state, which potentially explains the pseudogap state - the region of the phase diagram exhibiting a precursor energy gap but no superconductivity.
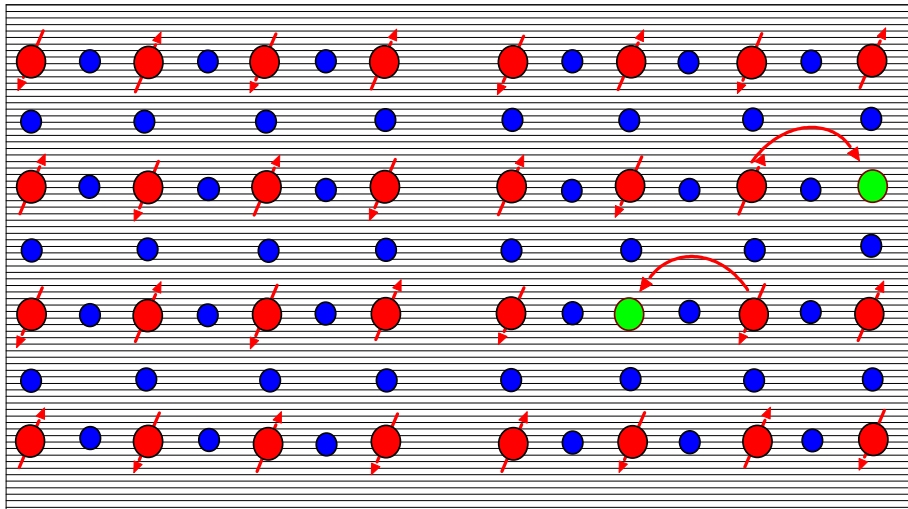
Figure 1.10: Simple model for the electronic degrees of freedom in the CuO2 plane of cuprate high temperature superconductors. Left panel: Square lattice with one spin (1/2) state at every vertex. Coulomb repulsion prevents electron hopping, and antiferromagnetic correlations impose an overall antiferromagnetic ground state. Right panel: With hole doping, electron hopping becomes possible. (Red = Cu, Blue = O).

It should be noted that, despite being the most frequently cited, the Zhang-Rice singlet is not the only plausible state to be proposed as the charge carrying unit in the cuprates. It is necessarily centred on the copper atoms of the CuO_2 plane, but experimental evidence of oxygen-centred, static charge ordered states has recently begun to emerge.
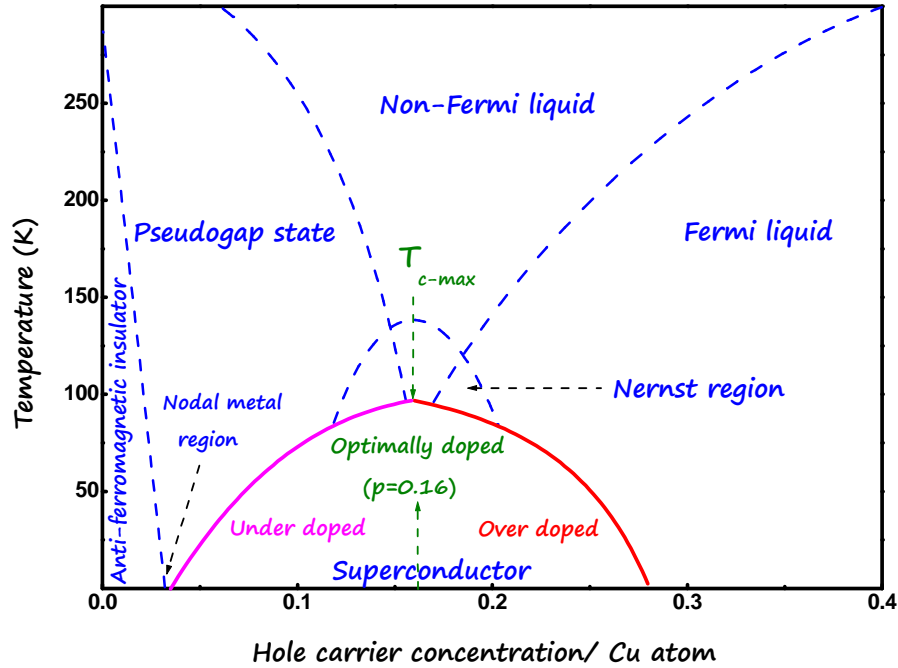
Figure 1.11: Generalized temperature - hole doping phase diagram of *HTS* dominated by the interplay of anti-ferromagnetism and superconductivity.

In the copper oxide superconductor parent materials, the Cu^{2+} spin ½ ions in this CuO_2 plane are ordered anti-ferromagnetically at a high temperature and the materials are insulating. The high anti-ferrimagnetic ordering temperature indicates that the copper spins are coupled very strongly. Superconductivity is induced when the electron count in the CuO_2 plane is changed from one electron per copper site. It means that, compounds are doped to make the formal copper valence differ from Cu^{2+}, typically higher. This is accomplished through manipulation of the charge reservoir layer, either by adding oxygen or by partial substitution of one atom of higher or lower valence for another. In other words, the parent compound is doped by either electrons or holes, and the anti-ferromagnetic ordering changes to superconductivity. This is because with doping, hoping of electrons from Cu to Cu becomes possible as shown in the right panel of the figure 1.10.

A schematic phase diagram of hole-doped cuprates (which are the most widely studied examples of the cuprate high-temperature superconductors) is presented in figure 1.11. They exhibit superconducting critical temperatures up to 150 K at optimum hole doping near $p \sim 0.16$, where $p \sim 0.16$ is the number of doped holes per Cu atom. At zero temperature, the undoped parent compound is a charge transfer (Mott) insulator, with an antiferromagnetic

ordering of spin states on the copper sites of the CuO_2 lattice. Unlike in regular band-gap insulators, charge transport in Mott insulators is inhibited at the cost of high Coulomb energy associated with doubly occupied copper sites. Removing electrons (in other words, creating holes) allows charge to flow by leaving some proportion of vacant sites for electrons to hop into, a process which also destroys the antiferromagnetism.

Introducing small numbers of mobile charge carriers in this way, with low levels ($p \leq \sim 0.06$) of hole doping, first produces a poorly conducting (and poorly understood) spin glass state. At slightly higher doping, when a sufficient concentration of charge carriers is present, the superconducting state mysteriously emerges. The exact reason for this is, one of the most important unsolved problems in physics. Superconductivity is most resilient against increases in
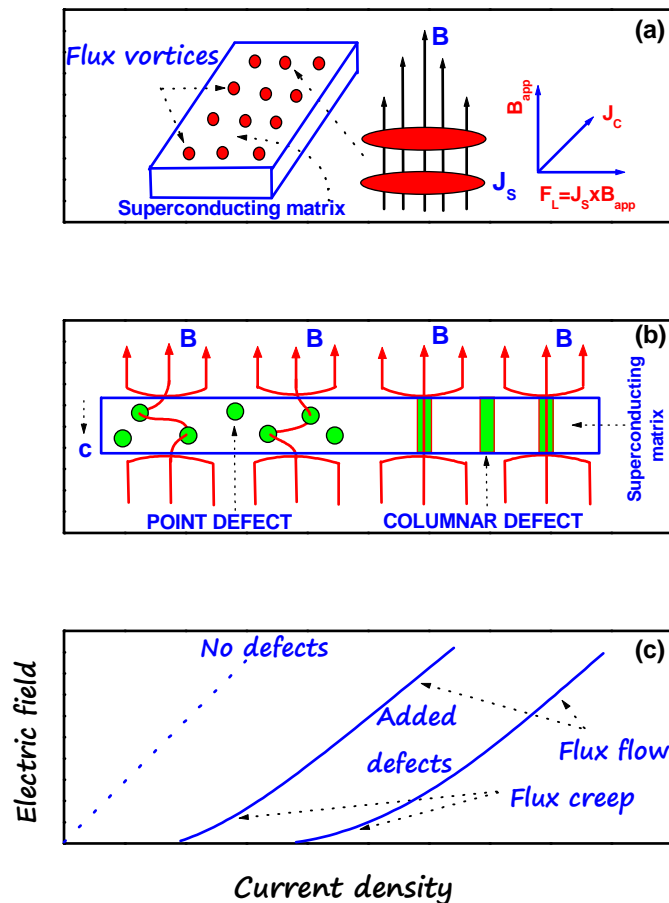
Figure 1.12: (a) The type II superconductor in the vortex state showing the flux vortices and the magnetic field (B) in a vortex core. Here J_S is the superconducting circulating screening currents associated with the vortices and F_L is the Lorentz force, (b) schematic illustrations for two kinds of pinning centers in HTS and (c) the $E - J$ characteristics for flux creep and flux flow of HTS materials.

temperature and magnetic field at an optimal doping level of around $p \sim 0.16$, but persists until above $p \sim 0.25$, at which point the crystal behaves like a metal, and any of the remaining antiferromagnetic order disappears [Wakimoto et al. (2004)].

1. 5   Flux pinning and critical current density

Based on the behavior of superconductors in the presence of magnetic fields, they are classified into two categories, Type I and Type II as mentioned in section 1.2. In Type I superconductors, above the thermodynamic critical field, H_C, perfect diamagnetism is destroyed and the superconductor is reverted back to the normal state. But in Type II superconductor, perfect diamagnetism is observed only up to a limit called the lower critical field H_{C1}. Above H_{C1}, the magnetic flux lines partially penetrate into the material up to a field called the upper critical field, H_{C2}, and above H_{C2}, the magnetic flux fully penetrates into the material and the material returns back to the normal state. Between H_{C1} and H_{C2} the material is said to in a mixed state or vortex state. Thus in the vortex state, the type II superconductor is filled with fluxons and each fluxons are quantized flux vortices which are shown in figure 1.12 (a). The number of quantized vortices increases with external field and in a perfect superconducting crystal the competition between the inter-vortex repulsion and the magnetic pressure from the outside field causes the vortices to arrange themselves in a regular lattice known as Abrikosov vortex lattice. An Abrikosov vortex has a normal core, which can be approximated by a long thin cylinder with its axis parallel to the external magnetic field. The diameter of the cylinder is of the order of 2ξ and the density of Cooper pairs $|\psi|^2$ decreases to zero at the vortex centers (Figure 1.13). The direction of the circulating super-current around the core is such that the direction of the magnetic field generated by the current coincides with that of the external field and is parallel to the normal core. The magnetic field and the circulating currents decay radially out from the core as, $B(r) \propto \ln(\lambda_L/r)$ at short distances and as, $B(r) \propto r \exp(-r/\lambda_L)$ at long distances from the vortex centers. The circulating super-currents surrounding the vortex core, predominantly located in the CuO_2 planes, cause an interaction between the vortices, which is repulsive (attractive) for parallel (antiparallel) vortices. The interaction extends to a distance of the order of λ_L [Minnhagen et al. (1987), Pearl et al. (1964)].
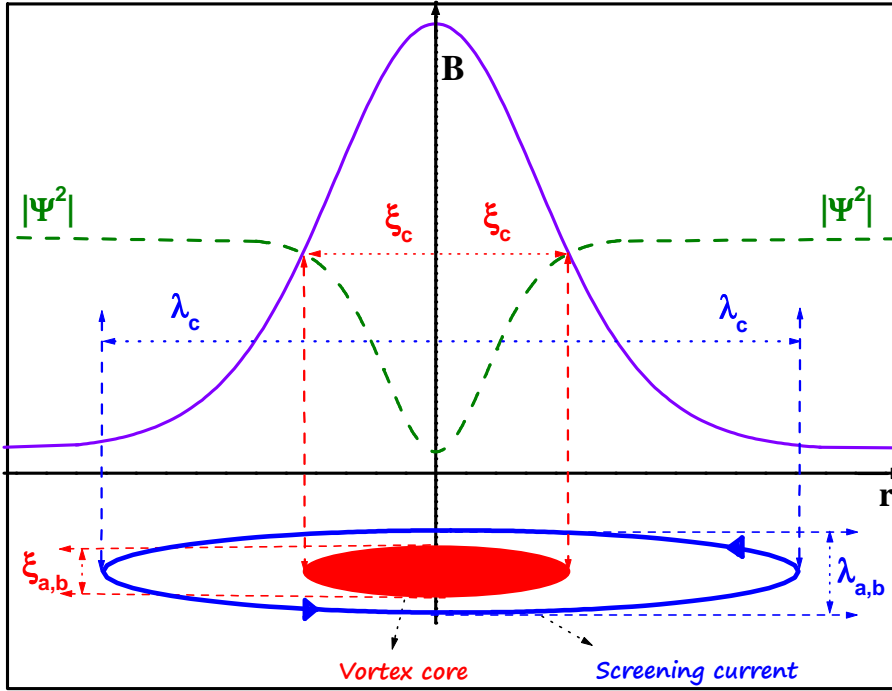
Figure 1.13: Sketch of an Abrikosov vortex in an anisotropic superconductor. The diameter of the vortex cylinder is of the order of 2ξ and the density of Cooper pairs $\left(\left|\psi\right|^2\right)$ decreases to zero at the vortex centers.

The ideal Type II superconductors are not suitable for many bulk applications, because when a macroscopic transport current flow through the superconductor, the fluxons experience a Lorentz force $F_L = J_S \times B_{app}$, in a direction perpendicular to both the super-current $\left(J_S\right)$ and applied magnetic field $\left(B_{app}\right)$ [figure 1.12 (a)]. This Lorentz force tends to move the flux lines and it will result an e.m.f equal to the rate of change of flux (the flux flow induces an electric field $E = n_f \phi_0 v_f$, where n_f is the number of fluxons, ϕ_0 is the quantum of flux and v_f is the velocity of flux flow). Therefore, the material acquires an electrical resistance, and hence energy is dissipated. Hence, in order to sustain the non dissipative current flow at high fields and temperatures the flux lines must be pinned. Most **HTS** materials contain point defects and columnar defects [Figure 1.12 (b)], which tend to pin the flux vortices and consequently the

magnetization curve becomes irreversible. The resultant pinning force opposes the movement of flux lines until the current density attains a critical value J_C, given by the balancing equation, $F_P = J_C \times B$ per unit volume of superconductor. When Lorentz force F_L exceeds a characteristic pinning force F_P, the flux lines can move and the voltage will be detected and hence, energy is dissipated [Lee et al. (2001)].

The physics and engineering of vortex dynamics and flux pinning are highly interesting and are active research fields in applied superconductivity. The atomic or crystal defects, grain boundaries, voids, strains, twin planes, inhomogeneities and secondary phases present in real superconductors are effective pinning sites. The flux pinning can be improved to maximize J_C in practical conductors by tailoring the microstructure of the superconductor. The tailoring of microstructure for optimized flux pinning can enhance the J_C by even one or two orders of magnitude in practical superconductors at higher magnetic fields. To nucleate a flux line within the superconductor, the system must provide enough energy to convert the core of the flux line to the normal state. This energy per unit length of flux line, called the condensation energy, is given by the volumetric free energy due to the magnetic field within the flux line and the cross sectional area of the fluxon core as $E_{cond} = \dfrac{\mu_0 H_C^2}{2} \pi \xi^2$, where H_C is the thermodynamic critical field and ξ is the coherence length. If the flux line is centered on a flux pinning center such as a void or normal conducting inclusion of radius ξ, the condensation energy needed to produce the normal core of the flux line would be saved, and the flux line would see a lower free energy at the location of the void than it would be in the bulk. That is, a pinned vortex has a lower free energy than a free vortex in a superconductor. The result of this free energy change is that the flux line requires an increase in its energy per unit length equal to the condensation energy, to move away from the flux pinning center. Thus, the flux pinning center holds the flux lines from moving and hence reduces the dissipation.

In a practical superconductor, there will be a large number of flux lines interacting with each other and interacting with different pinning centers. The bulk flux pinning depends on the basic interactions between the individual flux lines and between flux lines and individual pinning centers. For a weak interaction between the flux lines (the magnetic interaction between flux lines is repulsive) the flux line lattice acts as a two dimensional elastic crystalline solid. In this case there will be as many flux lines as possible are located on the pinning centers. If the

number density of flux lines is less than or equal to the number of pinning centers (for instance in small applied fields) then each flux line is individually pinned and the bulk pinning force is large. On the other extreme in which the interaction between the flux lines is strong, the flux line lattice acts as a two dimensional rigid crystalline solid. In this case, the bulk pinning force due to a collection of randomly distributed pinning centers will be small over the completely rigid flux line lattice. However, for practical polycrystalline systems the correct description of pinning lies somewhere between these two extremes of direct summation and rigid flux line lattice.

Again at finite temperature, the flux lines may jump from one pinning configuration to another by overcoming the energy barrier due to thermal fluctuations, resulting in energy dissipation. The net flux movement is zero in the absence of current, however in the presence of even a small current; there will be a net flux in the direction of Lorentz force [Lee et al. (2001)]. As the current increases, the number of forward jump increases while the backward jump decreases leading to an increase in net flux movement. The effect of thermally activated flux creep tend to dominate the early stages of dissipation in **HTS** materials due to the fact that the activation energy is smaller for conventional Type II materials and because they are usually used at higher temperatures, hence, the thermal energy is greater. This thermally activated flux creep causes a significant curvature of the $E - J$ characteristic curve around J_C as shown in Figure 1.12 (c).

1.6.   Applications

The unusual physical properties of superconductors resulted in some remarkable applications in specific areas. Superconducting materials can replace the conventional materials in many applications, with better performance. The choice between conventional and superconductive materials is generally related to technical and economical aspects, and the latter is the main factor limiting the widespread use of superconductors in practical applications. However, in many fields the superconducting technology is often the only possibility for achieving the required performance. By using superconducting components, the size and weight of instruments and devices can be reduced compared to conventional techniques which are an important issue for fields like space applications. Today, superconductors have a wide range of commercial and industrial applications in energy production, storage, and its distribution, in

sensor materials, in microwave communication systems and most importantly in high field magnets. The main application sectors of superconducting materials are given in ***table*** 1.3.

Superconducting magnets have exclusive uses in some commercially available instruments like *MRI* instruments in medical field, and for high field magnets for *NMR* and particle accelerators. *NbTi*, is the mostly used superconducting material for *MRI* magnets. For high field magnets, *Nb₃Sn* is mostly used and some **HTS** based inserts are also developed for still higher fields. **HTS** based magnets inserted in high field **LTS** magnets are tested upto ~ 25 T [Weijers et al. (2004)]. Superconducting solenoids are being used for bending and focusing of high energy particles in high-energy particle physics labs like *BNL*, *CERN*, *DESY* and the Fermi Laboratory. Besides solenoids, superconducting *RF* cavities are also finding applications in particle accelerators. Large-scale application of superconducting cavities to electron and ion accelerators is established at many laboratories around the world. With the development of cryocoolers, various kinds of cryogen free superconducting magnets with fields of the order of 20 T have been developed for practical applications [Watanabe et al. (2003). In fusion reactors, the plasma temperature needed for energy production is several million degrees, and high field superconducting magnets are required to confine the plasma. The International Thermonuclear Experimental Reactor (*ITER*) project is engaged in the development of fusion reactor and a large quantity of **LTS** superconductors is being industrially manufactured for the project [Potanina et al. (2003), Salpietro (2006)].

Table 1.3: General applications of superconductors.

Area/Field	Applications	Prefered geometry
Energy/Power: Generation & Storage	Generators, SMES, Superconducting bearings for flywheel storage	Coil, wire/tape
Energy/Power: Distribution	Cables, Transformers, Current leads, FCLs, Motors.	Coil, wire/tape (Bulk also in special cases)

Magnets	NMR, MRI instruments, Magnetic confinement of plasma in Fusion reactors, Particle accelerators, High field magnets.	Coil, wire/tape
Electronics	In microwave filters, Digital logic circuits as RSFQ, Sensor applications	thin films
Biomedical	Detection of extremely small neuromagnetic fields, Magnetoencephalanography (MEG), Magnetocardiography (MCG)	thin films, Josephson junctions.
Industrial	Magnets for shielding and separation, sensors	bulk, coil, wire/tape thin films, Josephson junctions
R & D	Superconducting RF cavities in particle accelerators, Synchrotrons and High field magnets.	Coil, Bulk, films, wire/tape.
Other applications	Magnetic levitation, Magnetohydrodynamics, Space applications	Bulk, wire/tape and thin films

Since the super-current in a superconductor persists for a very long time, superconductors have applications in energy storage also. Superconducting Magnetic Energy Storage (*SMES*) can store mega joules of energy, without resistive losses. *SMES* systems capable of storing mega joules of energy are already tested and installed in various places. They

are receiving more importance with regard to future electrical power grids. The Korea Electro-technology Research Institute ($KERI$) has already developed a $3\,MJ/750\,kVA$ $SMES$.

One of the specialities of superconductors is that they find applications in extremely weak and extremely high magnetic fields. Superconducting magnets provides high fields while superconducting thin films are used for the detection of extremely weak fields. The Superconducting Quantum Interference Device ($SQUID$) based on the Josephson effect is the most sensitive magnetometer. $SQUID$ based technology is widely used for the non-invasive clinical measurements of weak biomagnetic fields, especially in the mapping of extremely weak magnetic signals from the human brain. In material science and physics research $SQUID$ based magnetometers and susceptometers are being used for magnetic characterization of materials. The Magnetic Property Measurement System ($MPMS$) and Physical Property Measurement System ($PPMS$), the two well-known commercial instruments manufactured by Quantum Design, USA are based on superconductor technology.

Superconducting cables can replace the conventional copper/aluminium based cables in electric power transmissions and can minimize the transmission loss. However, the higher cost for the superconducting technology compared to the conventional methods is the main hurdle in the limited use of superconductors in this sector. Conductors made of $Bi-2223$ are being applied in variety of power transmission cables and distribution cables. The world's first grid using high temperature superconducting system was energized in New York, USA. Another major application of superconductors in electric power grid is for the control of fault currents in electrical transmission and distribution networks, as Superconducting Fault Current Limiters ($SFCL$). Fault Current Limiters (FCL) restrict the maximum current through a network and protect the devices from an accidental over current. Several groups are actively involved in developing $SFCL$ for industrial applications. A 1.2 MVA, 10.5 kV $Bi-2212$ LN_2 cooled $SFCL$ has been developed and commissioned for protecting a hydroelectric plant auxiliary transformer circuit.

Superconducting thin films are finding more applications in electronic industry. Rapid Single Flux Quantum ($RSFQ$) is an emerging digital electronics technology that relies on quantum effects in superconducting materials to switch signals, instead of transistors. The quantum pulses are switched by Josephson junctions. Superconducting components such as resonators, filters and delay lines with performance far superior to conventional technology are

being widely used in microwave electronics. *HTS* microwave technology is a promising one, especially at frequencies below 3 *Hz*. Superconducting microwave technology offers unique advantages derived from the low microwave loss of superconducting materials and the inherent low thermal noise in cryogenically cooled components. Several microwave communication base station receiver front ends consists of superconducting components.

Another important application of superconductors is magnetic levitation in transportation. Several superconducting magnetically levitated systems are operational around the world (for example: Maglev trains). Most of the present maglev systems use *YBCO* material since, it exhibits high magnetic irreversibility field at LN_2 temperatures and it has the ability to grow into large grains. Bulk or thin film is usually preferred in maglev applications. Due to the expulsion of magnetic field in the superconducting state, a superconductor can be used for magnetic shielding applications. $Bi-2223$ **HTS** is mainly used for magnetic shielding applications. Among the various applications described above the cuprate system has the potential of replacing existing superconductors in many fields with improved performance and/or low cost. The possible applications of cuprate based **HTS** wires/tapes/cables/coils include magnets for medium field applications and inserts for high field applications. Other possible applications include superconducting transformers, motors, generators, *SMES* and particularly in *SFCLs*. Besides the conductor applications, the thin films/junctions can find a place in future electronics also.

It is clear from the broad base of applications and their proximity to commercial side demonstrations that **HTS** technologies are on the threshold of the promised superconductor revolution. As manufacturers scale up production, prices will inevitably be driven down and the commercial viability will be further enhanced. Besides this, information technology industry is also exploring for faster communication, larger memory capacity and faster processing power and it is clear that the market pull for electronic **HTS** technologies will grow dramatically in the next few decades. Based on these considerations, a consortium of European companies has estimated that the total world market in superconducting products will reach 20 billion Euros by 2020. Finally, the recent discoveries of MgB_2 and Fe based superconductors which exhibit novel properties remind us that novel materials with strange and unexpected properties will continue to appear and our technology horizons will continue to expand.

1. 7.   Aim of the present work

As mentioned earlier, there are three superconducting phases in the *BSCCO* system, $Bi_2Sr_2Cu_1O_x$ $(Bi-2201)$, $Bi_2Sr_2Ca_1Cu_2O_x$ $(Bi-2212)$, and $Bi_2Sr_2Ca_2Cu_3O_x$ $(Bi-2223)$. The three phases differ mainly by the number of $Cu-O$ layers, which rest between the $Bi-O$ layers. The main advantage of Bi-based system is its layered structure and hence a high degree of texturing can be easily induced in it. Although single crystals of compounds such as $Y-Ba-Cu-O$ have very high critical current densities and strong flux pinning, they are not useful in polycrystalline form because super-current effectively cannot cross the boundaries between grains which are misaligned by around 10°, making most of the grains weakly linked [Dimos et al. (1990)]. Presently, the most promising $BSCCO$ compounds for long length conductor manufacture are $Bi-2223$, which is the phase having the highest T_c of ~110 K. Although, $Bi-2223$ can be made into useful conductor forms, its superconducting properties are not as good as $Bi-2212$ at low temperatures. The principal reason behind this is the comparatively larger anisotropy of $Bi-2223$ than that of $Bi-2212$.

In the proposed work, $Bi-2212$ system with T_c ~ 80 K is selected for the investigation because of the broad mono-phase field of stability as a function of temperature and chemical composition as well as chemical stability. Also, it carries high current densities in high fields at low temperatures, and significant currents at high temperatures. But, the two-dimensional character of the $Bi-2212$ is responsible for poor flux pinning within the grains. However, at temperatures below 30 K, where flux pinning is strong, $Bi-2212$ conductors can carry significant current densities in very high magnetic fields. While, conventional low T_c materials can carry significantly greater current densities at low magnetic fields, the $Bi-2212$ can carry higher current densities at fields above 8 T. The fact that $Bi-2212$ can carry high current densities in high fields at low temperatures, and significant currents at high temperatures, makes it a promising material for further investigation. Improvements in the current carrying capacity at either low temperatures and/ or high temperatures in the presence of external magnetic field could make $Bi-2212$ feasible for many practical applications. Therefore, enhancement of flux pinning in $Bi-2212$ has become one of the main challenges, and many research groups have attempted to achieve this by the introduction of pinning centres into the system by different methods [Villard et al. (1996), Kazin et al. (2001), Sarun et al. (2006), Wang et al. (2004), Makarova et al. (2005), Amira et al. (2005), Agranovski et al. (2006), Biju et al. (2006)].

Doping of impurity atoms which create point defects and/ or secondary phase precipitate of nano size in the system can act as flux pinners [Kazin et al. (2001), Sarun et al. (2006), Wang et al. (2004), Makarova et al. (2005), Amira et al. (2005), Agranovski et al. (2006), Biju et al. (2006)]. Even though such doping enhances flux pinning, very often it causes a reduction in T_c. Substitution of magnetic and non-magnetic transition metals namely, Fe, Co, Ni and Zn, respectively, at CuO_2 layers reduces the T_c or destroys the superconductivity in $Bi-2212$ [Maeda et al. (1990), Lonnberg et al. (1992), Shigemon et al. (2004), Gu et al. (1997)]. On the other hand there are scattered reports on improvement in the J_C of $Bi-2212$ by low level addition of Fe, Co, Ni and Ti [Ha et al. (1996), Li et al. (1997), Noetzel et al. (1998), Wang et al. (2002), Traholt et al. (1997)]. Studies on substitution, out of CuO_2 layer in $Bi-2212$ have also been performed, of which majority of them are done on the substitution of yttrium (Y) at Ca site [Tamegai et al. (1989), Mandal et al. (1991), Gao et al. (1992), Kazin et al. (2001), Murugakoothan et al. (1994), Mitzi et al. (1990), Mandrus et al. (1992), Kendziora et al. (1992), Maeda et al. (1990), Nowik et al. (1992), Veenendaal et al. (1993)] because of their comparable ionic size and a few at Sr and $Bi-$ sites [Hudakova et al. (2004), Prabhakaran et al. (1998)]. Tarascon et al. show that the effects of rare earth (RE) substitutions depend on the nature of RE and how nicely it accommodates in the crystal structure of $Bi-2212$ [Tarascon et al. (1989)]. But, the results are scattered due to different processing methods, processing parameters and many other different aspects of each study. Hence, comparison of the results is not possible. It is expected that cationic substitution of the divalent Ca^{2+}/Sr^{2+} by a trivalent RE ion induces variation in hole concentration of the CuO_2 planes in the $Bi-2212$ superconductors [Mandal et al. (1991), Gao et al. (1992), Kazin et al. (2001), Murugakoothan et al. (1994), Mitzi et al. (1990)]. By tuning the dopant concentration, an optimum carrier concentration in the system can be achieved, which enhances the critical temperature (T_c) of the system. All these studies were done on the general formula of $Bi_2Sr_2Ca_1Cu_2O_{8+\delta}$ which is a Pb-free system. However, no such RE doping studies were reported earlier in $Bi-2212$ except the preliminary investigations of rare earth addition in bulk $Bi-2212$ by Aloysius et al. [Aloysius et al. (2005)] and Biju et al. [Biju et al. (2006)] which turned out as the main motivation for the present study.

Therefore, the main objective of this work is to investigate the influence of RE doping and processing conditions on the structural, transport and flux pinning properties of $Bi-2212$ superconductor and to develop novel superconductors in the system with highly enhanced flux pinning properties. The investigations mainly focused on the following aspects:

(i) Standardize the stoichiometry of the precursor [RE doped $Bi-2212$], which can give highly improved superconducting properties.

(ii) Suppress the flux creep process and thereby improve the flux pinning properties.

(iii) Refine the processing conditions and microstructure for getting best self- and in-field critical current densities.

(iv) Study the disorder produced outside the CuO_2 planes systematically and compares its influence on the self-field J_C and flux pinning properties.

(v) Tune the doping concentration and maximize the flux pinning force, pinning potential values and $n-$index and improve the $E-J$ characteristics.

(vi) Compare the experimental results with theoretical prediction.

(vii) Scale the vortex liquid resistivity curves and analyze its significance.

Chapter 2

CHAPTER 2

Synthesis and characterization

2.1 Introduction

This chapter deals with the methods of synthesis and characterization of pristine and doped $(Bi, Pb) - 2212$ superconducting compounds. Of all the **HTS** so far discovered, *Bi, Tl* and *Hg* based superconductors are the most difficult materials to prepare in pure form. Improper choice of starting composition, sintering temperature, sintering time and atmospheric conditions would irreversibly result in the formation of certain impurity phases like Ca_2CuO_3, $SrCuO_2$, Ca_2PbO_4 etc. These impurity phases drastically affect the important physical properties of the superconductor, thereby limit their applicability range. For example, the usually observed insulating phases such as Ca_2CuO_3 and Ca_2PbO_4 present along the grain boundaries in $(Bi, Pb) - 2212$ reduce the value of critical current density (J_C) drastically. The preparation of high T_c superconductor precursor can be divided into three steps, namely, selection of starting materials, mixing and calcination.

2.2 Methods of synthesis

For the preparation of $Bi - 2212$ superconductor, many different starting materials like oxide and carbonate [Ochsenkühn-Petropoulou M, Argyropoulou R et al. (2002), De-Ninno et al. (1989), Motoi et al. (1989), Zhao et al. (1989), Fujii et al. (2000)], hydroxides [Fujii et al. (2000), Villard et al. (2000), Villard et al. (2001), Mitchell et al. (1995)], nitrates [Salah et al. (1996), Mancic et al. (2000), Sinha et al. (1991), Bhattacharya R N, Chen J et al. (2003), Krishnanraj et al. (1994)] and metals have been reported. Different preparation methods such as the sol-gel route solid state route [De-Ninno P G A, Marinelli M, Paerno G, Gambardella U, Paroli P et al. (1989), Motoi Y, Ikeda Y, Uwe H, Sakudo T (1989), Zhao et al. (1989), Mitchell et al. (1995)], melt quenching [Fujii et al. (2000)], precipitation [Salah et al. (1996), Sengupta et al. (1999)], spray pyrolysis [Mancic et al. (2000), Sinha S K, Gadkari S C, Sabharwal S et al. (1991)], freeze drying [Krishnanraj et al. (1994)], and electrostatic deposition route [Villard et al. (2000), Villard G, Legendre F, Poissonnet S et al. (2001), Bhattacharya R N et al. (2003),

Gendre et al. (1995)] have been described in the literature. The diversity of applied starting compounds and the preparation routes have the common goal to get a reactive and homogeneous mixture of the starting ingredients. This is very important for the preparation of $Bi-2212$ bulk superconductors with high critical current densities. Each preperation route has its own benefits and drawbacks. The major challenges are the control of the stoichiometry, achievement of homogeneity and the prevention of contamination.

The calcination process is usually done in several steps, at different temperatures ranging from 750 *to* $860\ ^oC$ and heating durations from minutes [Mancic et al. (2000), Sinha et al. (1991)] to days [Mitchell et al. (1995)]. These parameters mainly depend on the characteristics of the starting materials and the processing route [Sager et al. (2004)]. However, independent of the starting material chosen, a heat treatment in air in excess of $800\ ^oC$ is needed in order to get the $Bi-2212$ phase.

The solid state approach is the most often used route for the $Bi-2212$ precursor synthesis, because of its simplicity. In methods such as sol-gel, the starting materials react to form intermediates after decomposition of the organic ligands below $350\ ^oC$ upon heating in air. Therefore, the reaction pathways to $Bi-2212$ are similar, while the formation rates vary, depending on the nature of the starting materials. During calcination of the starting materials, after burnout or decomposition of the carbonates, the $Bi-2201$ phase starts to form around $600\ ^oC$. At $700\ ^oC$, the $Bi-2212$ phase starts to form, however only above $800\ ^oC$ it rapidly forms at the expense of $Bi-2201$ due to intercalation [Chen F H, Koo H S et al. (1990)]. The reaction rates can be accelerated using reactive precursors with high surface area or by tuning the calcination parameters such as temperature, heating rate and oxygen partial pressure in the atmosphere.

2.3 Steps used in the present work

In the present work Pb doped $Bi-2212$ $[(Bi,Pb)-2212]$ was used and its calcined precursors were prepared by conventional solid-state synthesis using high-purity chemicals such as oxides and carbonates as the ingredients $(>99.9\ \%,\ Aldrich\ Milwaukee,\ WI)$. The required amount of ingredients was estimated according to the stoichiometry used. The ingredients were accurately weighed using an electronic balance $(Metller\ AE\,240,\ Greifensee,\ Switzerland)$

having a least count of $10\,\mu g$. Subsequently, these ingredients were mixed and ground using a planetary ball mill $\left(FRISCH\ Pulversette\ 6,\ Idar-Oberstein,\ Germany\right)$ in an agate bowl with agate balls. After the milling process, the ingredients get homogenized with a reduction in particle size and increase in the contact area between different ingredients. Extreme care was taken to avoid contamination of the ingredients during weighing and milling process. The homogenized mixtures were placed in alumina crucibles and subjected to three stages of calcination in air between temperatures $800\ to\ 830\ ^{o}C/120\ h$ in air using a programmable furnace.
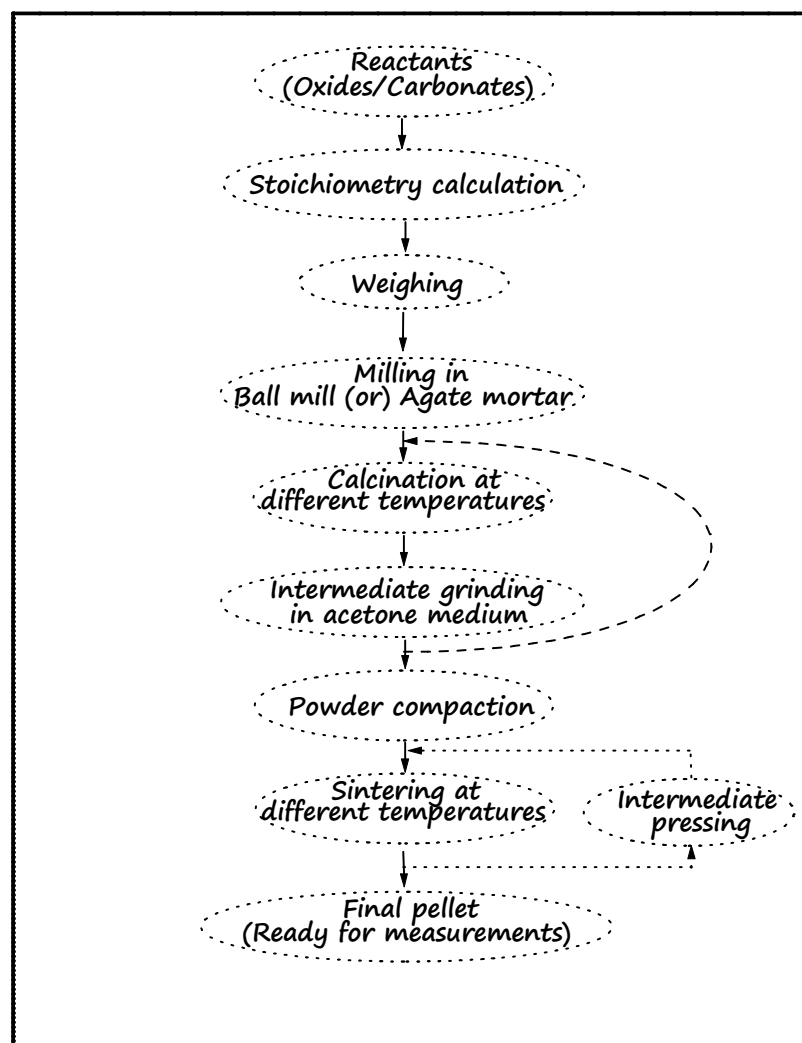
Figure 2.1: Flow chart showing the preparative method of $\left(Bi,Pb\right)-2212$ superconductor.

Intermediate grinding in acetone medium was employed between each calcination stage to avoid agglomerates and to improve homogeneity. The temperature and duration of calcination were varied depending on the nature of the samples. The calcined powders were compacted into pellets having a diameter of 12 mm and thickness of about 1 mm by filling in a cylindrical die. Uni-axial pressure of 500 MPa was applied using a hydraulic press $(Herzog\ TP\ 20P)$. The bulk density of the pellets prior to and after sintering were estimated by measuring the mass, thickness and diameter of the pellets. This is done to monitor the density variation during sintering because unlike other ceramic materials, Bi-based superconductors show retrograde densification behaviour due to its characteristic layered structure, i.e., upon sintering the density reduces from its value before sintering. The mass was precisely measured using an electronic balance, thickness and diameter of the pellets were measured using a micrometer screw gauge at different points and average values were taken.
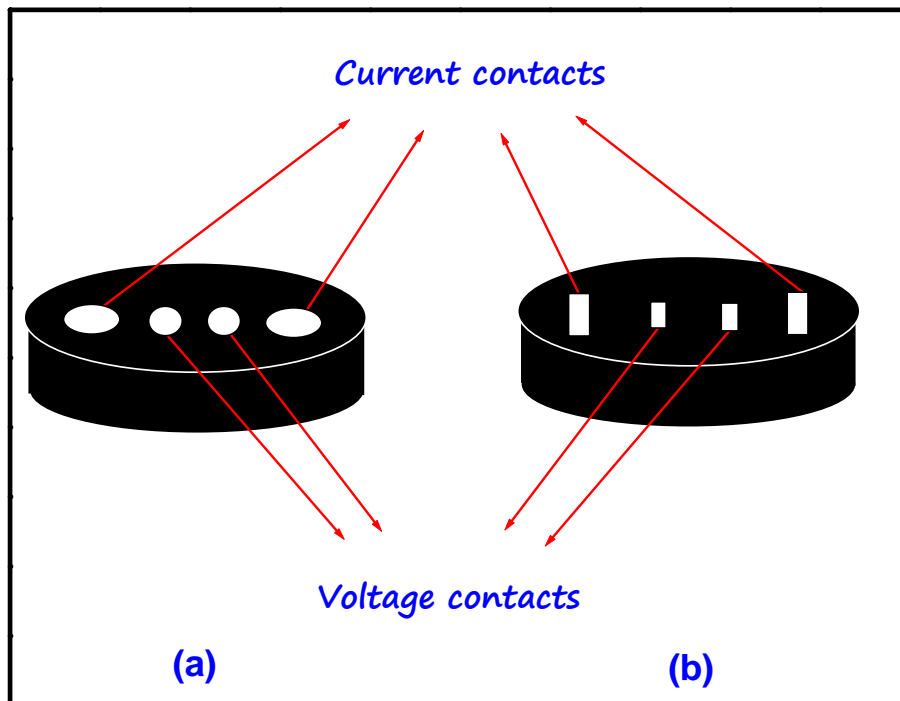
Figure 2.2: Schematic view of four probe contacts made to the $(Bi, Pb) - 2212$ pellets using (a) silver paste and (b) silver strip.

The pellets were sintered at a temperature in the range from $845\ to\ 860\ ^oC$ for $120\ h$ $\left(60\ h + 60\ h\right)$ in two stages with one intermediate pressing under the same pressure of $500\ MPa$. Intermediate pressing between the sintering stages is necessary to minimise the retrograde densification of the samples [Kumar et al. (2005)]. After heat treatment, the bulk samples were cut and polished to a typical dimension of $12\times3\times1\ mm^3$. The flow chart of the different stages of processing is shown in figure 2.1. Terminals for electrical contact were also made during compaction of calcined powder. This was done by embedding silver strips in the pellets during pressing or by coating high quality conducting silver paste on the surface of green pellets (figure 2.2). Silver strip remains embedded to the sample through out the sintering process while silver paste forms a strong coating which becomes a smooth surfaced metallic spot after the intermediate pressing process. Both these type of contacts can reduce the contact resistance by about an order compared to the usual method of making the electrical contact, i.e., coating silver paste on the final sintered pellets followed by an annealing.

2.4 Characterization

2.4.1 X-Ray Diffraction (*XRD*) analysis

X-ray diffraction is a very useful and easy method for the identification of phase of crystalline materials. *XRD* data can be used for a semi-quantitative phase analysis. Besides the phase analysis *XRD* data gives useful information regarding the crystal lattice parameters, strain, grain size and texture. In the present study, the powder samples were filled in standard holders and the *XRD* patterns of the samples were taken using $Philips\ X\ '\ pert\ Pro\left(PW\ 3040/60\right)$ X-ray diffractometer with $Cu\ K\alpha$ radiation $\left(\lambda = 1.540566\ \overset{\circ}{\mathrm{A}}\right)$ employing a proprietary high speed detector namely X'Celerator and a monochromator at the diffracted beam side. The system has $\theta - 2\theta$ Bragg-Brentano geometry with fully automated operation and data acquisition. Programmable slits were used to keep the exposed sample area constant throughout the whole scan range. Most of the scans were performed under a tube voltage and current of $40\,\mathrm{kV}$ and $30\ mA,$ respectively. The samples were scanned from $15 - 50^{\,o}$ $\left(2\theta\ values\right)$ with a step size of $\sim 0.01^{\,o}.$

The phase identification of the samples was performed using ***X'Pert Highscore*** software with support of the ***ICDD PDF II*** database. The phase assemblage of different phases (volume percentage) formed in the reaction mixture were quantitatively estimated from the integrated X-ray peak intensities obtained from the *XRD* patterns using the relation, $F_x = \left(\sum I_x / \sum I_{total} \right)$ where, x is any phase, F_x is the volume percentage of the phase, I_x is the integrated peak intensities of the phase x and I_{total} is the integrated peak intensities of all the phases in the mixture. As mentioned earlier, $Bi-2212$ has an orthorhombic structure with *Amaa* symmetry. The d-values of selected peaks of $Bi-2212$ were used for its lattice parameter calculations using the relation,

$$\left(\frac{1}{d^2} \right) = \left(\frac{h^2}{a^2} + \frac{k^2}{b^2} + \frac{l^2}{c^2} \right) \tag{2.1}$$

The determination of the preferred orientation of the crystallites in polycrystalline aggregates is referred to as texture analysis, and the term texture is used as a broad synonym for preferred crystallographic orientation in the polycrystalline material. The intensity of a given reflection $(h\, k\, l)$ is proportional to the number of h, k, l planes in reflecting condition (Bragg's law). The orientation of the unit cell is used to describe crystallite directions. By collecting data from several reflections, the complete orientation distribution of the crystallites can be built for single polycrystalline phase. Lotgering index (F) is a measure of texture in the material which is calculated from the peak intensity of the XRD patterns of sintered pellets and the corresponding randomized powder. It is calculated using the relation,

$$F = \left(\frac{I_a - I_r}{1 - I_r} \right) \tag{2.2}$$

Where, I is the ratio of intensities from the surface of sample and

$$I = \left(\frac{\sum I_{00l}}{\sum I_{total}} \right) \tag{2.3}$$

Here I_a refers to I measured for the pellets and I_r for the corresponding randomized powder [Lotgering (1959)]. A fully aligned sample will have a Lotgering index of 1 and a totally

random sample has an index of zero. The best-aligned samples with layered structure (as in $Bi - 2212$) have F in the range $0.80 - 0.95$.

2.4.2 Scanning Electron Microscopy (*SEM*)

The extremely high resolution and magnification and large depth of focus of the Scanning Electron Microscopy (SEM) make it a potential tool for studying the microstructure of materials. The SEM scan the sample with high energy electron beam in a raster scan pattern. The scan produces different signals including secondary electrons, back scattered electrons, characteristic X-rays, auger electrons etc, which contain the microstructural information of the sample. Hence, the SEM can generate three types of principal images, namely, secondary electron images (SEI), backscattered electron images (BSE), and elemental X-ray maps. In the present study, the microstructural analysis was done using a $JEOL\ JSM\ 5600LV$ scanning electron microscope equipped with an energy dispersive X-ray spectrometer (Phoenix) used in secondary electron imaging (SEI) mode. The typical images were magnified up to 5000 X. But in some cases, a magnification of 10,000 X was also used. Freshly fractured surfaces of the samples were mounted on brass studs using adhesive carbon tapes or conducting silver paste. Since, the superconducting $(Bi, Pb) - 2212$ is electrically conducting, gold coating was not required. Finally, the brass studs with the mounted samples were loaded on the sample holder of the Scanning Electron Microscope.

2.4.3 Energy Dispersive X-ray Spectroscopy (*EDS*)

Energy Dispersive X-Ray Spectroscopy is an analytical technique that qualitatively and quantitatively identifies the elemental composition of materials. EDS analyzes the top two microns of the sample with a spatial resolution of one micron. In the present study, an $EDS\ (Phoenix)$ system attached with SEM was used. The spectrum was taken either for a large area or for a single spot depending on the requirement. The EDS data can be compared to either known standard materials or computer-generated theoretical standards to produce either a full quantitative or a semi-quantitative analysis. The location of the peaks identifies the elements. The peak heights vary because each transition has a different probability of occurring

and the detector's efficiency is a function of energy. Using the peak intensities of the standard (I_s) and of the sample (I_i) the weight percent (C_i) were determined by:

$$\left(\frac{C_i}{C_s}\right) = (AZF_X)_i \times \left(\frac{I_i}{I_s}\right) \qquad (2.4)$$

Where $(AZF)_i$ is a correction factor which depends on the atomic number of element (Z), absorption coefficient of the material (A) and the flurosence caused by other atoms, when excited from the emitted X-rays (F_X).

2.4.4 Resistivity - Temperature measurement

The resistance (R) in ohms (Ω) versus temperature was measured using the four probe method for determining the critical temperature (T_c) and transition width (ΔT_c). The temperature at which resistivity starts falling is taken as the T_c and the difference between the temperatures corresponding to the 90 % and 10 % of normal state resistivity $(T_{90} - T_{10})$ is defined as ΔT_c. A current in the range $1-100$ mA was passed through the outer terminals of the sample (figure 2.2) using a programmable current source (Keithley 220, current range: 1 nA to 100 mA) while the voltage drop across the inner terminals was recorded with digital nano voltmeters, *Keithley 181 or 2182*, both have a resolution of 1 nano volt.

The electrical leads were soldered onto the silver stripes in the sample surface which were prepared during the processing stage. The measurements were performed from liquid nitrogen temperature $(77\ K)$ to room temperature by lifting the sample holder assembly from the bottom of a LN$_2$ dewar at regular intervals of time, keeping a constant lifting step-length. A silicon diode sensor $(DT-470)$ was used to measure the temperature. A Lakeshore temperature controller $(L340)$ was used to control and monitor the temperature. A schematic diagram of resistivity – temperature measurement setup used in the present study is given in figure 2.3. A set of three different values of current $(1, 10\ \&\ 100\ \text{mA})$ was used in order to check the ohmic behaviour of the sample. In addition, the direction of current was reversed periodically for each data point in order to remove the effect of any thermoelectric voltage. The measurements were performed on circular pellets or bar-shaped samples having collinear contact terminals to obtain
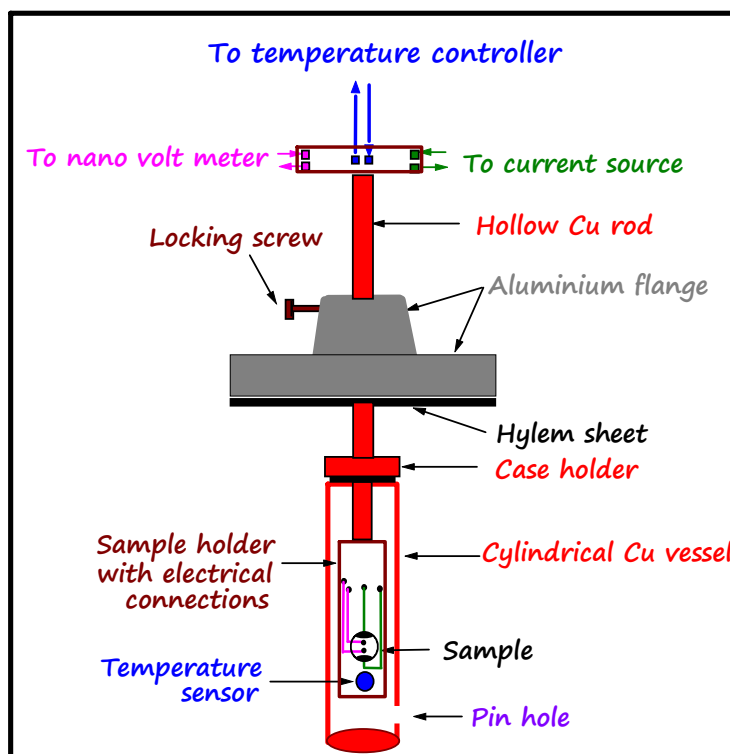
Figure 2.3: Schematic diagram of the set up used for the R-T measurement of $(Bi, Pb) - 2212$ **pellets.**

the resistivity. The resistance values were converted to resistivity using the equation, $\rho = (RA/l)$, where ρ is the resistivity in $\Omega\,cm$, R is the resistance in Ω, A is the cross section area in cm^2 of the sample and l is the distance between the two voltage terminals in cm. All the instruments used in the measurement were interfaced to a personal computer with $GPIB - IEEE - 488$ interface bus and the measurements were carried out using appropriate software.

2.5 Current – Voltage characteristics

Investigations of current versus voltage $(I - V)$ characteristics are very important for both the evaluation of the superconductor for practical applications and the understanding of its critical current limitation mechanism. For the high T_c materials, the flux pinning strength plays
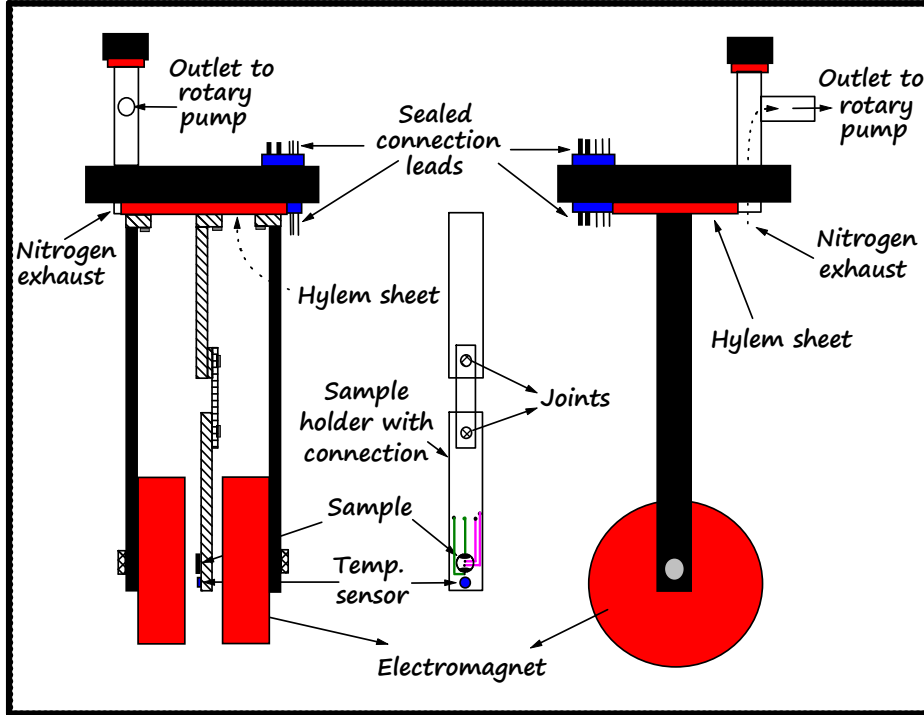
Figure 2.4: Schematic diagram of the set up used for the measurement of $I-V$ and $J_C - B$ characteridtics of the $(Bi, Pb) - 2212$ superconductor.

a very important role in deciding their $I-V$ characteristics, and the value of critical current density J_C can be obtained from the $I-V$ characteristics [Chen et al. (1959)]. Below T_c, the vortices are pinned and a true superconducting state is established for $J < J_C$. J_C is defined as the current density above which vortices become mobile (flux creep and flux flow region) and give rise to an induced electrical field. Above T_c the vortices are not pinned and a low applied current causes a linear resistance in the sample. For larger currents the vortices start to move (flux flow) and give rise to power law behaviour of the induced electrical field of the form, $V \propto I^n$ where, I is the current flowing, V is the voltage generated across the voltage leads and n is a function of applied magnetic field and temperature. Qualitatively, one can conclude that sharper the take off in the $I-V$ characteristics after the J_C value, higher can be the n-value $(n-index)$, which in turn implies the higher flux pinning ability of the superconductor.

In the present work, the transport $I-V$ properties were measured by the four probe method under self- and applied-fields. In order to reduce the Joule heating at the current contacts due to the large transport currents, a computer controlled pulsed current method was employed using DC power supply system ($Aplab\ 9711P\ \ or\ \ Sorrenson\ \ DHP-5$) for the $I-V$ measurement. After each current pulse, sufficient time was given to cool the sample before next measurement. The bar-shaped superconducting sample $\left(12\times3\times1\ mm^3\right)$ was fixed to the sample holder and mounted in a liquid nitrogen cryostat with a provision for evacuation, using a rotary pump $\left(Leybold\ Heraeus\ TRIVAC\right)$. The measurement temperature was reduced from $77\ to\ 64\ K$ by applying vacuum and was monitored by a temperature controller. The direction of the current was parallel to the direction of the pressed surface and that of the magnetic field was perpendicular to the pressed surface of the pellet. The voltage across the voltage leads was recorded by a digital nano voltmeter. The schematic diagram of the setup in which $I-V$ measurement was performed is shown in figure 2.4. The critical current I_C was determined from the $I-V$ measurements with a $1\ \mu Vcm^{-1}$ electric field criterion derived from the resistance between voltage terminals. The J_C values of the samples were calculated from I_C and the total cross-sectional area of the samples.

2.6 In-field $J_C\left[J_C\left(B\right)\right]$ measurements

The analysis of $J_C\left(B\right)$ characteristics gives valuable information regarding the flux pinning capability of the superconductor or the ability of the Abrikosov vortices to withstand the melting of the vortex lattice in presence of external magnetic fields. Samples showing higher flux pinning force are the promising candidates for magnetic applications. In the present study, $J_C\left(B\right)$ characteristics were measured using the setup shown in figure 2.4. The sample was fixed to the sample holder with the electrical leads soldered onto it and mounted in the liquid nitrogen cryostat. The magnetic field was produced by charging a bipolar electromagnet with required value of current which can generate a maximum field up to $1.5\ T$. A programmable constant current source $\left(30\ A,\ Aplab\ 9710P\right)$ was used for charging the magnet. The generated magnetic field was calibrated using a Gaussmeter $\left(Lakeshore\ 410\right)$ with

transverse hall probe. The temperature of the sample was kept fixed at $64\ K$ which was precisely monitored by a temperature controller $\left(Lakeshore\ L340\right)$. The voltage values were monitored by digital nano voltmeters. The measurement was automated using a computer which increases the magnetic field in steps of equal intervals and simultaneously records the value of current through the sample. The $100\ A$ rated constant current source was used for this purpose $\left(Aplab\ 9711P\ or\ Sorrenson\ DHP-5\right)$.

2.7 Conclusions

The major experimental facilities and techniques used for the preparation of $\left(Bi,Pb\right)-2212$ superconductor have been reviewed in the present chapter. The structural characterization was done using X-Ray Diffraction $\left(XRD\right)$, Scanning Electron Microscopy $\left(SEM\right)$ and Energy Dispersive X-ray Analysis $\left(EDAX\right)$, while the superconductor characterization was done using $\rho-T$, $I-V$ and $J_C\left(B\right)$ measurements.

Chapter 3

CHAPTER 3

Influence of rare earth substitution on the superconducting properties of (Bi, Pb)-2212 system

3.1 Introduction

Since the discovery of Bi-based high temperature superconductors, there have been many studies to improve the superconducting properties, in particular the critical temperature (T_c) and critical current density (J_C) of $Bi-2212$ system. This is because T_c and J_C are the parameters of primary importance for practical applications of **HTS**. The superconducting properties of high temperature cuprates are strongly dependent on the hole carrier concentration on the CuO_2 planes. The pure $Bi-2212$ system is slightly over-doped with holes and hence, a careful tuning of the carrier concentration is required to optimize the superconducting properties of the system [Gupta et al. (1994)]. Doping of alliovalent impurities or oxygen non-stoichiometry can change the charge carrier concentration considerably in Bi-based superconductors [Awana et al. (1993), Thamizhavel et al. (1997), Ilyushechkin et al. (2004), Chen et al. (1994)]. The chemical inhomogeneities and disorder produced due to the doping also strongly affect the T_c of Bi-based high temperature superconductors and hence J_C of the system.

In high T_c cuprates the CuO_2 plane is believed to be responsible for the superconductivity. Also for Bi-based superconductors, the impurities substituted at the Cu site are generally found to suppress the T_c [Tarascon et al. (1998), Hedt et al. (1994)] and the doping outside the CuO_2 plane changes the charge carrier concentration of the system. There are reports showing that small amount of Pb at Bi site of $Bi-2212$ improves structural modulation, enhances J_C and shift the irreversibility line (IL) to higher fields [Kim et al. (2003), Gladyshevskii et al. (2004)]. It also significantly improves the c-axis conductivity due to the reduction of the anisotropy [Zhao et al. (2003), Motohashi et al. (1999)] and consequently enhances the intrinsic pinning. The detailed analysis of the results on the substitution of Pb at Bi site of $Bi-2212$ revealed that the Pb doped $Bi-2212$ has much superior transport properties than undoped $Bi-2212$, even though, a slight reduction in the T_c was observed. The

range of Pb substitution for achieving the best superconducting properties for $Bi-2212$ was found to be within $x = 0.4 - 0.5$ [Sarun et al. (2009), Sarun et al. (2008), Vinu et al. (2008)] and closer to 0.5 gives the best result. Based on these experimental results, $x = 0.5$ was chosen as the Pb content for the present study. A few reports are available on the substitution of rare earth (RE) in $Bi-2212$ at Ca site. Most of these previous RE doping studies on $Bi-2212$ were done without Pb doping at Bi site [Uprety et al. (2001), Cao et al. (2000), Baca et al. (2000), Sanderson et al. (2005)], which concluded that even though RE substitution improves the structural stability of $Bi-2212$, the superconducting properties show a degrading trend with increase in dopant concentration [Singh (1998), Jin et al. (1999), Dos-Santos et al. (2001)]. Our studies on co-doping of Pb and RE in $Bi-2212$ have shown significant improvement in its superconducting properties [Sarun et al. (2009), Sarun et al. (2008), Vinu et al. (2008)]. As a continuation of the above studies, this chapter presents the preparation and superconducting characterization of $Bi-2212$ substituted with Pb at the Bi site and RE (Lanthanides Lu, Ho, Dy and Tb) at the Sr site, respectively, as typical examples.

3.2 Experimental details

The RE substituted $(Bi, Pb)-2212$ superconductors with a general stoichiometry of $Bi_{1.6}Pb_{0.5}Sr_{2-x}RE_xCa_{1.1}Cu_{2.1}O_{8+\delta}$ were prepared by solid state sintering using high purity chemicals $(>99.9\ \%, Aldrich\ Milwaukee, WI)$ such as oxides/carbonates of the ingredients. Here $RE = Lu, Ho, Dy, Tb$ and the samples with different RE stoichiometry will be hereafter denoted as REx, where x is the corresponding stoichiometry. The required amount of ingredients was estimated according to the stoichiometry used and the ingredients were accurately weighed using an electronic balance $(Metller\ AE240, Greifensee, Switzerland)$ having a least count of $1\ \mu g$. Subsequently, these ingredients were mixed and ground using a planetary ball mill $(FRISCH\ Pulversette\ 6, Idar-Oberstein, Germany)$ in an agate bowl with agate balls. After the milling process, the ingredients get homogenized with a reduction in particle size and increase in the contact area between different ingredients. Extreme care was taken to avoid contamination of the ingredients during weighing and milling process and then subjected to a three-stage calcination process in air at

$800\ {}^{\circ}C/15\ h + 820\ {}^{\circ}C/40\ h + 840\ {}^{\circ}C/60\ h$ using a programmable furnace. Intermediate grinding was done between each calcination stage to avoid agglomerates and compositional variations that may still exist or may arise due to calcination. The calcined powders were then pelletized at a pressure of $500\ MPa$ using a hydraulic press $(Herzog\ TP\ 20P)$ and having a diameter of $12\ mm$ and thickness of about $1\ mm$ by filling in a cylindrical die. The pellets were heat treated at $845\ {}^{\circ}C/60\ h +\ 848\ {}^{\circ}C/60\ h$, with one intermediate pressing under the same stress.

Phase analysis of the samples was done using X-ray diffractometer $\left[Philips\ X'pert\ Pro\left(PW\ 3040/60\right)\right]$ equipped with an X'celerator and a monochromator at the diffracted beam side. For all samples, scans were made in 2θ and at $0.01^{\circ}/$step. All the scans were done using $Cu\ K\alpha$ radiation with a tube voltage of $40\ kV$ and current $30\ mA$ by exposing a constant area of the sample. The phase identification of the samples was performed using $\textbf{\textit{X'Pert Highscore}}$ software in support with the $\textbf{\textit{ICDD PDF II}}$ data base. The microstructural and elemental analyses of the samples were done using scanning electron microscopy $(JEOL\ JSM\ 5600LV)$ and energy dispersive X-ray spectroscopy, respectively. For electrical measurements, the samples were cut into rectangular bar of dimension $12\times3\times1\ mm^3$. The transition temperature (T_c) of the samples was determined by the four-probe DC resistance method by cooling the sample in a liquid N_2 cryostat. In order to minimize the contact resistance, four silver strips were fixed on to one surface of the pellet during pressing. Leads of high quality copper were soldered to silver strips. The outer two leads were connected to a programmable DC current source (*Keithely model:* 220) and a constant current of $10\ mA$ was used for the resistance measurement. The voltage drop between the inner two leads was measured using a programmable nano voltmeter (*Keithely model:* 181). The temperature of the sample was monitored by a temperature controller (*Lakeshore model:* $L340$) using a temperature sensor $(DT-470)$. The transport critical currents of the samples in self-field was measured at $64\ K$ in a liquid N_2 bath cryostat under vacuum by employing four-probe method with the standard criterion of $1\ \mu Vcm^{-1}$. For these measurements an *Aplab* $9711P$ constant current source was used. The directions of the current were parallel to the pressed surface and all these measurements were automated using $GPIB$ interfaced with a personal computer.

3.3 Structural characterization

3.3.1 *XRD* analysis

The *XRD* patterns of the RE (*RE = Lu, Ho, Dy* and *Tb*) substituted $(Bi,Pb) - 2212$

pellets obtained after the last stage heat treatment is normalized with standard *XRD* pattern of

pure (*Bi,Pb*)-2212 sample and the resultant patterns are shown in Figure 3.1 (a) - (d). In order to

avoid the effect of slight variations in the processing conditions, the *RE* -free sample is prepared
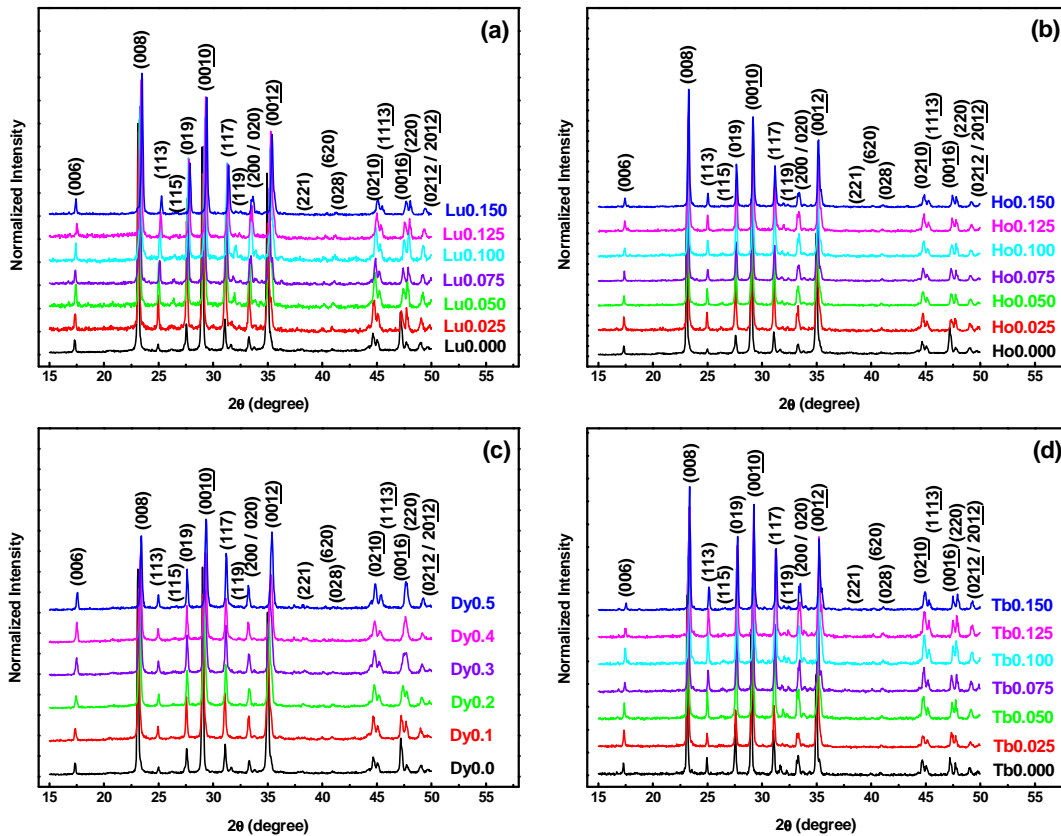
Figure 3.1 (a) - (d):   The normalized *XRD* patterns of the *RE* -free and *RE* substituted
$(Bi,Pb) - 2212$ **pellets after the last stage heat treatment at** $845 \,^{\circ}C / 60 \, h$ **and** $848 \,^{\circ}C / 60 \, h$.

with every batch of *RE* substitution for a better comparison. The *XRD* patterns are analyzed

using the *X'Pert Highscore* software. It shows that all the samples contain only the peaks

corresponding to the $(Bi,Pb) - 2212$ phase and no peaks of any secondary phase containing

RE or any other cation were detected at this stage within the detection limit of the instrument.

The absence of secondary phases suggests that all the reactant phases are converted into the

$(Bi, Pb) - 2212$ and the substituted RE is incorporated into the crystal lattice of $(Bi, Pb) - 2212$ superconductor. Also Figure 3.1 (a) - (d) shows that when the RE content increases, the peak height corresponding to the $(00l)$ planes systematically decreases. In order
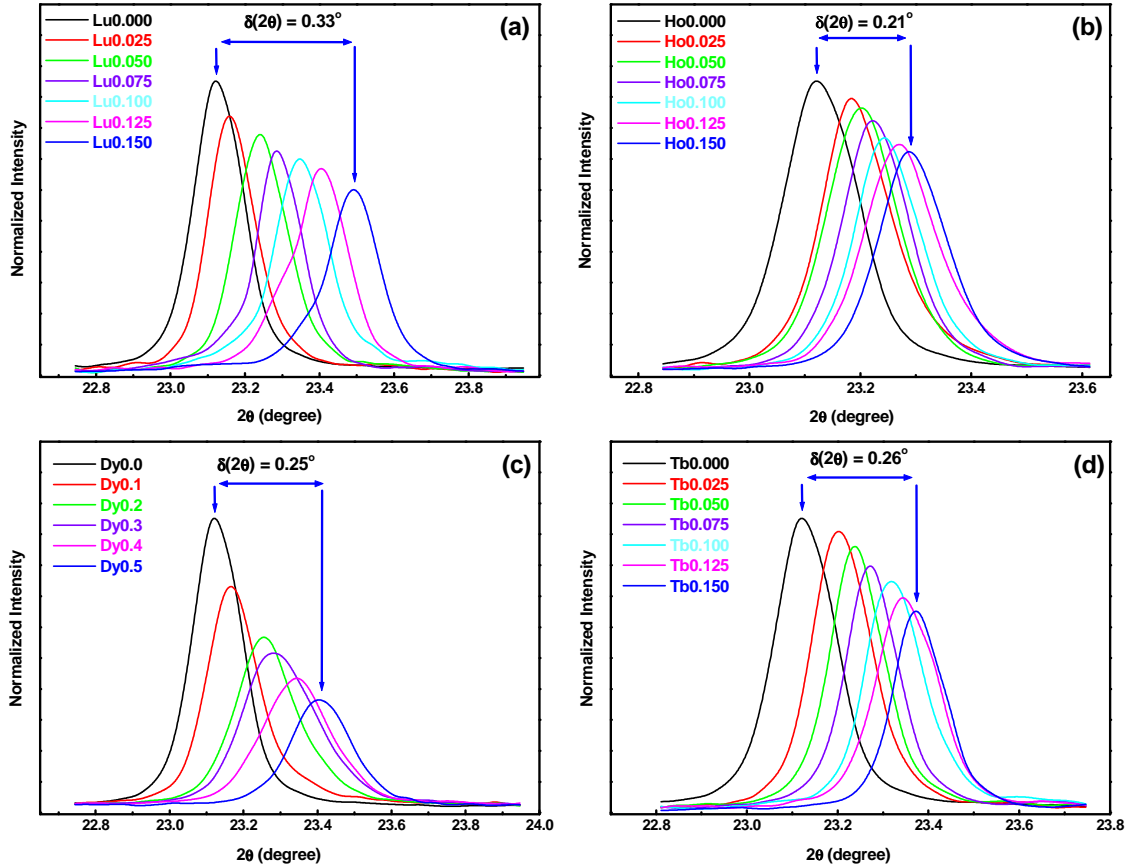
Figure 3.2 (a) - (d): The normalized XRD peaks of the RE -free and RE ($RE = Ho$, Dy, Gd and La) substituted $(Bi, Pb) - 2212$ pellets for the (008) plane at around 2θ = 23.1° and δ(2θ) represents the maximum peak-shift of RE substituted sample with respect to the RE -free sample.

to bring out the decrease in peak height of $(00l)$ planes, the (008) peaks of all samples are separately shown, with better resolution in Figure 3.2 (a) - (d). This shows that the texturing decreases with increase of RE content. This figure also shows that the (008) peaks of the RE doped sample shift towards higher angle [maximum peak shift δ(2θ) is marked in figure] with respect to the position of RE free $(Bi, Pb) - 2212$ sample, which indicates that c-axis length of

the *RE* substituted samples decreases with increase in *RE* content. This decreased c-axis length supports that the substituted *RE* atoms enter into the crystal structure of $(Bi, Pb) - 2212$ superconductor.
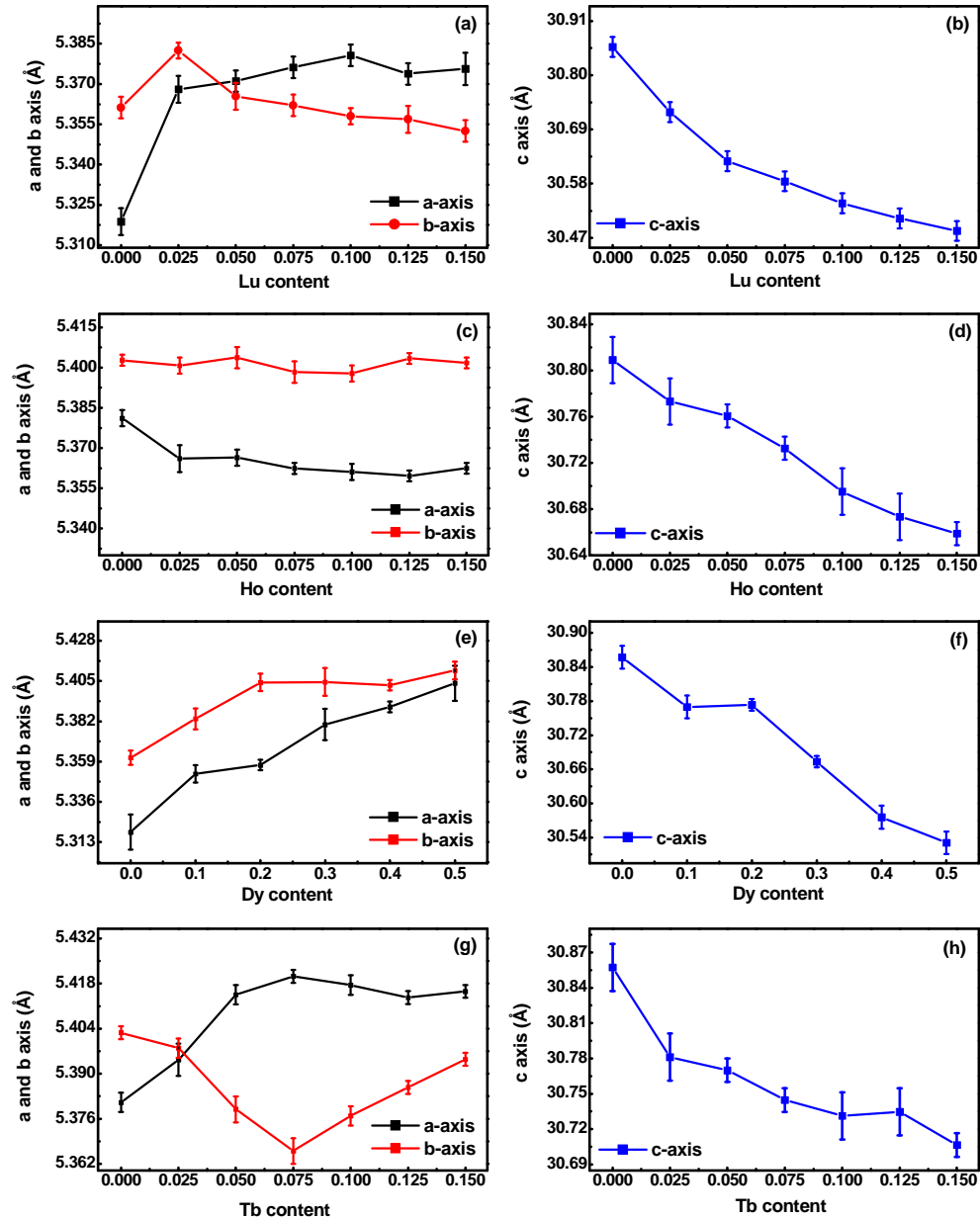
Figure 3.3 (a) - (h): The lattice parameters a, b **and** c **of the** *RE* **-free and all** *RE* **substituted samples calculated by considering an orthorhombic symmetry for the** $(Bi, Pb) - 2212$ **system.**

The lattice parameters *a, b* and *c* of RE-free and RE substituted samples calculated by considering an orthorhombic symmetry for $(Bi, Pb) - 2212$ system using the formula,

$$\frac{1}{d^2} = \frac{h^2}{a^2} + \frac{k^2}{b^2} + \frac{l^2}{c^2}$$

(3.1)

are shown in Figure 3.3 (a) – (h), where d is the inter-planar spacing and (hkl) are the Miller indices. A marked variation is observed in the crystal structure of RE substituted samples compared to RE-free sample. It is found that for the RE-free sample, b-axis value is greater than a-axis $(b > a)$. With increase in RE-content (except for Ho) the orthorhombic symmetry of the system changes to a pseudo-tetragonal symmetry at higher x (stoichiometry). The Ho substituted samples maintain its orthorhombic symmetry up to its highest level of doping. It is noted that the a and b-axis parameters of Dy substituted samples show an increasing trend, while Lu substituted sample shows an increasing trend for a-axis and a decreasing trend for b-axis. The Tb substituted samples show an increasing trend in a-axis while decreasing tendency in b-axis parameter upto $Tb0.075$ and then increases to form a pseudo tetragonal structure. No appreciable change in a and b-axis parameters is observed for Ho substituted samples. The variations in a and b-axis lattice parameters are associated with the increase in $Cu - O$ bond length in CuO_2 planes, which controls the dimensions in the basal planes of $(Bi, Pb) - 2212$ system [Uprety et al. (2001)].

A general tendency of systematic contraction in the c-axis length is observed with increase in RE-content, indicating the incorporation of RE atoms into the system. This is because in Bi-based cuprate superconductors, when a trivalent cation RE^{3+} replaces a divalent cation Sr^{2+}, additional oxygen is incorporated in the $Bi - O$ layers of the structure in order to establish the charge neutrality. As a result, the repulsion between $Bi - O$ planes gets reduced due to the reduction in the net positive charge in the $Bi - O$ planes. This results in the contraction of $Bi - O$ layers and causes the reduction of the c-axis length. The anisotropy of the system decreases with these changes in the lattice parameters [Sanderson et al. (2005)]. The

Table 3.1: The values of rare-earth (RE) stoichiometry (x), cell volume, Lotgering index (F), critical temperature (T_c), the transition width (ΔT_c), normal state resistivity (ρ_n), resistivity at 300 K ($\rho_{300\,K}$), hole carrier concentration per Cu atom (P) and self-field J_C for RE-free and all RE substituted $(Bi, Pb) - 2212$ samples.

RE	x	Cell volume (Å^3)	F	T_c K	ΔT_c K	ρ_n μΩcm	$\rho_{300\,K}$ μΩcm	P/Cu atom	J_C kAm^{-2}
RE-free	0.000	880	0.92	80.7	1.33	34.28	92.67	0.2074	1642
	0.025	888	0.88	84.9	2.87	44.74	150.17	0.2016	3421
	0.050	883	0.85	86.5	3.15	55.45	199.27	0.1992	7840
	0.075	882	0.82	90.3	3.33	61.38	207.77	0.1927	10150
Lu	0.100	880	0.80	93.0	3.87	73.34	264.15	0.1873	13810
	0.125	878	0.80	94.2	4.18	79.53	269.65	0.1844	9894
	0.150	877	0.75	95.8	4.89	89.91	395.64	0.1800	9089
	0.025	892	0.90	82.6	2.93	40.05	100.27	0.2032	2999
	0.050	892	0.87	87.7	3.27	50.83	106.30	0.1952	8736
	0.075	890	0.85	88.5	3.55	53.61	128.63	0.1937	12080
Ho	0.100	888	0.85	91.6	4.01	57.69	138.89	0.1874	9378
	0.125	888	0.83	91.8	4.45	65.37	147.34	0.1870	8784
	0.150	888	0.79	93.5	5.05	70.58	169.07	0.1828	4012
	0.1	887	0.75	91.7	4.85	66.57	177.91	0.1847	5872
	0.2	890	0.73	92.5	5.74	86.13	198.08	0.1826	13930
Dy	0.3	892	0.68	94.5	7.28	125.56	291.80	0.1762	8493
	0.4	890	0.64	96.6	8.92	136.03	413.21	0.1600	3241
	0.5	893	0.56	90.3	10.79	205.19	534.63	0.1319	847
	0.025	896	0.85	84.8	3.58	41.45	135.58	0.1994	3581
	0.050	896	0.78	86.4	3.96	48.90	176.05	0.1968	9603
	0.075	894	0.74	88.2	4.15	56.36	190.96	0.1936	18080
Tb	0.100	895	0.69	90.4	4.84	61.68	205.87	0.1893	13760
	0.125	896	0.63	92.2	5.09	81.92	221.84	0.1851	10510
	0.150	897	0.60	94.4	5.92	119.19	247.41	0.1790	7539

variation in lattice parameters is also reflected in the change in cell volume of *RE* substituted samples (Table 3.1). For example, the cell volume of *Dy* increases slightly with *RE* content. The *Tb* substituted samples also show an increase in cell volume after an initial decrease up to x= 0.075. The *Ho* and *Lu* substituted $(Bi, Pb) - 2212$ samples show a large reduction in cell volume which is due to the large reduction in the c-axis length of these superconductors. The important result noticed is that the c-axis contraction is dependent on the ionic radii of the *RE* dopant. The decrease in the c-axis length is smaller for the *RE* with larger ionic radii while the shrinkage is drastic when *RE* with smaller ionic radii is substituted. For example, when *Tb* (0.923 Å) is substituted, the value of c-axis parameter decreased from 30.85 ± 0.02 Å to 30.70 ± 0.02 Å, while for *Lu* (0.861 Å) substituted sample, the c-parameter decreases from 30.85 ± 0.02 Å to 30.48 ± 0.02 Å for a change in $x = 0.0$ to 0.150.

Using the *XRD* patterns of both pellet and powdered samples, the Lotgering index (F) is calculated (Table 3.1) using the equation,

$$F = \left(\frac{I_a - I_r}{1 - I_r} \right) \tag{3.1}$$

Where, I is the ratio of intensities from the surface of sample and

$$I = \left(\frac{\sum I_{00l}}{\sum I_{total}} \right) \tag{3.2}$$

Here I_a refers to I measured for the pellets and I_r for the corresponding randomized powder [Lotgering (1959)]. Lotgering index represents the degree of texturing in the grains. The $(Bi, Pb) - 2212$ system is inherently oriented in the $(00l)$ direction due to its characteristic layered growth along the $a - b$ plane, which is further enhanced by the repeated pressing process and hence, the reflections from the oriented $(00l)$ planes have high intensities. It is observed that as the *RE*-content increases, the F-value decreases monotonically for all the *RE* substituted samples. This supports that the texturing decreases with increase of *RE* content. It is also noted that the *RE*-free sample shows the best F value (0.92).

3.3.2   *SEM* analysis

The *SEM* images of freshly fractured surfaces of *RE*-free and typical *RE* substituted $(Bi, Pb) - 2212$ samples are shown in Figure 3.4. The structural morphology of the samples varies with increase in x value and no secondary phase is detected in any of the samples, even up to the highest value of investigated x. The grain morphology of *RE*-free (RE0.000) sample shows clear and flaky grains with a layered growth typical of $(Bi, Pb) - 2212$. Whereas, in the *RE* substituted sample, the flaky nature of grains disappears with distinct reduction in grain size and increased porosity. The systematic decrease of *XRD* peak height [Figure 3.2 (a - d)] and the microstructural variation in *SEM* images [Figure 3.4] confirm that the microstructure of $(Bi, Pb) - 2212$ deteriorates with increase of *RE* content. That is the *RE*-free sample shows
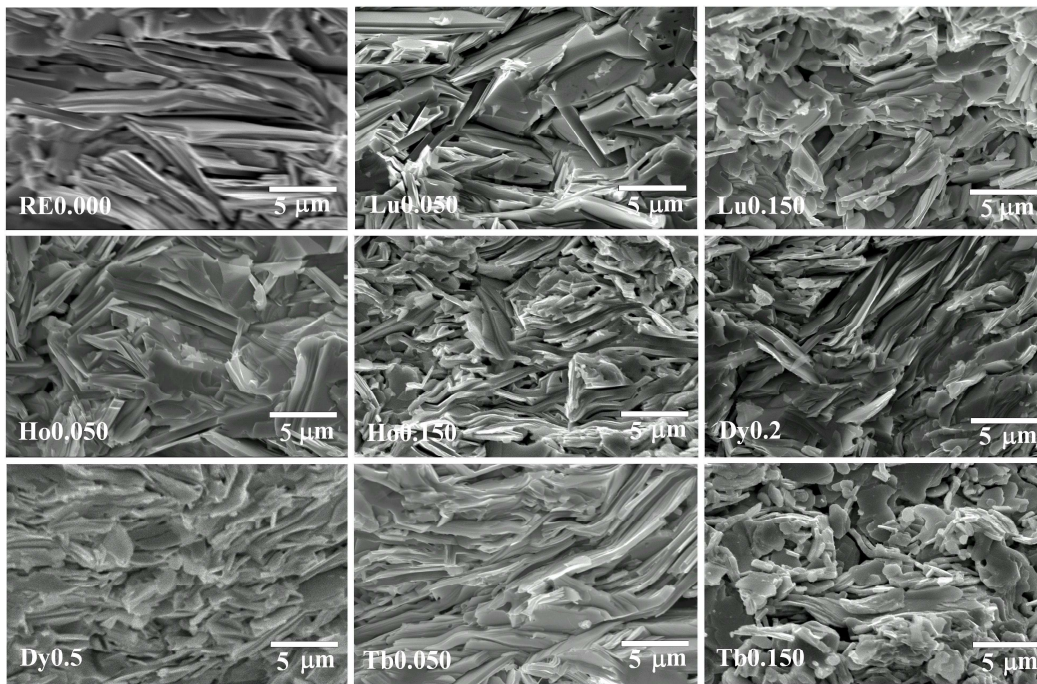
Figure 3.4: SEM micrographs of the fractured surface of the *RE*-free and *RE* (*RE* = *Lu*, *Ho*, *Dy* and *Tb*) substituted $(Bi, Pb) - 2212$ samples.

the best microstructure with respect to texturing or grain alignment compared to all other *RE* substituted samples. This is further evidenced from the Lotgering index (*F*) calculation of the samples (table 3.1). This deterioration in the microstructure plays an important role in limiting

the self-field J_C of the system, since the weak links associated with the grain boundaries are known to limit the J_C value. The possible reasons for the formation of these weak links are the misorientation of grain boundaries and the compositional variations at the grain boundaries. In the case of RE substituted samples, the misorientation gradually increases with increase of RE content (Figure 3.4) and hence the weak links also increases with increase of RE content.

3.3.3   Compositional analysis

Figure 3.5 (a) – (f): The *EDS* **spectra of** RE **-free and typical** RE ($RE = Lu$, Ho, Dy **and** Tb) **substituted** $(Bi, Pb) - 2212$ **grains. The cationic composition of** RE **substituted samples is given in table 3.2.**

Table 3.2: The rare-earth (RE) stoichiometry (x) and the initial and final cationic compositions of RE-free and RE substituted $(Bi, Pb)-2212$ grains obtained by EDS spot analysis, keeping the intensity of Cu as standard.

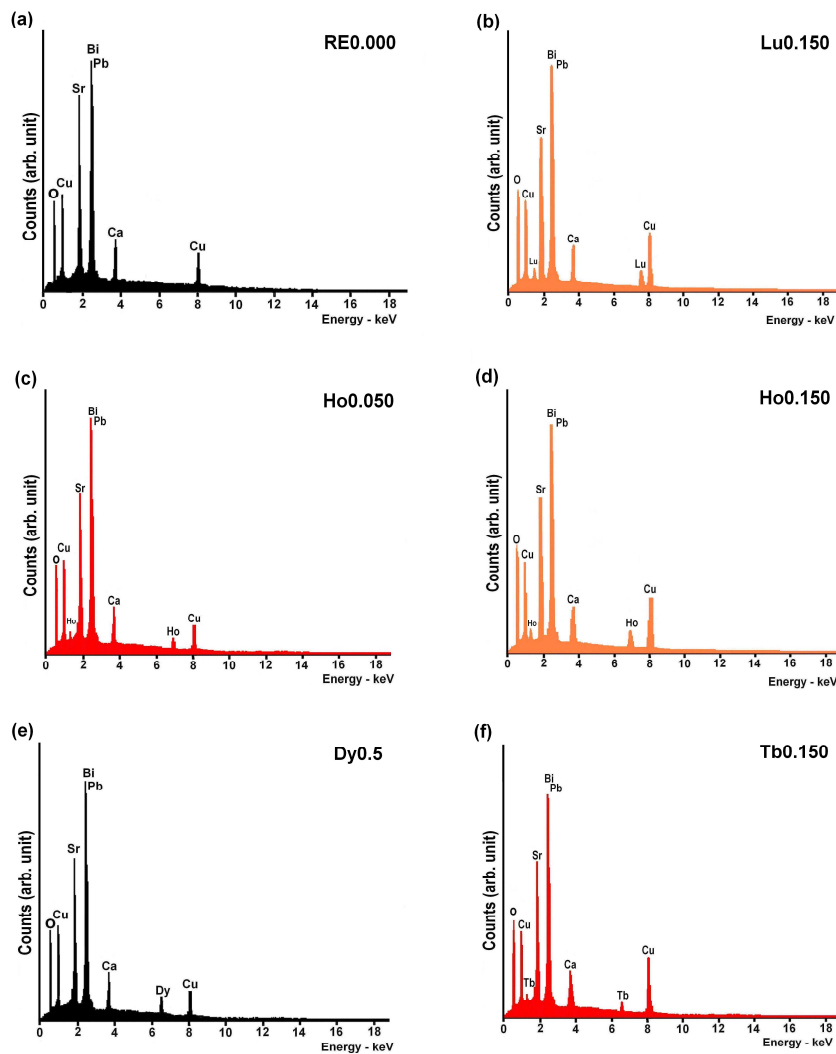| RE | x | Cationic composition of *RE*-free and *RE* substituted *(Bi, Pb)*-2212 grains | | | | | | | |
		(Bi, Pb)		Sr		RE		Ca	
		initial	final	initial	final	initial	final	initial	final
$RE-$free	0.000	2.10	2.04	2.0	1.96	0.000	0.00	1.10	1.07
	0.025	2.10	1.99	1.975	1.98	0.025	0.03	1.10	1.03
	0.050	2.10	2.05	1.950	1.94	0.050	0.04	1.10	1.05
	0.075	2.10	2.03	1.925	1.91	0.075	0.07	1.10	1.01
Lu	0.100	2.10	2.01	1.900	1.89	0.100	0.09	1.10	1.09
	0.125	2.10	2.07	1.875	1.86	0.125	0.11	1.10	1.04
	0.150	2.10	2.04	1.850	1.82	0.150	0.13	1.10	1.05
	0.025	2.10	2.02	1.975	1.97	0.025	0.01	1.10	1.06
	0.050	2.10	1.98	1.950	1.96	0.050	0.04	1.10	1.01
	0.075	2.10	2.09	1.925	1.93	0.075	0.06	1.10	1.05
Ho	0.100	2.10	2.02	1.900	1.89	0.100	0.08	1.10	0.99
	0.125	2.10	2.03	1.875	1.88	0.125	0.12	1.10	1.04
	0.150	2.10	2.07	1.850	1.86	0.150	0.13	1.10	1.02
	0.1	2.10	2.06	1.90	1.93	0.1	0.07	1.10	0.98
	0.2	2.10	1.99	1.80	1.78	0.2	0.15	1.10	0.99
Dy	0.3	2.10	2.03	1.70	1.67	0.3	0.24	1.10	1.02
	0.4	2.10	1.97	1.60	1.56	0.4	0.36	1.10	1.00
	0.5	2.10	2.00	1.50	1.43	0.5	0.44	1.10	1.05
	0.025	2.10	1.98	1.975	1.96	0.025	0.02	1.10	0.97
	0.050	2.10	2.03	1.950	1.95	0.050	0.04	1.10	1.01
	0.075	2.10	2.04	1.925	1.91	0.075	0.07	1.10	1.03
Tb	0.100	2.10	1.97	1.900	1.88	0.100	0.08	1.10	1.02
	0.125	2.10	2.02	1.875	1.86	0.125	0.11	1.10	0.99
	0.150	2.10	2.06	1.850	1.83	0.150	0.14	1.10	1.06

The compositional analysis has performed by *EDS* using the spot analysis mode and the *EDS* spectra of the *RE*-free and typical *RE* substituted $(Bi, Pb) - 2212$ grains are shown in figure 3.5 (a) – (f). The presence of *RE* is detected in the *RE* substituted $(Bi, Pb) - 2212$ grains with a corresponding reduction in *Sr* and its cationic composition is given in table 3.2 (estimated keeping the intensity of *Cu* as standard). This supports that the *RE* atoms are successfully doped into the $(Bi, Pb) - 2212$ system and form a structure with almost identical initial stoichiometry (table 3.2). It also shows that the ratio of RE/Sr in the $(Bi, Pb) - 2212$ grains is almost equal to that of the corresponding starting composition for each *x*, which indicates that the substituted *RE* is successfully incorporated in the crystal structure of $(Bi, Pb) - 2212$ The quantitative data in table 3.2 also shows that the stoichiometry of *Sr* and *RE* in the final samples varies according to the nominal stoichiometry envisaged, within a limit of around 10 %. Hence, the data confirms the successful substitution of *RE* at the *Sr*-site of $(Bi, Pb) - 2212$ system.

3.4 Superconductor characterization

3.4.1 $\rho - T$ measurements

The temperature dependences of the resistivity for *RE*-free and *RE* (*RE* = *Lu*, *Ho*, *Dy* and *Tb*) substituted $(Bi, Pb) - 2212$ samples are shown in figure 3.6 (a) – (d). The zero-field resistivity plot is extrapolated to zero for *RE*-free and all *RE* substituted samples to get the value of ρ_n (Table 3.1). It shows that the normal state resistivity (ρ_n) and the resistivity at 300 *K* ($\rho_{300\,K}$) [Table 3.1] is minimum for *RE*-free (34.28 and 92.7 $\mu\Omega cm$) and increases with increase of *RE* content (*x*) and the maximum value is obtained for *Dy*0.5 (205.19 and 534.63 $\mu\Omega cm$), i.e. the ρ_n and $\rho_{300\,K}$ values sensitively depend on the defect concentration. Also, the highest ρ_n value for *Dy*0.5 reflects the increased impurity scattering and higher amount of disorder in this sample and the enormous increase in the $\rho_{300\,K}$ is due to the increased porosity of *RE* substituted $(Bi, Pb) - 2212$ superconductor (figure 3.4), which increases the resistive weak links between the grains. The significance of ρ_n value is discussed in detail in chapter 7.

The critical temperature (T_c) of the samples (table 3.1) is determined by estimating the temperature at which the resistivity starts dropping from a linearly varying metallic behaviour ($d\rho/dt > 0$), while cooling it. It is observed that all the samples show metallic behavior above the T_c and the value of T_c increases with increase in RE concentration (table 3.1). The maximum T_c obtained for Lu, Ho, Dy and Tb substituted samples are 95.8 K ($x = 0.150$), 93.5 K ($x = 0.150$), 96.6 K ($x = 0.4$) and 94.4 ($x = 0.150$), respectively, while the T_c obtained for the RE-free sample is 80.7 K. It is clear from the figure 3.6 (c) and table 3.1 that the optimal value of RE gives the maximum T_c and in the case of Dy the T_c is higher by about 16 K (for Dy0.4) than the RE-free sample.
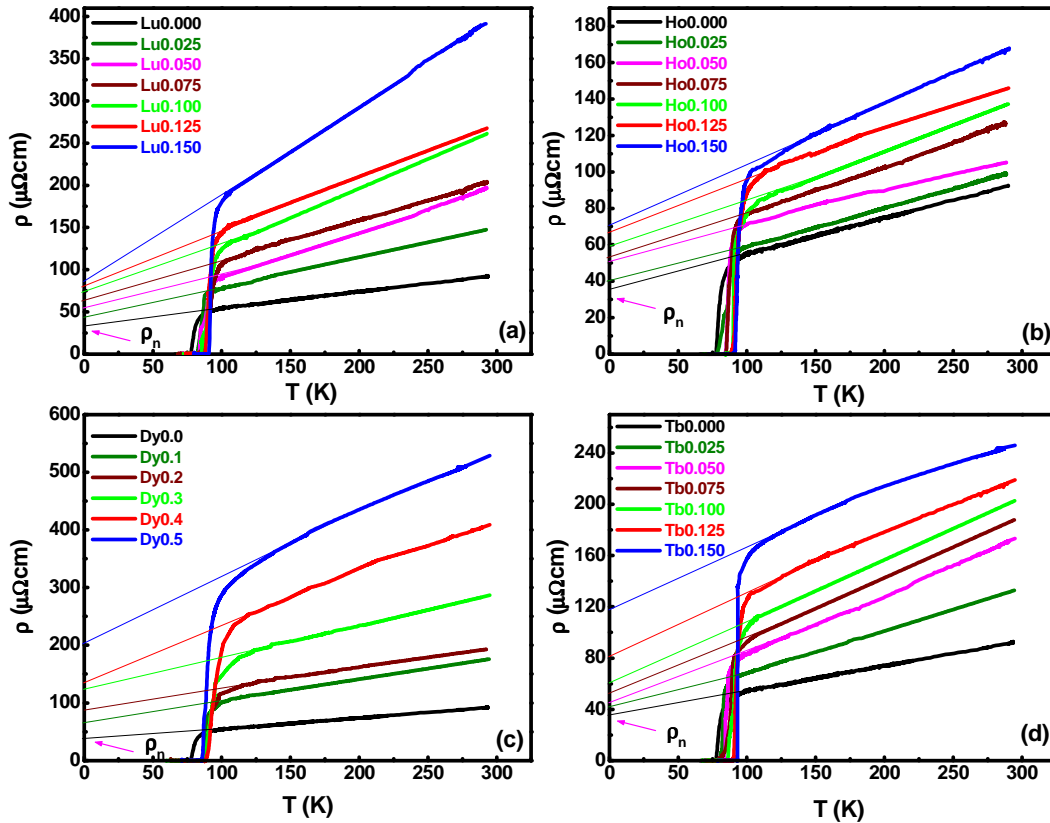

Figure 3.6 (a) – (d): Temperature dependent resistivity plots of RE-free and all RE (RE = Lu, Ho, Dy and Tb) substituted $(Bi, Pb) - 2212$ samples. The normal state resistivity (ρ_n) value is indicated by an arrow and the ρ_n values are given in table 3.1.

The hole carrier concentration of the *RE* substituted samples showing a superconducting transition is calculated using the phenomenological formula [Krusin-elbaum et al. (2004)],

$$P = \left[\left\{ 1 - \left(T_c / T_{c\max} \right) \right\} \big/ 82.6 \right]^{\frac{1}{2}} + 0.16 \qquad (3.3)$$

Here P is the hole carrier concentration $/ Cu$ atom and $T_{c-\max}$ corresponds to T_c for $P = 0.16$, the optimal concentration. The value of P for *RE*-free and all *RE* substituted samples is given in table 3.1 and the results show that as the dopant level increases, the hole carrier concentration continues to decrease which makes the system optimally doped ($P = 0.16$), where the T_c of the *RE* substituted samples becomes maximum. Beyond the optimum level, the system is transformed into an underdoped state with lesser amount of hole carrier concentration (< 0.16, for $Dy0.5$, $P = 0.1319$) and hence, T_c decreases. This can be understood by the following explanation. It is well known that the *RE*-free $(Bi, Pb) - 2212$ system is inherently "over-doped" with holes. When RE^{3+}/RE^{4+} ions are substituted for Sr^{2+}, each substitution of *RE* provides additional electrons to fill the vacant holes in the crystal. Hence, the hole concentration in the CuO_2 plane decreases. This controls the hole concentration in the CuO_2 planes and when the *RE* concentration reaches the optimal stoichiometry, the system becomes "optimally-doped" leading to enhanced T_c and J_C. Beyond this "optimally-doped state" the system becomes "under-doped" due to the large reduction of hole carrier concentration, which transform the conduction mechanism of $(Bi, Pb) - 2212$ from metallic to semiconductor or insulator. Also, the transition width, ΔT_c is found to increase with increase in *RE* content (Table 3.1). This increase in the ΔT_c is because of the changes in chemical as well as electronic inhomogeneity in the $(Bi, Pb) - 2212$ system caused by the variation in the charge carrier concentration due to *RE* substitution.

3.5 Self-field J_C measurement

Figure 3.7 (a) and (b) shows the variation of self-field J_C as a function of *RE* ($RE = Lu$, *Ho*, *Dy* and *Tb*) content. The self-field J_C is found to increase significantly with *RE* substitution and it reaches a maximum at $x = 0.075$ for *Tb*, *Ho* and at around $x = 0.1$ to 0.2

for *Lu*, *Dy* and then decreases at higher *RE* concentrations. Moreover, the value of J_C also depends on the substituted *RE*. The pure sample shows a J_C of 1642 kAm^{-2}, while the maximum J_C obtained by *RE* substitution is in the range of 12082 (for *Ho* at $x = 0.075$) to 18076 kAm^{-2} (for *Tb* at $x = 0.075$) at 64 K. This shows that the J_C is enhanced drastically at the optimum doping concentration. The increase in transport J_C is $\sim 7-11$ times higher than the *RE*-free $(Bi, Pb) - 2212$ sample and the enhancement can be explained as follows. The replacement of *Sr* with *RE* results in the chemical and electronic rearrangement of the charge
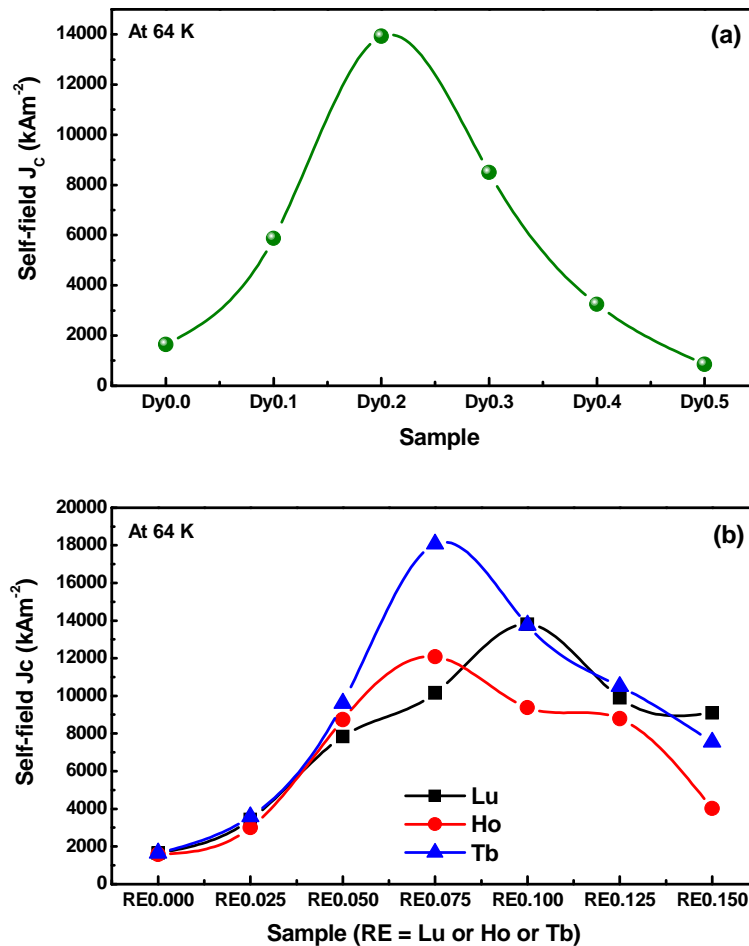

Figure 3.7 (a) and (b): Variation of self-field J_C value of the samples with *RE* (*RE* = *Dy*, *Lu*, *Ho* and *Tb*) content.

reservoir layers ($Sr-O/Bi-O/Sr-O$) adjacent to the CuO_2 layers through which the actual supercurrent is believed to flow. The crystal defects created due to the RE substitution is mainly confined in the Sr-layer. At self-fields, vortices confined in the CuO_2 layers are effectively pinned by the defects in the *Sr*-layer which leads to the formation of strongly coupled Josephsons vortices in the CuO_2 layer. Hence, RE substitution in $(Bi, Pb)-2212$ increases the Josephsons coupling strength between the CuO_2 layers across the blocking layers ($Sr-O/Bi-O/Sr-O$). This improves the self field J_C of the optimized RE substituted $(Bi, Pb)-2212$ superconductors. The improvement in the T_c of RE substituted $(Bi, Pb)-2212$ samples (due to the decrease in hole concentration in the CuO_2 plane) also contributes towards the improvement of transport J_C.

Further, RE substitution alone cannot produce the observed enhancement in J_C. The electrical conductivity of the blocking layers of $Bi-2212$ is systematically enhanced, and the anisotropy is substantially reduced by the doping of Pb atoms into the blocking layers ($Bi-O$) [Zhao et al. (2003), Motohashi et al. (1999)]. This increases the Josephson coupling strength between the CuO_2 layers across the insulating $Bi-O$ layers [Kleiner et al. (1994)], which in turn increases the c-axis conductivity, and as a result, J_C increases. In addition, the pinning centers introduced by the RE^{3+}/RE^{4+} ion in the $(Bi, Pb)-2212$ lattice enhance the self-field J_C. The above results show that the enhancement in J_C of RE substituted samples is because of the chemical and electronic re-arrangement introduced due to the dual effect of substitution of RE and Pb in $Bi-2212$. At higher x values, the J_C of the RE substituted samples decreases. This is because, at higher RE concentrations, the charge carrier concentration decreases while grain boundary weak-links and porosity increases. Thus, it is concluded that T_c does not depend on the microstructure while J_C strongly depends on it.

Furthermore, at higher RE concentrations (x), excess number of oxygen atoms are incorporated into the oxygen deficient $Bi-O$ layers, which makes it more insulating. This increases the c-axis resistivity, hence, weakens the Josephson coupling strength between the CuO_2 layers across the $Bi-O$ layers, resulting in the reduction of the self-field J_C. The reduction of the hole carrier concentration beyond the optimum level at higher RE

concentration also triggers the metal to insulator transition (MIT) in $(Bi, Pb) - 2212$ system [Shabna et al. (2008), Shabna et al. (2010)].

3.6 Conclusions

This chapter presents a systematic study on the structural and superconducting properties of RE substituted $(Bi, Pb) - 2212$ $[Bi_{1.6}Pb_{0.5}Sr_{2-x}RE_xCa_{1.1}Cu_{2.1}O_{8+\delta}]$ system with different RE concentrations ($0 \le x \le 0.5$ and $RE = Lu, Ho, Dy$ and Tb) and the results are compared with RE-free $(Bi, Pb) - 2212$ superconductor. It is observed that a significant structural and electronic change takes place in the system due to RE substitution. The XRD and EDS results give a clear evidence that the RE is substituted at the Sr site of $(Bi, Pb) - 2212$ system. As a result, the critical temperature (T_c) and self-field critical current density (J_C) increase remarkably at optimum RE concentrations. The SEM micrographs and Lotgering index results show that better grain growth or orientation is not the reason for enhancement of superconducting properties, because due to RE substitution grain size and orientation decreases. The increase in T_c as well as J_C is explained by the dual effect of the decrease in the hole concentration in CuO_2 planes from the over-doped to an optimally-doped state (as evidenced from the P value) and the improvement of coupling between the CuO_2 layers across the charge reservoir layer achieved by RE-doping. The J_C also decreases rapidly at higher x value because of the decreased inter-grain connectivity, mis-orientation of the grains and increased porosity as evidenced from the SEM micrographs and Lotgering index results. Beyond the optimum levels, the T_c gets reduced and an under-doped condition is attained due to reduced hole density.

Chapter 4

CHAPTER 4

Suppression of flux creep and flux pinning properties of rare earth (Lu, Ho, Dy, Tb, Gd and Eu) substituted (Bi, Pb)-2212

4.1 Introduction

Among the cuprate based high T_c superconductors $(\textbf{\textit{HTS}})$, $Bi-$ based systems are of great technological interest, since the superconducting transition temperature (T_c) of these materials exceed liquid nitrogen temperature and their properties are most suitable for the fabrication of long length of wires and tapes. The main advantages of $Bi-$ based systems are their layered structure and hence, texturing can be easily induced in it. Also, its oxygen stoichiometry is relatively invariant with respective to cationic doping, when samples are prepared in identical conditions and it has lesser weak link problems compared to $Bi-2223$. But their applications in magnetic fields and at high temperatures are limited because of their strong anisotropic properties, extremely short coherence length (ξ) and large penetration depth (λ). The crystal structure of $Bi-2212$ is highly two dimensional ($2D$) with alternate stacking of superconducting CuO_2 layers and poorly conducting thick blocking layers, which reduce the Josephson coupling between the superconducting CuO_2 layers. The transport and magnetic properties are highly anisotropic and the in-plane conductivity along the CuO_2 layers is much higher than that of the out-of-plane conductivity along the blocking layers [Kotaka et al. (1994)]. Due to the weak coupling between the superconducting layers, the $3D$ vortices melts into $2D$ pancake like vortices at higher temperatures and fields [Pradhan et al. (1994)]. The $2D$ pancake vortices are easily de-pinned causing flux creep and energy dissipation during transport current flow. The critical current density (J_C) and critical temperature (T_c) are the important parameters for potential applications of $\textbf{\textit{HTS}}$ and the J_C value is primarily limited due to the insufficient flux pinning properties [Larbalestier (1996), Su et al. (1995)]. In order to sustain high non-dissipative transport currents at elevated temperatures and fields the vortices must be pinned. There has been numerous efforts to enhance the flux pinning properties of $Bi-$ based systems, and hence the J_C value by introducing effective pinning sites [Li et al.

(1997), Biju et al. (2007), Ilyushechkin et al. (2004), Wang et al. (2001), Rahier et al. (2006), Yorimasa et al. (2003), Kazin et al. (2000)].

One of the effective methods to enhance the flux pinning properties of $Bi-$ based superconductors is to modify the system by selective doping. It has been experimentally found that the Pb doping at $Bi-$ site in $Bi-2212$ increases the $c-$ axis conductivity by more than one order of magnitude and reduces the electro-magnetic anisotropy [Zhao et al. (2003)], enhances the intrinsic pinning and there by improving the J_C in pure $Bi-2212$ crystals [Chong et al. (1997)]. A few studies reported that the flux pinning strength of cuprate superconductors increases on RE doping [Vinu S, Sarun P M, et al. (2008), Vinu S, Sarun P M, et al. (2008), Biju et al. (2007)]. On the technological side the substitution of Pb for Bi improve the superconducting properties of both bulks and tapes [Fujii et al. (2000)] and the substitution of rare earth (RE) ions in the place of Ca/Sr stabilize the crystal structure of $Bi-2212$ system [Jin et al. (1999)]. This chapter presents my studies on suppresson of flux creep and enhancement of flux pinning properties of $Bi-2212$ substituted with Pb at the Bi site and RE (Lanthanides Lu, Ho, Dy, Tb, Gd and Eu) at its Sr site, respectively, as typical examples.

4.2 Experimental details

The RE substituted $(Bi, Pb)-2212$ superconductors with a general stoichiometry of $Bi_{1.6}Pb_{0.5}Sr_{2-x}RE_xCa_{1.1}Cu_{2.1}O_{8+\delta}$ were prepared by solid state sintering using high purity chemicals $(>99.9\%, Aldrich\ Milwaukee, WI)$ such as oxides/carbonates of the ingredients. Here $RE = Lu$, Ho, Dy, Tb, Gd, Eu and the samples with different RE stoichiometry will be hereafter denoted as REx, where x is the corresponding stoichiometry. The preparation steps, phase identification, micro-structural and elemental analysis and superconductor characterization parts were already explained in detail in chapter 3. For the critical current versus magnetic field measurements, the directions of the current and magnetic field were kept parallel and perpendicular to the pressed surface of the pellet, respectively. The $E-J$ characteristics of the samples under zero and fixed fields namely, $0.32\ T$ and $0.64\ T$ were measured at $64\ K$ by four-probe method in a liquid nitrogen bath cryostat with provision for vacuum. A computer controlled $dc-$ pulse method with four-probe arrangement was used to

determine $E-J$ characteristics using a constant current source (*Aplab* 9711*P*) and subsequently to determine the transport I_C of the samples. The pulse method effectively minimizes the Joule heating from current leads and contacts by providing sufficient cooling time between each pulse. Thus it also avoids the influence of the ramp-rate on $E-J$ characteristics. The $J_c(B)$ characteristic was studied with field ranging from 0.0 - 1.4 T. All these measurements are automated using *GPIB* interfaced with a personal computer.

4.3 Theoretical background

To describe the pinning in high T_c materials, one can assume that the core pinning is dominant due to the large values of Ginzburg parameter (κ). This leaves two different sources of pinning, either by (*i*) non-superconducting (normal) particles embedded in the superconducting matrix leading to the scattering of the electron mean free path ($\delta l-$ pinning) or (*ii*) pinning provided by spatial variations of the κ associated with fluctuations in the transition temperature T_c (δT_c or $\Delta\kappa-$ pinning). Pinning is different for various sizes of pinning centers compared with the inter-flux line spacing (d) which is given by

$$ d = \left(\frac{2}{\sqrt{3}} \right) \left(\frac{\phi_0}{B} \right)^{\frac{1}{2}} \tag{4.1} $$

where ϕ_0 denotes flux quantum. The interaction volume, V_{pin} for point pinning centers is, $V_{pin} \sim \xi^3$ ($\xi-$ coherence length), whereas for volume pinning centers, $V_{pin} \sim d^3$. The Dew-Hughes model [Dew-Hughes et al. (1974)] is a direct summation model of elementary pinning forces and according to this model, the flux pinning force per unit volume can be represented by an expression of the form,

$$ F_P = \eta L f_P \tag{4.2} $$

where f_P is the pinning force per unit length of pinned flux line, L is the total length of flux-lines per unit volume that is directly pinned, and η is an efficiency factor, determined by the extent to which its neighbors in the flux lattice allow a flux line to relax towards a position of maximum pinning. Let ΔW be the work done in moving unit length of flux line from a pinning center to the nearest position where it is unpinned, and x be the effective range of the pinning interactions then,

$$f_P = \frac{(-\Delta W)}{x} \qquad (4.3)$$

Therefore equation (4.2) becomes,

$$F_P = -\frac{\eta L \Delta W}{x} \qquad (4.4)$$

Flux-lines interact with pinning centers because the superconducting properties of the latter are different from those of the bulk of the superconductor. Pinning centers may be classified on the basis of their dimensions compared with the value of $'d'$ given by equation (4.1). Point pins are regions whose dimensions in all directions are less than 'd'. A point pin can interact with only one flux line at a time. Line pins, such as dislocations or needle shaped precipitates have one dimension long compared with $'d'$. When lying parallel to the local direction of B, they can interact with one flux line over their whole length. Lying at an angle to B they can interact with several flux lines. Grain boundaries and plate-like precipitates have two dimensions greater than $'d'$, and act as surface pins. Large precipitates with all dimension larger than $'d'$ produces volume pin. It is now possible to evaluate the quantities in equation (4.4), appropriate to various pinning situations. The value of ΔW depends upon the nature of the pinning interaction, that is, whether it is magnetic or core pinning. When the pinning is due to core interaction, ΔW is equal to ΔG, the change in the Gibbs function of unit length of flux-line as it moves from the pinning center to the matrix. The Gibb's function per unit volume of a superconductor $G(H,T)$ in the mixed state is given by,

$$G(H,T) = G_N(H,T) - \frac{\mu_0 (H_{C2} - H)^2}{2.32(2k^2 - 1)}$$

(4.5)

Here $G_N(H,T)$ is the Gibbs function of the normal state. The second term is the free energy of the flux-lattice in the superconductor. An approximation to the core energy (E_C) alone may be arrived at by multiplying the Gibbs function per unit volume by the volume of the flux line core. Assuming a radius of ξ $\left[\xi = (\phi_0 / 2\pi\mu_0 H_{C2})^{0.5} \right]$ for the flux line core and area $\pi\xi^2$ we get,

$$E_C = -\frac{\pi\xi^2 \mu_0 (H_{C2} - H)^2}{2.32(2k^2 - 1)}$$

(4.6)

For small pinning centers, when size of the pinning center '$a < d$' (point or surface) then ΔW is equal to the change in core energy, E_C, as defined by equation (4.6). Therefore,

$$\Delta W = -\frac{\pi\xi^2 \mu_0 (H_{C2} - H)^2}{2.32(2k^2 - 1)}$$

(4.7)

For volume and surface pin, $L = S_V/2$, and for point pin $L = BV_F/\phi_0$. Here S_V is the surface area per unit volume projected in the direction of Lorentz force and V_F is the volume fraction of the superconductor. If the flux lines are perfectly rigid, then each will, on an average, have a fraction V_F of its length inside a pinning center [$V_F \sim (a/l)^3$. Where 'a' is the size of the pinning center and 'l' is the spacing between the pinning centers]. Similarly for volume pin, $x = d$, for surface pin $x = \xi$ and for point pin $x = a/2$. Pinning functions for specific situations like core, normal or $\Delta\kappa$, volume, surface or point may be determined by inserting the appropriate values η, L, ΔW and x into equation (4.4) and for point pins we get,

$$F_P = \frac{\mu_0 V_F H_{c2}^2 h^p (1-h)^q}{4.64 ak^2}$$

(4.8)

Here p and q describes the actual pinning mechanism. For normal point pins, $p = 1$ and $q = 2$, and the position of maximum F_P appeared at the reduced field value of $h = 0.33$. From equation (4.8) we get,

$$F_P = A \left(\frac{B}{B_{irr}} \right)^p \left(1 - \frac{B}{B_{irr}} \right)^q$$

(4.9)

Where A is a numerical parameter, and $(B/B_{irr}) = h$ is the reduced field. There are many different pinning mechanisms, simultaneously active in **HTS** and it is an important task to find the dominant one. The experimental F_P curves are theoretically fitted using equation (4.9).

The $RE-$free and RE substituted $(Bi, Pb) - 2212$ samples are further analyzed with the help of $E - J$ characteristics using one-dimensional flux-creep model, wherein the flux-creep is caused by a thermally activated motion of flux-lines. This motion is characterized by a velocity, which is strongly dependent on the local current density. To understand the flux motion in the presence of applied magnetic field we used the Maxwell's equation of the form,

$$\left(\frac{\partial B}{\partial t} \right) = - \left(\frac{\partial E}{\partial x} \right)$$

(4.10)

where, E is the local electric field which can be related to the flux density and the velocity of the thermally-activated flux motion v by the relation, $E = vB$. The velocity of the vortex motion in a thermally activated process is given by

$$v = v_c e^{-\left[U(J)/k_B T \right]}$$

(4.11)

where $U(J)$ is the pinning potential barrier and v_c is the velocity when $U(J) = 0$. If the pinning energy has a logarithmic dependence on the current density then,

$$U(J) = U_C \ln\left(\frac{J_C}{J}\right) \qquad (4.12)$$

Here, U_C is the pinning energy and equation (4.12) follows that the electric field equals [Shantsev et al. (2000)],

$$E = E_C \left(\frac{J_C}{J}\right)^n \qquad (4.13)$$

The $\log E - \log J$ curves is called $E - J$ characteristics and the slope of the curve gives the $n-$ index of the material.

4.4 Flux pinning analysis

4.4.1 $J_C(B)$ Characteristics

Figure 4.1 (a) - (f) shows the variation of J_C with magnetic field [$J_C(B)$ characteristics] for $RE-$free and $RE\left(RE = Lu,\ Ho,\ Dy,\ Tb,\ Gd\ and\ Eu\right)$ substituted $(Bi, Pb) - 2212$ superconductors at 64 K and magnetic field up to 1.4 T. This characteristic shows that the substitution of RE in optimum concentration (x = 0.075 to 0.1 for Lu, Ho, Tb and $x = 0.1\ to\ 0.2$ for Dy, Gd, Eu) in $(Bi, Pb) - 2212$ results in an enormous improvement in its $J_C(B)$ characteristic. To compare the flux pinning properties of the samples, the variation in normalized in-field critical current density of RE-free and all $RE\left(RE = Lu, Ho, Dy, Tb, Gd\ and\ Eu\right)$ substituted $(Bi, Pb) - 2212$ superconductors for magnetic fields up to 1.4 T is given in figure 4.2 $(a) - (f)$. The normalized $J_C(B)$ characteristics of the

RE substituted samples are found to be much better than those of the *RE* -free sample. This shows that *RE* substitution drastically enhances the flux pinning properties of $(Bi, Pb) - 2212$ system.
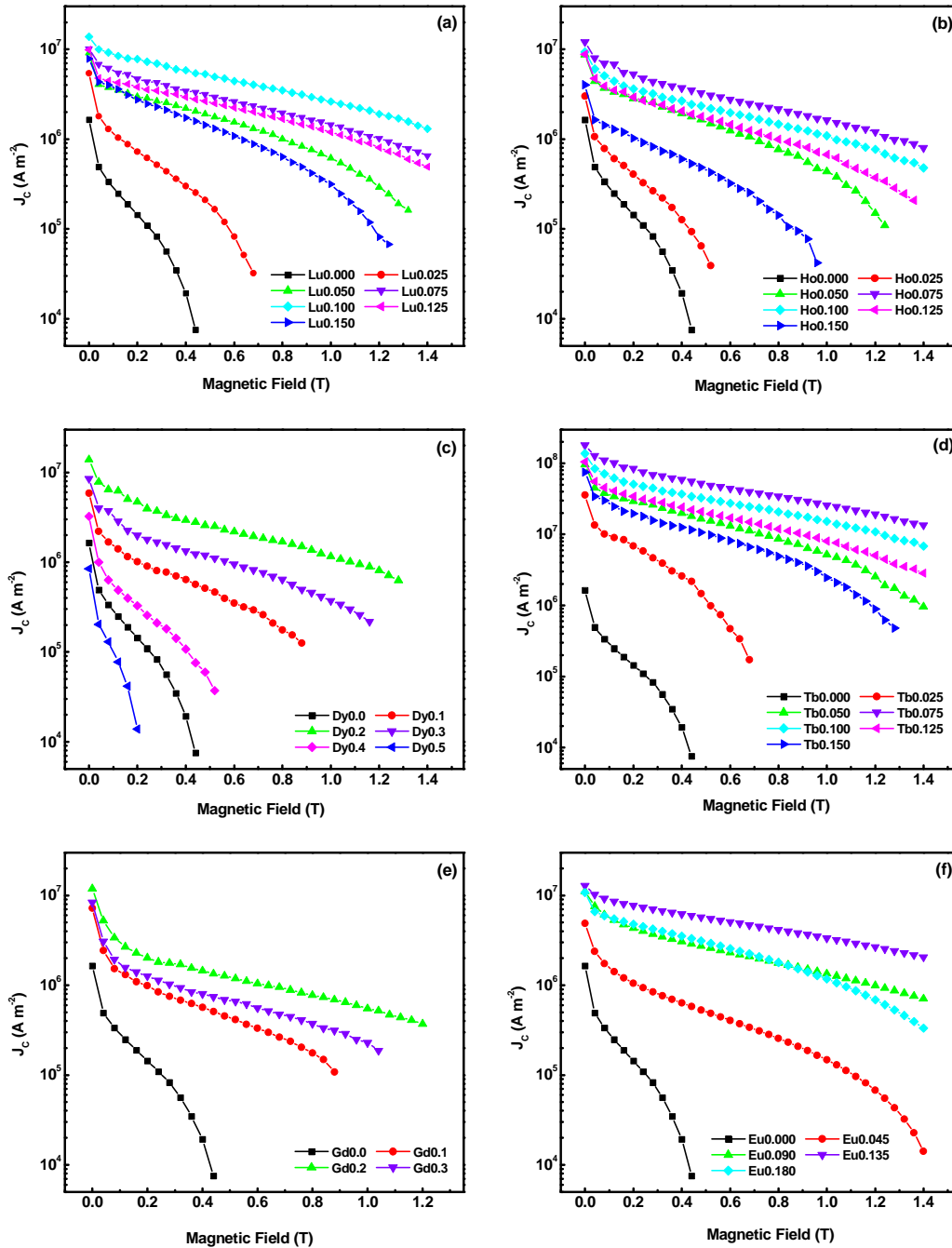

Figure 4.1 $(a) - (f)$: **Variation of** J_C **as a function of magnetic field** $\left[J_C (B) characteristics \right]$ **for** *RE* **-free and** *RE* $(RE = Lu, Ho, Dy, Tb, Gd \, and \, Eu)$ **substituted** $(Bi, Pb) - 2212$ **pellets.**
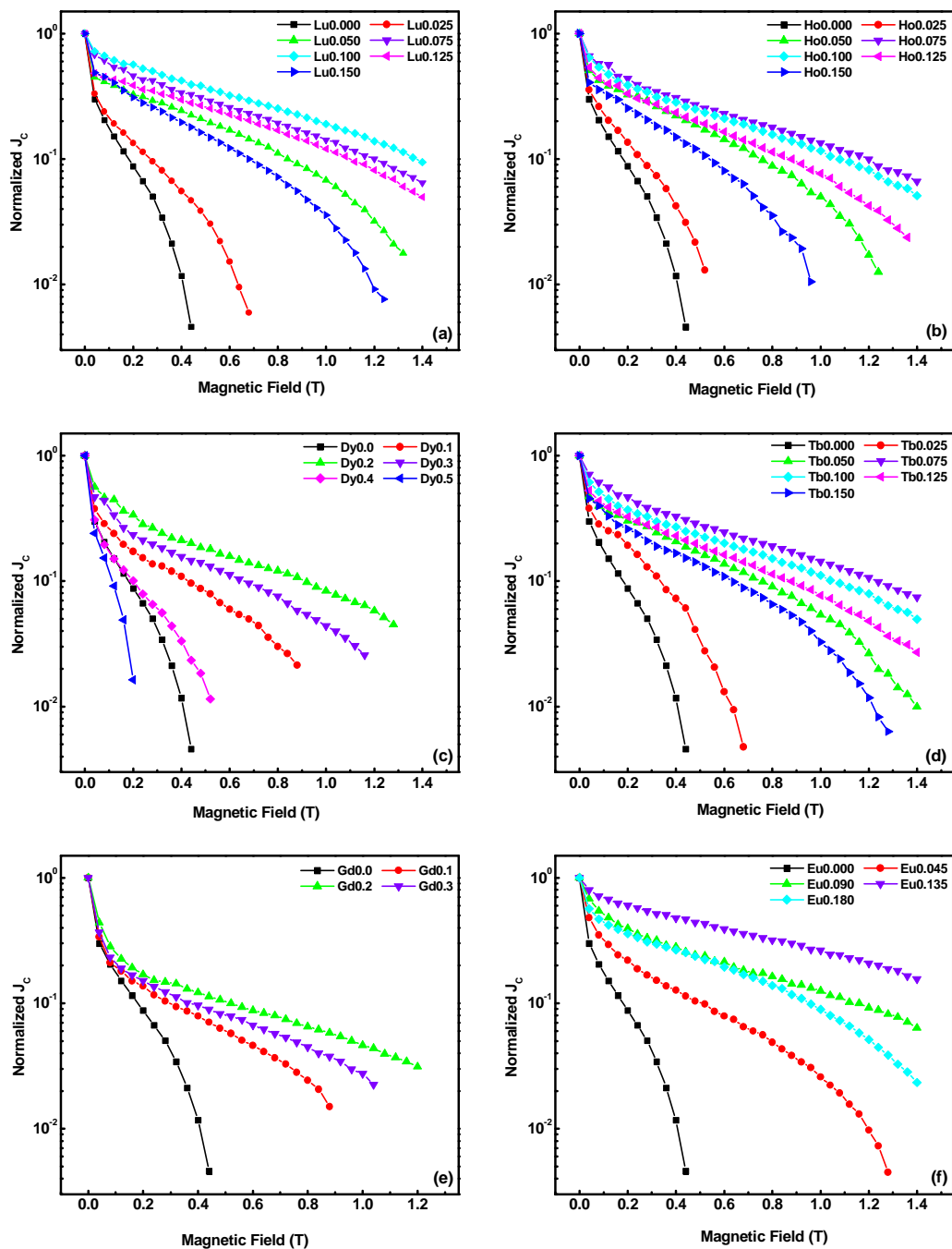
Figure 4.2 $(a)-(f)$: **Variation in normalized in-field critical current density of** RE **-free and all** $RE\left(RE = Lu, Ho, Dy, Tb, Gd \, and \, Eu\right)$ **substituted** $\left(Bi, Pb\right)-2212$ **superconductors for magnetic fields up to 1.4** T .
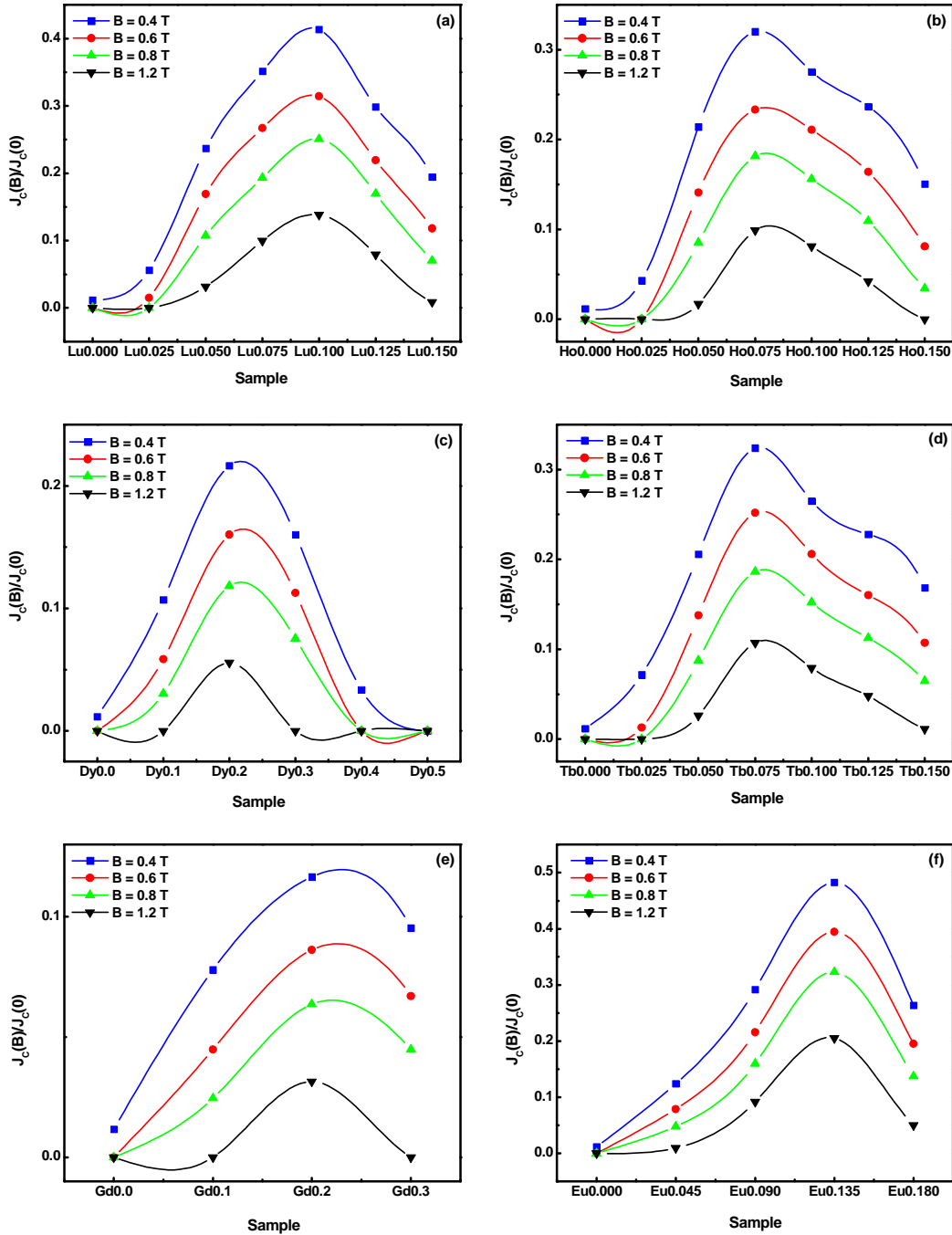
Figure 4.3 $(a) - (f)$: **Variation in** $J_C(B)/J_C(0)$ **with respect to the** $RE(RE = Lu, Ho, Dy, Tb, Gd \text{ and } Eu)$ **content and applied magnetic fields at 0.40, 0.60, 0.80 and 1.00** T **in order to understand the relative performance of the samples in the presence of magnetic field.**

Among the RE substituted samples, the $J_C(B)$ characteristics are found to be the best for Eu substituted samples ($Eu0.135$). The ratio, $J_C(B)/J_C(0)$, of $Eu0.135$ is higher than that of the Eu-free sample ($Eu0.000$) by a factor of 41.3 at 0.4 T and the decrease in J_C with increasing magnetic field is lower for $Eu0.135$ than for $Eu0.000$ and all other Eu doped samples. Similarly the ratio, $J_C(B)/J_C(0)$, of Lu is 35.4 ($Lu0.100$), Tb is 27.69 ($Tb0.075$), Ho is 27.3 ($Ho0.075$), Dy is 18.5 ($Dy0.2$) and Gd is 9.9 ($Gd0.2$) times higher than that of the RE-free sample ($RE0.000$). That is, the deterioration of J_C due to magnetic field is significantly reduced for optimal RE substitution. In order to bring out the increase in the $J_C(B)$ performance of optimally RE substituted samples, the $J_C(B)/J_C(0)$ values of all samples at 0.40, 0.60, 0.8 and 1.00 T are separately given in figure $4.3(a)-(f)$. This figure again clearly shows that the in-field performance and the flux pinning strength are very much improved for optimal RE content.

4.4.2 $F_P(B)$ characteristics

It is widely accepted that a very fruitful tool with which one can investigate the flux pinning properties of superconductors is the determination of pinning force density ($F_P = J_C \times B$) [Koblischka et al. (2000)]. The pinning force density F_P as a function of applied field is shown in $4.4(a)-(f)$. It is seen that the maximum value of F_P is shifted to much higher values for RE-substituted sample (Table 4.1). For example, for the optimal RE substituted samples, the F_P values are $1395 \pm 1\, kNm^{-3}$ (for $Lu0.100$), $1725 \pm 1\, kNm^{-3}$ (for $Ho0.075$), $1355 \pm 1\, kNm^{-3}$ (for $Dy0.2$), $2752 \pm 1\, kNm^{-3}$ (for $Tb0.075$), $645 \pm 1\, kNm^{-3}$ (for $Gd0.2$), $3413 \pm 1\, kNm^{-3}$ (for $Eu0.135$) as against $30 \pm 1\, kNm^{-3}$ for the RE-free ($RE0.000$) sample. This means the F_P value is at the least 22 (for $Gd0.2$) to a maximum of 114 (for $Eu0.135$) times greater than the RE-free ($RE0.000$) sample. This increase strongly support that the flux pinning strength of $(Bi, Pb)-2212$ samples significantly increases with RE substitution and the maximum value of F_P sensitively depends on the selected RE.

Table 4.1: **The values of rare-earth (RE) stoichiometry (x), critical temperature (T_c), the self-field J_C, the maximum value of F_P ($F_{P\max}$), the fitting parameters (p, q) and the irreversibility field (B_{irr}) for RE-free and all RE substituted $(Bi, Pb) - 2212$ samples.**

RE	x	T_c K	J_C kAm^{-2}	$F_{P\max}$ kNm^{-3}	B at which $F_{P\max}$ occurs (T)	p (± 0.05)	q (± 0.05)	B_{irr} ($\pm 0.05\ T$)
RE-free	0.000	80.7	1642	30	0.16	0.62	1.43	0.49
Lu	0.025	84.9	3421	148	0.24	0.66	1.49	0.78
	0.050	86.5	7840	870	0.44	0.74	1.54	1.37
	0.075	90.3	10152	1110	0.72	0.81	1.65	2.14
	0.100	93.0	13810	1395	0.76	0.85	1.72	2.31
	0.125	94.2	9894	918	0.68	0.88	1.76	2.06
	0.150	95.8	9089	713	0.56	0.91	1.83	1.64
Ho	0.025	82.6	2999	81	0.2	0.65	1.45	0.63
	0.050	87.7	8736	791	0.48	0.72	1.55	1.43
	0.075	88.5	12082	1725	0.80	0.77	1.64	2.27
	0.100	91.6	9378	1209	0.68	0.80	1.67	2.11
	0.125	91.8	8784	880	0.56	0.82	1.70	1.76
	0.150	93.5	4012	245	0.36	0.83	1.74	1.12
Dy	0.1	91.7	5872	256	0.40	0.66	1.47	1.21
	0.2	92.5	13927	1355	0.80	0.84	1.71	2.14
	0.3	94.5	8493	577	0.56	0.87	1.75	1.67
	0.4	96.6	3241	65	0.20	0.90	1.80	0.68
	0.5	90.3	847	5	0.08	0.92	1.83	0.26
Tb	0.025	84.8	3581	139	0.24	0.65	1.51	0.72
	0.050	86.4	9603	810	0.56	0.70	1.58	1.61
	0.075	88.2	18076	2752	0.84	0.77	1.69	2.37
	0.100	90.4	13763	1695	0.76	0.82	1.74	2.15
	0.125	92.2	10506	1031	0.64	0.85	1.80	1.93
	0.150	94.4	7539	513	0.48	0.88	1.83	1.49
Gd	0.1	92.5	7233	228	0.40	0.63	1.46	1.28
	0.2	94.3	11910	645	0.68	0.78	1.52	2.02
	0.3	94.9	8353	345	0.56	0.83	1.56	1.64
Eu	0.045	86.8	4895	271	0.36	0.64	1.44	1.50
	0.090	90.9	11095	1465	0.80	0.72	1.51	2.31
	0.135	93.3	12874	3413	0.96	0.89	1.73	2.74
	0.180	94.4	10785	1339	0.60	0.91	1.87	1.83

4.4.3 Theoretical fitting for F_P

     The value of F_P as a function of reduced magnetic field ($h = B/B_{irr}$) is shown in Figure $4.5(a)-(f)$ and all sets of data are found to fit well (Figure $4.5(a)-(f)$, solid parabolic line) with the Dew-Hughes equation [Dew-Hughes et al. (1974)] given by equation 4.9. For normal point pinning, the values of p and q are 1 and 2, respectively, and the maximum value of F_P appear at a reduced field value $h = 0.33$. For RE-free sample, the values of p and q are found to be 0.62 ± 0.05 and 1.43 ± 0.05, respectively. But for RE substituted samples, the values of p and q are found to be 0.91 ± 0.05, 1.83 ± 0.05 (for $Lu0.150$), 0.83 ± 0.05, 1.74 ± 0.05 (for $Ho0.150$), 0.92 ± 0.05, 1.83 ± 0.05 (for $Dy0.5$), 0.88 ± 0.05, 1.83 ± 0.05 (for $Tb0.150$), 0.83 ± 0.05, 1.56 ± 0.05 (for $Gd0.3$), 0.91 ± 0.05, 1.87 ± 0.05 (for $Eu0.135$), respectively, and the p and q values of all samples are given in table 4.1. Here the p and q values are closer to 1 and 2 as predicted by the theory and also the maximum value of F_P ($F_{P\max}$) appeared at $h = 0.33 \pm 0.02$ [Figure $4.5(a)-(f)$], which agrees with the theoretically predicted value ($h = 0.33$). Hence, the main pinning mechanism of these samples is the point pinning due to point defects aroused out of the substitution of RE atoms at the Sr site of $(Bi, Pb) - 2212$ system.

4.4.4 Normalized F_P

     The normalized pinning force density ($F_P/F_{P\max}$) as a function of applied field is shown in figure $4.6(a)-(f)$. It is seen that the maximum values of $F_P/F_{P\max}$ of RE substituted samples appeared at $0.68\,T\,(Gd0.2) - 0.96\,T\,(Eu0.135)$ as against $0.16\,T$ (table 4.1) for RE-free sample ($RE0.000$) at $64\,K$. These results show that the irreversibility line of the RE substituted samples gets shifted toward higher magnetic fields and temperatures if the RE content is in the range $x = 0.075 - 0.1$ for Lu, Ho, Tb and $x = 0.1 - 0.2$ for Dy, Gd, Eu, respectively. In other words the flux pinning strength of RE substituted samples improves considerably compared to the RE-free sample when RE content is in the optimum level ($x = 0.075 - 0.1$, for Lu, Ho, Tb and $x = 0.1 - 0.2$ for Dy, Gd, Eu) and is decreased if the RE content deviates from this range (table 4.1).
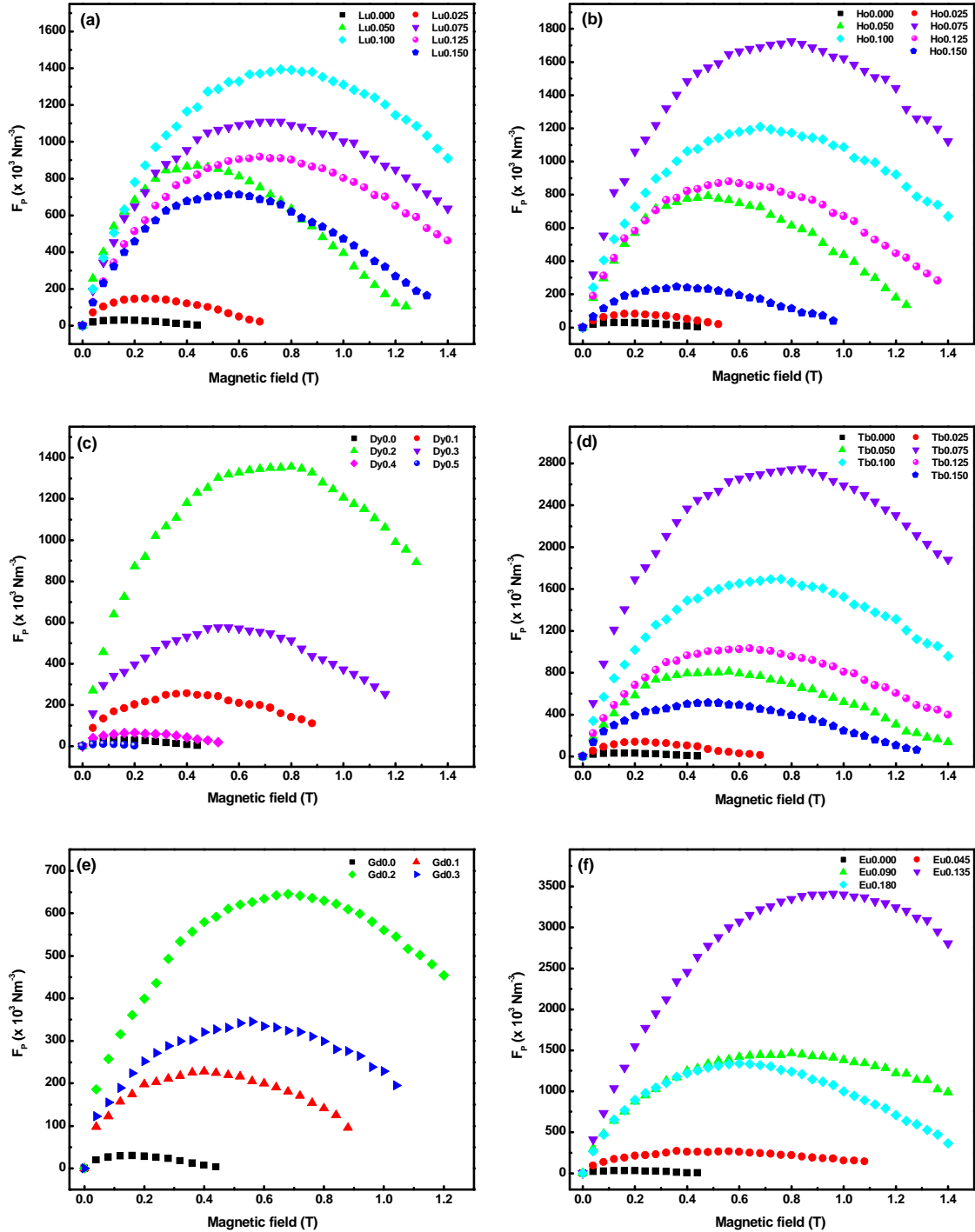
Figure 4.4 $(a)-(f)$: **Variation of pinning force density F_P as a function of magnetic field for RE-free and $RE\left(RE = Lu, Ho, Dy, Tb, Gd\ and\ Eu\right)$ substituted $(Bi, Pb) - 2212$ samples.**
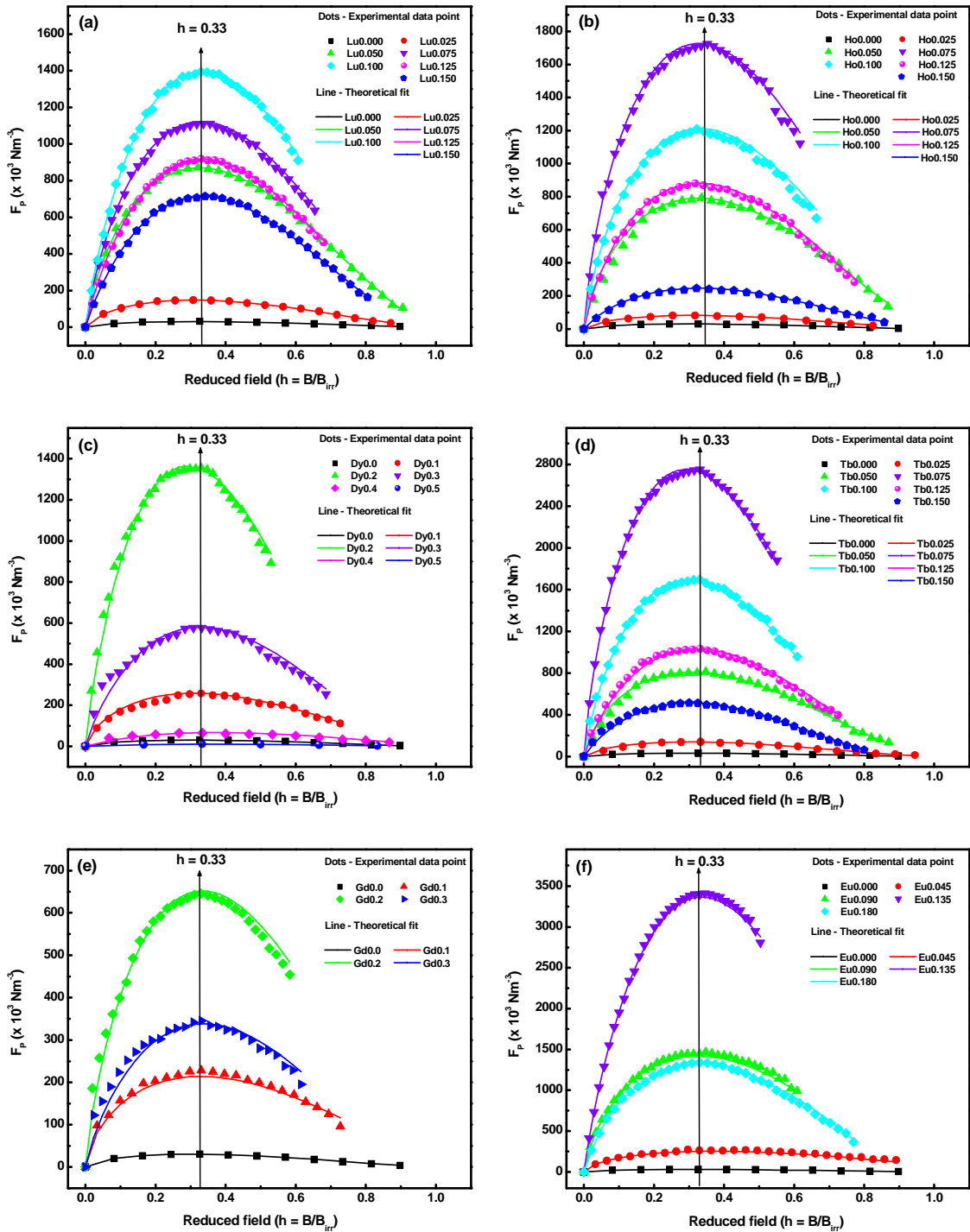
Figure 4.5 (a) – (f) : Variation of pinning force density F_P as a function of reduced magnetic field $(h = B/B_{irr})$ for RE-free and $RE (RE = Lu, Ho, Dy, Tb, Gd$ and $Eu)$ substituted $(Bi, Pb) - 2212$ samples. The parabolic solid line represents the theoretical fit and the vertical solid line at $h = 0.33$ represents the theoretical position of the maximum value of the flux pinning force $(F_{P\max})$ according to the Dew-Hughes theory.
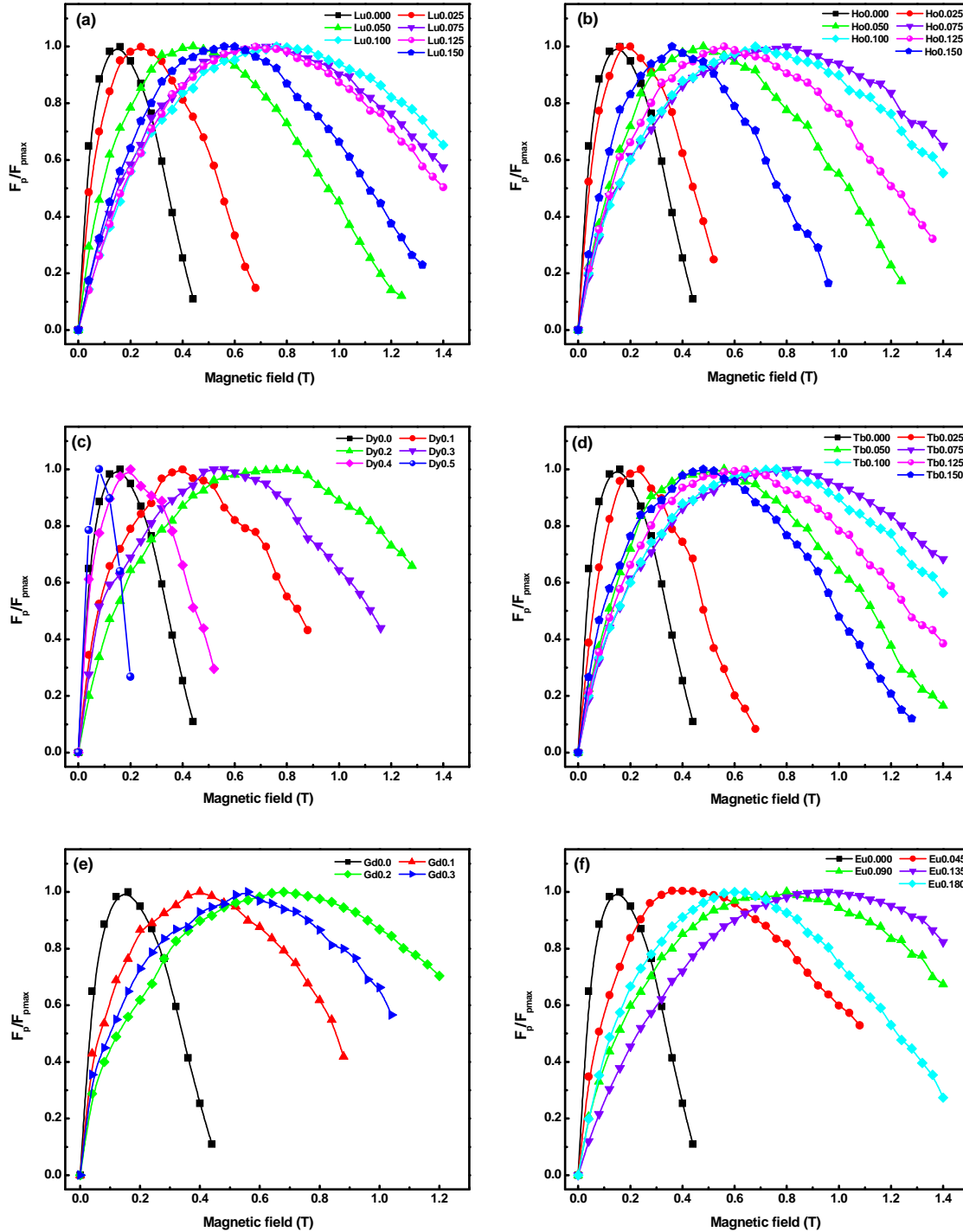
Figure 4.6 $(a)-(f)$: **Variation of normalized pinning force density (FP/FPmax) as a function of applied magnetic field up to** 1.4 *T* **for RE-free and** $RE\left(RE = Lu, Ho, Dy, Tb, Gd\ and\ Eu\right)$ **substituted** *(Bi, Pb)-2212* **samples.**

When RE atoms are substituted in the $(Bi, Pb) - 2212$ system at its Sr site, the RE^{3+} ions replace the Sr^{2+} ions and there is a consequent change in the carrier concentration in the CuO_2 planes. The replacement of divalent cations by trivalent ions will cause changes in the hole concentration and can lead to chemical as well as electrical inhomogenities (chapter 3). By the substitution of the REs at the Sr site, the inhomeogenity introduced may be the local lattice distortion caused by the difference between the ionic radii for the two ions. These lattice distortions can also act as pinning centers as point defects. There is also the possibility of formation of nano-size precipitate containing RE ions, which can enhance the flux pinning strength of the system [Su et al. (1995), Majewski et al. (1995)]. The enhancement of in-field J_C is due to the changes in the flux pinning properties. When the RE content increases beyond a critical level, the number of defects increase, which are likely to form larger defects larger than the coherence length of the system. These larger defects inhibit the transport of super-current and thus reduce the in-field critical current density and flux pinning properties.

In the case of $Bi - 2212$, the flux lines undergo a crossover from three-dimensional flux lines to $2D$ pancake vortices at higher magnetic fields and temperatures. The $2D$ pancake vortices are mainly confined in the CuO_2 layers. Pb in the system improves the Josephson coupling between the CuO_2 layers by reducing the anisotropy and increasing the c-axis conductivity, [Zhao et al. (2003), Hamadneh et al. (2007)]. RE substitution in $(Bi, Pb) - 2212$ decreases the c-axis length and hence, increases the Josephson coupling strength between the CuO_2 layers across the blocking layers $(Sr - O/Bi - O/Sr - O)$. This improves the self- and in-field J_C of the optimized RE substituted samples. The crystal defects created due to Pb doping are mainly confined in the Bi layer, but the defects produced by RE substitution are mainly in the Sr layer. The vortices are confined in the CuO_2 layers, which are closer to the Sr layer than to the Bi-layers. Thus, it is likely that the strongly coupled vortices in the CuO_2 layer are effectively pinned by the defects in the nearer Sr layer than the defects produced in the distant Bi layer. This is attributed to the enhanced flux pinning and the unusually high $J_C(B)$ performance of RE substituted $(Bi, Pb) - 2212$ samples. Also, B_{irr} is inversely proportional to the resistivity along c-axis (ρ_c) and the distance between adjacent CuO_2

planes (d_s); i.e., $B_{irr} \propto 1/(\rho_c d_s)$ [Kim et al. (1991)]. This implies that a decrease in c-axis length and/or resistivity could enhance the flux pinning properties of the material. The present experimental results clearly show that the substitution of RE decreases the c-axis length and substitution of Pb at Bi-site decreases the resistivity [Biju et al. (2007)]. Thus the combined effect of Pb and RE increases the B_{irr} and flux pinning properties. Again, the experimental results showed that there must be a competition between the carrier concentration and interlayer interaction [Wang et al. (2004)]. At lower RE doping levels the contribution of the interlayer interaction dominates over the c-axis resistivity (ρ_c) and hence improves the flux pinning properties. When RE content exceeds the optimum level, the effect of resistivity on flux pinning become dominant over the contribution from c-axis lattice parameter shrinking (d_s). This in turn reduces the flux pinning strength at higher RE content.

4.4.5 E-J characteristics

Figures $4.7(a)-(c)$ and $4.8(a)-(c)$ show the $E-J$ characteristics ($log\,E$ – $log\,J$ curves) of the RE-free and RE (Ho and Tb) substituted $(Bi,Pb)-2212$ samples measured at $0.00,\ 0.32,\ 0.64\,T$ and at $64\,K$ as typical examples. Almost a linear behaviour is seen in the $E-J$ characteristics, which is due to the thermally activated flux-creep and flux-flow. All the $E-J$ characteristics fit well with the equation $\log E = n \log J + C$, where C is a constant and the slopes of these curves give the $n-$index, which has been tabulated in table 4.2. It is found that, both in self- and applied-fields, the maximum value of $n-$index is obtained at the same x ($x=0.075$) value for each RE where their best superconducting and flux pinning properties are obtained and hence, a maximum current will flow with minimum dissipation of energy. At self-fields all the samples show relatively high $n-$index value while at in-fields the $n-$index value decreases (Table 4.2), since the $n-$index is a field dependent parameter.

The samples substituted with optimal Ho and Tb content have better $n-$index ($n>15$) at $0.00, 0.32$ and $0.64\,T$. The $n-$index greater than 15 even at an applied field of $0.64\,T$ and at the temperature $64\,K$ show that the flux lines are effectively pinned in these samples. In other words, these observations reveal that at self- and applied-fields (0.32 and $0.64\,T$), the flux-lines are in glass-state (weak creep) for samples with $n>15$ and for the remaining samples with $n<15$, the flux-lines are in liquid-state (strong creep) [Kumakura et al.

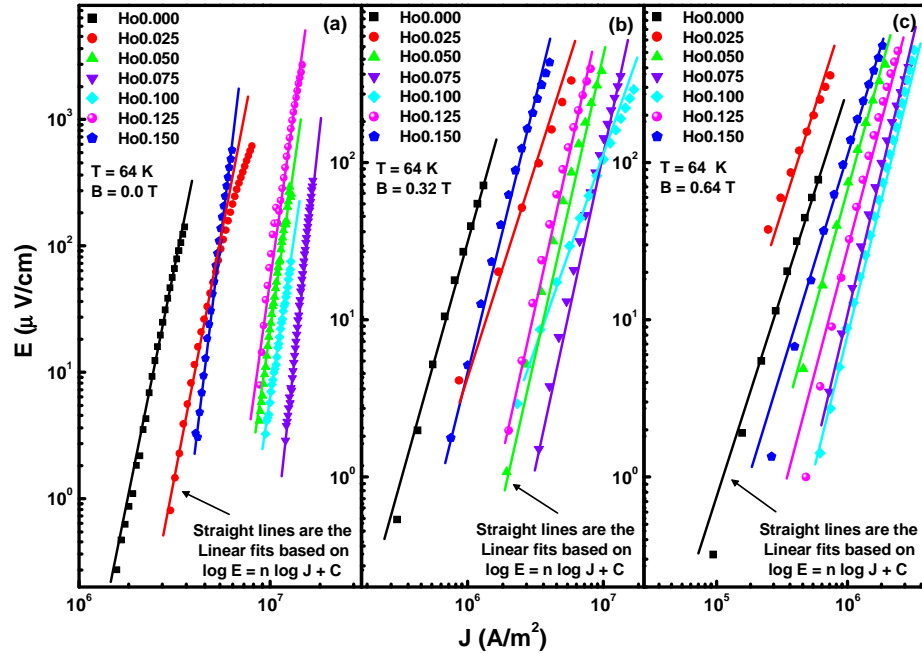**Figure 4.7** $(a)-(c)$: The $E-J$ characteristics of Ho-free and Ho substituted $(Bi, Pb)-$ 2212 samples at $0.00, 0.32$ and $0.64\ T$.
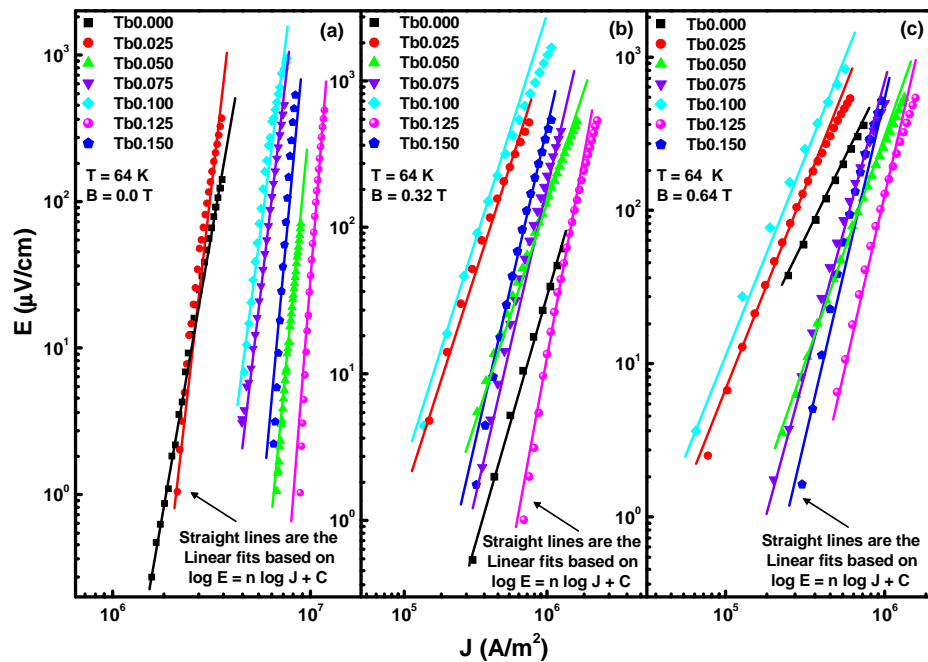

Figure 4.8 $(a)-(c)$: The $E-J$ characteristics of Tb-free and Tb substituted $(Bi, Pb)-$ 2212 samples at $0.00, 0.32$ and $0.64\ T$.

Table 4.2: **The values of rare-earth (RE) stoichiometry (x), n-indices and pinning energy (U_c) obtained for RE-free and Ho and Tb substituted $(Bi, Pb) - 2212$ samples.**

RE	x	n-index at			Uc (meV) at		
		0.00 T	0.32 T	0.64 T	0.00 T	0.32 T	0.64 T
RE-free	0.000	5.20	3.30	1.20	29.0	18.4	6.6
Ho	0.025	16.60	14.00	10.56	87.9	74.0	55.8
	0.050	21.14	19.60	15.68	111.8	103.7	83.0
	0.075	32.72	22.50	19.15	173.1	118.9	101.2
	0.100	24.75	21.80	18.00	131.0	115.4	95.3
	0.125	20.60	19.02	17.40	109.0	100.7	92.0
	0.150	20.04	13.17	10.14	106.0	69.7	53.7
Tb	0.025	13.00	8.47	3.35	71.8	46.8	18.4
	0.050	21.90	15.50	10.00	121.1	85.6	55.2
	0.075	35.90	30.95	19.80	198.4	170.9	109.5
	0.100	31.30	26.10	16.70	172.8	144.1	92.3
	0.125	23.85	18.40	13.00	131.7	101.6	71.7
	0.150	17.20	12.60	7.60	95.0	69.5	41.9

(2003)]. The RE substituted $(Bi, Pb) - 2212$ samples with n around 15 at applied-fields under transport current flow can be used for magnetic applications such as insert-magnets for high field NMR magnet system [Shantsev et al. (2000)]. A correlation between n-value ($or U_c$) and J_C for different samples is observed by comparing the U_c values [Figures 4.9 (a) and (b)] with the J_C values (Table 4.1), i.e., high J_C values are generally found for samples with large n-values ($n > 15$), while small J_C values are typically observed for samples with low n-values ($n < 15$). Thus, the general trend in the observed dissipation is that the flux-creeping effects in RE substituted $(Bi, Pb) - 2212$ samples are weaker for the samples with larger n-indices and vice-versa. In the present work, the observed high n-indices in RE substituted $(Bi, Pb) - 2212$ samples are for the experimental data measured at a temperature as high as

64 K and hence, there is a great scope for further drastic increase in $n-$indices as the temperature comes down to 4.2 K.
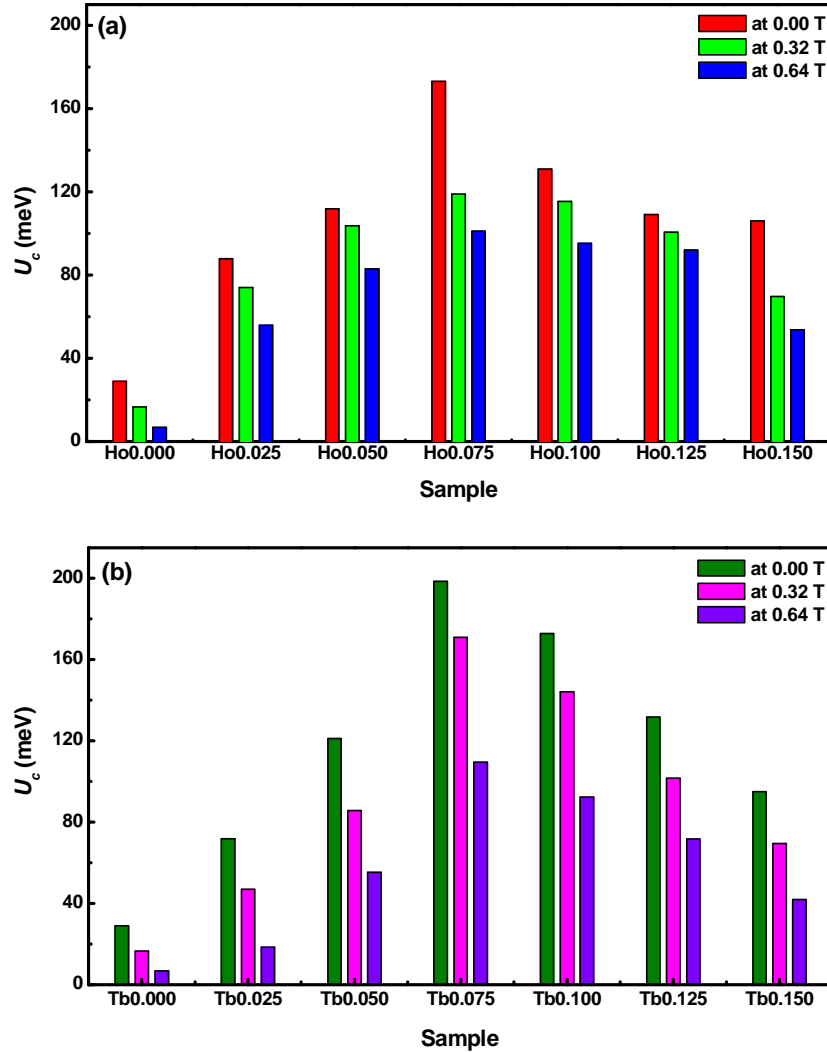

Figure 4.9 (a) and (b): The variation of characteristic pinning energy (U_c) with RE ($Ho \, and \, Tb$) content at $0.00, 0.32, 0.64 \, T$ and at 64 K.

Figures 4.9 (a) and (b) show the variation of U_c as estimated from the $n-$index with respect to x. It reveals that REs [Ho and Tb] when substituted with $x = 0.075$ show the best flux pinning capability as evident from a peaking of U_c, both for self- and in-fields namely, 0.32 and 0.64 T, respectively. The relative performance of RE substituted samples in self- and in-fields is evaluated by comparing its U_c values with those of the RE-free sample and the U_c

values are given in table 4.2. The RE-free sample shows U_c values of $29.0 \pm 0.1\, meV$ in the self-field (~ 6 and 7 times lesser than the best sample of Ho and Tb) and $18.4 \pm 0.1\, meV$ and $6.6 \pm 0.1\, meV$ at 0.32 and $0.64\, T$ (which is also less than the Ho and Tb substituted samples). It is also observed that all the RE substituted samples have better U_c compared to the RE-free sample. Hence, it is concluded that the RE substituted samples have much better flux pinning properties than the RE-free sample.

4.4.6 $U(J) - J$ characteristics

The variation of activation barrier for vortex motion $[U(J)]$ with respect to J in self- and applied-fields are shown in figures $4.10(a) - (c)$ and $4.11(a) - (c)$ for Ho and Tb substituted $(Bi, Pb) - 2212$ samples at 0.00, 0.32, $0.64\, T$ and at $64\, K$, which show a logarithmic dependence on the current density over a wide range. The results show that deterioration of $U(J)$ due to the magnetic field is significantly reduced as a result of RE substitutions. This shows that doping of RE atoms at the Sr-site enhances the flux pinning properties of $(Bi, Pb) - 2212$ superconductor. The activation potential required for the motion of fluxons is higher for RE substituted samples with higher U_c $(n - values)$, while the least is observed for the RE-free under the transport super-current flow. From the figures $4.10(a) - (c)$ and $4.11(a) - (c)$, it is clear that the REs [Ho and Tb] when substituted with $x = 0.075$ has the best flux pinning strength. On extrapolating the curve to a point $U(J) = 0$ [figure $4.10(a) - (c)$ and $4.11(a) - (c)$], the J_C (at $64\, K$) at self- and applied-fields can be found out. From the relation, $U(J) = U_c \ln(J_C/J)$, it is seen that when current density (J) becomes $(1/e)$ times J_C (denoted as J_g) then $U_c = U(J_g)$, where J_g is the current density for the transition from vortex-glass to vortex-liquid state. The value of J_g determines the onset of the solid vortex-glass to liquid transition, i.e., the vortices are in the solid-glass state for $J < J_g$ and it starts to melt to vortex-liquid state for $J > J_g$. This clearly reveals that RE substituted $(Bi, Pb) - 2212$ superconductors exist in a solid-glass state at a much higher current density in self- and applied-fields as compared with RE-free samples. This is another evidence for the strong pinning effect of vortices in the RE substituted $(Bi, Pb) - 2212$ samples.
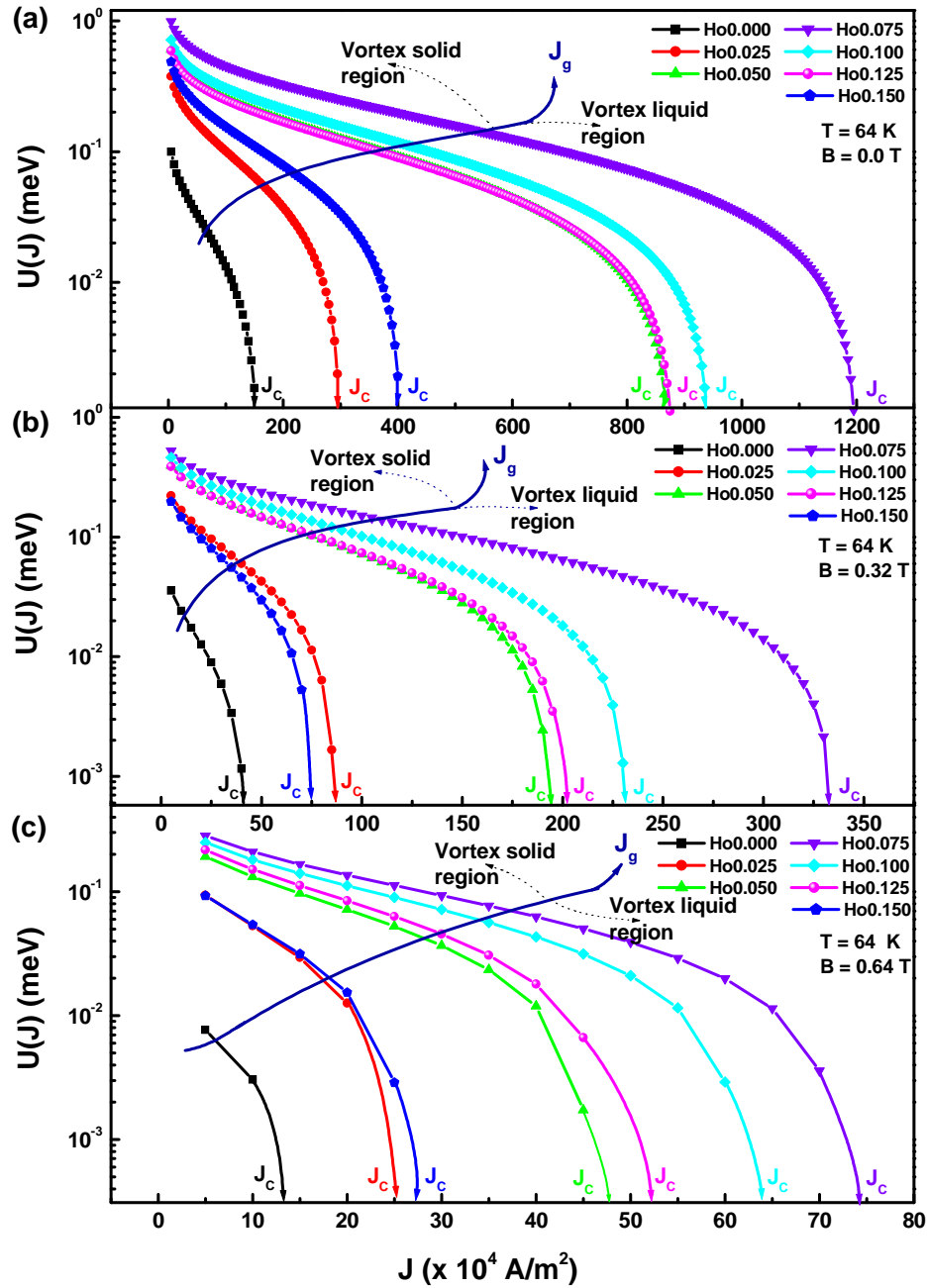
Figure 4.10(a)−(c): The variation of flux creep activation barrier of *Ho*-free and *Ho* substituted $(Bi, Pb) - 2212$ samples at $0.00, 0.32$ and 0.64 *T*.
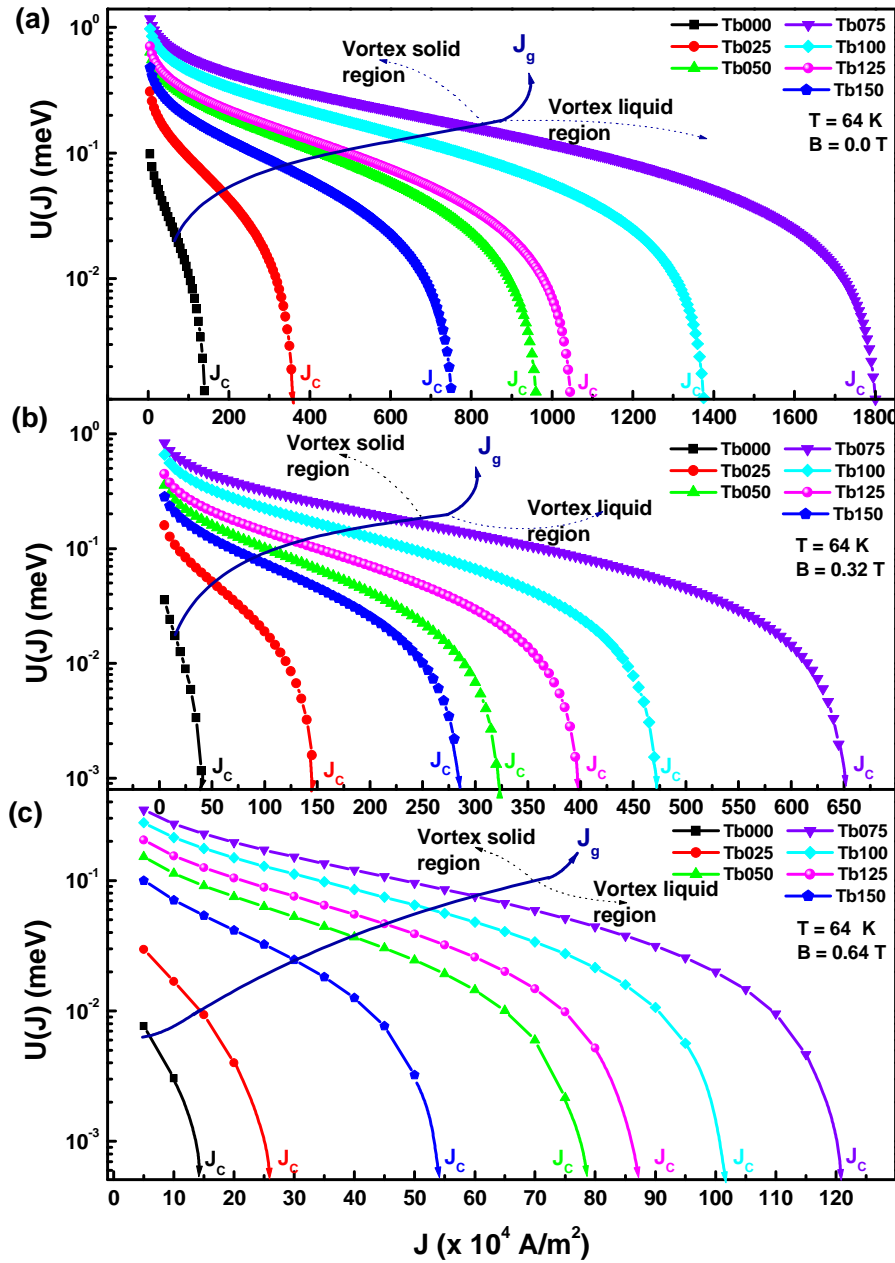
Figure 4.11 $(a) - (c)$:   The variation of flux creep activation barrier of *Tb*-free and *Tb* substituted $(Bi, Pb) - 2212$ samples at $0.00, 0.32$ and $0.64\ T$.

The origin of the $n-$ value is generally attributed to the distribution in the elementary flux pinning centers (intrinsic effects) and from the non-uniformities in the cross-sectional area of the superconductor (extrinsic effects). Here, for samples with $n > 15$, the intrinsic effects dominate and hence high $n-$ values are observed [Hampshire et al. (1987)] leading to higher self and in-field J_Cs. This reveals that these samples have good flux pinning capabilities and homogeneity and are the potential candidates for magnetic applications. At higher RE concentrations, the $n-$ index decreases due to the domination of extrinsic effects such as the non-uniformities in the microstructure of $(Bi, Pb) - 2212$ (weak-links). Thus, the reduction of $n-$ index and hence, J_C is primarily due to the collective effect of the weak-links, distributed throughout the sample.

4.5 Conclusions

This chapter presents a systematic study on the flux pinning properties of RE substituted $(Bi, Pb) - 2212$ $\left[Bi_{1.6}Pb_{0.5}Sr_{2-x}RE_xCa_{1.1}Cu_{2.1}O_{8+\delta} \right]$ system with different RE concentrations $(0 \le x \le 0.5$ and $RE = Lu, \ Ho, \ Dy, \ Tb, \ Gd$ and Eu) and the results are compared with RE-free $(Bi, Pb) - 2212$ superconductor. The enhancement of flux pinning properties is evident from the improved $J_C(B)$ and normalized $J_C(B)$ characteristics. The maximum values of bulk pinning force densities $(F_{P\max})$ of the RE-substituted samples are found to shift towards higher fields and temperature. This means that the irreversibility line (IL) of the RE substituted samples shift towards higher fields and temperatures. The enhancement of these superconducting and flux pinning properties are attributed to the changes in the hole concentration and disorder of the lattice due to the replacement of Sr^{2+} by RE^{3+} ions. Also, the Dew- Hughes pinning analysis shows that the main pinning mechanism is the point defects aroused out of the substitution of RE atoms at the Sr-site of $(Bi, Pb) - 2212$ system. The samples are further analyzed by $E - J$ characteristics and these characteristics are successfully explained by the flux-creep theory. It is found that most of the RE substituted samples show a glass-state for flux-lines, indicating their improved flux-pinning ability due to the creation of point defects by the substituted RE atoms. The improved U_c values also support this. A correlation between $n-$ indices and J_C of RE substituted $(Bi, Pb) - 2212$ superconductor is also observed. A deeper insight into the superconducting behaviour of RE substituted

$(Bi, Pb) - 2212$ superconductors has been obtained by comparing the self- and in-field $n-$indices. The highly improved $J_C(B)$, $F_P(B)$, $E-J$, $U(J)-J$ characteristics and enhanced U_c and $n-$value (>15) at applied fields under transport current flow show that the modified material is a promising candidate for magnetic applications.

Chapter 5

CHAPTER 5

Effect of refinement of microstructure on the flux pinning properties of rare earth (Ho, Dy, Gd and La) substituted (Bi, Pb)-2212

5.1 Introduction

One of the most important characteristics of the high temperature superconducting cuprates is the large electromagnetic anisotropy manifested in their transport and magnetic properties. This is caused by a highly two dimensional crystal structure which consists of alternate stacking of superconducting CuO_2 and poorly conducting blocking layers. Generally, in all high temperature superconducting cuprates, the out-of-plane resistivity [ρ_c], corresponding to the electrical conduction across the blocking layers, is always large with respect to the in-plane resistivity [ρ_{ab}] along the well conducting CuO_2 planes, and the anisotropic parameter is usually determined from the relation [Kotaka et al. (1994)] $\gamma = (\rho_c/\rho_{ab})^{0.5}$. Among the well known cuprate-based high temperature superconductors [HTS], $Bi-2212$ exhibits one of the largest electromagnetic anisotropy due to its thick blocking layers which consist of insulating $Bi-O$ double layers. Although $Bi-2212$ and its homologous compound $Bi-2223$ are the materials widely used for wire and tape applications at high temperatures, their poor performance under fields still prohibits the extensive use of these materials for high magnetic field applications. In order to overcome this problem, enormous efforts have been made for improving the critical current properties of $Bi-2212$ and $Bi-2223$ systems under magnetic fields [Pradhan et al. (1994), Larbalestier et al. (2001) and Zhao et al. (2003)].

The flux pinning ability and hence, the transport properties of $Bi-2212$ superconductor at high temperatures and high magnetic fields can be enhanced by reducing the anisotropy of the material [Nomura et al. (1993)] and by introducing artificial defects having a size matching the coherence length. First method strengthens the inter-layer coupling between CuO_2 layers which increases the flux pinning potential and in the later case, the artificial defects act as extra pinning centers. It is known that the Pb substitution at Bi site in $Bi-2212$ significantly reduces the electromagnetic anisotropy [Zhao et al. (2003)]. Also, the Pb and RE substituted

$Bi - 2212$ [$(Bi, Pb) - 2212$] has shown enhanced $J_C s$ in applied fields, compared to the Pb free $Bi - 2212$ [Chong et al. (1997)] and the results were already discussed in detail in chapter 4. In chapter 4, we found that when RE ions are substituted in the place of Sr in $(Bi, Pb) - 2212$, the flaky nature and the texture of the grains gradually deteriorate with increase of RE concentration. However, in spite of the deterioration of the microstructure, RE and Pb substituted samples showed much better J_C values compared to the RE-free sample. Therefore, it is expected that there is a great scope for further improvement of J_C if the deterioration of microstructure of RE and Pb substituted $Bi - 2212$ could be suppressed. In order to refine the microstructure of RE and Pb substituted $Bi - 2212$, a systematic study has been conducted on the system by precisely varying the sintering temperature within a narrow range between between 846 and 860 $°C$. The study has lead to the achievement of refined microstructure, highly enhanced transport J_C in self- and applied-fields and very stable flux pinning capabilities in $(Bi, Pb) - 2212$ substituted with RE (Lanthanides *Ho, Dy, Gd* and *La*).

5.2 Experimental details

The RE substituted $(Bi, Pb) - 2212$ superconductors with a general stoichiometry of $Bi_{1.6}Pb_{0.5}Sr_{2-x}RE_xCa_{1.1}Cu_{2.1}O_{8+\delta}$ were prepared by solid state sintering using high purity chemicals ($> 99.9\ \%, Aldrich\ Milwaukee, WI$) such as oxides/carbonates of the ingredients. Here $RE = Ho, Dy, Gd, La$ and x is the corresponding stoichiometry [x = 0.000 (for RE-free), 0.075 (for Ho) and 0.2 (for Dy, Gd and La)] which has given the best superconducting and flux pinning properties (chapter 3 and 4). The required amount of ingredients was estimated according to the stoichiometry used and the ingredients were accurately weighed using an electronic balance ($Metler\ AE240, Greifensee, Switzerland$) having a least count of $1\ \mu g$. Subsequently, these ingredients were mixed and ground using a planetary ball mill ($FRISCH\ Pulversette\ 6, Idar - Oberstein, Germany$) in an agate bowl with agate balls. After the milling process, the ingredients get homogenized with a reduction in particle size and increase in the contact area between different ingredients. Extreme care was taken to avoid contamination of the ingredients during weighing and milling process. The dried powder was subjected to a three-stage calcination process in air at $800\ °C/15\ h + 820\ °C/40\ h + 840\ °C/60\ h$ using a programmable furnace. Intermediate

grinding was done between each calcination stage to avoid agglomerates and compositional variations. The calcined powders were then pelletized at a pressure of $500\,MPa$ using a hydraulic press $(Herzog\,TP\,20P)$ and a cylindrical die. Pellets having an approximate diameter of $12\,mm$ and thickness of $1\,mm$ were made. The pellets of RE-free sample were heat treated at $848\,^{\circ}C/120\,h$, which is the optimized sintering temperature for this sample and hereafter denoted as $REF848$ ($REF=RE$-free). The pellets of RE substituted samples were grouped into eight sets. The first set was heat treated at $846\,^{\circ}C$ and the remaining sets at 848, 850, 852, 854, 856, 858 and $860\,^{\circ}C$, respectively, for $120\,h$ (*60 h + 60 h*), with one intermediate pressing under the same pressure used for the initial pressing. The samples with different sintering temperature will be hereafter denoted as RET, here $RE = Ho, Dy, Gd, La$ and T is the corresponding sintering temperature. The heat treatment was done in a large volume programmable muffle furnace with a Eurotherm (Model: 2404) temperature controller. The stability and accuracy of the temperature was $\pm 0.5\,K$.

Phase analysis of the samples was done using X-ray diffractometer [$Philips\,X\,'pert\,Pro(PW\,3040/60)$] equipped with an X'celerator and a monochromator at the diffracted beam side. For all samples, scans were made in 2θ and at 0.01°/step. All the scans were done using $Cu\,K\alpha$ radiation with a tube voltage of $40\,kV$ and current $30\,mA$ by exposing a constant area of the sample. The phase identification of the samples was performed using $X\,'Pert\,Highscore$ software in support with the $ICDD\,PDF\,II$ data base. The microstructural and elemental analyses of the samples were done using scanning electron microscopy $(JEOL\,JSM\,5600LV)$ and energy dispersive X-ray spectroscopy, respectively. For electrical measurements, the samples were cut into rectangular bar of dimension $12\times3\times1\,mm^3$. The transition temperature T_c of the samples was determined by the four-probe DC resistance method by cooling the sample in a liquid N_2 cryostat. In order to minimize the contact resistance, four silver strips were fixed on to one surface of the pellet during pressing. Leads of high quality copper were soldered to the silver strips. The outer two leads were connected to a programmable DC current source ($Keithely\,model$: 220) and a constant current of $10\,mA$ was used for the resistance measurement. The voltage drop between the inner two leads was measured using a programmable nano voltmeter ($Keithely\,model$: 181). The temperature of the sample was

monitored by a temperature controller (*Lakeshore model*: $L340$) using a temperature sensor ($DT-470$). The transport critical currents of the samples in self- and applied-field was measured at $64\,K$ in a liquid N_2 bath cryostat under vacuum by employing four-probe method with the standard criterion of $1\,\mu Vcm^{-1}$. For these measurements an *Aplab* $9711P$ constant current source was used. The directions of the current and field are parallel and perpendicular, respectively, to the pressed surface of the pellet. The $J_C(B)$ characteristic was studied with field ranging from $0.0-1.4\,T$. All these measurements are automated using *GPIB* interfaced with a personal computer.

5.3 Structural characterization

5.3.1 *XRD* and *EDS* analysis

The *XRD* patterns of the *RE* (*RE = Ho, Dy, Gd* and *La*) substituted $(Bi,Pb)-2212$ pellets obtained after the last stage heat treatment is normalized with standard *XRD* patterns of pure $(Bi,Pb)-2212$ sample and the resultant patterns are shown in figure 5.1 (a) - (d). The *XRD* patterns are analyzed using the *X'Pert Highscore* software. It shows that all the samples contain only the peaks corresponding to the $(Bi,Pb)-2212$ phase and no peaks of any secondary phase containing *RE* or any other cation were detected at this stage within the detection limit of the instrument. This suggests that almost all the reactant phases are converted into $(Bi,Pb)-2212$ and the substituted *RE* is incorporated into the crystal lattice of $(Bi,Pb)-2212$ superconductor. Also, figure 5.1 (a) - (d) shows that when the sintering temperature of the *RE* substituted samples increases, the peak height corresponding to the $(00l)$ planes systematically increases. In order to bring out the increase in peak height of $(00l)$ planes, the (008) peaks of all samples are separately shown, with better resolution in Figure 5.2 $(a)-(d)$. This shows that the texturing increases with increase of sintering temperature (up to 856 - 858 $^\circ C$) and thereafter the peak height gradually decreases which show that the texturing decreases beyond this temperature. This figure also shows that the (008) peaks of the *RE* doped sample shift towards higher angle [peak shift $\delta(2\theta)$ is marked in figure] with respect to the position of *RE* free $(Bi,Pb)-2212$ sample. Even though all the patterns are taken under identical conditions, only the *RE* substituted sample will show a peak shift. This supports that

the *RE* atoms enter into the crystal structure of $(Bi, Pb) - 2212$ superconductor and the *c*-axis length of *RE*-substituted samples decreases. This decreased *c*-axis length also supports that the substituted *RE* atoms enter into the crystal structure of $(Bi, Pb) - 2212$ superconductor.
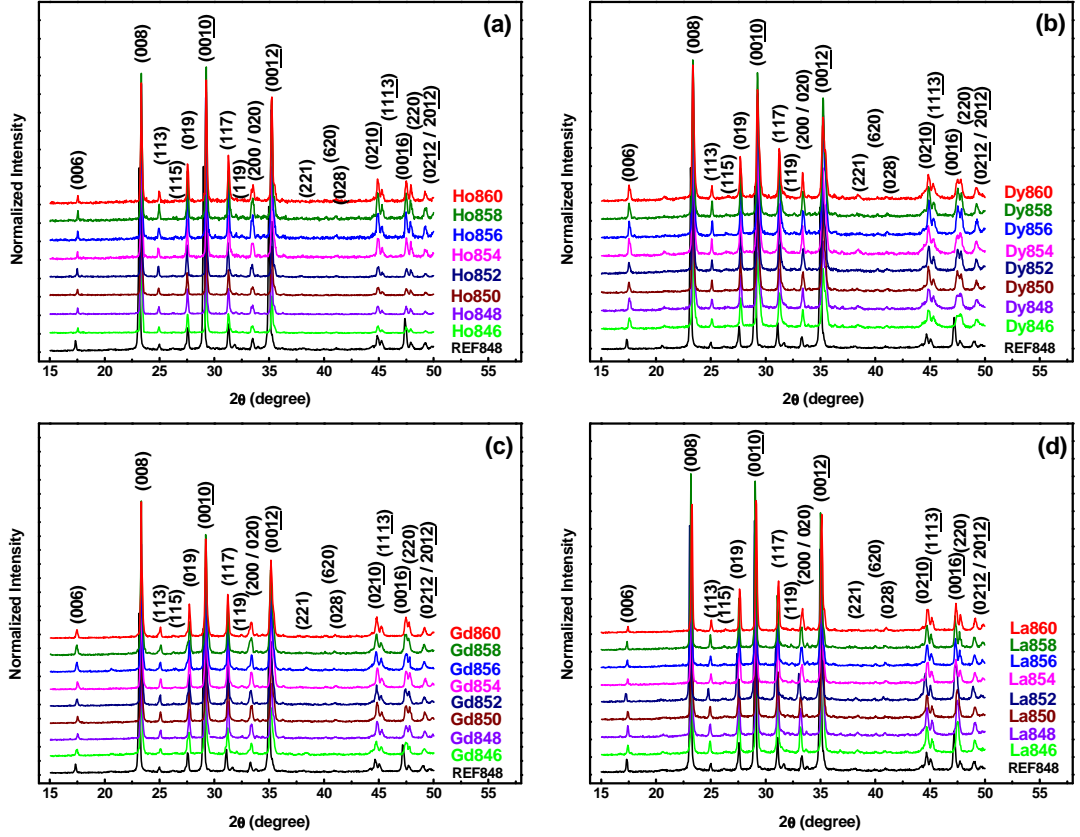

Figure 5.1 $(a) - (d)$: The normalized *XRD* patterns of the *RE*-free and *RE* substituted $(Bi, Pb) - 2212$ pellets after the last stage heat treatment.

The lattice parameter variations of *RE*-free and *RE* substituted samples calculated by considering an orthorhombic symmetry for $(Bi, Pb) - 2212$ system using the formula,

$$\frac{1}{d^2} = \frac{h^2}{a^2} + \frac{k^2}{b^2} + \frac{l^2}{c^2}$$

(5.1)

Here *d* is the inter-planar spacing and (*hkl*) are the Miller indices. A marked variation is observed in the crystal structure of *RE* substituted samples compared to the *RE*-free sample. The *c*-axis lattice parameter of all the *RE*-doped samples is 30.732 Å (for *Ho*), 30.763 Å (*Dy*), 30.749 Å (*Gd*), 30.725 Å (*La*) with in the accuracy of 0.002 Å. Similar behavior has been

observed in the case of a and b axes where $a = 5.362 \pm 0.002$ Å and $b = 5.398 \pm 0.002$ Å (for *Ho*), $a = 5.357 \pm 0.002$ Å and $b = 5.404 \pm 0.002$ Å (for *Dy*), $a = 5.359 \pm 0.002$ Å and $b = 5.401 \pm 0.002$ Å (for *Gd*), $a = 5.406 \pm 0.002$ Å and $b = 5.392 \pm 0.002$ Å (for *La*), are obtained. A contraction in c-axis length is observed in all the *RE* substituted samples as compared with the *RE*-free samples ($c = 30.885 \pm 0.002$ Å), indicating the incorporation of *RE* atoms into the $(Bi, Pb) - 2212$ system. However, the c-axis length does not vary with increase in the sintering temperature. The reason for the shrinkage in c-axis length is described in detail in chapter 3. The anisotropy of the system decreases with these changes in the lattice parameters [Sanderson et al. (2005)].
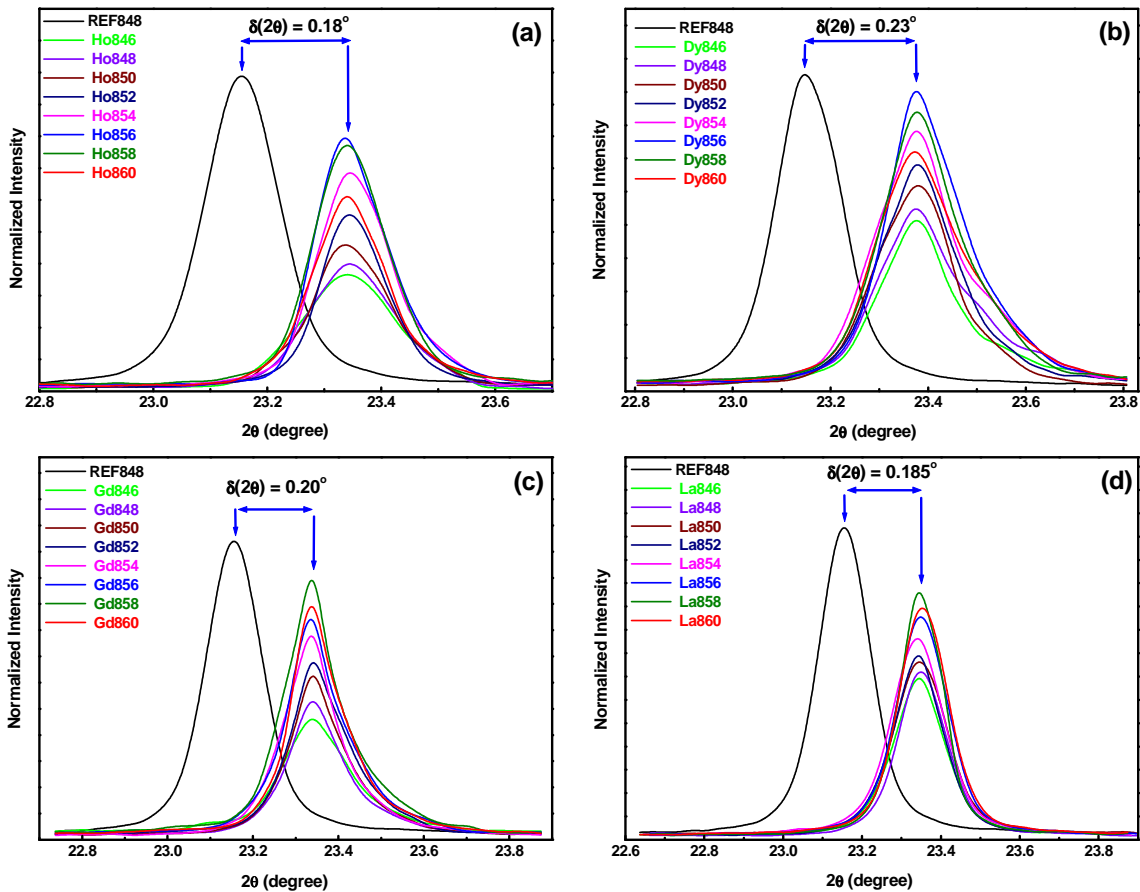

Figure 5.2 $(a) - (d)$: The normalized *XRD* peaks of the *RE*-free and *RE* (*RE* = *Ho, Dy, Gd* and *La*) substituted $(Bi, Pb) - 2212$ pellets for the (008) plane at around $2\theta = 23.1°$ and $\delta(2\theta)$ represents the maximum peak-shift of *RE* substituted sample with respect to the *RE*-free sample.

Again, the results show that the Lotgering index (a measure of the texture of the samples) calculated from the *XRD* data (Table 5.1) is found to be strongly dependent on the sintering temperature. As the sintering temperature increases, the F value of the doped samples increases monotonically up to a temperature of $856-858 \, ^{\circ}C,$ which indicates the increase of texturing with increase of sintering temperature. Thus, a very good texturing is expected to be induced in the microstructure of *RE* substituted samples by sintering the samples at its optimized temperatures. It is also noted that the *RE*-free sample shows the best F value (0.92).

The energy dispersive *X*-ray spectroscopic (*EDS*) analysis of *RE* substituted $(Bi, Pb)-2212$ grains (spot analysis) reveals the presence of *RE* in $(Bi, Pb)-2212$ grains. The quantitative estimation of the cations from *EDS* patterns of these samples (keeping *Cu* as reference) shows that the approximate cationic composition are $Bi_{1.63}Pb_{0.46}Sr_{1.93}Ho_{0.06}Ca_{1.05}Cu_{2.1}$, $Bi_{1.59}Pb_{0.52}Sr_{1.83}Dy_{0.21}Ca_{1.04}Cu_{2.1}$, $Bi_{1.65}Pb_{0.44}Sr_{1.75}Gd_{0.19}Ca_{1.09}Cu_{2.1}$, $Bi_{1.53}Pb_{0.45}Sr_{1.87}La_{0.18}Ca_{1.05}Cu_{2.1}$, for *Ho, Dy, Gd* and *La* substituted $(Bi, Pb)-2212$ superconductors. This clearly supports that the *RE* atoms are successfully substituted into the crystal structure of $(Bi, Pb)-2212$ system.

5.3.2 *SEM* analysis

Figure 5.3 and 5.4 shows the SEM images of the fractured surfaces of the *RE*-free sample sintered at $848 \, ^{\circ}C$ and *RE* substituted samples sintered between 846 and $860 \, ^{\circ}C.$ The grain morphology of the *RE*-free sample shows clear and flaky grains with layered growth typical of $(Bi, Pb)-2212$, whereas for *RE* substituted samples, a systematic change in microstructure with respect to the sintering temperature is observed. For example, in *RE*846 the characteristic flaky morphology of $(Bi, Pb)-2212$ grains transforms into round grains with a reduced texture. As we go from *RE*846 to $RE856(for \, Ho \, and \, Dy)/RE858(for \, La \, and \, Gd)$, the flaky morphology and texture reappear with a gradual improvement in microstructure with respect to an increase in sintering temperature [the intensity variation in XRD shown in figure 5.2 $(a)-(d)$ also clearly supports this]. For temperatures above $856 \, ^{\circ}C \, (for \, Ho \, and \, Dy)/858 \, ^{\circ}C \, (for \, La \, and \, Gd)$, the microstructure again deteriorates, which shows that the optimum sintering temperature (T_{opt}) for obtaining the best microstructure for the *RE*-substituted samples is $854 \, ^{\circ}C < T_{opt} < 860 \, ^{\circ}C.$ This improved microstructure plays an
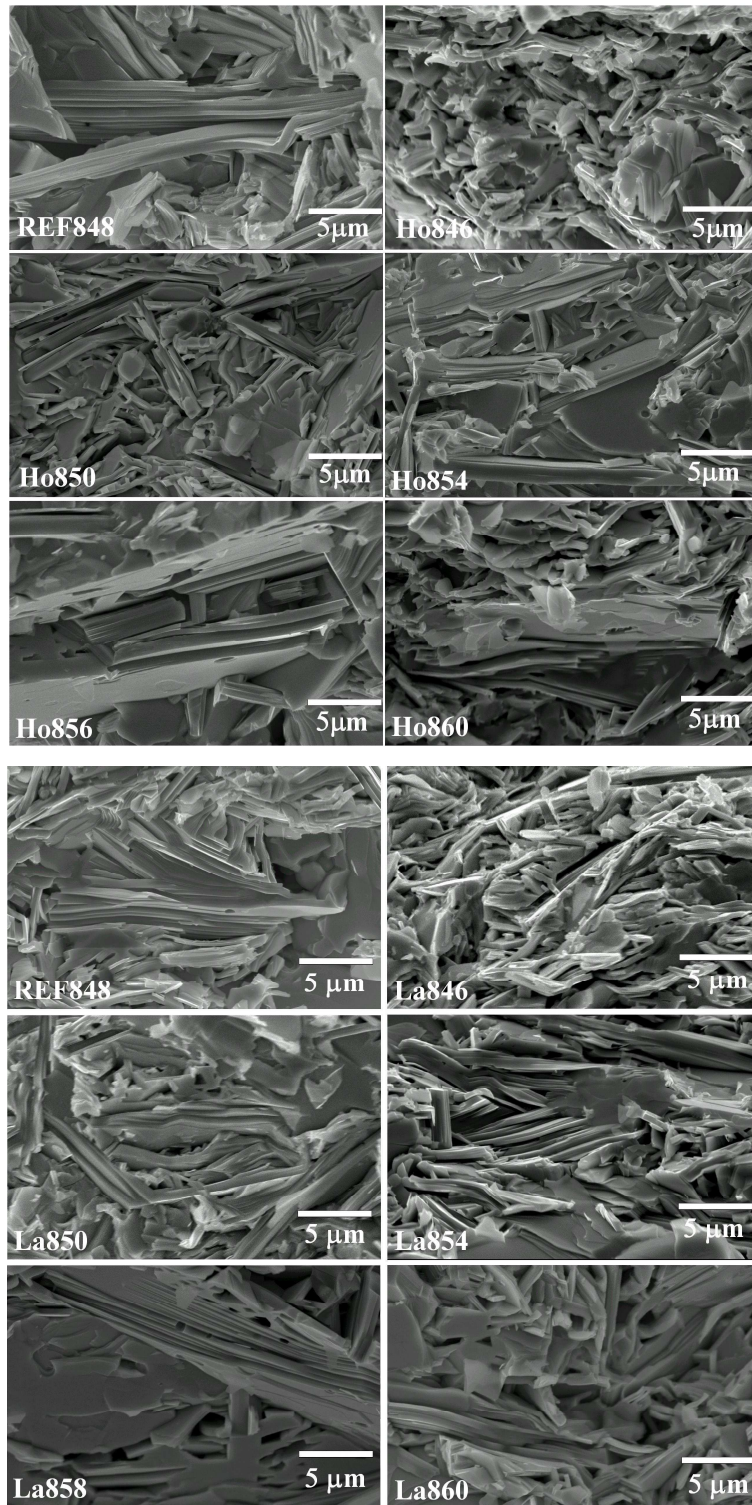
Figure 5.3: The *SEM* images of the fractured surfaces of *RE* -free and typical *RE* （*RE = Ho* and *La*) substituted $(Bi, Pb) - 2212$ pellets sintered between 846 and 860 $^\circ C$.
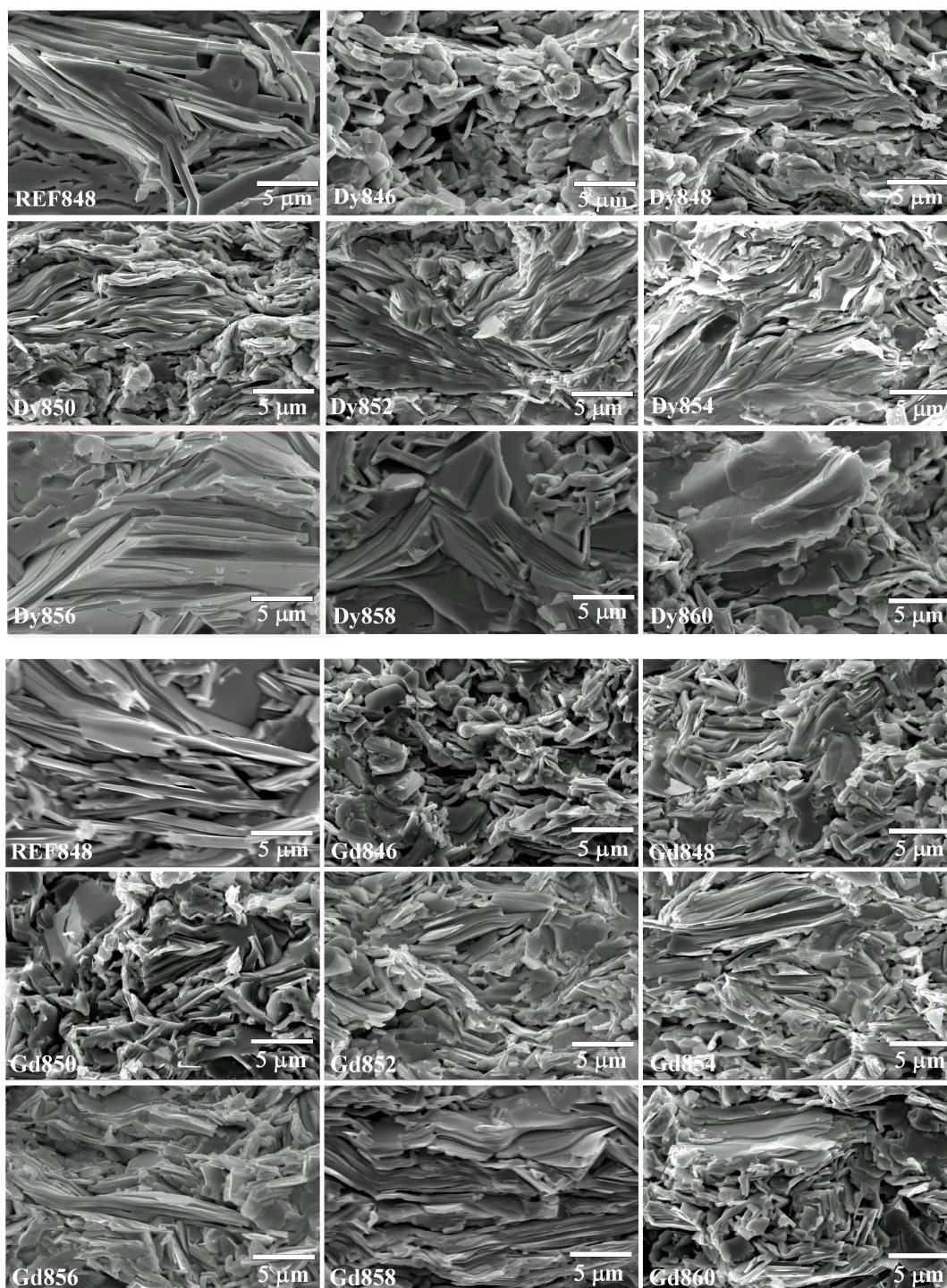
Figure 5.4 : **The** *SEM* **images of the fractured surfaces of** *RE* **-free and all** *RE* **(** *RE = Dy* **and** *Gd*) **substituted** $(Bi, Pb) - 2212$ **pellets sintered between 846 and 860** $^{\circ}C$ **in order to view the systematic change in microstructure with respect to sintering.**

important role in increasing the self-field J_C of the system. Since, the weak links associated with the grain boundaries are known to limit the J_C values of superconductors, and the possible reasons for the formation of these weak links are the misorientation of grain boundaries and the compositional variations at the grain boundaries. In the present case, the maximum misorientation is observed for $RE846$, and it gradually decreases with an increase in sintering temperature, and it is least for the sample sintered at $856\ °C\ (for\ Ho\ and\ Dy)/858\ °C\ (for\ La\ and\ Gd)$, as shown in figures 5.3 and 5.4. Also, among the RE-substituted samples, $RE856\ (for\ Ho\ and\ Dy)/RE858(for\ La\ and\ Gd)$, has the least number of grain boundaries and hence has the minimum amount of weak links. Thus, by tuning the sintering temperature, the effect of weak links in the system can be minimized.

5.4 Superconductor characterization

Figure 5.5 (a) shows the variation in T_C with RE content and sintering temperature, and it shows that the RE substituted samples have much higher T_C values $(88.1\ K\ for\ Ho,$ $92.2\ K\quad for\ Dy,\quad 94.7\ K\ for\ Gd,\quad 90.8\ K\ for\ La)$ compared to the RE-free sample $(80.6\ K)$. It is found that the T_C value is same for samples doped with a specific RE [Figure 5.5 (a)] irrespective of the sintering temperature, and this is because the same amount of RE is is present in all the doped samples. Again, there is a systematic trend observed between the sintering temperature and self-field J_C values [Figure 5.5 (b) and table 5.1]. In the case of RE substituted samples, the lower sintering temperature $(846\ °C)$ resulted in lower J_C values at 64 K. The J_C value increases with an increase in sintering temperature, as shown in figure 5.5 (b), and finally the sample, $RE856(for\ Ho\ and\ Dy)/RE858(for\ La\ and\ Gd)$, shows maximum J_C. The enhancement of self-field J_C with respect to the sintering temperature is obviously due to the improvement in the microstructure of the sample. The samples sintered above the optimum sintering temperature (T_{opt}) show lesser J_C [Figure 5.5 (b)] than the sample sintered at T_{opt} because of reduced texturing (Figure $5.2(a)-(d)$, 5.3 and 5.4). The RE-Free sample, which was sintered at its optimum sintering temperature, $(848\ °C)$, shows a J_C value of only

1642 kAm^{-2} while the *RE* substituted sample gives a maximum J_C of 31960 kAm^{-2} (*for Gd*858).

The doping of each *RE* atom in $(Bi, Pb) - 2212$ supplies one electron to the system, which reduces the number of holes and thus shifts the system from the "over-doped" to the "optimally-doped" condition, as far as the hole density is concerned [Gupta et al. (1994)]. The attainment of optimum hole concentration is responsible for the enhancement of T_C and hence the J_C value of the *RE* substituted samples. Further, the variation in self-field J_C with respect to the sintering temperature is due to the refinement in microstructure with respect to grain alignment and grain size.
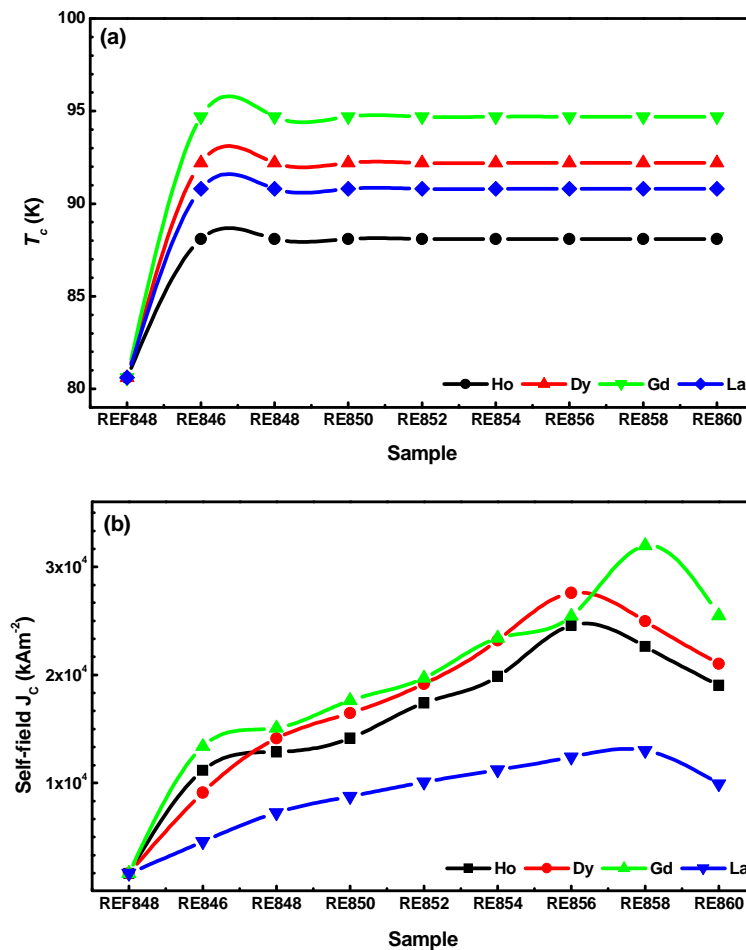

Figure 5.5: (*a*) **Critical temperature values of** *RE* **-free and all** *RE* **substituted samples sintered between 846 and 860** $^\circ C$, (*b*) **Variation in self-field** J_C **value of the samples with respect to the sintering temperature.**

5.5 Flux pinning analysis

5.5.1 Normalized $J_C(B)$ characteristics

Figure 5.6 $(a) - (d)$ shows the normalized in-field critical current density characteristics of RE-free and RE substituted $(Bi, Pb) - 2212$ samples at 64 K and at a magnetic field up to 1.4 T. The normalized $J_C(B)$ characteristics of the RE substituted samples are found to be much better than those of the RE-free sample. That is, the deterioration of J_C due to the magnetic field is significantly reduced because of RE doping. This shows that the RE doping enhances the flux pinning properties of the $(Bi, Pb) - 2212$ system. In the case of $Bi - 2212$, the flux lines undergo a crossover from three-dimensional flux lines $(3D)$ to $2D$ pancake vortices at higher magnetic fields and temperatures. The 2D pancake vortices are mainly confi-
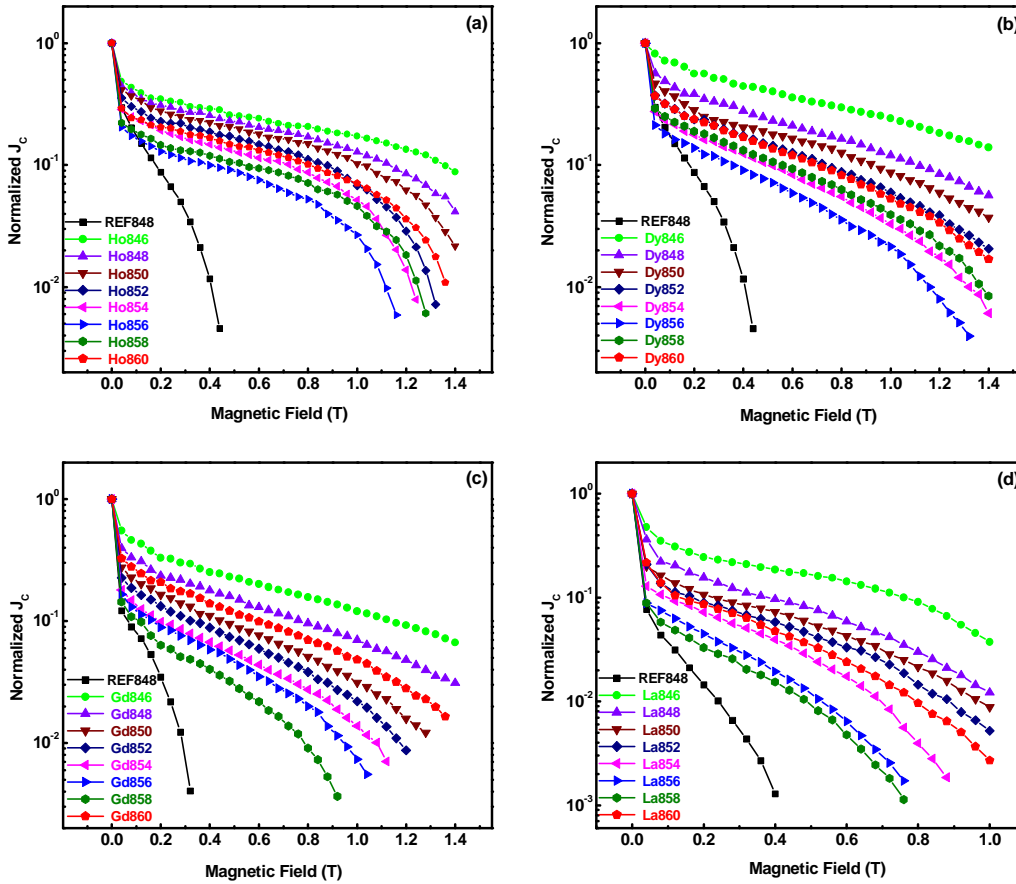

Figure 5.6 $(a) - (d)$: **Variation in normalized in-field critical current density of RE-free and RE ($RE = Ho, Dy, Gd$ and La) substituted $(Bi, Pb) - 2212$ samples for magnetic fields up to 1.4 T.**

Table 5.1: The values of sintering temperature (T_{sinter}), Lotgering index (F), self-field J_C, the maximum value of F_P (F_{Pmax}) and the magnetic field at which F_{Pmax} obtained for RE-free and RE substituted $(Bi, Pb) - 2212$ samples.

RE	T_{sinter} ($^\circ C$)	F	J_C (kAm^{-2})	F_{Pmax} (kNm^{-3})	Field at F_{Pmax} occurs (T)
$RE - free$	848	0.92	1642	27	0.24
	846	0.58	11183	1937	1.00
	848	0.62	12879	1747	0.80
	850	0.69	14152	1671	0.80
Ho	852	0.75	17396	1609	0.72
	854	0.79	19862	1437	0.68
	856	0.88	24599	1111	0.60
	858	0.86	22636	1343	0.68
	860	0.85	19032	1575	0.72
	846	0.70	9115	2228	0.96
	848	0.75	14133	1874	0.84
	850	0.77	16465	1707	0.76
Dy	852	0.82	19173	1465	0.68
	854	0.88	23196	1198	0.56
	856	0.90	27589	1029	0.52
	858	0.89	24976	1403	0.60
	860	0.86	21031	1523	0.64
	846	0.68	13390	1697	0.84
	848	0.72	15090	1191	0.68
	850	0.73	17650	812	0.56
Gd	852	0.77	19710	711	0.52
	854	0.80	23400	642	0.48
	856	0.83	25440	616	0.44
	858	0.88	31960	543	0.36
	860	0.84	25490	915	0.60
	846	0.69	4581	462	0.52
	848	0.71	7251	287	0.44
	850	0.75	8765	258	0.44
La	852	0.76	10089	233	0.40
	854	0.80	11205	184	0.32
	856	0.87	12415	114	0.28
	858	0.90	13012	93	0.28
	860	0.88	9937	202	0.32

ned in the CuO_2 layers. The Pb substituted in the Bi site of the $Bi-2212$ system improves the Josephson coupling between the CuO_2 layers by reducing the anisotropy and increasing the c-axis conductivity [Zhao et al. (2003) and Hamadneh et al. (2007)]. The RE doping in $(Bi,Pb)-2212$ decreases the c-axis length and hence, increases the Josephson coupling strength between the CuO_2 layers across the blocking layers $(Sr-O/Bi-O/Sr-O)$. This improves the self- and in-field J_C of the optimized holmium doped samples. The crystal defects created due to Pb doping are mainly confined in the Bi layer, but the defects produced by RE doping are mainly in the Sr layer. The vortices are confined in the CuO_2 layers, which are closer to the Sr layer than to the Bi layers. Thus, it is likely that the strongly coupled vortices in the CuO_2 layer are effectively pinned by the defects in the nearer Sr layer than the defects produced in the distant Bi layer. This is attributed to the enhanced pinning and the unusually high $J_C(B)$ performance of $(Bi,Pb)-2212$, doped with RE.

Among the RE substituted samples, the $J_C(B)$ characteristics are found to be much better for the RE substituted samples, at the sintering temperature of $846 \,^{\circ}C$. The ratio, $J_C(B)/J_C(0)$, of $Ho846$ is higher than that of the RE-free sample by a factor of ~ 4.6 at 0.2 T and of ~ 14 at 0.40 T, and the decrease in J_C with increasing magnetic field is lower for $RE846$ than for RE-free and all other RE substituted samples. That is, the deterioration of J_C due to magnetic field is significantly reduced for RE substituted samples sintered at $846 \,^{\circ}C$. In order to bring out the enhancement in the $J_C(B)$ performance of $RE846$, the $J_C(B)/J_C(0)$ values of all samples at 0.40, 0.60, 0.8 and 1.00 T are separately given in figure $5.7(a)-(d)$. This figure clearly shows that the in-field performance and the flux pinning strength are very much improved for $RE846$. When the sintering temperature increases, the $J_C(B)$ performance of RE substituted samples gradually decreases and the sample sintered at $856 \; and/or \; 858 \,^{\circ}C$ shows the least $J_C(B)$ performance. The result can be understood again from the microstructure of the samples (Figures 5.3 and 5.4). In sample $RE846$, the grains are smaller, more rounded, and less textured with a maximum number of grain boundaries, and hence the pinning due to grain boundary is more effective, leading to the best $J_C(B)$ performance. However, more grain boundary weak links in the sample reduce the self-field J_C. In $RE856 \; or \; RE858$, the larger

flaky grains are highly textured and have lesser grain boundaries and hence lesser weak links due to the optimum sintering temperature. This leads to lesser pinning and higher self-field J_C. Sample $RE860$ has better pinning than $RE856$ *or* $RE858$, which is obvious from the earlier observations on the deterioration of the microstructure (Figures 5.3 and 5.4).

5.5.2 $F_P(h)$ characteristics

The flux pinning strength of a superconductor can be determined by measuring the flux pinning force density $F_P = J_C \times B$ [Koblischka et al. (2000)]. In figure 5.8 $(a)-(d)$ the value
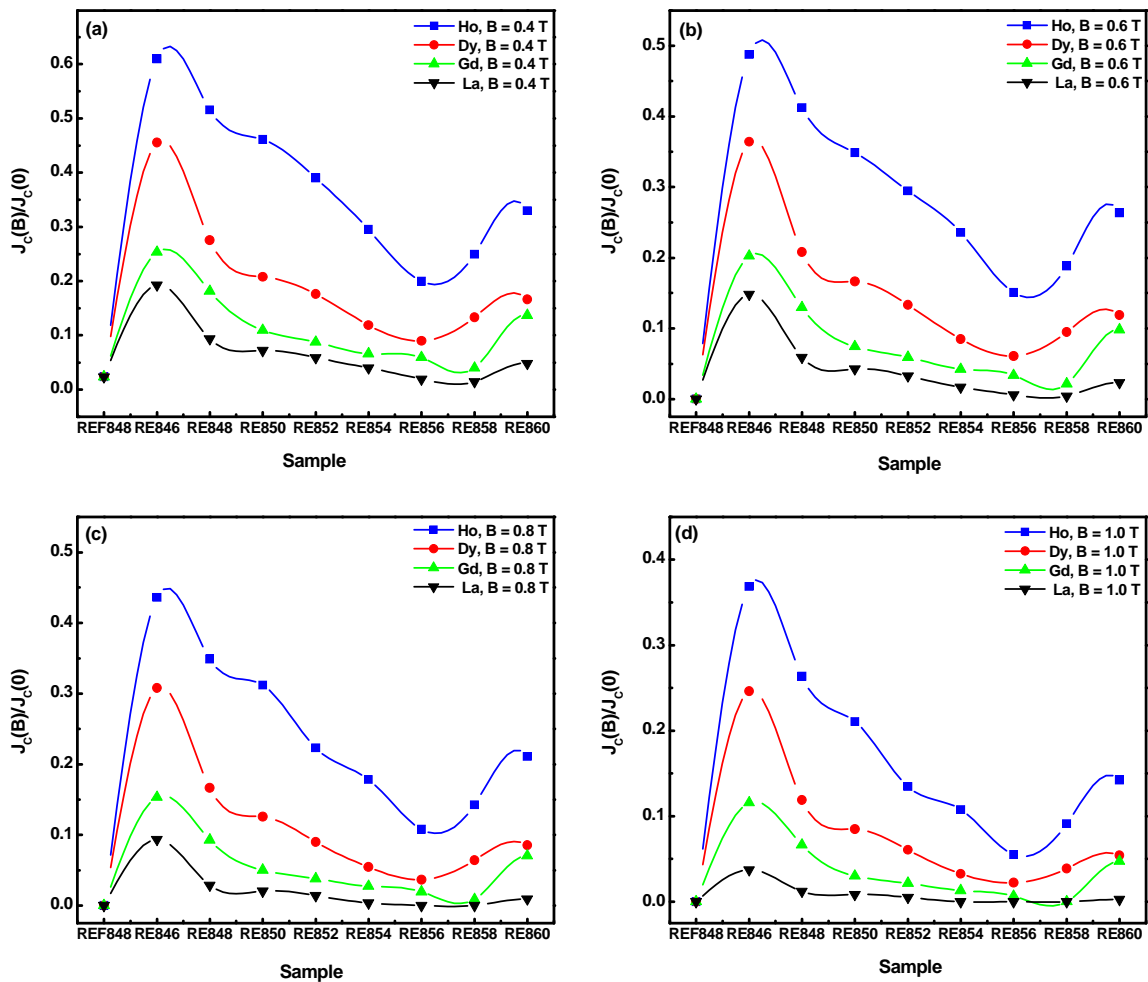
Figure 5.7 $(a)-(d)$: Variation of $J_C(B)/J_C(0)$ with respect to the sintering temperature and applied magnetic fields at 0.40, 0.60, 0.80 and 1.00 T in order to understand the relative performance of the RE-free and RE ($RE = Ho, Dy, Gd$ and La) substituted $(Bi,Pb)-2212$ samples.
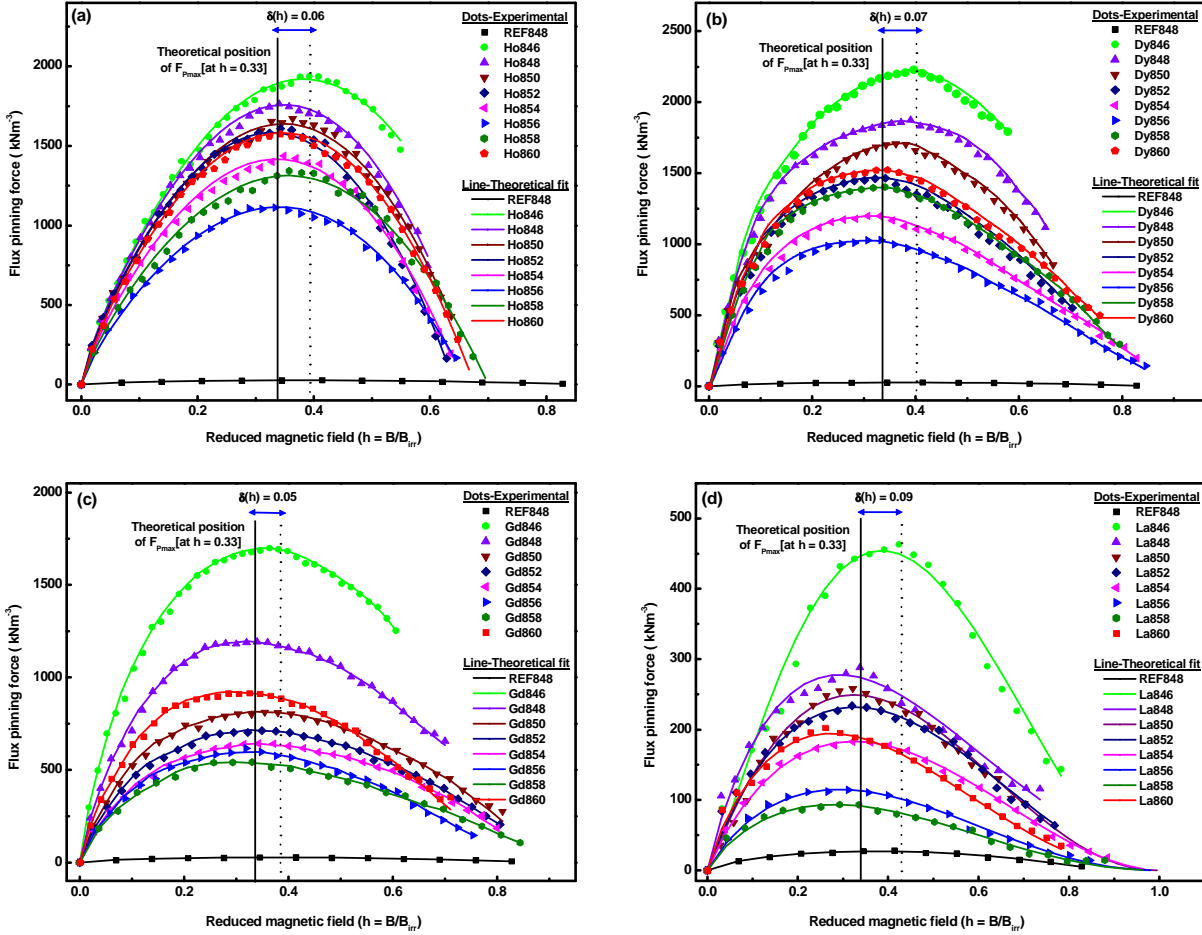
Figure 5.8 (a)−(d): **Variation in pinning force density (F_P) as a function of reduced magnetic field $(h = B/B_{irr})$. The parabolic solid line represents the theoretical fit, and the vertical solid line $(at\ h = 0.33)$ represents the theoretical position of the maximum value of the flux pinning force $(F_{P\max})$ according to the Dew-Hughes theory. The vertical dotted line $(at\ around\ h = 0.38 - 0.42)$ represents the (experimental) position of $F_{P\max}$ of the *RE* substituted sample sintered at 846 $^{\circ}C$. The δh represents the maximum deviation observed as compared with the theoretical position of $F_{P\max}$.**

of F_P as a function of reduced magnetic field $(h = B/B_{irr})$ is shown. All sets of data are found to fit well (figure 5.8 (a)−(d), solid parabolic line) with the Dew-Hughes equation [Dew-Hughes et al. (1974)] given by $F_P = A(B/B_{irr})^p (1 - B/B_{irr})^q$, where A is a numerical parameter. For normal point pinning, the values of p and q are 1 and 2, respectively, and the maximum

value of F_P (table 5.1) should appear at a reduced field value $h = 0.33$. For RE-free sample, the values of p and q are found to be 0.61 and 1.41, respectively. But for RE substituted samples, sintered between 846 and 860 $^\circ C$, the values of p and q are found to be 0.80 ± 0.05 and 1.65 ± 0.09, respectively. In our case, for samples sintered at 856 $^\circ C$, the maximum value of $F_{P\max}$ appeared much closer to the theoretically predicted value $h = 0.33$ [$figure$ 5.8 $(a) - (d)$]. Hence, the main pinning mechanism of this sample is the point pinning due to point defects aroused out of the substitution of RE atoms at the Sr site.

However, for samples sintered at 846 $^\circ C$, the peak position of $F_{P\max}$ appears beyond $h = 0.38$. That is, compared to the theoretical position, a maximum shift of $\delta h = 0.09$ (La846) is found, and this supports the fact that in addition to point pinning, grain boundary pinning is also effective in sample sintered at 846 $^\circ C$. Based on the above pinning analysis, it is found that the sample sintered at 846 $^\circ C$ shows the maximum flux pinning strength among all the RE substituted samples and F_P attains a maximum value [figure 5.8 $(a) - (d)$].

5.5.3 Normalized $F_P(B)$ characteristics

The normalized pinning force density $(F_P/F_{P\max})$ as a function of applied magnetic field (B) is shown in figure 5.9 $(a) - (d)$. The solid parabolic lines are the theoretical fit based on the Dew-Hughes equation $F_P = A(B/B_{irr})^p (1 - B/B_{irr})^q$, where A is a numerical parameter. It is seen that the maximum value of $F_P/F_{P\max}$ of Ho846, Dy846, Gd846 and La846 appeared beyond 1.00, 0.96, 0.84 and 0.52 T, respectively, as against 0.24 T for RE-free sample (table 5.1). The samples sintered at temperatures other than 846 $^\circ C$ have improved microstructure and self-field J_C values but the maximum value of $F_P/F_{P\max}$ and the field at which F_{Pmax} appeared are less than that of RE846. These results show that the irreversibility line of the RE substituted samples (especially, RE846) gets shifted toward higher magnetic fields and temperatures, and the flux pinning strength of RE substituted samples sensitively depends on the sintering temperature. The results also show that for magnetic field applications, the sample sintered at a comparatively lower sintering temperature (846 $^\circ C$) is useful, whereas for self-field applications, the samples need to be sintered at a higher temperature (856 $^\circ C$). That is,

depending on the applications in self- or applied field, a fine tuning of sintering temperature is essential for a doped $(Bi, Pb) - 2212$ superconductor for technological applications.
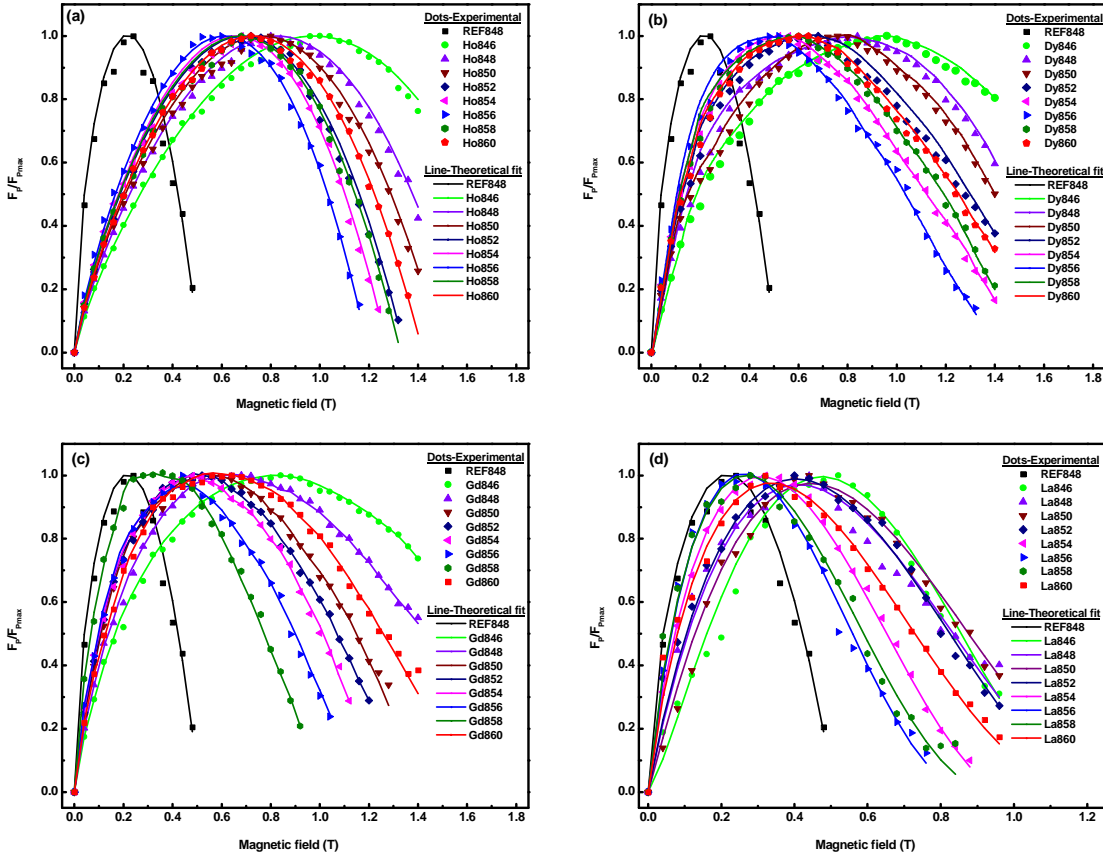

Figure 5.9 $(a) - (d)$: Variation in normalized flux pinning force density $(F_P/F_{P\max})$ as a function of applied magnetic field. The solid parabolic lines are the theoretical fit based on Dew-Hughes equation.

5.6 Conclusions

It is possible to tailor the microstructure and hence, the critical current density and flux pinning properties of *RE* substituted $(Bi, Pb) - 2212$ superconductors by appropriate choice of the sintering temperature $(T_{\sin ter})$. The results indicate that the self- and in-field properties are highly temperature sensitive. Since all the substituted samples with a specific *RE* have the same amount of *RE,* the additional electrons supplied to the $(Bi, Pb) - 2212$ system due to *RE* substitution is almost the same. Consequently, the hole concentration in that type of *RE*

substituted $(Bi, Pb) - 2212$ superconductors are identical and hence T_C is invariant for these samples. Now, the J_C value of RE substituted samples depends only on the microstructural and flux pinning aspects. The reason for the enormous increase of self-field J_C value of the samples heat treated at relatively higher sintering temperatures is evident from the refinement of microstructure with respect to the grain texturing as seen in SEM images while disruption of the microstructure with decreased texture reduces the self-field J_C of the samples heat treated at relatively lower sintering temperatures. Also, the analysis demonstrates that the substitution of RE in $(Bi, Pb) - 2212$ superconductor significantly enhances its flux pinning strength at a relatively higher temperature of 64 K, which also contributes to the final J_C of the RE substituted $(Bi, Pb) - 2212$ superconductors. Again, the Dew- Hughes pinning analysis shows that in addition to point pining, the grain boundary pining is also effective for samples sintered below or above the optimized sintering temperature.

The observed results from the investigation of the microstructural and flux pinning properties of RE substituted $(Bi, Pb) - 2212$ superconductors prepared at different sintering temperatures ranging from 846 to 860 $^{\circ}C$ point towards the importance of fine tuning of heat treatment temperature in the preparation of RE substituted $(Bi, Pb) - 2212$ superconductors. The results show that it is possible to tailor the properties of $(Bi, Pb) - 2212$ superconductors by proper selection of the sintering temperature. For instance, the RE substituted samples prepared at comparatively low sintering temperatures (846 – 850 $^{\circ}C$) are useful for magnetic field applications due to their better flux pinning properties. Whereas, the samples prepared at higher sintering temperatures (854 – 860 $^{\circ}C$) are useful for self-field applications due to their enhanced self-field current carrying capacity. The results also open up an opportunity to prepare RE substituted $(Bi, Pb) - 2212$ superconductors incorporating hybrid self- and in-field properties by selecting a suitable sintering temperature. The enhancement of electrical properties and magnetic performance is discussed based on the microstructural variation and changes in the chemical as well as electronic inhomogeneities due to the substitution of RE atoms in the $(Bi, Pb) - 2212$ system.

Chapter 6

CHAPTER 6

Novel effects of disorder outside the CuO$_2$ planes on the flux pinning properties of rare earth (Ce and Nd) substituted (Bi, Pb)-2212

6.1 Introduction

Since the discovery of bismuth based high temperature superconductors (HTS), the effect of doping of other cations on the superconducting properties of $(Bi, Pb) - 2212$ system has been a subject of great interest for both technologists and theoreticians. This is because doping is an effective method for improving the structural, transport, superconducting and flux pinning properties of Bi-based superconductors and to make the material suitable for the application at higher temperature and magnetic fields. The main advantages of Bi-based systems are their layered structure and hence, texturing can be easily induced in it. However, their applications in magnetic fields and at high temperatures are limited because of their strong anisotropic properties, extremely short coherence length (ξ), and large penetration depth (λ). The crystal structure of $(Bi, Pb) - 2212$ is highly two dimensional $(2D)$ with alternate stacking of superconducting CuO_2 layers and poorly conducting thick blocking layers, which reduce the Josephson coupling between the superconducting CuO_2 layers. Due to the weak coupling between the superconducting layers, the $3D$ vortices melts into $2D$ pancake like vortices at higher temperatures and fields [Pradhan et al. (1994)]. The $2D$ pancake vortices are easily de-pinned, causing flux flow and energy dissipation during transport current flow. In order to sustain high non-dissipative transport currents at higher temperatures and fields, the vortices must be pinned.

In high T_C cuprate based superconductors, the CuO_2 plane is believed to be responsible for the superconductivity. The impurities substituted at the Cu site are generally found to suppress the T_c [Vom Hedt et al. (1994) and Tarascon et al. (1998)]. A few studies reported that the self-field J_C and flux pinning strength of cuprate superconductors increases on rare-earth (RE) doping and the results were already discussed in detail in chapters 3 and 4. On the technological side the substitution of Pb for Bi improve the superconducting properties of both bulks and tapes [Fuji et al. (2000)] and the substitution of RE ions in the place of Ca/Sr

stabilize the crystal structure of the system [Jin et al. (1999)]. In all of the above works, only one site (*either Sr or Ca*) is considered at a time. Therefore, in the present chapter, in $(Bi, Pb) - 2212$ superconductor the effect of disorder at various cationic sites outside the CuO_2 planes (*Bi, Sr and Ca*) on the self- and in-field properties are investigated.

6.2 Experimental details

RE-free [$(Bi_{1.6}Pb_{0.5})Sr_2Ca_{1.1}Cu_{2.1}O_{8+\delta}$ here after denoted as RE00] and RE ($RE = Ce\ or\ Nd$) substituted at the Bi site [$(Bi_{1.525}Pb_{0.5}RE_{0.075})Sr_2Ca_{1.1}Cu_{2.1}O_{8+\delta}$ here after denoted as $BiRE$], at the Ca site [$(Bi_{1.6}Pb_{0.5})Sr_2(Ca_{1.025}RE_{0.075})Cu_{2.1}O_{8+\delta}$ here after denoted as $CaRE$], and at the Sr site [$(Bi_{1.6}Pb_{0.5})(Sr_{1.925}RE_{0.075})Ca_{1.1}Cu_{2.1}O_{8+\delta}$ here after denoted as $SrRE$], were prepared by solid state method. The details of sample preparation, characterization and measurements are the same as given in chapter 3.

6.3 Structural characterization

6.3.1 *XRD* analysis

Figures 6.1 (a) and 6.2 (a) show the normalized XRD patterns of the RE ($RE = Ce\ or\ Nd$)-free and RE substituted $(Bi, Pb) - 2212$ pellets after the last stages of heat treatment. It shows that all the samples contain only the peaks corresponding to the $(Bi, Pb) - 2212$ phase and no peaks of any secondary phase containing RE ($Ce\ or\ Nd$) or any other cation were detected at this stage within the detection limit of the instrument. The absence of secondary phases suggests that all the reactant phases are converted into the $(Bi, Pb) - 2212$ and the substituted RE is incorporated into the crystal lattice of $(Bi, Pb) - 2212$ superconductor. Also figures 6.1 (a) and 6.2 (a) show that when the dopant site changes, the peak height corresponding to the (*00l*) planes decreases and the peak height is least for $SrRE$. In order to clearly bring out the decrease in peak height of the (*00l*) planes, the (*008*) peaks of all samples are separately shown, with better resolution in figures 6.1 (b) and 6.2 (b). It shows that the texturing is maximum for RE00 and is strongly dependent on the site at which the RE (Ce) is doped. A measure of texture known as Lotgering index (F) is calculated from the

peak intensity of the *XRD* patterns of sintered pellets and the corresponding randomized powder using the relation,

$$F = \left(\frac{I_a - I_r}{1 - I_r} \right) \tag{6.1}$$

Where, *I* is the ratio of intensities from the surface of sample and

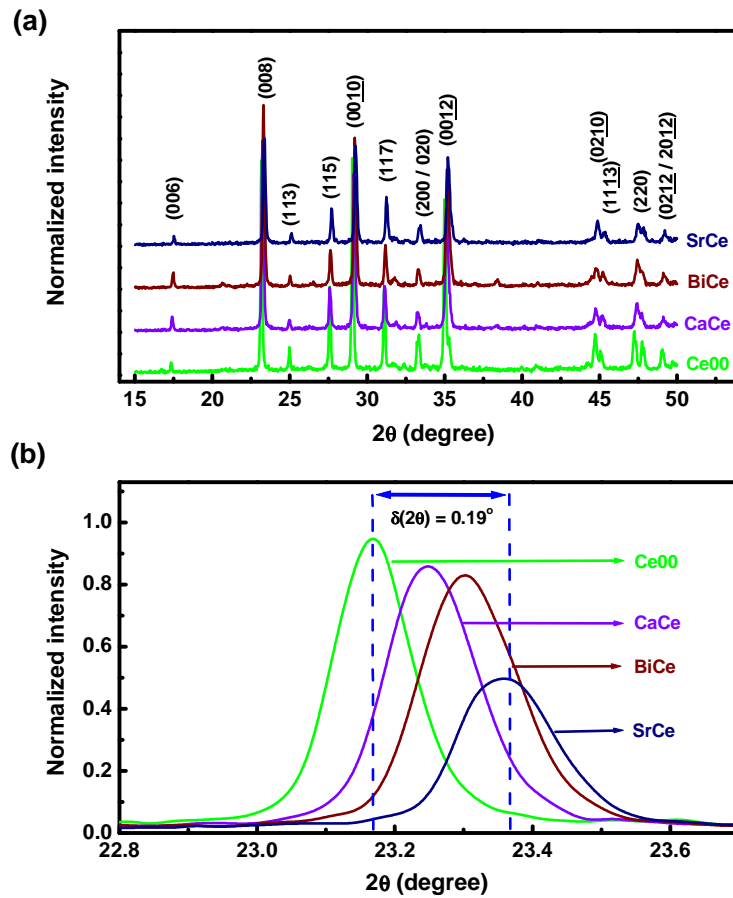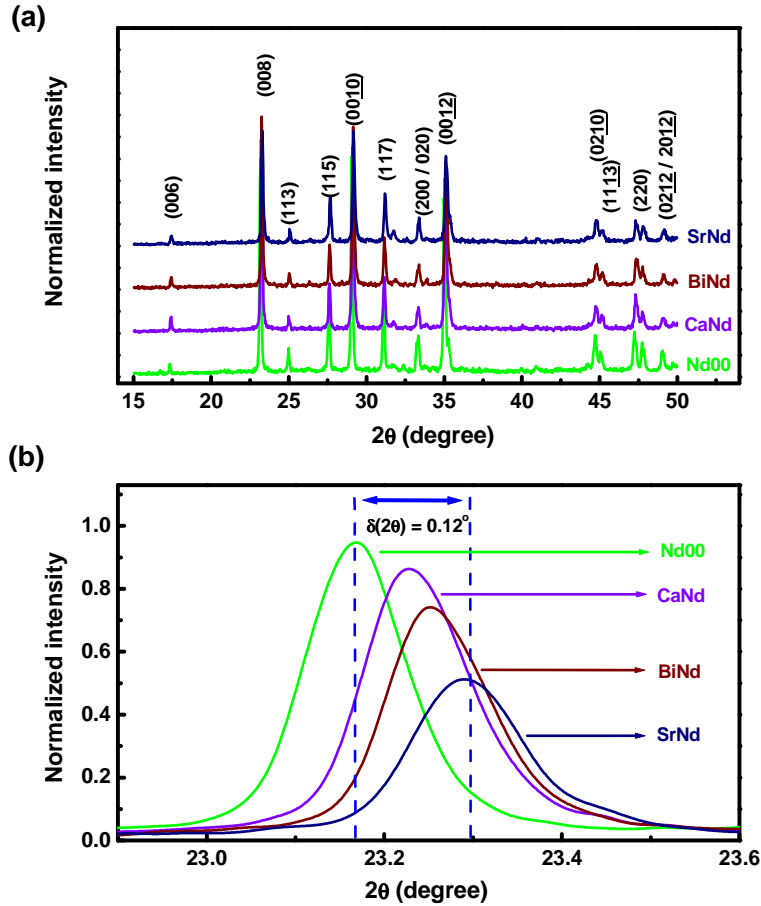$$I = \left(\frac{\sum I_{00l}}{\sum I_{total}} \right) \tag{6.2}$$

(a)

(b)

Figure 6.1: (a) The normalized *XRD* patterns of the *Ce*-free and *Ce* substituted (Bi, Pb)-2212 pellets after the last stage heat treatment and (b) the normalized *XRD* peaks for the *(008)* plane at around 2θ = 23.1° and δ(2θ) = 0.19° represents the maximum peak-shift of *Ce* substituted sample with respect to the *Ce*-free sample.

Figure 6.2: **(a) The normalized *XRD* patterns of the *Nd*-free and *Nd* substituted (Bi, Pb)-2212 pellets after the last stage heat treatment and (b) the normalized XRD peaks for the *(008)* plane at around 2θ = 23.1° and δ(2θ) = 0.12° represents the maximum peak-shift of *Nd* substituted sample with respect to the *Nd*-free sample.**

Here I_a refers to I measured for the pellets and I_r for the corresponding randomized powder [Lotgering (1959)]. The F value calculated from the XRD data (Table 6.1) is found to be dependent on the site in which RE is substituted. It is also noted that the RE-free sample has the highest F value and hence, the texturing is maximum for this sample. These figures [6.1 (b) and 6.2 (b)] also show that the (008) peaks of the RE (Nd) substituted sample shift towards higher angle with respect to the position of the RE-free $(Bi, Pb) - 2212$ sample, even though all the patterns are taken under identical condition. Among the Ce substituted samples, a maximum peak shift of $\delta(2\theta) = 0.19°$ obtained for $SrCe$ and for Nd substituted sample, it is $0.12°$ (for $SrNd$). This supports the fact that the doped RE atoms entered into the crystal

structure, and the *c*-axis length of the *RE* substituted $(Bi, Pb) - 2212$ system decreases. Since the shift is higher for *SrRE*, the c-axis length is smaller for this sample as compared to *BiRE* and *CaRE*. The lattice parameters of the *RE*-free and *RE* substituted samples were calculated by considering an orthorhombic symmetry for the $(Bi, Pb) - 2212$ system [Figure 6.3 and 6.4].
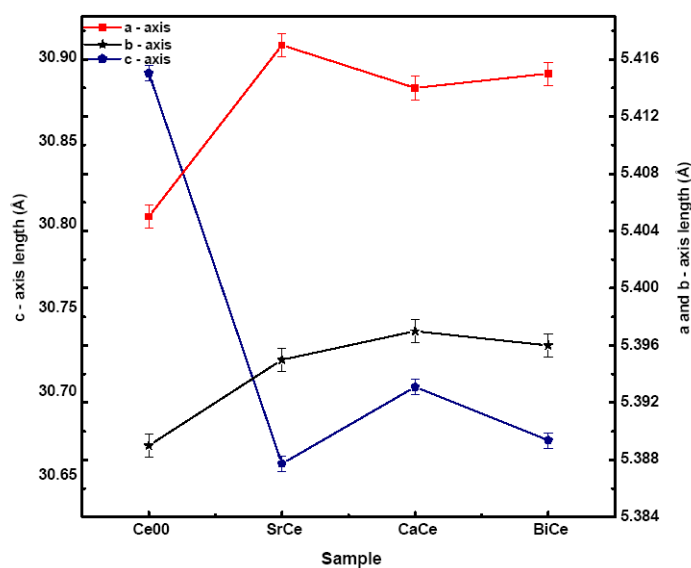

Figure 6.3: The lattice parameters (*a*, *b* and *c*) of the *Ce* free and all *Ce* substituted samples calculated by considering an orthorhombic symmetry for the $(Bi, Pb) - 2212$ system.
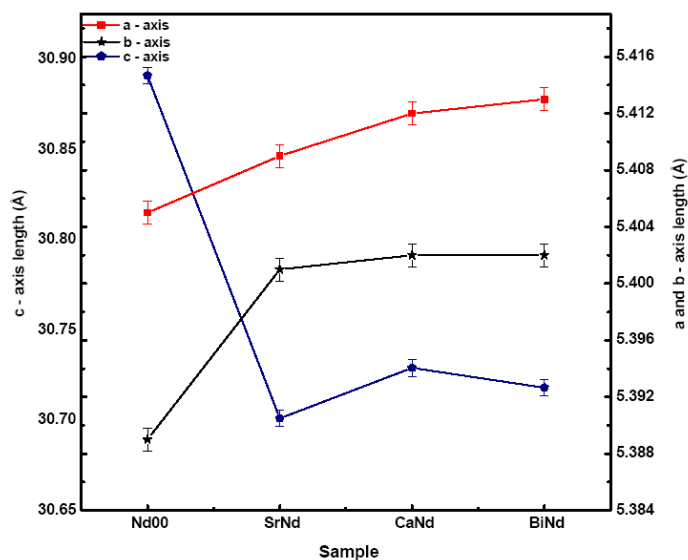

Figure 6.4: The lattice parameters (*a*, *b* and *c*) of the *Nd* free and all *Nd* substituted samples calculated by considering an orthorhombic symmetry for the $(Bi, Pb) - 2212$ system.
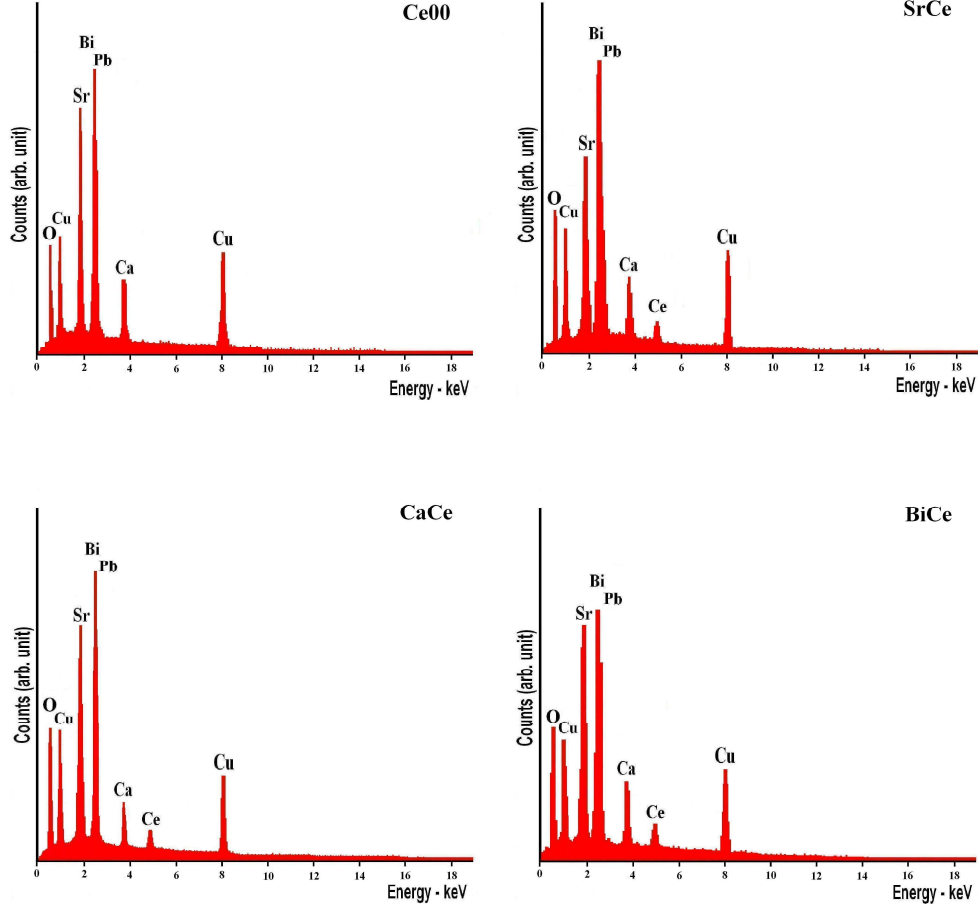
Figure 6.5: The *EDS* **spectra of** *Ce* **-free and** *Ce* **substituted at different cationic sites** $(Sr, Ca \text{ and } Bi)$ **of** $(Bi, Pb) - 2212$ **grains.**

It also shows that the c-axis lattice parameter value decreases with RE substitution and the decrease is higher for substitution at Sr site as compared with other two sites (Bi and Ca). The contraction in c-axis length of all RE substituted samples as compared with the RE - free sample indicates the incorporation of RE atoms into the $(Bi, Pb) - 2212$ system. This is because when the Ce^{4+}/Nd^{3+} enters into the $(Bi, Pb) - 2212$ system, the interlayer distances $\Delta z(Cu - Ca - Cu)$ and $\Delta z(Ca - Sr)$ expand but $\Delta z(Sr - Bi)$, $\Delta z(Bi - Bi)$ and $\Delta z(Sr - Bi - Bi - Sr)$ shrink because the extra oxygen resides in the $Bi - O$ double layers. The extra oxygen balances the increased valency due to the replacement of cations by Ce^{4+}/Nd^{3+}. Consequently, the net positive charge in the $Bi - O$ layers reduces. Hence, the repulsion

between them is reduced, and the distance between all the layers along the c-axis in the structure contracts [Ekin et al. (1989)]. In addition to this, the difference in ionic radii (ionic radii of Sr^{2+}, Ca^{2+}, Bi^{3+} are 1.18, 1.00, 1.03 and that of Ce^{4+} and Nd^{3+} are 0.87 and 0.983 Å, respectively) between the cations and RE is also responsible for c-axis reduction. Again, as compared with RE-free sample, a and b-axis values are slightly increases for RE substituted samples. The elongation of a and b-axis is generally associated with the increase in the $Cu-O$ bond length in CuO_2 planes, which controls the dimension in the basal plane [Narsaiah et al. (1992)].

6.3.2 Compositional analysis

The compositional analysis has been performed by EDS using the spot analysis method, and the EDS spectra of the Ce free and all Ce substituted $(Bi, Pb)-2212$ grains are shown in figure 6.5 as a typical example. The presence of Ce is detected in the Ce substituted $(Bi, Pb)-2212$ grains with a corresponding reduction in cations and the composition is found to be $(Bi_{1.54}Pb_{0.47})Sr_{2.08}Ca_{1.06}Cu_{2.1}$ for $Ce00$, $(Bi_{1.51}Pb_{0.53}Ce_{0.05})Sr_{2.11}Ca_{1.13}Cu_{2.1}$ for $BiCe$, $(Bi_{1.57}Pb_{0.51})Sr_{2.04}(Ca_{1.01}Ce_{0.06})Cu_{2.1}$ for $CaCe$ and $(Bi_{1.56}Pb_{0.53})(Sr_{1.93}Ce_{0.08})Ca_{1.08}Cu_{2.1}$ for $SrCe$. Similarly for Nd substituted samples the composition is found to be $(Bi_{1.54}Pb_{0.47})Sr_{2.08}Ca_{1.06}Cu_{2.1}$ for $Nd00$, $(Bi_{1.50}Pb_{0.54}Nd_{0.08})Sr_{2.15}Ca_{1.09}Cu_{2.1}$ for $BiNd$, $(Bi_{1.54}Pb_{0.53})Sr_{2.10}(Ca_{1.05}Ce_{0.07})Cu_{2.1}$ for $CaNd$ and $(Bi_{1.61}Pb_{0.48})(Sr_{1.97}Ce_{0.07})Ca_{1.02}Cu_{2.1}$ for $SrNd$. This supports the fact that the RE atoms are successfully substituted into the $(Bi, Pb)-2212$ system at the respective cationic sites and forms a structure with almost identical initial stoichiometry (as given in the experimental part).

6.4 Superconductor characterization

Figure 6.6 (a) shows the temperature dependences of the resistivity for cerium free and cerium doped $(Bi, Pb)-2212$ samples as a typical example. It shows that for cerium doped samples the normal state resistivity (ρ_n) is minimum for $CaCe$ (55.08 $\mu\Omega cm$) (Table 6.1) and maximum for $SrCe$ (72.1 $\mu\Omega cm$), i.e. the ρ_n value sensitively depends on the dopant site. Also, low residual resistivity ratio (RRR) and high ΔT_c values (Table 6.1) are obtained for $SrCe$ which reflect the increased impurity scattering and higher level of disorder in this sample. The Nd substituted samples also show similar results (Table 6.1). Further insight into the

effect of disorder outside the CuO_2 planes can be obtained from the value of $\sigma^2(r,x)$. Here, $\sigma^2(r,x)$ is the variance of ionic radii of cations, which also represents the amount of disorder in the system [Attfield et al. (1998)]. The value of $\sigma^2(r, x)$ can be calculated using the formula,

$$\sigma^2\left(r,x\right)=\frac{x}{2}r_R^2+\left(1-\frac{x}{2}\right)r_C^2-\left[\frac{x}{2}r_R+\left(1-\frac{x}{2}\right)r_C\right]^2 \tag{6.3}$$

Here x is the amount of Ce/Nd substituted at different cationic sites, $R=Ce^{4+}$ for Ce substituted samples and Nd^{3+} for Nd substituted samples and $C=Bi^{3+}$ or Sr^{2+} or Ca^{2+}. Also r_R and r_C are the radius of the corresponding cation. The plot of ρ_n and $\sigma^2(r,x)$ is given in figure 6.6 (*b*) and (*c*) and it shows that both ρ_n and $\sigma^2(r,x)$ values are maximum for the sample *SrCe* and *SrNd* (Table 6.1) and hence it is concluded that the out-of-plane disorder is maximum when *RE* is doped at the strontium site.

The T_c values of *RE*-free and *RE* substituted samples are given in table 6.1, and it is interesting to note that the *RE* substituted samples have much higher T_c values compared to the *RE*-free sample. The doping of each *RE* atom in the $(Bi,Pb)-2212$ system supplies one or two electron to the system depending on the dopant site, which reduces the number of holes and thus shifts the system from over doped to the optimally doped condition as far as the hole density is concerned [Guptha et al. (1994)]. The attainment of hole concentration closer to the optimum value is responsible for the enhancement of T_c. The hole concentration of the doped sample showing superconducting transition is calculated using the phenomenological formula [Krusin Elbaum et al. (2004)],

$$P=\left[\frac{\left[\left(1-\frac{T_c}{T_{c\max}}\right)\right]^{\frac{1}{2}}}{82.6}\right]+0.16 \tag{6.4}$$

Here P is the hole carrier concentration $/Cu$ atom and $T_{c\max}$ corresponds to T_c for $P=0.16$, the optimal concentration. The value of P obtained for *RE*-free and *RE* substituted samples is given in table 6.1 and the P value is closer to 0.16 for *SrCe*. Since the hole concentration is

closer to the optimal value, this sample shows the maximum T_c. Again, there is a systematic trend observed between [$\sigma^2(r,x)$ *and* ρ_n] and self-field J_C values [Figure 4(a), (b), (c) and table 6.1]. In the case of *RE* substituted samples, the defect concentration is less for *RE* substituted at the *Ca* site and hence, the J_C is higher for this sample ($20414\pm5\ kA/m^2\ for\ CaCe$ and $13526\pm5\ kA/m^2\ for\ CaNd$). Even though T_c is maximum for *SrRE*, the lower self-field J_C of this sample is due to the increased disorder as evidenced from figure 6.6 (a), (b) and (c) and hence, the reduced intra-grain J_C.
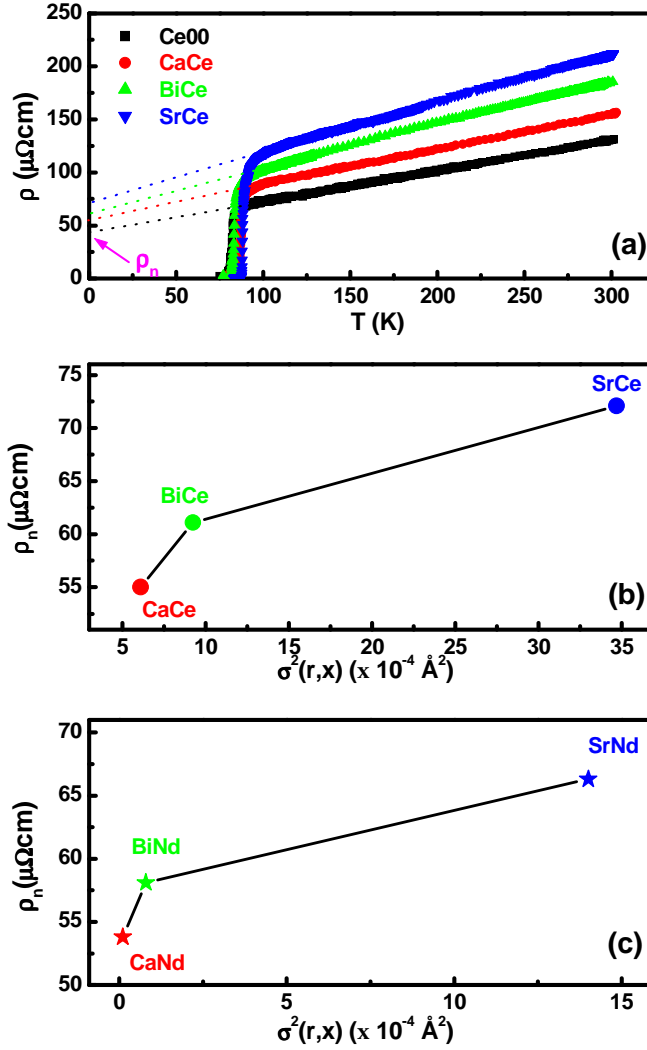

Figure 6.6: (a) Temperature dependent resistivity plots of *Ce*-free and *Ce* substituted $(Bi,Pb)-2212$ samples as a typical example. The normal state resistivity (ρ_n) value is indicated by an arrow and (b) and (c) the plot between variance of ionic radii $\sigma^2(r,x)$ and ρ_n for *Ce* and *Nd* substituted samples.

Table 6.1: The values of Lotgering index (F), normal state resistivity (ρ_n), residual resistivity ratio (RRR), critical temperature (T_c), ΔT_c, hole carrier concentration/Cu atom (P), self-field J_C, and $\sigma^2(r, x)$ values of RE-free and all RE (Ce and Nd) substituted $(Bi, Pb) - 2212$ samples.

RE	$Site$	F	ρ_n $\mu\Omega cm$	RRR	T_c K	ΔT_c K	P	J_C kAm^{-2}	$\sigma^2(r, x)$ $\times 10^{-4}\ \overset{\circ}{A}^2$
$RE - free$	NIL	0.91	44.3	2.17	81.3	1.33	0.1897	1913	NIL
	$SrCe$	0.82	72.1	1.88	87.4	5.01	0.1664	14312	34.686
Ce	$CaCe$	0.88	55.0	2.08	86.7	2.81	0.1717	20414	6.099
	$BiCe$	0.87	61.1	1.93	84.1	3.83	0.1822	18436	9.240
	$SrNd$	0.84	66.3	1.95	89.6	4.19	0.1663	8016	14.007
Nd	$CaNd$	0.89	53.8	2.34	89.1	2.35	0.1746	13526	0.104
	$BiNd$	0.87	58.1	2.12	87.8	2.98	0.1796	9864	0.797

6.5 Flux pinning analysis

6.5.1 Normalized $J_C(B)$ characteristics

Figure 6.7 (a) and (b) shows the normalized in-field critical current density characteristics of RE-free and RE substituted $(Bi, Pb) - 2212$ samples at 64 K and magnetic field up to 1.4 T. The normalized $J_C(B)$ characteristics of the RE substituted samples are found to be much better than that of RE-free sample. That is, the deterioration of J_C due to the magnetic field is significantly reduced because of RE substitution. This shows that the RE substitution enhances the flux pinning properties of $(Bi, Pb) - 2212$ system. Among the RE substituted samples, the $J_C(B)/J_C(0)$ characteristics are found to be much better for all the RE substituted samples and the best result is for that substituted at the Sr site ($SrCe$ and $SrNd$). The ratio, $J_C(B)/J_C(0)$ of $SrCe$ is higher than that of cerium free sample ($Ce00$) by a factor of ~ 5.5 at 0.2 T and of ~ 13.2 at 0.40 T, and the decrease in J_C with increasing magnetic field is lower for $SrCe$ than for $Ce00$ and all other cerium doped samples ($BiCe$ and $CaCe$). That is, the deterioration of J_C due to the magnetic field is significantly reduced for $SrCe$. Similar

results were obtained for *SrNd* also [figure 6.7 (b)]. These figures clearly show that the in-field performance and the flux pinning strength are very much improved for *SrRE* ($RE = Ce$ and Nd). When the dopant site changes, the $J_C(B)$ performance of *RE* substituted samples also changes and the samples doped with *RE* at the calcium site (*CaCe* and *CaNd*) show the least $J_C(B)$ performance. The result can be understood again from the disorder of the samples. The large difference in ionic radii between the Sr^{2+} and Ce^{4+}/Nd^{3+} may produce comparatively larger lattice disorder than *CaRE* and *BiRE* (this is also a reason for increased normal state resistivity of *SrRE* as mentioned earlier). The *Pb* and *RE* substitution in $Bi-2212$ improves the Josephson coupling between the CuO_2 layers by reducing the anisotropy and increasing the c-axis conductivity [the reason is explained in detail in chapter 4]. The *RE* substitution in $(Bi,Pb)-2212$ decreases the *c*-axis length and hence increases the Josephson coupling strength between the CuO_2 layers across the blocking layers ($Sr-O/Bi-O/Sr-O$). This improves the self- and in-field J_C of the *RE* substituted samples. The crystal defects created due to the *Pb* doping are mainly confined in the $Bi-$ layer, but the defects produced by *RE* substitution are mainly in the $Sr/Ca/Bi$ layer depending on the dopent site. The vortices are confined in the CuO_2 layers, which are closer to the Sr/Ca layer than to the $Bi-$ layers. Thus it is likely that the strongly coupled vortices in the CuO_2 layer are effectively pinned by the defects in the nearer $Sr-$ layer than the defects produced in the distant $Bi-$ layer. This is attributed to the enhanced pinning and the unusually high $J_C(B)$ performance of $(Bi,Pb)-2212$ substituted with *RE* at its $Sr-$ site. Since the ionic radii difference between calcium and *RE* is very small [the disorder is less as evidenced from figure 6.6 (a), (b)], and hence, the pinning efficiency is very much reduced for *CaCe* as compared with *SrCe*. Even though $Bi-$ layer is away from CuO_2 layer, the pinning efficiency of *BiRE* is greater than *CaRE*, which suggests the possibility of entrance of few of the *RE* atoms at the *Sr* site due to site mixing in the case of *BiRE*. The *Sr* content from the *EDAX* result $[(Bi_{1.51}Pb_{0.53}Ce_{0.05})Sr_{2.11}Ca_{1.13}Cu_{2.1}$ obtained from *EDAX* result for *BiCe* and $(Bi_{1.50}Pb_{0.54}Nd_{0.08})Sr_{2.15}Ca_{1.09}Cu_{2.1}$ for *BiNd* as compared with the starting composition $(Bi_{1.525}Pb_{0.5}RE_{0.075})Sr_2Ca_{1.1}Cu_{2.1}O_{8+\delta}]$ also supports this.

6.5.2 $F_P(B)$ characteristics

It is widely accepted that a very useful tool with which one can investigate the flux pinning strength of a superconductor is the determination of flux pinning force density $F_P = J_C \times B$ [Koblischka et al. (2000)]. The value of F_P as a function of reduced magnetic field ($h = B/B_{irr}$) is shown in figure 6.7 (c), (d) and all sets of data are found to fit well (solid parabolic line) with the Dew-Hughes equation [Dew-Hughes (1974)] given by,

$$F_P = A \left(\frac{B}{B_{irr}} \right)^p \left(1 - \frac{B}{B_{irr}} \right)^q \qquad (6.5)$$

Here A is a numerical parameter. The fitting parameters for different Ce and Nd substituted $(Bi, Pb) - 2212$ samples are given in table 6.2.

Table 6.2: The values of different pinning parameters of RE-free and RE (Ce and Nd) substituted $(Bi, Pb) - 2212$ samples.

RE	Site	p	q	$B_{irr}(T)$
$RE - free$	NIL	0.66	1.59	0.72
	SrCe	0.91	1.93	3.25
Ce	CaCe	0.80	1.71	1.81
	BiCe	0.84	1.77	2.54
	SrNd	0.88	1.89	3.46
Nd	CaNd	0.81	1.74	2.29
	BiNd	0.82	1.78	2.82

For normal point pinning the value of p and q are 1 and 2, respectively, and the maximum value of F_P appeared at a reduced field value $h = 0.33$. For cerium free sample, the values of p and q are found to be 0.66 and 1.59, respectively. But for $SrCe$, $p = 0.91$, $q = 1.93$ and for $SrNd$, $p = 0.88$, $q = 1.89$ are obtained, which are closer to the theoretically predicted value. Also, in our case, for all samples we get the peak position of F_P at $h = 0.33 \pm 0.03$ [in figure 6.7 (c) and (d), for all samples we get the peak position of F_P closer to the vertical solid line drawn at the

reduced field of $h = 0.33$], which shows that the main pinning mechanism is due to point defects aroused out of the substitution of *RE* atoms at the respective cationic sites. The slight deviation of *p* and *q* values from the theoretical values for point pinning may be due to the influence of surface pinning by grain boundaries. Based on the above pinning analysis, it is found that the samples *SrCe* and *SrNd* show the maximum flux pinning strength among *Ce* and *Nd* substituted samples and F_P attains a maximum value of 2512 kNm^{-3} for *SrCe* and 885 kNm^{-3} for *SrNd*.
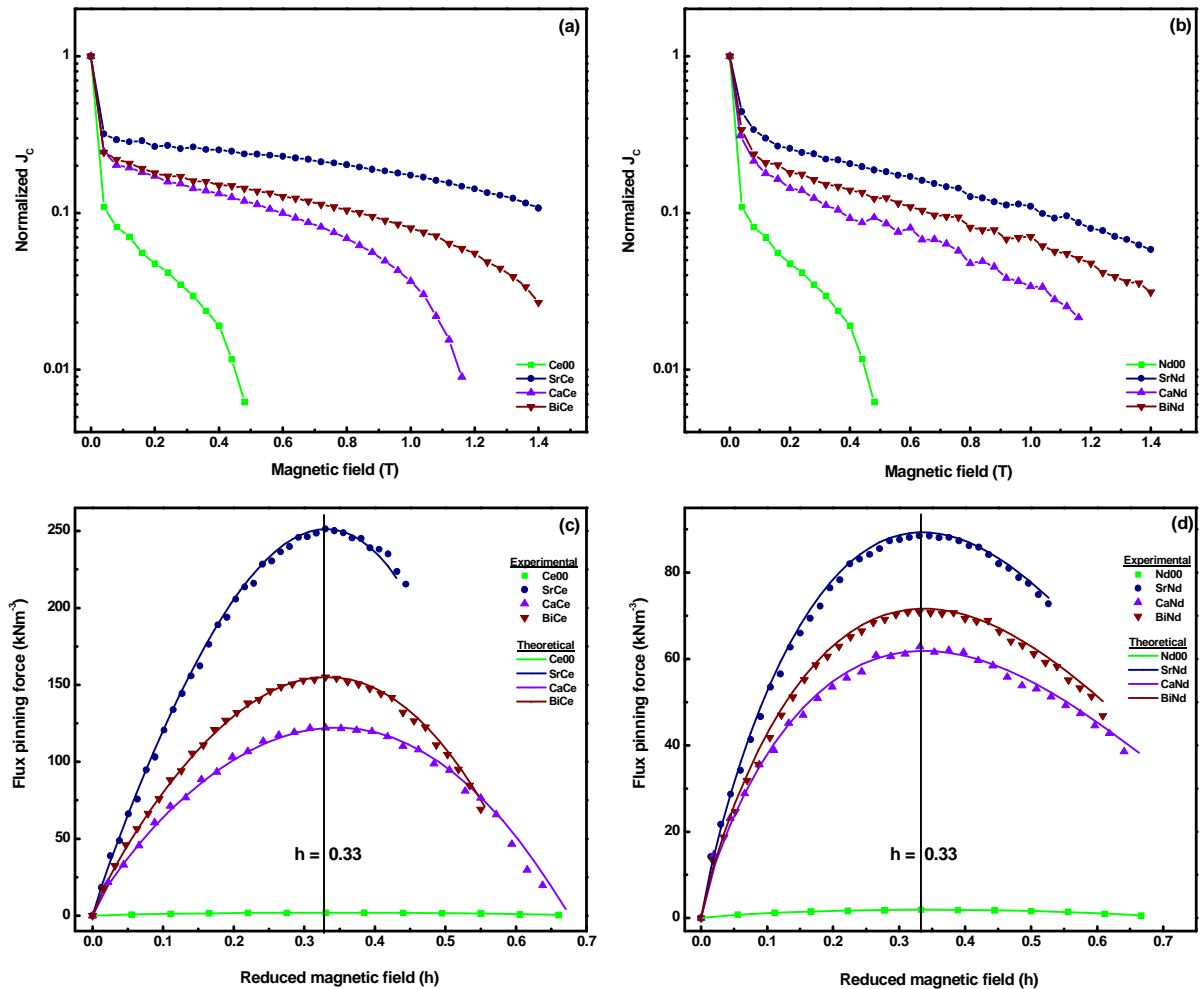

Figure 6.7: (a), (b) Variation of normalized in-field critical current density of $RE -$ free and RE substituted samples for magnetic fields up to 1.4 T and (c), (d) Variation of flux pinning force density (F_P) as a function of reduced magnetic field $(h = B/B_{irr})$. The parabolic solid line represents the theoretical fit and the vertical solid line (at $h = 0.33$) represents the theoretical position of maximum value of flux pinning force $(F_{P\max})$ according to the Dew-Hughes theory.

6.5.3 Normalized $F_P(B)$ characteristics

The normalized pinning force density $(F_P/F_{P\max})$ as a function of applied magnetic field is shown in figure $6.8\,(a)$ and (b). It is seen that the maximum value of $F_P/F_{P\max}$ of *SrCe* and *SrNd* appeared beyond $1.00\ T$ as against $0.60\ T$ for *CaRE* and $0.24\ T$ for *RE*00. These results show that the irreversibility line of the *Ce* and *Nd* substituted samples [especially *SrCe*
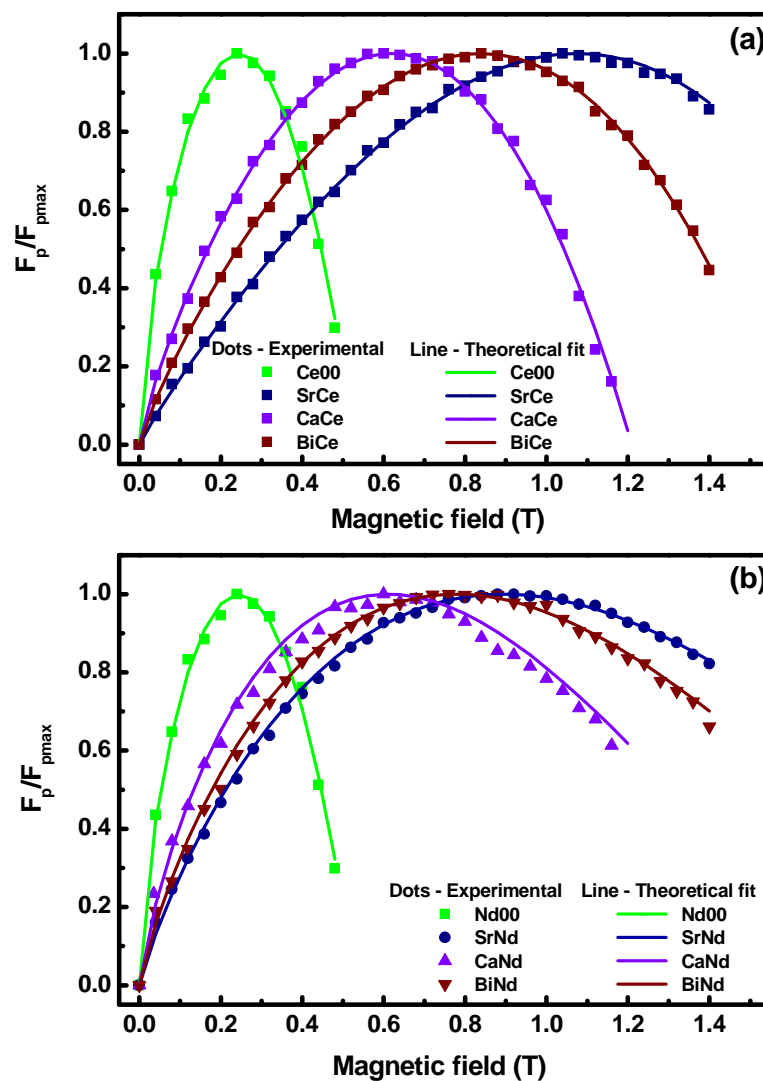

Figure 6.8 (a) and (b): Variation of normalized flux pinning force density $(F_P/F_{P\max})$ as a function of applied magnetic field up to 1.4 T for $RE-$free and RE substituted $(Bi,Pb)-2212$ samples.

and *SrNd*] gets shifted towards higher magnetic fields and temperatures, and the flux pinning strength of *Ce* and *Nd* substituted samples sensitively depends on the site in which *Ce* and *Nd* is substituted. Also the experimental results show that for magnetic field applications, the *RE* substituted at its *Sr* site is useful, where as for self-field applications, the *RE* need to be substituted at the *Ca* site. That is, depending on the applications in self- or applied-field, the suitable selection of doping site is very much essential for the *RE* doped $(Bi, Pb) - 2212$ superconductor, for technological applications.

6.6 Conclusions

This chapter presents a systematic study on the effect of disorder at various out-of-plane lattice sites on T_c, self- and in-field J_C and flux pinning properties of *RE* (*Ce* and *Nd*) substituted $(Bi, Pb) - 2212$ superconductor. It is found that the self-field J_C and $J_C(B)$ characteristics of *Ce* and *Nd* substituted samples are highly sensitive to the dopant site. The enhancement of flux pinning properties are evident from the improved $J_C(B)$ characteristics and the Dew-Hughes pinning analysis shows that the enhanced flux pinning is mainly because of the point defects produced by the substituted *RE*. Among the *RE* substituted samples, *SrRE* shows the best $J_C(B)$ performance and the least self-field J_C, while *CaRE* shows the least $J_C(B)$ performance and the best self-field J_C. Also, the shifting of the peak position of pinning forces density $(F_{P\,max})$ towards the higher fields for *Ce* and *Nd* substituted samples shows a shifting of the irreversibility line towards the higher fields. The enhancement of superconducting and flux pinning properties are discussed based on the variation of out-of-plane disorder, changes in the chemical as well as electronic inhomogeneities due to the doping of *RE* atoms in the $(Bi, Pb) - 2212$ system.

Chapter 7

CHAPTER 7

Scaling of vortex liquid resistivity in rare earth (Lu, Ho, Eu, La and Ce] modified (Bi, Pb)-2212

7.1 Introduction

The future application of high-temperature superconductors [*HTS*] strongly depends on their capacity for carrying large loss-free currents in the presence of magnetic fields. However, especially close to the transition to the normal state, flux creep and flux flow effects are unusually large and counteract the flux pinning, thus, causing a reduction of critical current density. In *HTS* the vortex system is soft due to large anisotropy, the extreme type II character and the short coherence length and hence, a molten vortex liquid replaces the conventional Abrikosov vortex lattice in the wide regions of the vortex-matter phase diagram [Nelson et al. (1989)]. Strong thermal fluctuations lead to the melting of a flux line lattice over a substantial part of the mixed state phase diagram and at temperatures below the melting temperature, T_m, the vortex system is in a (pinned) superconducting vortex-solid phase with non-zero critical current, while at $T > T_m$ it is in a dissipative vortex-liquid state [Houghton et al. (1989)].

The melting transition of the vortex matter and the nature of the vortex solid are strongly affected by disorder. The vortex solid in a clean system undergoes a first order Bragg glass melting transition into vortex liquid due to strong thermal fluctuations but turns into a second order transition for highly disordered systems involving point defects or a Boss glass to liquid transition in systems with columnar defects. The strong anisotropic properties together with short coherence length leads to the pronounced thermally assisted motion of vortices in HTS and one important result is the resistive transition broadening of HTS in applied magnetic fields and under bias currents. However, there is no complete consensus on how the relative higher temperature and strong anisotropy lead the observed resistive transitions. This is because neither the pinning mechanisms nor the high-temperature dynamics of vortices in these anisotropic systems are well understood [Blatter et al. (1994)]. One of the fundamental assumptions of the vortex glass theory introduced by Fisher [Fisher (1989)] to explain this resistive transition

broadening is the concept of divergence of a vortex glass correlation length $\xi_g(T)$ at the glass transition temperature T_g and according to this theory,

$$\xi_g(T) \propto \left| T - T_g \right|^{-\nu} \tag{7.1}$$

and here ν is the static critical exponent. For a second order phase transition, applied to ξ_g and to the characteristic time scale, $\tau_g \propto \xi_g^z$, the DC current-voltage characteristics for a vortex glass with quenched disorder are scaled with $E\xi_g^{z+1} \propto F_+(J\xi_g^{d-1})$. Where, E is the electric field, z, the dynamic critical exponent, F_+, a scaling function, J, the current density and d, the dimensionality. Above T_g, and for $J \ll J_C$, $F_+ \to 1$, giving a linear glass resistivity, $\rho \propto \left| T/T_g - 1 \right|^{\nu(z+2-d)}$, i. e., the linear resistivity vanishes according to the power law [Rydh et al. (1999), M. Andersson et al. (2000), Rydh et al. (2000)],

$$\rho = \rho_0 \left| \frac{T}{T_g} - 1 \right|^s \tag{7.2}$$

Here $s = \nu(z+2-d)$ is the critical exponent and ρ_0 is the characteristic resistivity. The value of ρ_0 is proportional to the flux flow resistivity ρ_{ff}, which is related to the normal state resistivity through the Bardeen- Stephen equation, $\rho_{ff} = \rho_n(B/B_{c2})$. Hence, ρ_0 is proportional to ρ_n. Therefore,

$$\rho = \rho_n \left| \frac{T}{T_g} - 1 \right|^s \tag{7.3}$$

The influence of a magnetic field on the glass transition cannot be directly derived from the glass scaling theory. It is instead usually introduced through the behavior of the coherence length in the zero-field fluctuation regime [Fisher et al. (1991)]. A consistent and more complete description of the resistivity can be achieved by introducing a modified expression for ξ_g, without affecting the general ideas of a vortex glass. The present chapter describes a modified model for scaling the vortex liquid resistivity of **HTS** by the introduction of the modified ξ_g. Here it is referred that the vortex glass as a state separated from the vortex liquid

through a second order phase transition displaying glass scaling. Also, it is proposed that the driving force of the glass transition is given by the energy difference $K_B T - U_0$, where U_0 is the current independent mean pinning energy, instead of the temperature difference $(T - T_g)$. This explains the position of the glass transition $B_g(T)$ in a simple way. The model is successfully applied to the measurements on RE-free and RE ($RE = Lu$, Ho, Eu, La and Ce) substituted $(Bi, Pb) - 2212$ superconductors. The implications on the dissipation in the vortex liquid state and on the critical current in the vortex solid state are also discussed.

7.2 The Model

For the vortex glass model presented in equation 7.3, the linear resistivity close to T_g mainly depends on the distance to T_g and the relevant energy scales are therefore $k_B T$ and $k_B T_g$. In a superconductor, however, energy scales as the condensation energy or the pinning energy are changing with both temperature and magnetic field. Therefore, as depicted in figure 7.1, one should consider the distance to the transition line $B_g(T)$ in the two-dimensional $B - T$ diagram instead of the one-dimensional distance to T_g at constant B. Similar effects are well known from corrections to the temperature dependence of the superconducting condensation energy close to B_{C2}. In a general description, we denote the relevant energy scale determining flux motion in the vortex liquid by $U_0(B, T)$. The linear resistivity caused by thermal fluctuations will be determined from the competition between $U_0(B, T)$ and the thermal energy, $k_B T$. In this picture, it is natural to assume that a specific resistivity level corresponds to a constant $U_0(B, T)/k_B T$, i.e., the resistivity scales as,

$$\frac{\rho}{\rho_n} = F\left(\frac{U_0(B, T)}{k_B T}\right)$$

(7.4)

Here, F is a scaling function and the normal state resistivity ρ_n is choosen as the characteristic resistivity. This is based both on the empirical results presented below and on the fact that any characteristic energy should be related to ρ_n in some way. The vortex solid-to-liquid transition then occurs when the two relevant energy scales are equal, i.e., when,

$$U_0(B,T) = k_B T_g \qquad (7.5)$$

Since disordered materials are discussed in the following, the transition temperature is denoted by T_g as for a glass transition. The main arguments could possibly be valid also for the resistivity above a melting transition. An interesting observation is that the proposed model directly suggests that a curve in the $B-T$ diagram containing points of equal resistivity should follow the same behavior as the vortex solid-to-liquid line. This gives a natural explanation of the experimental fact that a determination of the solid-to-liquid transition line by different experimental methods give similar result although some methods only correspond to a constant (low) resistivity level [Brandt et al. (1995)].
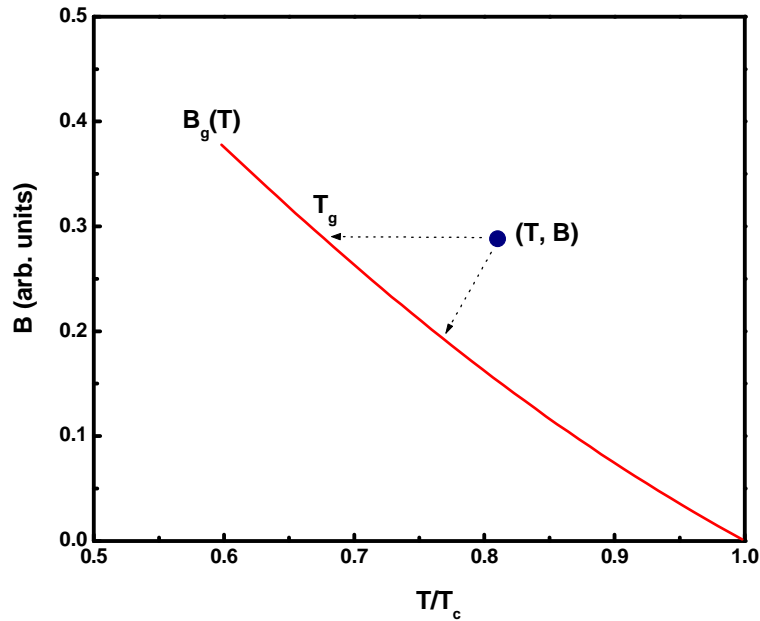

Figure 7.1: Sketch showing the principal physical idea behind the approach. The relevant energy scale, $U_0(B,T)$, at a specific point (T, B) in the vicinity of the vortex solid-to-liquid transition is determined by the distance to the transition line, $B_g(T)$, in a $B-T$ diagram. This is in contrast to other approaches, where only the temperature distance to T_g is taken into account.

The main difficulty is to find the explicit magnetic field and temperature dependence of U_0. In the following, an approach to do this for a vortex glass transition is presented. It should be noted here that differences from a conventional vortex glass model are rather subtle as far as the temperature dependence of the resistivity is concerned. In the present picture, the

characteristic energy $U_0(B,T)$ replaces the thermal energy at the glass transition line, $k_B T_g$, in the vortex glass expressions and thus, gives a more detailed description of the resistivity at temperatures away from T_g. Since U_0 is expected to be a slowly varying function of temperature and the resistivity disappears rapidly close to T_g, it may seem hard to observe any differences between these two models from experiments. However, such differences can be detected by plotting the experimental data in a proper way, as will be shown below. The main advantage of the present model is that it gives a consistent and detailed description of the magnetic field dependence of the resistive transition.

A direct consequence of the arguments above and equation (7.3) is that the resistivity close to a vortex glass transition, should be written as

$$\rho = \rho_n \left| \frac{k_B T}{U_0(B,T)} - 1 \right|^s \tag{7.6}$$

Where $U_0(B,T)$ has replaced $k_B T_g$ as the relevant energy scale. Now by solving the equation (7.6) for $U_0(B,T)$ one can obtain,

$$\left(\frac{U_0(B,T)}{k_B} \right) = T \left[1 + \left(\frac{\rho}{\rho_n} \right)^{\frac{1}{s}} \right]^{-1} \tag{7.7}$$

and $U_0(B,T)/k_B$ can be calculated directly from the experimental data provided one knows the critical exponent s and ρ_n.

To proceed, we note that a good scaling of the resistivity curves of disordered *HTS* can be obtained empirically by writing the effective pinning energy,

$$U_0(B,T) = \frac{k_B T_c}{(B/B_0)^\beta} \left[1 - \frac{T}{T_c} \right] = U_0(B) \left[1 - \frac{T}{T_c} \right] \tag{7.8}$$

Although, the exact interpretation of U_0 and the precise temperature and field dependencies are not completely clear, the form used in equation (7.8) is quite reasonable. Here, B_0 and β are temperature and magnetic field independent constants. Also along the zero resistance temperature $[T_g(B)]$ line,

$$B = B_0 \left[\frac{1-t}{t} \right]^{\alpha} \tag{7.9}$$

Here, $t = T_g / T_c$ and $\alpha = 1/\beta$, hence equation (7.9) becomes,

$$\left(\frac{B}{B_0} \right)^{\beta} = \left[\frac{T_c - T_g}{T_g} \right] \tag{7.10}$$

Now on substituting equation (7.10) in (7.8) one can obtain,

$$U_0(B,T) = \frac{k_B T_c T_g}{\left(T_c - T_g \right)} \left[1 - \frac{T}{T_c} \right] = U_0(B) \left[1 - \frac{T}{T_c} \right] \tag{7.11}$$

Now from equation (7.11), it is found that,

$$U_0(B) = \frac{k_B T_c T_g}{\left(T_c - T_g \right)} \tag{7.12}$$

and also in equation (7.11) the field dependence is implicit through the field dependence in $T_g(B)$. Now substituting equations (7.11) in (7.6) and simplifying, one can obtain the relation,

$$\rho = \rho_n \left| \frac{T(T_c - T_g)}{T_g(T_c - T)} - 1 \right|^{s} \tag{7.13}$$

and it will be very much useful for analyzing the experimental data. It should be noted that the field dependence of the resistivity only comes in through $T_g(B)$ in this relation.

From the similarities between the equations (7.3) and (7.6), it is clear that the description can be seen as a modification of the vortex glass theory. Let us therefore explore the consequences of these modifications and compare them with the existing theory to find the values of T_g and s. From equation (7.3) one directly obtains,

$$\left(\frac{\partial \ln \rho}{\partial T} \right)^{-1} = \frac{T - T_g}{s} \tag{7.14}$$

The usual way of extracting the vortex glass temperature (T_g) is to calculate the inverse of the logarithmic derivative of equation (7.3) from the experimental data (given in equation 7.14) and to extrapolate the plotted data to $(\partial \ln \rho / \partial T)^{-1} = 0$. But in the present approach, instead of equation (7.3), the equation (7.13) is used to find the logarithmic derivative and the following relation is obtained.

$$\left(\frac{\partial \ln \rho}{\partial T} \right)^{-1} = \frac{T - T_g}{s} \left(\frac{T_c - T}{T_c - T_g} \right)$$
(7.15)

The only difference between equations (7.14) and (7.15) is a factor $[(T_c - T)/(T_c - T_g)]$ which is nearly one for temperatures sufficiently close to T_g. Now, rearranging the terms in equation (7.15) one obtains,

$$\left(\frac{\partial \ln \rho}{\partial T} \right)^{-1} \left(\frac{T_c - T_g}{T_c - T} \right) = \frac{T - T_g}{s}$$
(7.16)

Now, extrapolate the plotted data to $(\partial \ln \rho / \partial T)^{-1} \left[(T_c - T_g)/(T_c - T) \right] = 0$ in order to obtain T_g. The slope for the linear portion closer to T_g directly gives the value of $1/s$ and hence the value of s is directly determined. Equation (7.13) also predicts a scaling behavior between the normalized resistivity, ρ/ρ_n, and the scaled temperature $[T(T_c - T_g)/T_g(T_c - T)] - 1$, with $T_g = T_g(B)$. The slope of the curve give the critical exponent s. Also the normal state resistivity ρ_n is determined by the linear extrapolation of the zero-field resistivity plot to zero.

7.3 Experimental details

RE-free $[(Bi_{1.6}Pb_{0.5})Sr_2Ca_{1.1}Cu_{2.1}O_{8+\delta}$ hereafter denoted as *RE*0.000] and *RE* (*RE* = *Lu*, *Ho*, *Eu*, *La and Ce*) substituted at the *Sr* site $[(Bi_{1.6}Pb_{0.5})(Sr_{2-x}RE_x)Ca_{1.1}Cu_{2.1}O_{8+\delta}$ hereafter denoted as *REx or SrREx* and x is the corresponding stoichiometry], *Bi* site $[(Bi_{1.525}Pb_{0.5}RE_{0.075})Sr_2Ca_{1.1}Cu_{2.1}O_{8+\delta}$ here after denoted as *BiREx*], at the *Ca* site $[(Bi_{1.6}Pb_{0.5})Sr_2(Ca_{1.025}RE_{0.075})Cu_{2.1}O_{8+\delta}$ here after denoted as *CaREx*], were prepared by solid state method. The details of sample preparation, characterization and measurements are the same as given in chapter 3.

7.4 In-field $\rho - T$ plots

The temperature dependence of the normalized resistivity plots of RE-free and RE substituted $(Bi, Pb) - 2212$ samples at different magnetic fields with in the range 0.2 and 1.5 T are shown in figure 7.2 $(a) - (f)$. Here, in the case of figures 7.2 $(a) - (d)$, the resistivity is measured for samples with different RE stoichiometry [dopant site same (Sr site) and the fixed magnetic field values used are 0.4, 0.8 and 1.2 T], in figure 7.2 (e), the resistivity is measured for different magnetic fields from 0.2 to 1.5 T [Keeping dopant site and stoichiometry remains same] and in 7.2 (f), dopant site varied [stoichiometry constant and the fixed magnetic field values used are 0.4, 0.8 and 1.2 T]. The downward curvature at the lowest temperatures indicates that a glassy regime is approached, which is characterized by a diverging activation energy (which will be discussed in detail in the subsequent sections) for flux motion and a truly zero resistivity is obtained below the field-dependent glass transition temperature $T_g(B)$. Using equation (7.6) the resistivity at the glass transition region can be represented as $\rho_g = \rho_n \left| k_B T / U_0(B,T) - 1 \right|^s = \rho_n \left| 1/x - 1 \right|^s$, where $x \equiv U_0(B,T)/k_B T$. The temperature and field dependence of $U_0(B,T)$ can be estimated from the measurements by considering constant resistivity levels in the glassy regime. For each such level, the above equation for ρ_g predicts the energy ratio x to be constant under the condition of linear resistivity. The relation between magnetic field and temperature should therefore be implicitly given by $x(\rho) = constant = U_0(B,T)/k_B T$ with $x = 1$ corresponding to the glass line and the upper limit of the studied glass scaling region is marked by a parabolic dotted black line in figure 7.2. Also in figure 7.2, a broadening of the resistive transition with an increase in magnetic field is obtained, which is a direct consequence of thermal fluctuations in the vortex system. The strong thermal fluctuation leads to melting of flux line lattice at a temperature, known as melting temperature (T_m) and below T_m, the vortex system is in superconducting vortex-solid phase with non-zero critical current, while at $T > T_m$, it is in dissipative vortex-liquid state. When disorder is introduced, the vortex-solid transforms into glassy vortex state. Also, depending on the type and strength of the disorder, different types of glassy-solid state (vortex-glass state in presence of point disorder and Boss-glass state in presence of correlated disorder) can be obtained. The linear resistivity disappears in all cases as a power law given by equation (7.2).
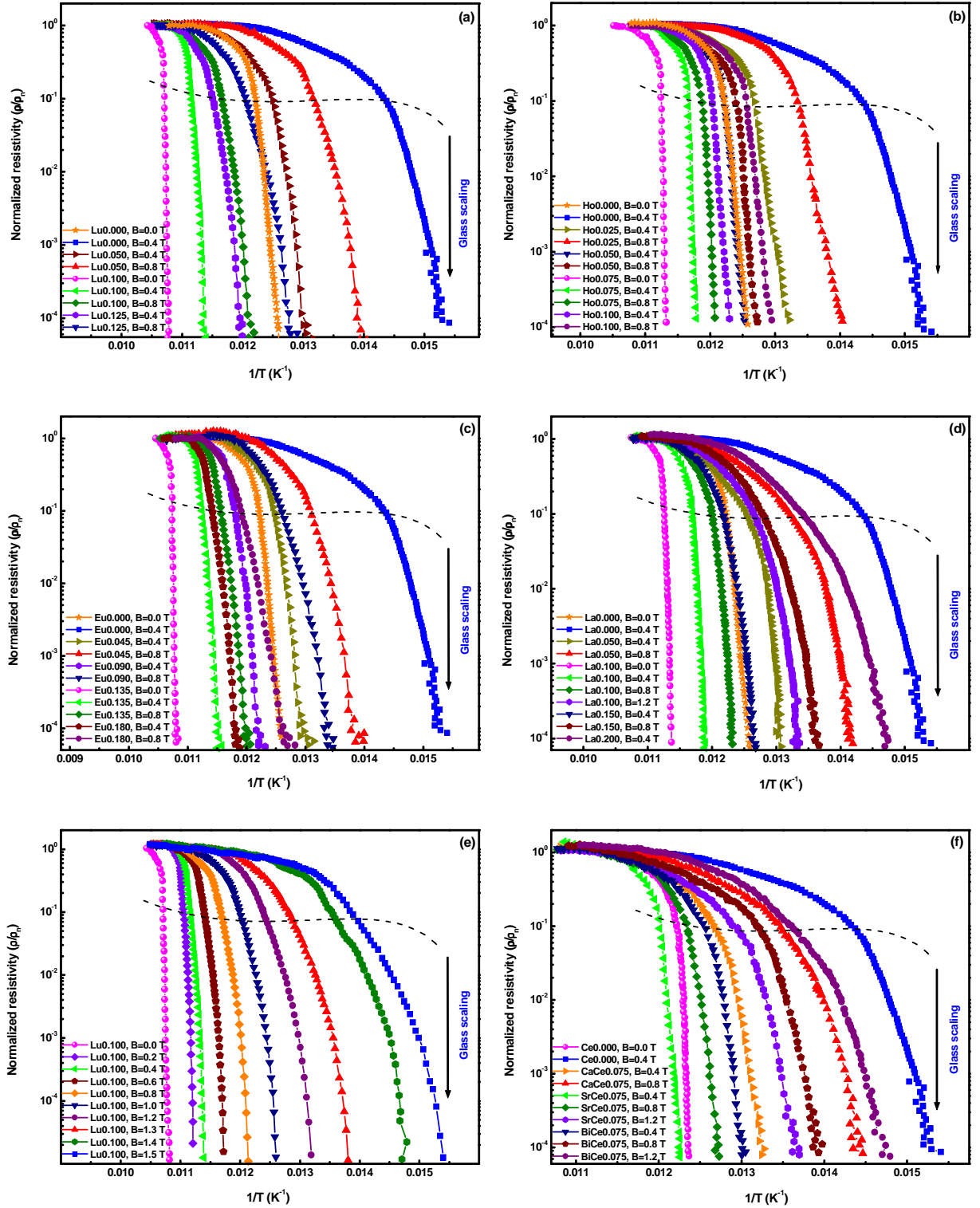
Figure 7.2 (*a*)−(*f*): **The temperature dependence of the normalized resistivity at different magnetic fields for** *RE*-**free and** *RE* **substituted** (*Bi*, *Pb*)−**2212 samples at different magnetic fields. Here, the zero-field plot is also given for comparison and the studied glass scaling region is marked by parabolic dotted (black) line.**
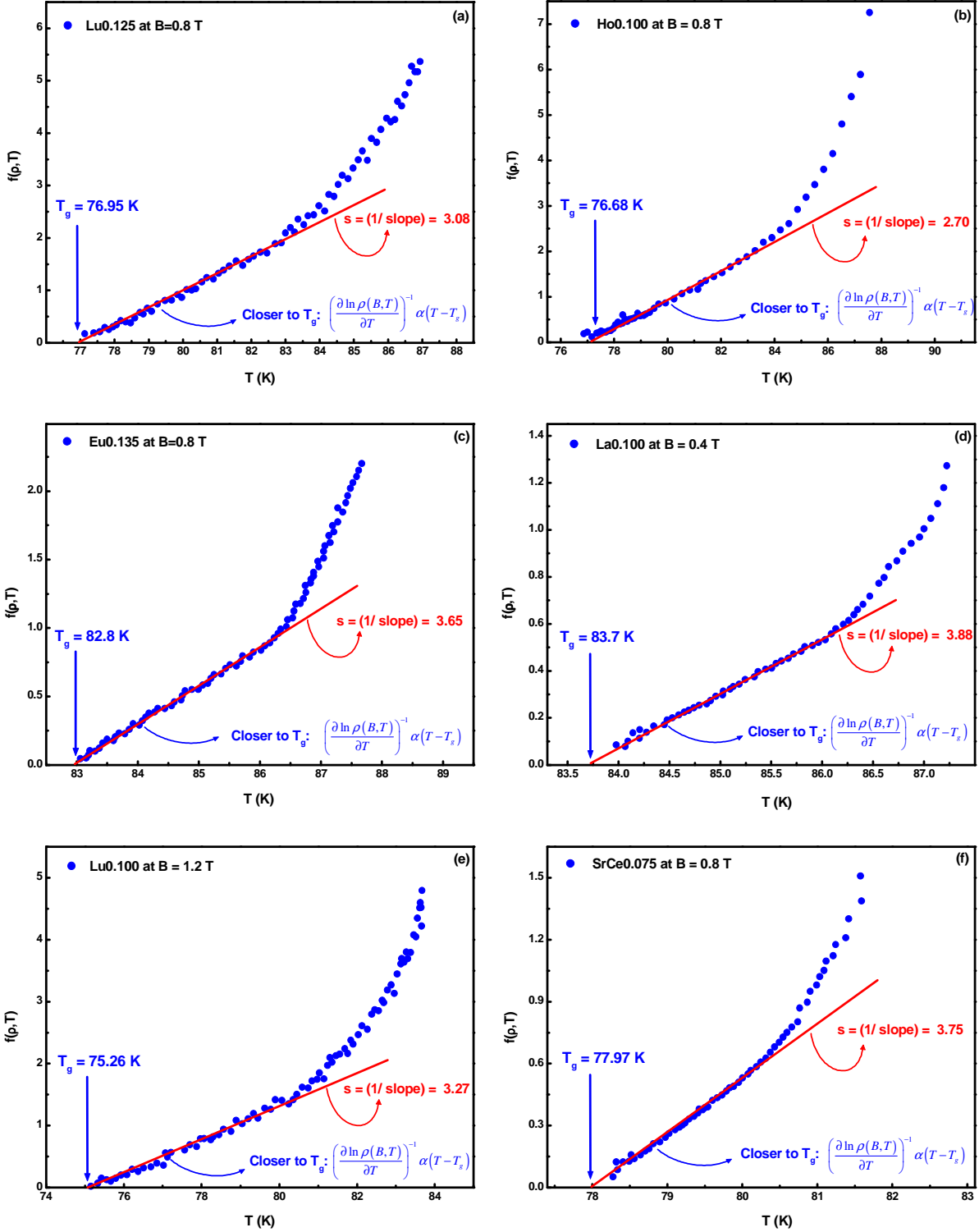
Figure 7.3 $(a) - (f)$**: Plot of** $f(\rho, T)$ **vs. T (Here,** $f(\rho, T) = (\partial \ln \rho / \partial T)^{-1}[(T_c - T_g)/(T_c - T)]$
and T_g **value is shown by arrow) and** s **value is determined from the linear portion closer to** T_g
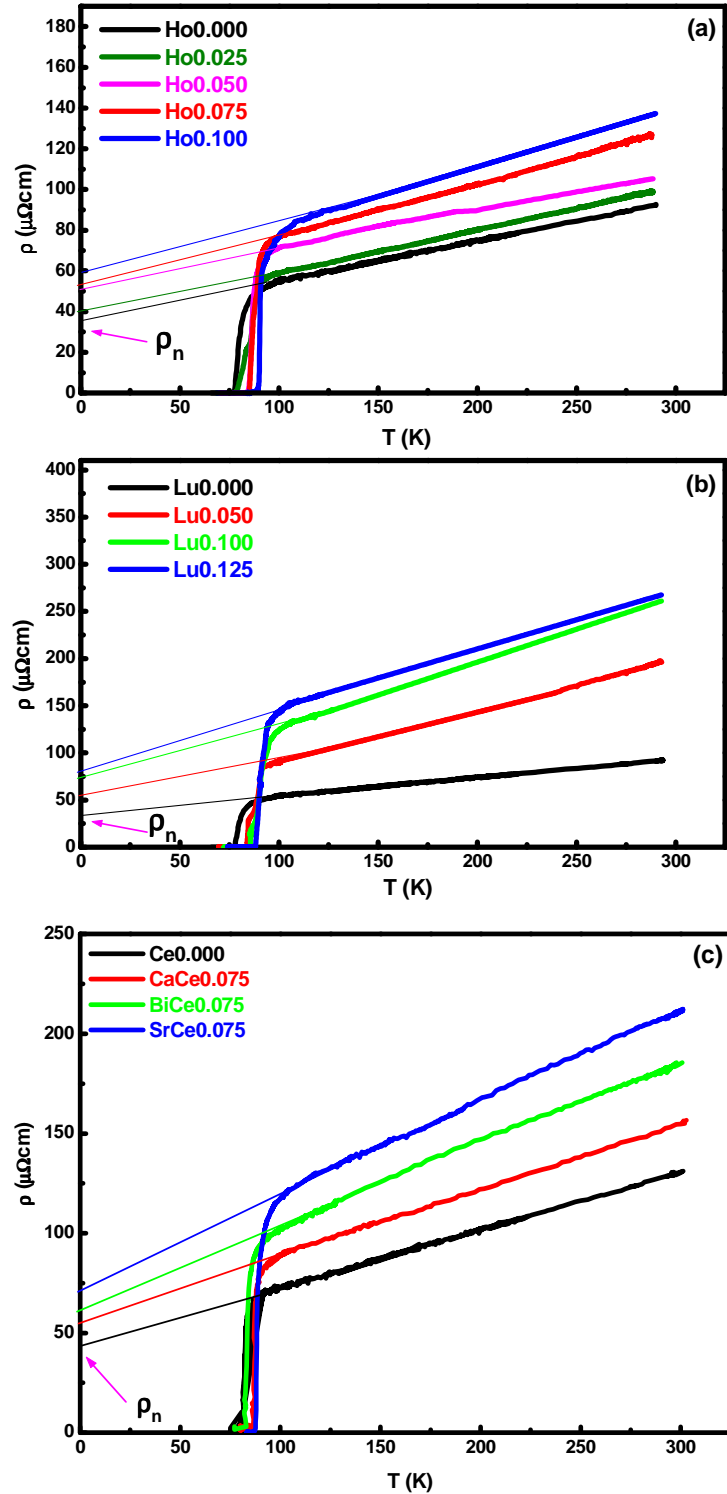$(s = 1/slope)$ **for the** RE **substituted samples.**

Figure 7.4 *(a)−(c)*: **The zero-field resistivity plot of typical *RE*-free and *RE* substituted $(Bi, Pb)−2212$ samples and it is extrapolated to zero to get the value of ρ_n.**

The linear resistivity caused by thermal fluctuations was determined from the competition between the characteristic energy $[U_0(B,T)]$ and the thermal energy $k_B T$. The vortex-solid to liquid transition occurs when $U_0(B,T) = k_B T_g$ as mentioned earlier and hence, the characteristic energy $U_0(B,T)$ replaces the thermal energy $(k_B T_g)$ at the glass transition line. Therefore the linear resistivity equation can be written as given in equation (7.6).

The parameter $U_0(B,T)$ is dependent on magnetic field and temperature, which is having a form of $U_0(B,T) = U_0(B)U_0(T)$. Here, $U_0(B)$ contains the magnetic field dependent part [equation 7.12] and $U_0(T)$ is a general function of temperature [equation 7.11]. Now, by solving the above linear resistivity equation for $U_0(B,T)$, equation (7.7) can be obtained, and using equation (7.7) the value of $U_0(B,T)$ can be calculated, provided $\rho_n(T)$ and the critical exponent s is known. In order to find the value of T_g, the relation $(\partial \ln \rho / \partial T)^{-1}[(T_c - T_g)/(T_c - T)] = (T - T_g)/s$ is used (equation 7.15) and hence, the graph between $(\partial \ln \rho / \partial T)^{-1}[(T_c - T_g)/(T_c - T)]$ vs. T is plotted using the experimental data and extrapolated the plotted data to $(\partial \ln \rho / \partial T)^{-1}[(T_c - T_g)/(T_c - T)] = 0$. Typical examples are given in Figure 7.3. To find the value of s, the inverse of slope for the linear portion closer to T_g can be calculated. Typical examples are also included in Figure 7.3. Also, the zero-field resistivity plot is extrapolated to zero for _RE_-free (x= 0.000) and the _RE_ substituted samples to get the value of ρ_n [Table 7.1 and figures 7.4 (a) – (c)].

The variation of T_c with _RE_-content is given in table 7.1. It shows that the T_c value gradually increases from 80.7 K (_RE_-free sample) to 94.4 K (_Eu_0.180) with increasing the amount of x value and the maximum value of T_c depends on the specific _RE_ substituted. Doping of each _RE_ atom in $(Bi, Pb) - 2212$ supplies additional elections to the system due to the higher valence state of _RE_, which reduces the number of holes and thus shifts the system from the 'over-doped' state to 'optimally doped' condition, as far as the hole carrier density is concerned. The attainment of optimum hole concentration is responsible for the enhancement of T_c. Figure $7.3(a) - (f)$ and table 7.1 show the variation of T_g and s values as a function of _RE_-content at different magnetic fields. It shows that, the T_g value gradually increase up to an

Table 7.1: **The rare-earth (RE) stoichiometry (x), critical temperature (T_c), the normal state resistivity (ρ_n), T_g, and s values for RE-free and RE substituted $(Bi, Pb) - 2212$ superconductors.**

RE	x	T_c from RT plot	T_c from figure 7.5	ρ_n Using fig. 7.4	T_g using the method given in figure 7.3 (± 0.05 K)			s using the method given in figure 7.3 (± 0.07 K)		
		(± 0.1) K	(± 0.05) K	(μΩcm)	0.4 T	0.8 T	1.2 T	0.4 T	0.8 T	1.2 T
RE-free	0.000	80.7	80.78	39.81	65.63	--	--	2.39	--	--
	0.050	86.5	86.62	55.43	75.66	71.13	--	2.93	2.95	--
Lu	0.100	93.0	93.17	73.36	87.73	82.11	--	3.27	3.31	--
	0.125	94.2	94.46	79.51	83.25	76.99	--	3.11	3.08	--
	0.025	82.6	84.51	40.05	75.80	70.83	--	2.55	2.52	--
Ho	0.050	87.7	87.68	50.83	79.58	78.33	--	2.79	2.75	--
	0.075	88.5	88.45	53.61	84.35	82.89	--	2.93	2.91	--
	0.100	91.6	91.63	57.69	81.50	76.68	--	2.75	2.7	--
	0.045	86.8	86.75	65.75	77.03	71.81	--	3.05	3.02	--
Eu	0.090	90.9	90.97	69.12	81.61	73.95	--	3.21	3.24	--
	0.135	93.3	93.33	72.85	86.42	82.82	--	3.67	3.65	--
	0.180	94.4	94.35	76.33	84.04	78.64	--	3.49	3.44	--
	0.050	85.7	85.32	66.34	75.94	69.83	--	3.62	3.59	--
La	0.100	88.6	88.74	76.92	83.72	80.62	73.83	3.88	3.85	3.90
	0.150	90.6	90.51	85.57	78.24	72.24	--	3.71	3.66	--
	0.200	92.3	92.28	90.14	67.21	--	--	3.24	--	--
$SrCe$	0.075	87.3	87.41	72.11	81.15	77.97	72.10	3.74	3.75	3.73
$CaCe$	0.075	86.8	86.75	55.04	74.57	68.03	--	3.72	3.76	--
$BiCe$	0.075	84.7	84.12	61.13	76.56	71.21	66.93	3.71	3.73	3.74

RE	B	T_c from RT plot	T_c from figure 7.5	ρ_n Using fig. 7.4	T_g using the method given in figure 7.3	s using the method given in figure 7.3
	T	(± 0.1) K	(± 0.05) K	(μΩcm)	(± 0.05) K	(± 0.07) K
	0.2	93.0	93.17	73.36	89.04	3.25
	0.4	93.0	93.17	73.36	87.57	3.27
	0.6	93.0	93.17	73.36	85.09	3.25
	0.8	93.0	93.17	73.36	82.12	3.23
Lu 0.100	1.0	93.0	93.17	73.36	78.83	3.28
	1.2	93.0	93.17	73.36	75.23	3.27
	1.3	93.0	93.17	73.36	71.76	3.25
	1.4	93.0	93.17	73.36	67.39	3.28
	1.5	93.0	93.17	73.36	64.14	3.24

optimum stoichiometry (*Lu*0.100, *Ho*0.075, *Eu*0.135, *La*0.100, *SrCe*0.075) and then decreases. The *s* values are found to be identical irrespective of the magnetic field; i.e., the *s* value is independent of the applied magnetic field. Since the T_g value is maximum for *Lu*0.100, *Ho*0.075, *Eu*0.135, *La*0.100 *and SrCe*0.075, the flux lines are in glass state and the flux pinning strength is maximum for these sample, i.e., the flux lines are effectively pinned in these samples.

7.5 *T* and *B* dependent activation energy

The calculated temperature and magnetic field dependent pinning energy $[U_0(B,T)]$ using equation (7.7) in Kelvin scale is shown in figure $7.5(a)-(f)$ which shows that the pinning energy of optimally *RE* substituted samples (*Lu*0.100, *Ho*0.075, *Eu*0.135, *La*0.100 *and SrCe*0.075) increases noticeably compared to *RE*-free sample (not a superconductor at T = 64 K and B = 0.8 T) and other *RE* substituted samples. A striking feature is the linear behavior of $U_0(B,T)$ at the temperature close to T_g and it is found that on extrapolating this linear behavior for different magnetic fields, the entire lines corresponding to each stoichiometry merge at a point $T = T_c$ [figure 7.5 (e)] and at this point the value of $U_0(B,T)$ is found to be zero. Also, this linear portion well obeys the equation $U_0(B,T) = U_0(B)(1 - T/T_c)$ with a magnetic field dependent $U_0(B)$ as given in equation (7.11). Furthermore, T_g can be directly obtained from figure 7.5 by considering the crossing points of the lines $U_0(B,T)$ and the solid line $k_B T$, which is the criterion used for finding T_g in equation (7.5). It is therefore concluded that figure 7.5 is a strong evidence for the validity of this modified model. Also the above calculated T_c and T_g values well agree with the values given in table 7.1.

Another important point is that the temperature dependence of $U_0(B,T)$ illustrated by figure $7.5(e)$ directly shows that the ordinary vortex glass expression is insufficient for describing the data. For an ordinary vortex glass model, one expects a horizontal line since equation (7.2) implies a constant $U_0(B) = k_B T_g(B)$ at all temperatures close to T_g. This is obviously not the case as described in figure 7.5.
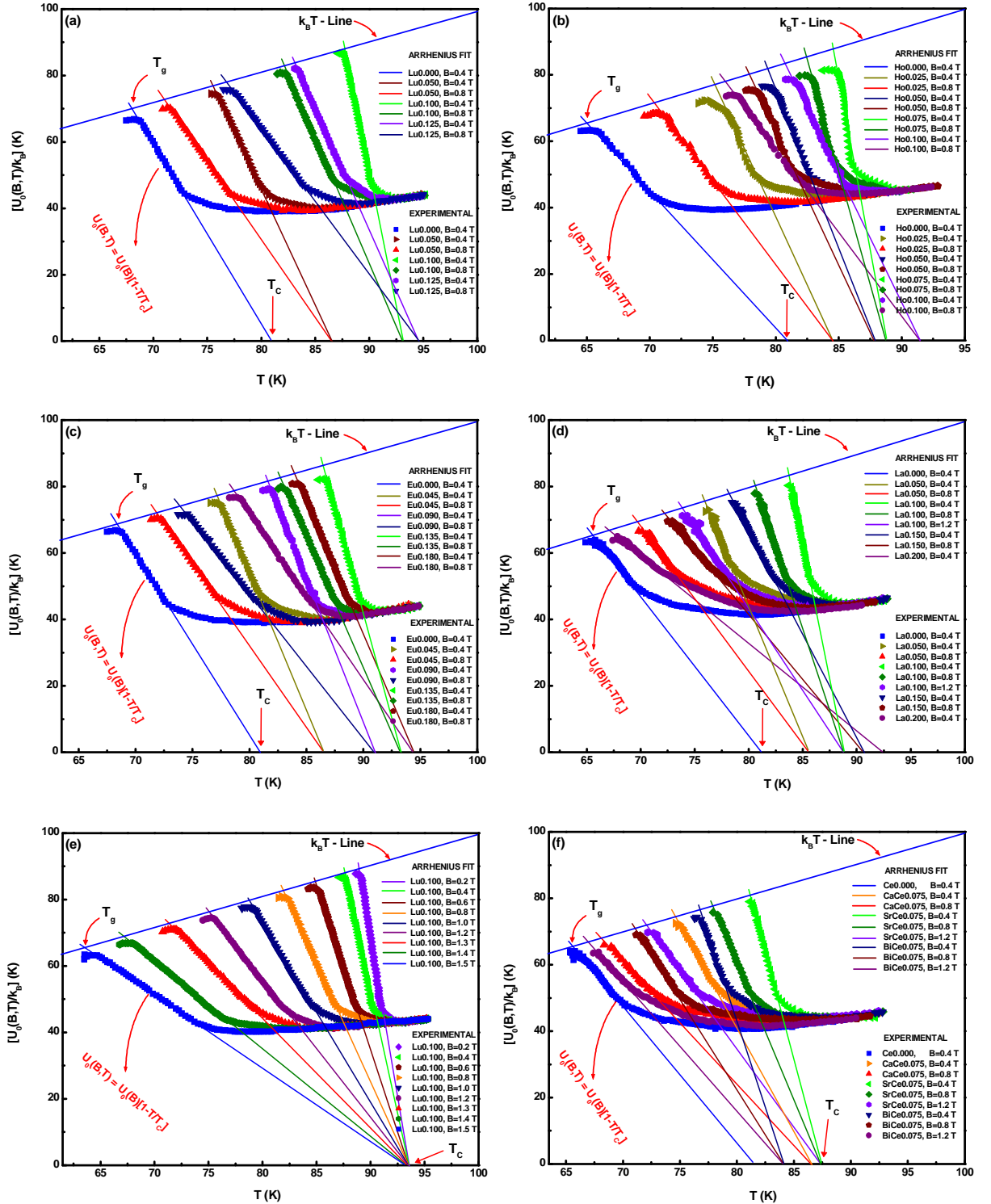
Figure 7.5 *(a)−(f):* **The energy** $U_0(B,T)/k_B$ **determined from equation (7.7) for all samples at different magnetic fields. As shown by the solid lines, the low resistivity parts of the curves are well described by equation (7.11) with a magnetic field dependent** $U_0(B)$**. The** T_g **value is obtained when** $U_0(B,T)$ **crosses the solid line** $k_B T$ **and the** $X-$**intercept gives the value of** T_c**.**

7.6 *B* dependent activation energy
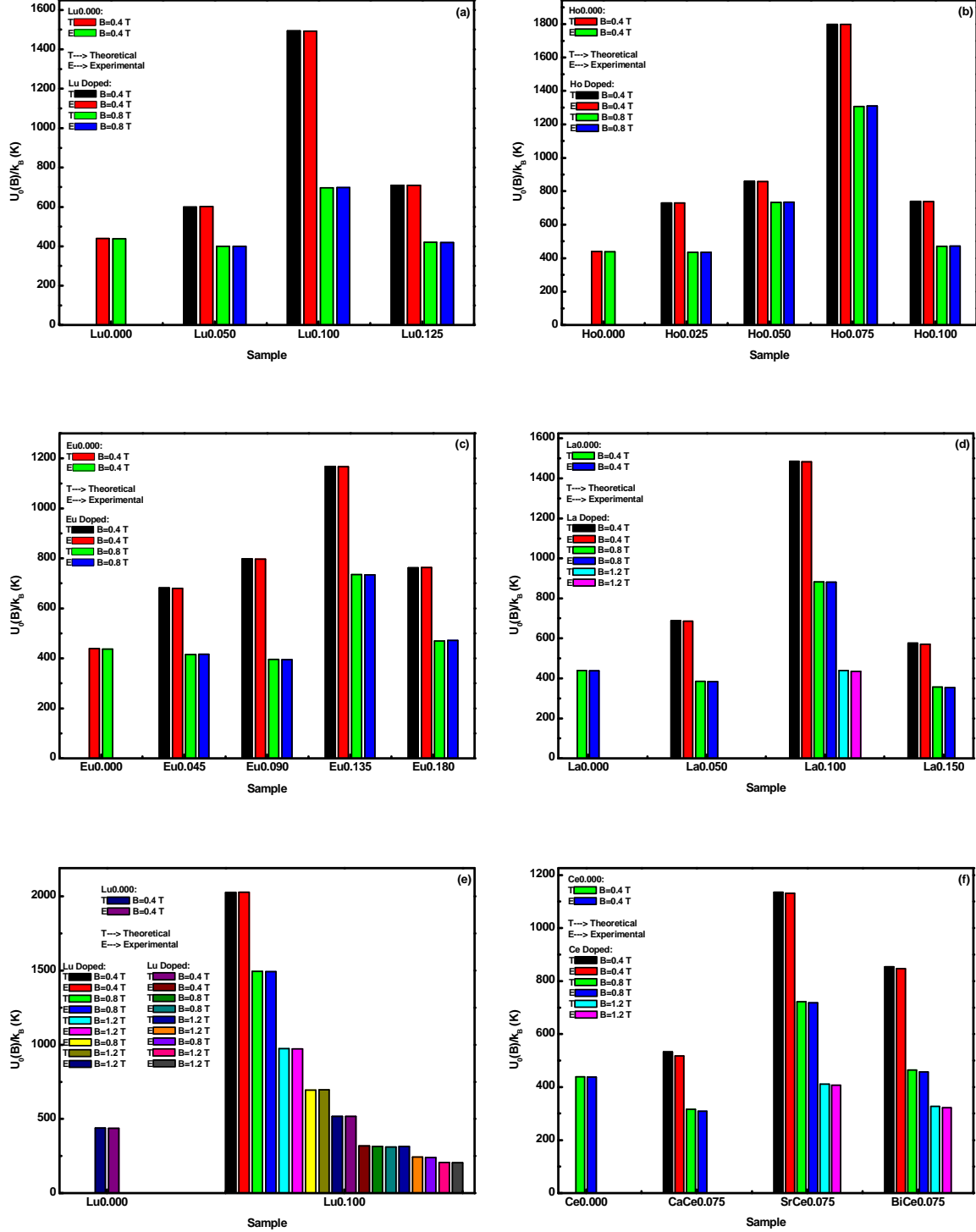
Figure 7.6 (a)–(f): The $U_0(B)$ values of RE-free and RE substituted $(Bi, Pb) - 2212$ samples calculated using the equation $U_0(B) = k_B T_c T_g / (T_c - T_g)$ (theoretical) and from the slopes of figure 7.5 (experimental). The peak values are given in table 7.2. For RE-free and certain RE substituted samples the plots at higher magnetic fields are not included because of poor performance at 64 K.

Table 7.2: **The magnetic field dependent activation energy [$U_0(B)$] values of RE-free and RE substituted $(Bi,Pb)-2212$ superconductors.**

RE	x	$U_0(B)/k_B$ determined from the slopes of figure 7.5 (Experimental) (K)			$U_0(B)/k_B = T_c T_g/(T_c - T_g)$ using equation (7.12) (Theoretical) (K)		
		0.4 T	0.8 T	1.2 T	0.4 T	0.8 T	1.2 T
RE-free	0.000	437.6	--	--	439.1	--	--
Lu	0.050	601.8	399.3	--	599.3	398.7	--
	0.100	1493.1	698.2	--	1493.9	697.5	--
	0.125	708.6	418.9	--	709.5	420.2	--
Ho	0.025	730.2	433.5	--	728.7	435.1	--
	0.050	857.8	735.7	--	859.5	733.1	--
	0.075	1799.3	1309.8	--	1798.7	1307.6	--
	0.100	738.6	472.1	--	739.1	470.7	--
Eu	0.045	679.8	415.4	--	682	415.4	--
	0.090	797.1	395.1	--	797.5	395.1	--
	0.135	1166.9	735.7	--	1168.2	735.7	--
	0.180	763.5	469.6	--	762.4	469.6	--
La	0.050	685.2	382.8	--	688.7	384.1	--
	0.100	1482.9	881.3	435.6	1484.8	882.6	439.3
	0.150	571.5	353.2	--	575.3	357.1	--
	0.200	243.6	--	--	247.8	--	--
SrCe	0.075	1130.3	717.5	407.3	1134.8	722.6	411.8
CaCe	0.075	517.4	308.6	--	532.9	315.9	--
BiCe	0.075	846.8	457.6	321.8	853.9	464.6	327.8

RE	B	$U_0(B)/k_B$ determined from the slopes of fig. 7.5 (Experimental)	$U_0(B)/k_B = T_c T_g/(T_c - T_g)$ using equn. (7.12) (Theoretical)
	T	K	K
Lu 0.100	0.2	2027.5	2026.1
	0.4	1492.6	1494.3
	0.6	971.9	974.3
	0.8	696.2	694.1
	1.0	517.8	516.0
	1.2	315.4	317.4
	1.3	313.4	310.9
	1.4	240.1	242.9
	1.5	204.9	207.5

From equation (7.11), it is clear that the field dependence only comes in through the term $U_0(B)$. The magnetic field dependent activation energy $U_0(B)$ calculated directly from the slopes of the linear portion of $U_0(B,T)$ [figure 7.5] and the corresponding value calculated using the equation (7.12) at different magnetic fields (from 0.2 to 1.5 T) are given in table 7.2. The values of $U_0(B)$ calculated by both the ways, also agree well with each other and the optimally doped samples *Lu*0.100, *Ho*0.075, *Eu*0.135, *La*0.100 and *SrCe*0.075 show maximum value. This explains the strong pinning effect of vortices in these samples. Also, the high $U_0(B,T)$ values of *Lu*0.100, *Ho*0.075, *Eu*0.135, *La*0.100, *SrCe*0.075 and other *RE* substituted samples justify the shifting of the irreversibility line of the *RE* substituted samples to higher temperatures and magnetic fields compared to the *RE*-free sample. The crystal defects created due to the *Pb* doping in $Bi-2212$ are mainly confined in the $Bi-$ layer, but the defects produced by *RE* substitution are mainly in the $Sr-$ layer. The vortices are confined in the CuO_2 layers, which are closer to the $Sr-$ layer than the $Bi-$ layers. Thus, it is likely that the strongly coupled vortices in the CuO_2 layer are effectively pinned by the defects in the nearer $Sr-$ layer than the defects produced in the distant $Bi-$ layer. This is attributed to the enhanced pinning and the unusually high activation energy values of *RE* substituted $(Bi,Pb)-2212$ superconductor.

7.7 Scaling of the resistivity curves

Another important feature is that equation (7.13) predicts a scaling behavior between the normalized resistivity, $\rho(B,T)/\rho_n$, and the scaled temperature $[T(T_c-T_g)/T_g(T_c-T)]-1$ with $T_g = T_g(B)$. Such a scaling is shown in figures 7.7 – 7.10, where the resistive transitions at different magnetic fields have been scaled onto one curve. From the corresponding slopes (the linear portion indicated by solid line) in figure 7.7 – 7.10, the values of critical exponent s for all the samples are found and these are in good agreement with the values given in table 7.1. This scaling behavior indicates that the temperature dependent resistivity under various magnetic fields can be described with equation (7.6) in the regime of $T_g < T \leq T_c$. Also, an interesting point is that the scaling also works for temperatures close to T_c, although we begin

the discussion for temperatures close to T_g. This clearly indicates that the arguments used here are of fundamental nature for understanding the full behavior of the vortex-liquid.
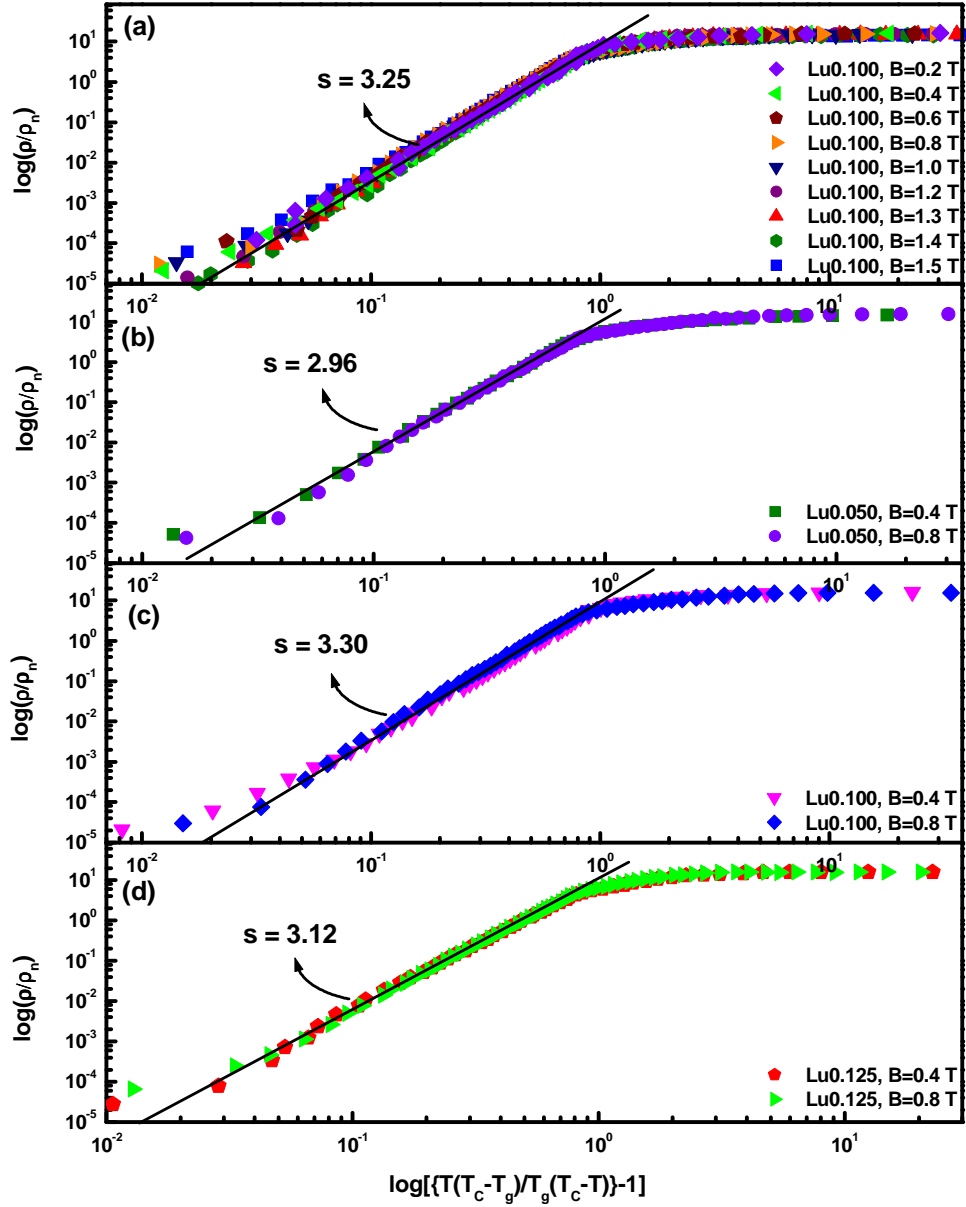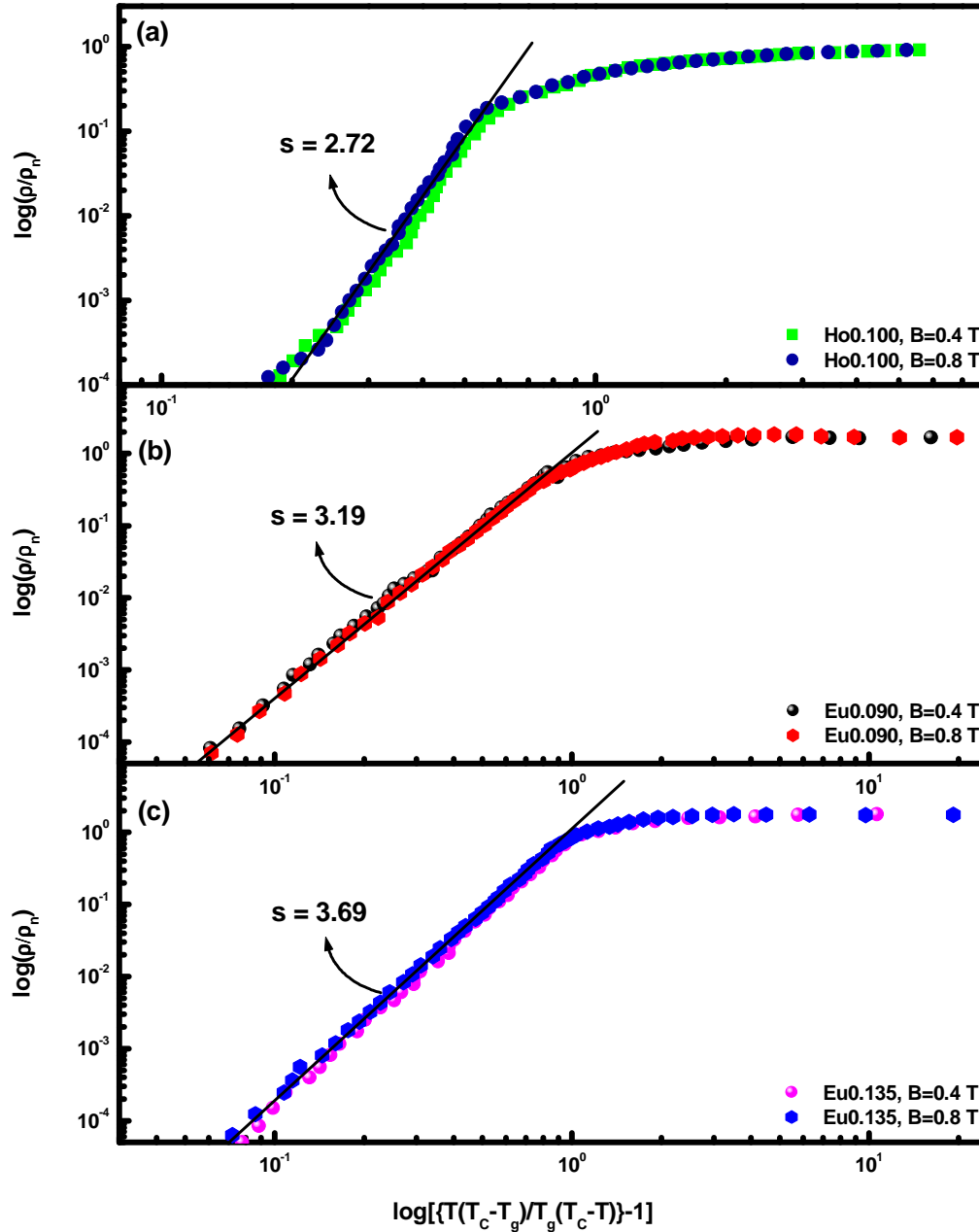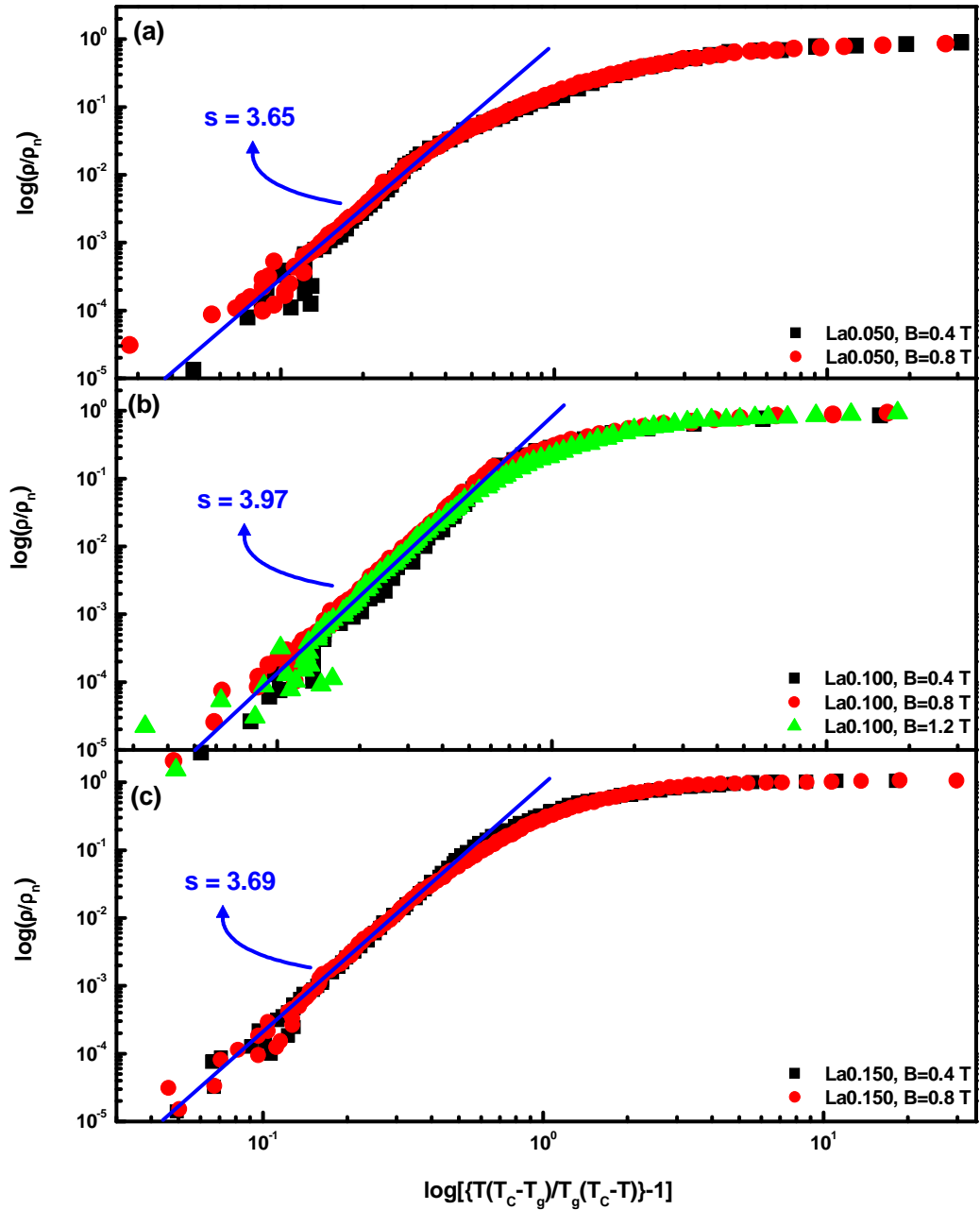

Figure 7.7: **Scaling of the normalized resistivity, $\rho(B,T)/\rho_n$, curves for the samples (a) Lu0.100 at B = 0.2 to 1.5 T, (b) Lu0.050 at B = 0.4 and 0.8 T, (c) Lu0.100 at B = 0.4 and 0.8 T, (d) Lu0.125 at B = 0.4 and 0.8 T. The slope of the curve (the portion indicated by black solid line) gives the critical exponent, s. These values are in agreement with the values given in table 7.1.**
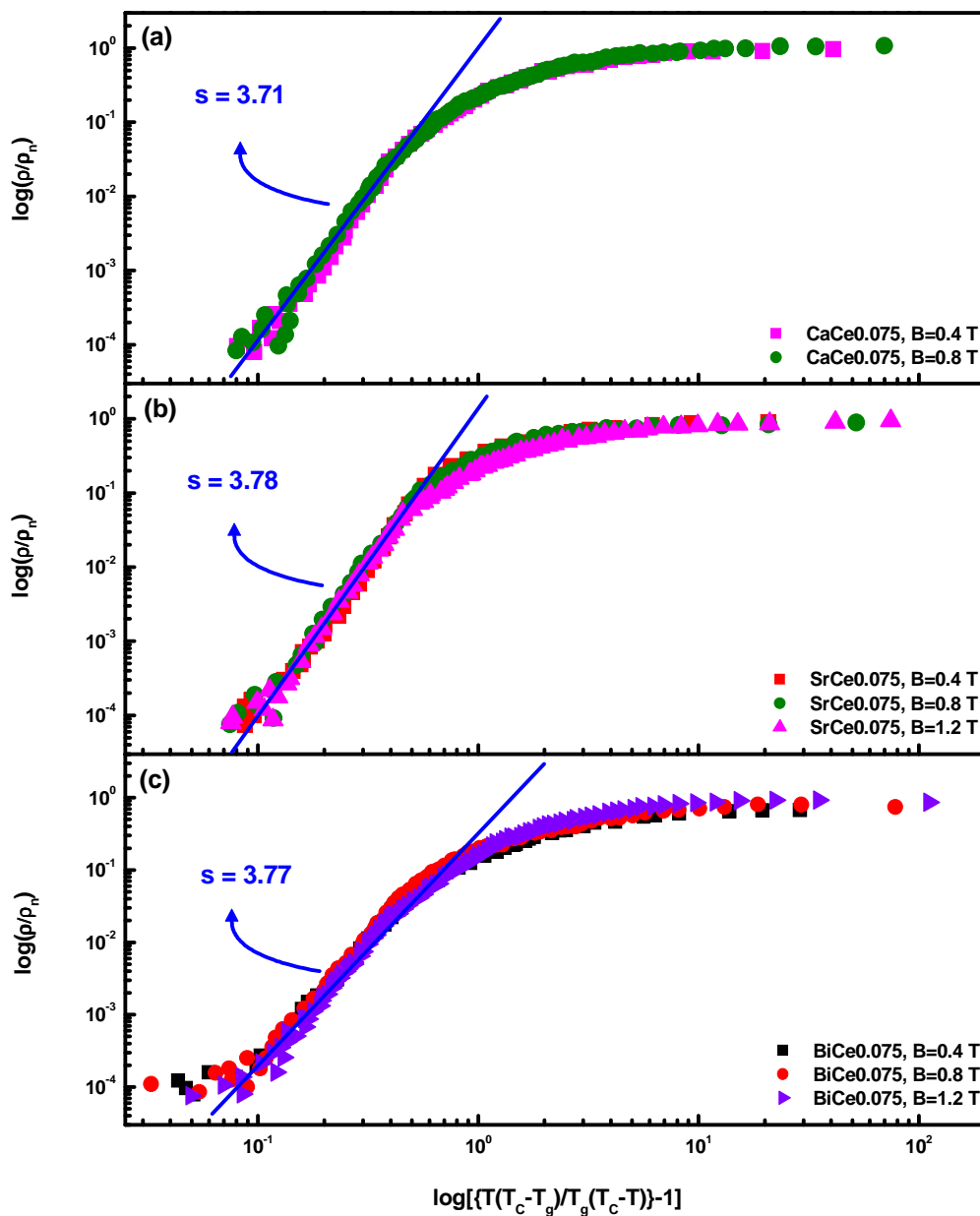
Figure 7.8: **Scaling of the normalized resistivity, $\rho(B, T)/\rho_n$, curves for the samples (a) Ho0.100 at B = 0.2 to 1.5 T, (b) Eu0.090 at B = 0.4 and 0.8 T, (c) Eu0.135 at B = 0.4 and 0.8 T. The slope of the curve (the portion indicated by black solid line) gives the critical exponent, s. These values are in agreement with the values given in table 7.1.**

Figure 7.9: Scaling of the normalized resistivity, $\rho(B, T)/\rho_n$, curves for the samples (a) La0.050 at B = 0.4 and 0.8 T, (b) La0.100 at B = 0.4, 0.8 and 1.2 T, (c) La0.150 at B = 0.4 and 0.8 T. The slope of the curve (the portion indicated by blue solid line) gives the critical exponent, s. These values are in agreement with the values given in table 7.1.

Figure 7.10: **Scaling of the normalized resistivity,** $\rho(B, T)/\rho_n$, **curves for the samples (a)
CaCe0.075 at B = 0.4 and 0.8 T, (b) SrCe0.075 at B = 0.4, 0.8 and 1.2 T, (c) BiCe0.075 at B = 0.4,
0.8 and 1.2 T. The slope of the curve (the portion indicated by blue solid line) gives the critical
exponent, s. These values are in agreement with the values given in table 7.1.**

7.8 Comparison of Arrhenius and modified vortex-glass model

The temperature and magnetic field dependent resistance transitions of RE-free and RE $(RE = La \ and \ Ce)$ substituted $(Bi, Pb) - 2212$ samples at different magnetic fields (0.0, 0.4, 0.8 and 1.2 T) are shown in figure 7.11 (a) and (b). The upper limit of the studied glass scaling region is marked by a blue dashed line and the solid lines in figure 7.11 (a) and (b) are the Arrhenius fits and these linear fits are based on the assumption of equation (7.11) and here the values of each $U_0(B)$ was determined from the corresponding slopes of $\ln \rho(B,T)$ *vs.* $1/T$ plot [based on the Arrhenius equation $\rho(B,T) = \rho_0 e^{-U_0/k_B T}$ from Anderson (1962) and Anderson et al. (1964)]. From figure 7.11 (a) and (b), it is found that the fits do not exactly coincide on the low resistive portion where the experimental data shows a deviation. Hence, the value of $U_0(B)$ determined from the slope does not give the exact value.

Figure 7.12 shows the graph between the magnetic field dependent apparent activation energy $[-\partial \ln \rho(B,T)/\partial(1/T)]$ and temperature (T) determined from the Arrhenius method for RE-free and RE $(RE = La \ and \ Ce)$ substituted $(Bi, Pb) - 2212$ samples at different fields. In the case of Ce substituted samples, the results show that the $-\partial \ln \rho(B,T)/\partial(1/T)$ values are better for $SrCe0.075$ than Ce-free and other Ce substituted $(BiCe0.075 \ and \ CaCe0.075)$ samples. Similarly for La substituted samples, $La0.100$ show the best result [which is given as a typical example in figure 7.11 (a)]. This shows that the magnetic field performance is very much improved for these samples [$SrCe0.075 \ and \ La0.100$] compared to the other RE substituted samples. Also in figure 7.12 (a) and (b), $U_0(B)$ $[U_0(B) = -\partial \ln \rho(B,T)/\partial(1/T)]$ plots have (red) horizontal solid lines, where each of them has a limited length. Each length covers the temperature interval which corresponds to the interval of the reciprocal temperature for determining $U_0(B)$ in the Arrhenius plot. In these figures, it is interesting to note that each $-\partial \ln \rho(B,T)/\partial(1/T)$ plot can be divided into five regions (indicated by red numerals). The first region is the normal state region at higher temperature, where $-\partial \ln \rho(B,T)/\partial(1/T)$ is almost temperature and magnetic field independent. The second region is the primary superconducting transition regime, where $-\partial \ln \rho(B,T)/\partial(1/T)$ quickly increases and the resistivity begin to decrease sharply (flux flow regime). The third region is a plateau region, where $-\partial \ln \rho(B,T)/\partial(1/T)$ for each field measurement shows a step structure, and possibly relate to
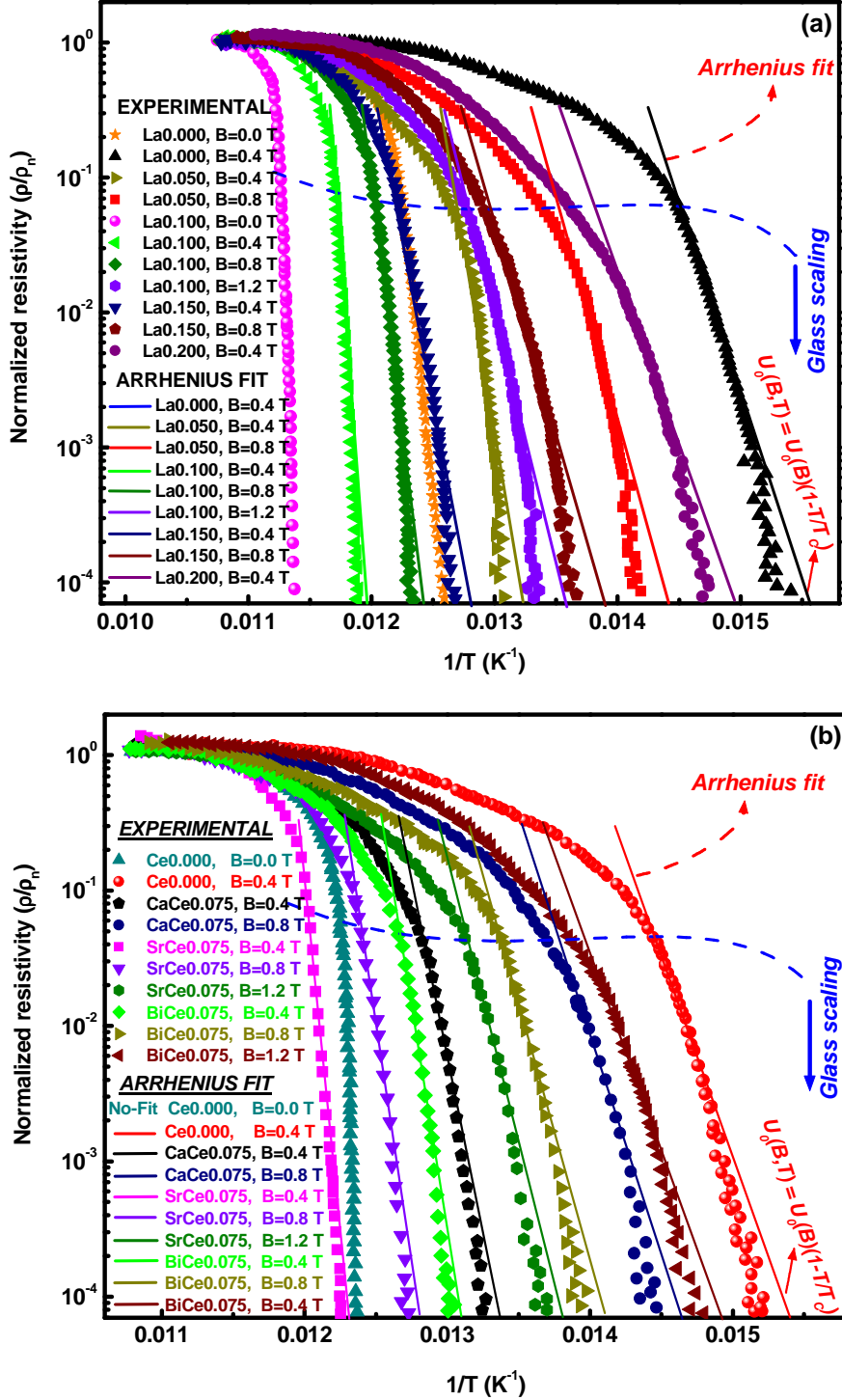
Figure 7.11 (a) and (b): The Arrhenius plot of the normalized resistivity, $\rho(B,T)/\rho_n$, of RE-free and all RE [(a) La and (b) Ce] substituted $(Bi,Pb)-2212$ superconductors at different magnetic fields. Here, the zero-field plot of $RE\,0.000$ is also given for comparison. The linear Arrhenius fits are based on equation (7.11) and $U_0(B)$ is determined from the corresponding slope.
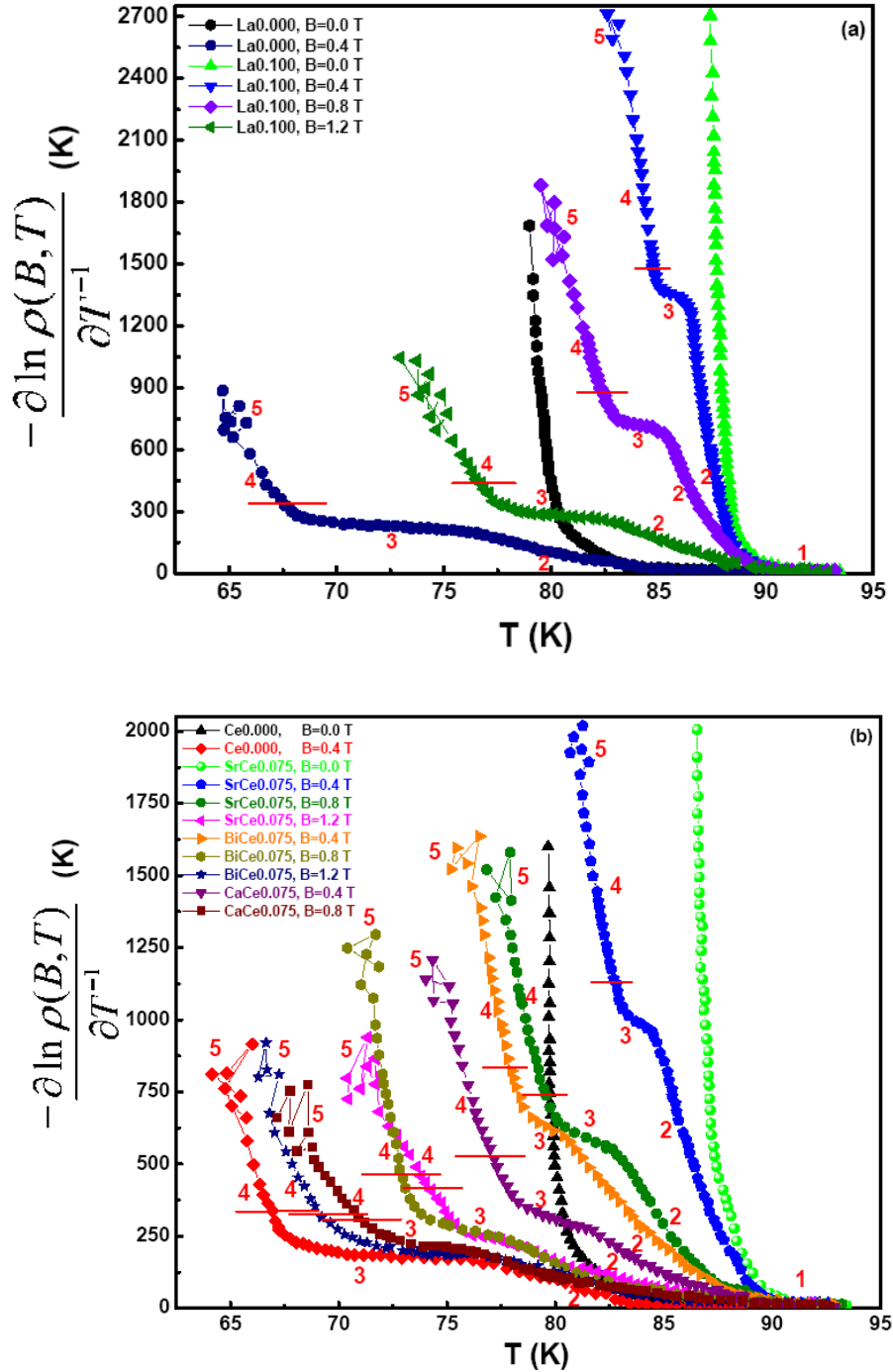
Figure 7.12 (*a*) *and* (*b*): Plot of $-\partial \ln \rho(B,T)/\partial(1/T)$ *vs.* *T* of *RE*-free and all *RE* [(*a*) *La and* (*b*) *Ce*] substituted (*Bi,Pb*) − 2212 samples at different magnetic fields. The $-\partial \ln \rho(B,T)/\partial(1/T)$ curve in the presence of magnetic fields is divided into five regions (indicated by red numerals) for *TAFF* analysis. The horizontal solid lines (red lines) with limited length represent the reciprocal temperature interval for determining $U_0(B)$ in the Arrhenius plot.

TAFF behavior. But the resistivity data in the third region are only about one order of magnitude less than that of region one, where the resistivity is in normal state. Therefore, it is concluded that the data in the third region are not in the *TAFF* regime. The fourth region is again a sharply increasing region, where $-\partial \ln \rho(B,T)/\partial(1/T)$ quickly increases. Also, in this region the resistivity values are about two to three orders of magnitude less than that in region one. Hence, the resistivity in this range is in the *TAFF* regime. The fifth region is a strongly fluctuating region, where the $-\partial \ln \rho(B,T)/\partial(1/T)$ curves show an irregular shape because the material is going to a strongly superconducting state and the resistivity reaches the lowest measurable range. The analysis concludes that the *TAFF* resistivity is in the fourth region. Also, according to the vortex glass transition theory, the linear ohmic resistivity vanishes based on the relation, $\rho \propto \left|T - T_g\right|^s$ [equation (7.3)]. This means that the plot of $[\partial \ln \rho(B,T)/\partial(T)]^{-1}(T_c - T_g)/T_g(T_c - T)$ *vs. T* should be a straight line (closer to T_g). The plots of inverse logarithmic derivative of the resistivity $[\partial \ln \rho(B,T)/\partial(T)]^{-1}(T_c - T_g)/T_g(T_c - T)$ *vs. T* of *RE* substituted samples are shown in figure 7.3, and this plot also shows linear curve in the low resistivity region (region four). Hence, the resistivity analysis based on equation 7.6 (obtained by vortex glass transition theory) is most suitable for the analysis of the resistivity data of the present case.

7.9 Conclusions

The thermally activated flux flow resistivity (*TAFF*) of *RE*-substituted $(Bi,Pb) - 2212$ superconductor has been discussed in detail with the help of two theoretical methods [(i) Arrhenius method and (ii) modified vortex-glass model]. The analysis of the resistivity data using the Arrhenius plot [figures 7.12 (a) and (b)] show that with decreasing temperature, the activation energy $U_0(B)$ initially shows a plateau region and subsequently changes to a divergent behavior which indicates the crossover from the Arrhenius to the vortex-glass regime. Again, the divergence of $U_0(B)$ is suppressed for *SrCe*0.075 and *La*0.100, which indicates that the critical region of the vortex-glass transition is enhanced by comparatively larger point defects produced due to the substitution of *Ce* and *La* atoms in the place of *Sr*. The vortex-glass model assumes that the vortex correlation length at the glass transition temperature is proportional to $\left|T - T_g\right|^{-\nu}$ and the linear resistivity vanishes according to the power law,

$\rho = \rho_n \left| T/T_g - 1 \right|^s$. By using the modified vortex-glass model, equations (7.6), (7.7) and (7.11) are obtained and the outcome of the analyses using these equations are in good agreement with the experimental data. In addition, the scaling analysis is shown to be applicable for the whole vortex-liquid regime of the *RE* substituted samples, and this clearly indicates that the arguments used here are of fundamental nature for the understanding of the full behavior of the vortex-liquid. Hence, the analysis of *TAFF* behavior in any high T_c superconductor using the modified vortex-glass model is highly advantageous over the Arrhenius method. Also, among the *RE* substituted samples, the optimally rare earth substituted samples (*Lu*0.100, *Ho*0.075, *Eu*0.135, *La*0.100 *and SrCe*0.075) show the best magnetic field performance and the reason for these improvements are mainly due to the creation of point defects due to the substitution of *RE* atoms at the *Sr* site as discussed in detail in the previous chapters. Again, among the cerium doped samples, *SrCe*0.075 shows the best in-field performance and hence, the flux flow resistivity is very much suppressed for this sample while *CaCe*0.075 shows the least. Thus, it is concluded that for magnetic field applications defects created at the *Sr* site is more influential than defects at *Bi or Ca* sites. The enhancement of superconducting and magnetic properties is discussed based on the variation of out-of-plane disorder, changes in the chemical as well as electronic inhomogeneities due to the substitution of *RE* atoms in the $(Bi, Pb) - 2212$ system.

Chapter 8

CHAPTER 8

Summary and future directions

8.1 Summary

The salient features of the thesis are summarized in this chapter. The compound used for the present study is $(Bi, Pb) - 2212$ and the *REs* used are (*i*) *Lutitium* (Lu), (*ii*) *Holmium* (Ho), (*iii*) *Dysprosium* (Dy), (*iv*) *Terbium* (Tb), (*v*) *Gadolinium* (Gd), (*vi*) *Europium* (Eu), (*vii*) *Cerium* (Ce), (*viii*) *Neodymium* (Nd) and (*ix*) *Lanthanum* (La). The objectives of the present work, as stated in section 1.6 of chapter 1 were to develop RE substituted $(Bi, Pb) - 2212$ superconductor with novel properties by proper selection of the RE, doping level, refining the processing parameters and microstructures and to investigate the effects of RE substitution on the structural and superconducting properties, suppression of flux creep, $n-$index, $E - J$ characteristics and temperature and magnetic field dependent activation energy values. Another important objective of the work was to scale the vortex liquid resistivity curves and to bring out the significance.

High temperature superconductors are mostly application oriented materials and have many superior superconducting properties over metallic low temperature superconductors. The role of RE substitution on the superconducting and flux pinning properties of Pb substituted $Bi - 2212$ superconductor $[(Bi, Pb) - 2212]$ has been studied since, it is an efficient tool to understand the underlying mechanism of high T_c superconductors. Earlier RE substitution studies in $Pb-$ free $Bi - 2212$ have shown that there is hardly any improvement in T_c or in the flux pinning properties and there is no work which reports the effect on J_C. In the present work, to evaluate the performance of the samples, various characterization techniques such as phase analysis, lattice parameter calculation and texture analysis by XRD, microstructural examination by SEM equipped with EDS and measurement of T_c, J_C, $J_C(B)$ and $E - J$. The main findings of the work are summarized below.

The structural and superconducting properties are studied for different RE concentrations in the range $0 < x < 0.5$ and the results are compared with the RE-free $(Bi, Pb) - 2212$ superconductor. Significant structural changes occur due to RE substitution and

these changes increase with increase in RE content. The systematic change in the lattice parameters together with the EDS analysis has shown the successful substitution of RE atoms in $(Bi, Pb) - 2212$ system. The maximum values of T_c as well as J_C are observed at different x ($x = 0.075 - 0.200$) values and as compared with the RE-free $(Bi, Pb) - 2212$ system, T_c improvements are in the range $13 - 16$ K and the J_C improvements are $8 - 11$ times depending on the substituted RE. The results show that T_c value systematically increases with decrease of hole carrier concentration (P). The increase in T_c as well as J_C is explained by the dual effect of the decrease in the hole concentration in CuO_2 planes from the over-doped to an optimally-doped state (as evidenced from the P value) and the improvement of coupling between the CuO_2 layers which is achieved by RE substitution. Beyond the optimum levels, the T_c gets reduced and an under-doped condition is attained due to reduced hole density, which triggers a metal to insulator transition in $(Bi, Pb) - 2212$ system.

The suppression of flux creep and flux pinning properties of RE (Lu, Ho, Dy, Tb, Gd and Eu) substituted $(Bi, Pb) - 2212$ system is analyzed in detail between the range $0 < x < 0.5$ and the results are compared with the RE-free $(Bi, Pb) - 2212$ system. The enhancement of flux pinning properties is evident from the highly improved $J_C(B)$ and normalized $J_C(B)$ characteristics. The $J_C(B)/J_C(0)$ value of optimally substituted sample is around 42 times greater than that of RE-free sample at 0.4 T and the similar trend is also observed for higher magnetic fields. The maximum values of bulk pinning force densities ($F_{P\max}$) of the RE substituted samples are found to shifts towards higher fields and temperatures and this means that the irreversibility line (IL) of the RE substituted samples shift towards higher fields and temperatures. Also, samples with $n > 15$ and $J < J_g$ show a glass-state for flux-lines, indicating their improved flux-pinning ability. The improved U_C values also support this. A correlation between $n -$ indices and J_C of RE substituted $(Bi, Pb) - 2212$ superconductor is also observed. The $J_C(B), F_P(B), E - J, U(J) - J$ characteristics are highly enhanced for RE substituted $(Bi, Pb) - 2212$ superconductors. Again a systematic dependence is observed between ionic radii of RE and the above mentioned properties. With increase of ionic radii from Lu to Eu, the maximum values of F_P, B_{irr},

$n-$index and U_C systematically increase (except for *Dy* and *Gd*). This again shows that larger defects at the *Sr* site is not desirable. The *Dy* and *Gd* substituted samples show deviations and this may be due to the higher dopant level. Also enhanced U_C and n values at applied fields under transport current flow show that the *RE* modified material is a promising candidate for magnetic applications. The pinning analysis clearly demonstrates that the substitution of *RE* in $(Bi, Pb)-2212$ superconductor drastically enhances its flux pinning strength at a relatively high temperature of 64 K by the introduction of point defects, which also contribute to the J_C of the *RE* substituted $(Bi, Pb)-2212$ superconductor.

Investigation on the effect of temperature on microstructure and flux pinning properties of *RE* (*Ho, Dy, Gd and La*) substituted $(Bi, Pb)-2212$ system show that the microstructural variations and flux pinning properties are highly temperature sensitive. The T_c value is found to be invariant with the sintering temperature for the same *RE* content. The enormous increase of self-field J_C of the samples (with same *RE* content) heat treated at optimum sintering temperatures is due to the microstructure refinement. While formation of disrupted grains with decreased texturing reduces the self-field J_C of the samples heat treated above or below the optimum sintering temperature (T_{opt}). The investigation of the microstructural and flux pinning properties of *RE* substituted $(Bi, Pb)-2212$ superconductors prepared at different temperatures ranging from 846 to 860 $^\circ C$ point towards the importance of fine tuning of heat treatment temperature in the preparation of *RE* substituted $(Bi, Pb)-2212$ superconductors to tailor their properties depending on different applications. For instance, the *RE* substituted samples prepared at comparatively lower sintering temperatures (846 – 850 $^\circ C$) are useful for magnetic field applications due to their better flux pinning properties. Whereas, the samples prepared at higher sintering temperatures (854 – 860 $^\circ C$) are useful for self-field applications due to their enhanced self-field current carrying capacity.

Studies on the effects of disorder at various out-of-plane lattice sites on the superconducting and flux pinning properties of *RE* substituted $(Bi, Pb)-2212$ system show that the self-field J_C and $J_C(B)$ characteristics of *RE* substituted samples are highly sensitive to the dopant site. The enhancement of flux pinning properties is evident from the improved $J_C(B)$ characteristics. Dew-Hughes pinning analysis, it is found that the peak position of F_P

appeared at $h = 0.33 \pm 0.03$ which shows that the main pinning mechanism is due to the point defects aroused out of the substitution of RE atoms at the respective cationic sites. Among the RE substituted samples, $SrRE$ exhibits the best $J_C(B)$ and the least self-field J_C, while $CaRE$ shows the least $J_C(B)$ and the best self-field J_C. This shows that for self-field application the defects at Ca site are desirable while for magnetic field application defects at Sr site are highly advantageous. It is also seen that the maximum value of $F_P/F_{P\max}$ of $SrRE$ appeared beyond 1.00 T as against 0.60 T for $CaRE$ and 0.24 T for $RE00$ at a comparatively higher temperature of 64 K. These results show that the irreversibility line of the RE substituted samples [especially $SrRE$] gets shifted towards higher magnetic fields and temperatures, and the flux pinning strength of RE substituted samples sensitively depends on the site in which RE is substituted. The enhancement of superconducting and flux pinning properties are discussed based on the variation of out-of-plane disorder, changes in the chemical as well as electronic inhomogeneities due to the substitution of RE atoms in the $(Bi, Pb) - 2212$ system.

The thermally activated flux flow ($TAFF$) resistive transition curves in magnetic fields of RE ($RE = Lu$, Ho, Eu, La and Ce) substituted $(Bi, Pb) - 2212$ superconductor is analyzed using both Arrhenius and modified vortex-glass model. The analysis of the resistivity data using the Arrhenius plot shows that with decreasing temperature, the activation energy $U_0(B)$ initially shows a plateau region and subsequently changes to a divergent behavior which indicates the crossover from the Arrhenius to the vortex-glass regime. Again, the divergence of $U_0(B)$ is suppressed for $SrRE$, which indicates that the critical region of the vortex-glass transition is enhanced by comparatively larger point defects produced due to the substitution of optimum amount of RE at Sr site of $(Bi, Pb) - 2212$ system. By using the modified vortex-glass model, the equations for ρ and $U_0(B,T)$ are obtained and the outcome of the analyses using these equations is in good agreement with the experimental data. In addition, the scaling analysis suggested from this model is shown to be applicable for the whole vortex-liquid regime of the RE substituted samples. Thus it is concluded that the analysis of $TAFF$ behavior in any high T_c superconductor using the modified vortex-glass model is highly advantageous over the Arrhenius method. Again, among the RE samples, $SrRE$ shows the best in-field performance and hence the flux flow resistivity is very much suppressed for this sample while $CaRE$ shows

the least. Thus it is concluded that for magnetic field applications defects created at the Sr site is more influential than defects at Bi or Ca sites. The highly enhanced temperature and magnetic field dependent activation energy at applied fields under transport current flow suggests that the RE modified $(Bi, Pb) - 2212$ superconducting materials are promising candidates for magnetic applications.

8.2 Scope for future directions

The present work reports the preparation of RE modified $(Bi, Pb) - 2212$ superconductors with highly enhanced T_c, self- and in-field J_C values analysis of flux creep and thermally activated flux flow and scaling of vortex liquid resistivity. At higher RE concentrations, the occurrence of the phenomenon known as metal to insulator transition (MIT) has been observed due to the large decrease in the hole carrier concentration and subsequent transformation of $(Bi, Pb) - 2212$ system into an extreme under-doped state. A systematic and a careful study of this unusual normal state property of $(Bi, Pb) - 2212$ system is necessary to understand its impact on high temperature superconductivity and to enlighten the mechanisms, since it can reveal the reason behind the origin of insulating states as well as the basic character of the metallic state induced by the cation substitution (RE). Future efforts may be directed towards the nano-structural aspects of the system and preparation of wires and tapes using the newly developed formulations, so that their highly improved superconducting properties can be exploited for conductor applications in self- and in-fields at a relatively high temperature of 64 K.

List of Publications

List of Publications

In SCI Journals:

[1]   **Vinu S**, Sarun P M, Shabna R and Syamaprasad U, "*Dissipative flux motion and flux flow resistivity analysis in La doped $(Bi, Pb) - 2212$ superconducting ceramics*", *J. Am. Ceram. Soc.* **94** (2011) 1634-1638.

[2]   **Vinu S**, Sarun P M, Shabna R, Biju A, Guruswamy P and Syamaprasad U, "*Microstructure and transport properties of $Bi_{1.6}Pb_{0.5}Sr_{2-x}Lu_xCa_{1.1}Cu_{2.1}O_{8+\delta}$ superconductor*", *Materials Chem. Phys.* **119** (2010) 135-139.

[3]   **Vinu S**, Sarun P M, Shabna R, Aswathy P M, Anooja J B and Syamaprasad U, "*Suppression of flux creep in $(Bi, Pb) - 2212$ superconductor by Holmium doping* ", *Physica B* **405** (2010) 4355-4359.

[4]   **Vinu S**, Sarun P M, Shabna R, Biju A and Syamaprasad U, "*Analysis of thermo-magnetic fluctuations in $Bi_{1.6}Pb_{0.5}Sr_{2-x}Lu_xCa_{1.1}Cu_{2.1}O_{8+\delta}$ $(0.000 \le x \le 0.125)$ superconductor*", *J. Alloy and Comp.* **487** (2009) 1-4.

[5]   **Vinu S**, Sarun P M, Shabna R and Syamaprasad U, "*Refinement of microstructure and highly improved electrical properties of $Bi_{1.6}Pb_{0.5}Sr_{1.925}Ho_{0.075}Ca_{1.1}Cu_{2.1}O_{8+\delta}$ superconductor*", *J. Appl. Phys.* **106** (2009) 063920.

(Selected for October 1, 2009 issue of Virtual journal of Applied Superconductivity, which is published by the American Institute of Physics and the American Physical Society)

[6]   **Vinu S**, Sarun P M, Shabna R and Syamaprasad U, "*Analysis of thermo-magnetic fluctuations above the glass-transition temperature in $Bi_{1.6}Pb_{0.5}Sr_{2-x}Eu_xCa_{1.1}Cu_{2.1}O_{8+\delta}$ $(0.000 \le x \le 0.180)$ system*", *Solid State Sci.* **11** (2009) 1530-1534.

[7] **Vinu S**, Sarun P M, Shabna R and Syamaprasad U, "*Erratum: Enhancement of critical current density and flux pinning properties of Gd -doped* $(Bi, Pb) - 2212$ *superconductor [J. Appl. Phys. 104, 043905 (2008)]*", *J. Appl. Phys.* **105** (2009) 129901.

(Selected for July 1, 2009 issue of Virtual journal of Applied Superconductivity, which is published by the American Institute of Physics and the American Physical Society)

[8] **Vinu S**, Sarun P M, Shabna R, Biju A and Syamaprasad U, "*Scaling of vortex-liquid resistivity and temperature and magnetic field dependent activation energy in Ho doped* $(Bi, Pb) - 2212$ *superconductor*", *J. Appl. Phys.* **105** (2009) 123901.

(Selected for July 1, 2009 issue of Virtual journal of Applied Superconductivity, which is published by the American Institute of Physics and the American Physical Society)

[9] **Vinu S**, Sarun P M, Shabna R, Biju A, Guruswamy P and Syamaprasad U, "*Influence of sintering temperature on microstructure, critical current density and pinning potential of superconducting* $Bi_{1.6}Pb_{0.5}Sr_{1.8}Dy_{0.2}Ca_{1.1}Cu_{2.1}O_{8+\delta}$ *ceramics*", *Solid State Sci.* **11** (2009) 1150-1155.

[10] **Vinu S**, Sarun P M, Shabna R, Biju A and Syamaprasad U, "*Enhancement of flux pinning and Anderson-Dew-Hughes pinning analysis in* $Bi_{1.6}Pb_{0.5}Sr_{2-x}Tb_x Ca_{1.1}Cu_{2.1}O_{8+\delta}$ *superconductor*", *J. Alloy and Comp.* **477** (2009) L13-16.

[11] **Vinu S**, Sarun P M, Shabna R, Biju A, Guruswamy P and Syamaprasad U, "*Effect of Dy substitution at the Sr -site on the critical current density and flux pinning properties of* $(Bi, Pb) - 2212$ *superconductor*", *J. Am. Ceram. Soc.* **11** (2008) 3585-3589.

[12] **Vinu S**, Sarun P M, Shabna R, Biju A and Syamaprasad U, "*Improved microstructure and flux pinning properties of Gd-substituted* $(Bi, Pb) - 2212$ *superconductor sintered between 846 and 860* $^\circ C$", *Mater. Lett.* **62** (2008) 4421-4424.

[13]   **Vinu S**, Sarun P M, Shabna R, Biju A and Syamaprasad U, "*Enhancement of critical current density and flux pinning properties of Gd-doped* $(Bi, Pb) - 2212$ *superconductor*", *J. Appl. Phys.* **104** (2008) 043905.

   (Selected for September 1, 2008 issue of Virtual journal of Applied Superconductivity, which is published by the American Institute of Physics and the American Physical Society)

[14]   **Vinu S**, Sarun P M, Shabna R, Biju A and Syamaprasad U, "The i*nfluence of sintering temperature on the microstructure and superconducting properties of* $Bi_{1.7}Pb_{0.4}Sr_{1.8}Nd_{0.2}Ca_{1.1}Cu_{2.1}O_{8+\delta}$ *superconductor*", *Supercond. Sci. Technol.* **21** (2008) 085010.

[15]   **Vinu S**, Sarun P M, Biju A, Shabna R, Guruswamy P and Syamaprasad U, "The e*ffect of substitution of Eu on the critical current density and flux pinning properties of* $(Bi, Pb) - 2212$ *superconductor*", *Supercond. Sci. Technol.* **21** (2008) 045001.

   (Included in the collection of 'FEATURED ARTICLE' in 2008)

[16]   Sarun P M, **Vinu S**, Shabna R and Syamaprasad U, "*Suppression of dissipative flux-motion in a high-T_c* $(Bi, Pb) - 2212$ *superconductor by Dy-doping*", *J. Alloy and Comp.* **497** (2010) 6-9.

[17]   Sarun P M, **Vinu S**, Shabna R, Aswathy P M, Anooja Babu J B and Syamaprasad U, "*Structural and transport properties of the* $Bi_{1.6}Pb_{0.5}Sr_{2-x}Lu_xCa_{1.1}Cu_{2.1}O_{8+\delta}$ *superconductor*", *IEE Trans. Appl. Phys.* **20** (2010) 61-65.

[18]   Sarun P M, **Vinu S**, Shabna R and Syamaprasad U, "Investigation of self- and in-field dependent n-value of Tb-doped $(Bi, Pb) - 2212$ superconductor", *J. Appl. Phys.* **106** (2009) 043910.

[19] Sarun P M, **Vinu S**, Shabna R, Biju A and Syamaprasad U, "*Properties of superconducting, polycrystalline dysprosium-doped* $Bi_{1.6}Pb_{0.5}Sr_{2-x}Dy_xCa_{1.1}Cu_{2.1}O_{8+\delta}$ $(0 \leq x \leq 0.5)$", *Mater. Res. Bull.* **44** (2009) 1017-1021.

[20] Sarun P M, **Vinu S**, Shabna R, Biju A and Syamaprasad U, "*Microstructural and superconducting properties of* Yb *-substituted* $(Bi,Pb)-2212$ *superconductor sintered at different temperatures*", *J. Alloy and Comp.* **472** (2009) 13-17.

[21] Sarun P M, **Vinu S,** Shabna R, Biju A, Guruswamy P and Syamaprasad U, "*Effect of sintering temperature on the microstructural and flux pinning characteristics of* $Bi_{1.6}Pb_{0.5}Sr_{1.8}La_{0.2}Ca_{1.1}Cu_{2.1}O_{8+\delta}$ *superconductor*", *J. Am. Ceram. Soc.* **92** (2009) 411-415.

[22] Sarun P M, **Vinu S**, Shabna R, Biju A, Guruswamy P and Syamaprasad U, "Influence of Ho -Doping on the Electromagnetic Field-Dependent $E-J$ Characteristics of $(Bi,Pb)-2212$ superconductor", *IEE Trans. Appl. Phys.* **19** (2009) 35-38.

[23] Sarun P M, **Vinu S**, Shabna R, Biju A and Syamaprasad U, "Highly enhanced superconducting properties of Eu -doped $(Bi,Pb)-2212$", *Mater. Lett.* **62** (2008) 2725-2728.

[24] Shabna R, Sarun P M, **Vinu S** and Syamaprasad U, "*Superconductor-metal-insulator crossover in* $Bi_{1.7}Pb_{0.4}Sr_{2-x}Ce_xCa_{1.1}Cu_{2.1}O_{8+\delta}$ $(0.2 \leq x \leq 0.6)$ *sintered between* $845 \,^{\circ}C \leq T_s \leq 865 \,^{\circ}C$", *Mater. Sci. Eng. B.* **172** (2010) 196-200.

[25] Shabna R, Sarun P M, **Vinu S** and Syamaprasad U, "*Charge carrier localization and metal to insulator transition in cerium substituted* $(Bi,Pb)-2212$ *superconductor*", *J. Alloy Comp.* **493** (2010) 11-16.

[26] Shabna R, Sarun P M, **Vinu S** and Syamaprasad U, "*Doping dependent metal to insulator transition in the* $(Bi,Pb)-2212$ *system: The evolution of structural and electronic properties with europium substitution*", *Chinese Phys B.* **18** (2009) 4000-4007.

[27]   Shabna R, Sarun P M, **Vinu S** and Syamaprasad U, "*Transport properties near the metal to insulator transition in samarium substituted $(Bi, Pb) - 2212$ system*", *J. Appl. Phys.* **105** (2009) 113925.

[28]   Shabna R, Sarun P M, **Vinu S**, Biju A and Syamaprasad U, "*Structural and electrical properties of $Bi_{1.7}Pb_{0.4}Sr_{2-x}Ho_xCa_{1.1}Cu_{2.1}O_{8+\delta}$ system across the metal to insulator transition*", *J. Alloy Comp.* **481** (2009) 797-801

[29]   Sarun P M, Shabna R, **Vinu S**, Biju A and Syamaprasad U, "*Highly enhanced superconducting properties of $Bi - 2212$ by Y and Pb co-doping*", *Physica B* **404** (2009) 1602-1606.

[30]   Shabna R, Sarun P M, **Vinu S**, Biju A and Syamaprasad U, "*Doping controlled metal to insulator transition in the $(Bi, Pb) - 2212$ system*", *Supercond. Sci. Technol.* **22** (2009) 045016.

[31]   Shabna R, Sarun P M, **Vinu S**, Biju A, Guruswamy P and Syamaprasad U, "*Metal-insulator transition and conduction mechanism in dysprosium doped $Bi_{1.7}Pb_{0.4}Sr_2Ca_{1.1}Cu_{2.1}O_{8+\delta}$ system*", *J. Appl. Phys.* **104** (2008) 013919.

[32]   Biju A, Sarun P M, **Vinu S**, Guruswamy P and Syamaprasad U, "*Critical current density and flux pinning in a $Bi_{1.7}Pb_{0.4}Sr_{2-x}La_xCa_{1.1}Cu_{2.1}O_y$ system*", *Supercond. Sci. Technol.* **20** (2007) 781-784.

[33]   Biju A, Shabna R, Sarun P M, **Vinu S** and Syamaprasad U, "*Effect of Yb, Gd, and Nd Substitution at the Sr Site on the Metal–Insulator Transition of the $(Bi, Pb) - 2212$ System*", *Int. J. App. Ceramic. Tech.* **71** (2010) 1622.

In international/National conference proceedings:

[1]   **S. Vinu,** P.M. Sarun and U. Syamaprasad "*Analysis of thermo-magnetic fluctuations and scaling of the vortex liquid resistivity in $Bi_{1.6}Pb_{0.5}Sr_{2-x}Ho_xCa_{1.1}Cu_{2.1}O_{8+\delta}$ system*", Presented in UGC sponsored National Seminar on Recent and Emerging Developments in Physics, Nagercoil, January 7-9, 2010. (Page No. 39).

[2]   **S. Vinu,** P.M. Sarun, R. Shabna and U. Syamaprasad "*Thermo-Magnetic Fluctuations above the Glass-Transition Temperature in Eu-doped (Bi, Pb)-2212 Superconductor*", Presented in International Conference on Advanced Functional Materials (ICAFM-2009), Trivandrum, December 9-10, 2009. (Page No. 53).

[3]   **S. Vinu,** "*Influence of Ho doping on the electrical properties of (Bi, Pb)-2212 superconductor*", Presented in National Seminar on Crystalline Materials and Nanotechnology, Mariagiri, February 26-27, 2009. (Page No. 17).
*(**Invited talk**).*

[4]   **S. Vinu,** P.M. Sarun, R. Shabna, A. Biju and U. Syamaprasad "*Highly enhanced superconducting properties of Pb and rare earth doped Bi-2212 system*", Presented in 21st Kerala Science Congress, Kollam, January 28-31, 2009. (Page No. 750-52).

[5]   **S. Vinu,** P.M. Sarun, R. Shabna, A. Biju and U. Syamaprasad, "*Enhanced critical current density and flux pinning properties of $Bi_{1.6}Pb_{0.5}Sr_{2-x}Eu_xCa_{1.1}Cu_{2.1}O_y$*", Presented in International Seminar on Mineral Processing Technology (MPT-2008), Trivandrum, April 22-24, 2008. (Page No. 255-58).

[6]   **S. Vinu,** P.M. Sarun, R. Shabna, A. Biju, P. Guruswamy and U. Syamaprasad "*Effect of dual substitution of Pb and Dy on the flux pinning properties of Bi-2212 superconductor*", Presented in National Seminar on Special Purpose, Strategic and Futuristic Materials for High Technology Sectors (IIM-2008), Trivandrum, October 16-17, 2008. (Page No. 72).

[7]   **S. Vinu,** P.M. Sarun, R. Shabna, A. Biju and U. Syamaprasad, "*Pinning force density of Y-added (Bi,Pb)-2212 superconductor*", Presented in International Conference on Advanced Materials and Composites (ICAMC-2007), Trivandrum, October 24-26, 2007.(Page No. 789-93).

[8]   **S. Vinu,** P.M. Sarun, A. Biju, P. Guruswamy and U. Syamaprasad, "*Enhanced Flux pinning in La substituted (Bi,Pb)-2212 superconductor*", Presented in DAE-Solid State Physics Symposium 2007, Mysore, December 27-31, 2007. (Page No. 793-94).

[9]   P.M. Sarun, **S. Vinu,** R. Shabna and U. Syamaprasad "*Microstructural and Flux Pinning Characteristics of $Bi_{1.6}Pb_{0.5}Sr_{1.8}La_{0.2}Ca_{1.1}Cu_{2.1}O_{8+\delta}$ Superconductor Sintered at Different Temperatures*", Presented in International Conference on Advanced Functional Materials (ICAFM-2009), Trivandrum, December 9-10, 2009. (Page No. 54).

[10]   P.M. Sarun, **S. Vinu** and U. Syamaprasad "*Structural and superconducting properties of Gd substituted $(Bi, Pb)_2Sr_2Ca_1Cu_2O_{8+\delta}$ superconductor*", Presented in 21st Kerala Science Congress, Kollam, January 28-31, 2009. (Page No. 783-85).

(Awarded best poster presentation award in Physical Science).

[11]   P.M. Sarun, **S. Vinu,** R. Shabna, A. Biju and U. Syamaprasad "*Critical Current Density and Flux Pinning Properties of $Bi_{1.7}Pb_{0.4}Sr_{2-x}Gd_xCa_{1.1}Cu_{2.1}O_{8+\delta}$ (Bi,Pb)-2212 superconductor*", Presented in DAE-Solid State Physics Symposium 2008, Mumbai, December 16-20, 2008. (Page No. 895-96).

[12]   R. Shabna, P.M. Sarun, **S. Vinu** and U. Syamaprasad "*Metallic, superconducting and semiconducting properties of praseodymium substituted (Bi,Pb)-2212 system*", Presented in National Seminar on Special Purpose, Strategic and Futuristic Materials for High Technology Sectors (IIM-2008), Trivandrum, October 16-17, 2008. (Page No. 73).

[13]   R. Shabna, P.M. Sarun, **S. Vinu** and U. Syamaprasad "*Transport Property near the Metal to Insulator Transition in Samarium Substituted (Bi, Pb)-2212 System*", Presented in

International Conference on Advanced Functional Materials (ICAFM-2009), Trivandrum, December 9-10, 2009. (Page No. 54).

(Awarded best poster presentation award)

[14]   R. Shabna, A. Biju, P.M. Sarun, **S. Vinu** and U. Syamaprasad, "*Metal to insulator transition in gadolinium substituted (Bi,Pb)-2212 system*", Presented in International Seminar on Mineral Processing Technology (MPT-2008), Trivandrum, April 22-24, 2008. (Page No. 292-96).

References

REFERENCES

Abrikosov A A, "On the magnetic properties of superconductors of the second group", Sov. Phys. JETP 5 (1957) 1174

Abrikosov A A, "Nobel Lecture: Type-II superconductors and the vortex lattice", Rev. Mod. Phys. 76 (2004) 975

Agranovski E, Ilyushechkin A Y, Altman I S, Bostrom T E and Choi M, "Methods of introduction of MgO nanoparticles into Bi-2212/Ag tapes", Physica C 434 (2006) 115

Aloysius R P, Guruswamy P and Syamaprasad U, "Highly enhanced critical current density in Pr-added (Bi, Pb)-2212 superconductor", Supercond. Sci. Technol. 18 (2005) L23

Amira A, Mosbah M F, Molinie P and Leblanc A, "Improvement of magnetic properties in Bi-2212 ceramics by fluorine doping", Solid. State. Sci. 7 (2005) 53

An R Z, Wei L, Jie Y, Wei Y, Li S X, Cai L Z, Can C G, Li D X, Ling S L, Fang Z and Xian Z Z, "Superconductivity at 55 K in Iron-Based F-Doped Layered Quaternary Compound $SmO_{1-x}F_xFeAs$", Chin. Phys. Lett. 25 (2008) 2215

Anderson P W, "The Resonating Valence Bond State in La_2CuO_4 and Superconductivity", Science 235 (1987) 1196

Anderson P W, "Theory of Flux Creep in Hard Superconductors", Phys. Rev. Lett. 9 (1962) 309

Andersson M, Rydh A and Rapp O, "Vortex liquid resistivity in disordered $YBa_2Cu_3O_{7-\delta}$ single crystals", Physica C 341-348 (2000) 1239

Anderson P W and Kim Y, "Hard Superconductivity: Theory of the Motion of Abrikosov Flux Lines", Rev. Mod. Phys. 36 (1964) 39

Attfield J F, Kharlanov A L and Mcallister J A, "Cation effects in doped La_2CuO_4 superconductors", Nature 394 (1998) 157

Awana V P S, Agarwal S K, Narlikar A V and Das M P, "Superconductivity in Pr- and Ce-doped $Bi_2CaSr_2Cu_2O_y$ systems", Phys. Rev. B 48 (1993)1211

Baca E, Holguin V, Lopera W and Prieto P, "Effect of Y-substitution on the electrical properties of epitaxial $Bi_2Sr_2Ca_{1-x}Y_xCu_2O_{8+\delta}$ thin films", Physica C 341-348 (2000) 655

[a]Bardeen J, Cooper L N and Shrieffer J R, "Microscopic Theory of Superconductivity", Phys. Rev. 106 (1957) 162

[b]Bardeen J, Cooper L N and Shrieffer J R, "Theory of Superconductivity", Phys. Rev. 108 (1957) 1175

Babaev E, "Vortices with Fractional Flux in Two-Gap Superconductors and in Extended Faddeev Model", Phys. Rev. Lett. 89 (2002) 067001

Bednorz J G, Müller K A, "Possible high T_c superconductivity in the Ba-La-Cu-O System", Z. Phys. B 64 (1986) 189

Bhattacharya R N, Chen J and Blaughter R D, "Biaxially textured superconductor Bi-oxide films via an electrodeposition process", IEEE Trans. Appl. Supercond. 13 (2003) 3343

Biju A, Kumar R G A, Aloysius R P and Syamaprasad U, "Structural and superconducting properties of $Bi_{1.7}Pb_{0.4}Sr_{2-x}Gd_xCa_{1.1}Cu_{2.1}O_y$ system", Physica C 449 (2006) 109

Biju A, Sarun P M, Vinu S, Guruswamy P and Syamaprasad U, "Critical current density and flux pinning in a $Bi_{1.7}Pb_{0.4}Sr_{2-x} La_x Ca_{1.1}Cu_{2.1}O_y$ system", Supercond.Sci. Technol. 20 (2007) 781

Biju A, Vinod K, Sarun P M and Syamaprasad U, "Highly enhanced flux pinning in Pb and rare earth codoped Bi-2212", Appl. Phys. Lett. 90 (2007) 072505

Blatter G, Feigelman M V, Geshkenbein V B, Larkin A I and Vinokur V M, "Vortices in high-temperature superconductors", Rev. Mod. Phys. 66 (1994) 1125

Brandt E H, "The flux-line lattice in superconductors", Rep. Prog. Phys. 58 (1995) 1465

Buzea C, Yamashita T, "Review of the superconducting properties of MgB_2", Supercond. Sci. Technol. 14 (2001) R115

Buzea C, Robbie K, "Assembling the puzzle of superconducting elements: a review", Supercond. Sci. Technol. 18 (2005) R1

Cao Q, Ruau K Q, Li S Y, Chen X H, Qian G G and Cao L Z, "The comparable effects on transport properties in $Bi_2Sr_2Ca_{1-x}Pr_xCu_2O_y$ and $Bi_2Sr_2Ca_{1-x}Y_xCu_2O_y$ single crystals", Physica C 334 (2000) 237

Chen F H, Koo H S and Tseng T Y, "Synthesis of high-Tc superconducting (Bi,Pb)-Sr-Ca-Cu-O ceramics prepared by an ultrastructure processing via the oxalate route", J. Mater. Sci. 25 (1990) 3338

Chen X, Liang J, Min J, Li J and Rao G, "Phase separation and oxygen variation in Pr-doped $Bi_2Sr_2CaCu_2O_{8+\delta}$", Phys. Rev. B 50 (1994) 3431

Chong I, Hiroi Z, Izumi M, Shimoyama J, Nakayama Y, Kishio K, Terashima T, Bando Y and Takano Y, "High Critical-Current Density in the Heavily Pb-Doped $Bi_2Sr_2CaCu_2O_{8+\delta}$ Superconductor: Generation of Efficient Pinning Centers", Science 276 (1997) 770

Dagotto E, "Correlated electrons in high-temperature superconductors", Rev. Mod. Phys. 66 (1994) 763

Dos-Santos C A M, Pinto G S, Ferreira B and Machado A J S, "Influence of Pr content on the kinetics of $Bi_2Sr_2CaCu_2O_{8+\delta}$ phase formation", Physica C 354 (2001) 388

De-Ninno P G A, Marinelli M, Paerno G, Gambardella U, Paroli P and Balestrino G, "Transport critical currents in Bi-Sr-Ca-Cu-O pellets and single crystals", Physica C 162-164 (1989) 359

Dew-Hughes D, "Flux pinning mechanisms in type II superconductors", Philos. Mag. 30 (1974) 293

Dimos D, Chaudhari P and Mannhart J, "Superconducting transport properties of grain boundaries in $YBa_2Cu_3O_7$ bicrystals", Phys. Rev. B 41 (1990) 4038

Ekin J W, Larson T M, Hermann A M, Sheng Z Z, Togano K and Kumakura H, "Double-step behavior of critical current vs. magnetic field in Y, Bi and Tl - based bulk high - T_c superconductors", Physica C 160 (1989) 489

Emery V J, "Theory of high-Tc superconductivity in oxides", Phys. Rev. Lett. 58 (1987) 2794

Fuji H, Kumakura H and Togano K, "Microstructure and Superconducting Properties of $Bi_{2-x}Pb_xSr_2CaCu_2O_y$ Transformed from an Amorphous State under Different Oxygen Partial Pressures", Jpn. J. Appl. Phys. 39 (2000) 2591

Fujii H, Hishinuma Y, Kitaguchi H, Kumakura H and Togano K, "Study on the heat treatment condition to improve coupling of grains in $Bi_{2-x}Pb_xSr_2CaCu_2O_y$/Ag tapes", Physica C 331 (2000) 79

Fisher M P A, "Vortex-glass superconductivity: A possible new phase in bulk high-T_c oxides", Phys. Rev. Lett. 62 (1989) 1415

Fisher D S, Fisher M P A and Huse D A, "Thermal fluctuations, quenched disorder, phase transitions, and transport in type-II superconductors", Phys. Rev. B 43 (1991) 130

Gao L, Xue Y Y, Chen F, Xiong Q, Meng R L, Ramirez D, Chu C W, Eggert J H and Mao H K, "Superconductivity up to 164 K in $HgBa_2Ca_{m-1}Cu_mO_{2m+2+\delta}$ (m=1, 2, and 3) under quasihydrostatic pressures", Phys. Rev. B 50 (1994) 4260

Gao Y, Pernambucwise P, Crow J E, Oreilly J, Spencer N, Chen H and Salomon R E, "Superconducting and magnetic phase boundaries in $Bi_2Sr_2Ca_{1-x}M_xCu_2O_8$, with M=Y, Gd, and Pr", Phys. Rev. B 45 (1992) 7436

Geballe T H, "Superconductivity Super Boron", Science 293 (2001) 223

Gendre P, Schmirgeld L, Regnier R, Legendre F, Senoussi S and Marquet A, "High quality Bi-2212 tapes prepared by oxidation of metallic precursors", Appl. Supercond. 3 (1995) 21

Ginzburg V L, "Nobel Lecture: On superconductivity and superfluidity as well as on the "physical minimum" at the beginning of the XXI century", Rev. Mod. Phys. 76 (2004) 981

Gladyshevskii R, Musolino N and Flukiger R, "Structural origin of the low superconducting anisotropy of $Bi_{1.7}Pb_{0.4}Sr_2Ca_{0.9}Cu_2O_8$ crystals", Phys. Rev. B 70 (2004) 184522

Goodenough J B, Manthiram M, "Crystal chemistry and superconductivity of the copper oxides", J. Solid State Chem. 88 (1990) 115

Gu G D, Russell G J and Koshizuka N, "Magnetism and flux pinning of $Bi_{2.1}Sr_{1.9}Ca_1(Cu_{1-y}Fe_y)_2O_{8+x}$ single crystals", Physica C 282-287 (1997) 2107

Gupta R P, Gupta M, "Electronic-structure calculation of the hole-carrier-density distribution in $Bi_2Sr_2CuO_6$, $Bi_2Sr_2CaCu_2O_8$, and $Bi_2Sr_2Ca_2Cu_3O_{10}$ superconductors", Phys. Rev. B 49 (1994) 13154

Gutzwiller M C, "Effect of Correlation on the Ferromagnetism of Transition Metals", Phys. Rev. Lett. 10 (1963) 159

Ha D H, Lee K W, Oka K, Yamaguchi Y, Iga F and Nishihara Y, "Magnetization anomaly and anisotropy of $Bi_2Sr_2CaCu_{2-x}Ni_xO_8$ single crystals", Physica C 260 (1996) 242

Hagen S J, Jing T W, Wang Z Z, Horvath J and Ong N P, "Out-of-plane conductivity in single-crystal $YBa_2Cu_3O_7$", Phys. Rev. B. 37 (1988) 7928

Hamadneh I, Agil A, Yahya A K and Halim S A, "Superconducting properties of bulk $Bi_{1.6}Pb_{0.4}Sr_2Ca_{2-x}Cd_xCu_3O_{10}$ system prepared via conventional solid state and coprecipitation methods", Physica C 463-465 (2007) 207

Hampshire D P and Jones H, "Analysis of the general structure of the E-I characteristic of high-current superconductors with particular reference to a Nb-Ti SRM wire", Cryogenics 27 (1987) 608

Hedt B V, Liieck W, Westerholt K and Back H, "Superconductivity in $Bi_2Sr_2CaCu_2O_{8+\delta}$ single crystals doped with Fe, Ni, and Zn", Phys. Rev. B 49 (1994) 9898

Hott R, Kleiner R, Wolf T and Zwicknagl G, "Frontiers in Superconducting Materials", (Editor: A. V. Narlikar), Springer-Verlag Berlin Heidelberg, New York (2005)

Houghton A, Pelcovits R A and Sudbo A, "Flux lattice melting in high-T_c superconductors", Phys. Rev. B 40 (1989) 6763

Hubbard J, "Electron correlations in narrow energy bands", P. Roy. Soc. Lond. A. Mat. 276 (1963) 238

Hudakova N, Knizek K and Hejtmanek J, "The infrared properties of $Bi_2Y_{0.1}Sr_{1.9}CaCu_2O_{8+\delta}$ superconductor", Physica C 406 (2004) 58

Ilyushechkin A Y, Yamashita T, Boskovic L and Mackinnon I D R, " The effect of Yb addition in $Bi_2Sr_2Ca_{1-x}Yb_xCu_2O_y$ partial melted thick films", Supercond. Sci. Technol. 17 (2004) 1201

Ishiguro T, Yamaji K and Saito G, "Organic superconductors", Second edition, Springer-Verlag Berlin Heidelberg, New York (1998)

Jia Y, Cheng P, Fang L, Luo H Q, Yang H, Ren C, Shan L, Gu C Z and Wen H H, "Critical fields and anisotropy of $NdFeAsO_{0.82}F_{0.18}$ single crystals", Appl. Phys. Lett. 93 (2008) 032503

Jin H and Kotzler J, "Effect of La-doping on growth and superconductivity of Bi-2212 crystals", Physica C 325 (1999) 153

Jrome D, Mazaud A, Ribault M and Bechgaard K, "Superconductivity in a synthetic organic conductor $(TMTSF)_2PF_6$", J. Phys. Lett. Paris 95 (1980) 41

Kamihara Y, Watanabe T, Hirano M and Hosono H, "Iron-based layered superconductor $La[O_{1-x}F_x]FeAs$ (x=0.05-0.12) with T_c=26 K", J. Am. Chem. Soc. 130 (2008) 3296

Kazin P E, Shuba R A, Tretyakov Y D, Knotko A V, Jansen M and Freitag B, "Formation of Bi-2212-based composites with submicrometre-grained $(Sr, Ca)SnO_3$", Supercond. Sci. Technol. 13 (2000) 134

Kazin P E, Tretyakov Y D, Lennikov V V and Jansen M, "Formation of the $Bi_2Sr_2CaCu_2O_{8+\delta}$ superconductor with Mg1 − xCuxOinclusions: the phases compatibility and the effect of the preparation routeon the material microstructure and properties", J. Mater. Chem. 11 (2001) 168

Kazin P E, Zaitsev D D, Tretyakov Y D and Jansen M, "Phase Relations in the Bi–Sr–Ca–Cu–M–O (M = Y, Dy, Ho, Er, Tm, Yb, Lu) Systems", Inorg. Mater. 37 (2001) 812

Kendziora C, Forro L, Mandrus D, Hartge J, Stephens P, Mihaly L, Reeder R, Moecher D, Rivers M and Sutton S, "Composition, structure, and electrical properties of $Bi_2Sr_2Ca_{1-y}Y_yCu_2O_8$: A single-crystal study", Phys. Rev. B 45 (1992) 13025

Kim D H, Gray K E, Kampwirth R T, Smith J C, Richeson D S, Marks T J, Kang J H, Talvacchio J and Eddy M, "Effect of Cu-O layer spacing on the magnetic field induced resistive broadening of high-temperature superconductors", Physica C 177 (1991) 431

Kim G C, Kim B J, Cheon M Y and Kim Y C, "Variation of pinning mechanism in $Bi_{1.6}Pb_{0.4}Sr_2CaCu_2O_{8+\delta}$ single crystal", Physica C 391 (2003) 305

Kleiner R and Muller P, "Intrinsic Josephson effects in high-T_c superconductors", Phys. Rev. B 49 (1994) 1327

Koblischka M R and Murakami M, "Pinning mechanisms in bulk high-T_c superconductors", Supercond. Sci. Technol. 13 (2000) 738

Kotaka Y, Kimura T, Ikata H, Shimoyama J, Kitazawa K, Yamafuji K, Kishio K and Pooke D, "Doping state and transport anisotropy in Bi-2212 single crystals", Physica C 235-240 (1994) 1529

Krishnanraj P, Lrlovic M, Eror N G and Balachandran U, "Synthesis and oxygen stoichiometry of $Bi_2Sr_2CaCu_2O_{8+x}$", Physica C 234 (1994) 318

Krusin-elbaum L, Blatter G and Shibauchi T, "Zeeman and orbital limiting fields: Separated spin and charge degrees of freedomin cuprate superconductors", Phys. Rev. B 69 (2004) 220506

Kumakura H, Matsumoto A, Sung Y S and Kitaguchi H, "E–J characteristics of Bi-2212/Ag and Bi-2223/Ag tape conductors", Physica C 384 (2003) 283

Kumar R R, Aloysius R P, Bose J, Guruswamy P and Syamaprasad U, "Preparation of dense, high J_C Bi-2223 superconductors by multistage cold pressing", Supercond. Sci. Technol. 18 (2005) 689

Larbalestier D C, "Superconductor Flux Pinning and Grain Boundary Control", Science 274 (1996) 736

Larbalestier D C, Gurevich A, Feldmann D M and Polyanskii A, "High-T_c superconducting materials for electric power applications", Nature (London) 414 (2001) 368

Lee P A, Nagaosa N and Wen X G, "Doping a Mott insulator: Physics of high-temperature superconductivity", Rev. Mod. Phys. 78 (2006) 17

Lee P J (Ed.), , "Engineering superconductivity", Wiley-Interscience, John Wiley & Sons Inc., USA, 391 (2001)

Li T W, Drost R J, Kes P H, Tracholt C, Zandbergen H W, Hien N T, Menovsky A A and Franse J J M, "Enhanced flux pinning in Bi-2212 single crystals by planar defects introduced via Ti-substitution", Physica C 274 (1997) 197

Liu A Y, Mazin I I and Kortus J, "Beyond Eliashberg Superconductivity in MgB_2: Anharmonicity, Two-Phonon Scattering, and Multiple Gaps", Phys. Rev. Lett. 87 (2001) 087005

London F, London H, "The Electromagnetic Equations of the Supraconductor", Proc. Roy. Soc. A 149 (1935) 71

Lonnberg B, Lundstrom T and Norling P, "Substitution of vanadium and chromium for copper in $Bi_2Sr_2CaCu_2O_8$", Physica C 191 (1992) 147

Lotgering F K, "Topotactical reactions with ferrimagnetic oxides having hexagonal crystal structures-I", J. Inorg Nucl. Chem. 9 (1959) 113

Maeda H, Tanaka Y, Fukutomi M and Asano T, "A New High-T_c Oxide Superconductor without a Rare Earth Element", Jpn. J. Appl. Phys. 27 (1988) L209

Maeda A, Yabe T, Takebayashi S, Hase M and Uchinokura K, "Substitution of 3d metals for Cu in $Bi_2(Sr_{0.6}Ca_{0.4})_3Cu_2O_y$", Phys. Rev. B 41 (1990) 4112

Maeda A, Hase M, Tsukada I, Noda K, Takebayashi S and Uchinokura K, "Physical properties of $Bi_2Sr_2Ca_{n-1}Cu_nO_y$ (n=1,2,3)", Phys. Rev. B 41 (1990) 6418

Majewski P, Elschner S and Aldinger F, "Enhanced pinning by second-phase precipitates in Sr rich "$Bi_2Sr_2CaCu_2O_8$" ceramics", Physica C 249 (1995) 234

Makarova M V, Kazin P E, Tretyakov Y D, Jansen M, Reissner M and Steiner W, "Zr, Hf, Mo and W-containing oxide phases as pinning additives in Bi-2212 superconductor", Physica C 419 (2005) 61

Mandal P, Podder A, Ghosh B and Choudhury P, "Variation of T_c and transport properties with carrier concentration in Y- and Pb- doped Bi- based superconductors", Phys. Rev. B 43 (1991) 13102

Mancic L, Milosevic O, Marinkovic B, Lopez M and Rizzo F, "Rapid formation of high T_c phase in Bi-Pb-Sr-Ca-Cu-O system", Physica C 341-348 (2000) 503

Mandrus D, Forro L, Kendziora C and Mihaly L, "Resistivity study of $Bi_2Sr_2Ca_{1-x}Y_xCu_2O_8$ single crystals", Phys. Rev. B 45 (1992) 12640

Meissner W, Oschenfeld R, "Ein-neuer Effekt bei Eintritt-der Supraleitfähigkeit", Naturwissenschaften 21 (1933) 787

Minnhagen P, "The two-dimensional Coulomb gas, vortex unbinding, and superfluid-superconducting films", Rev. Mod. Phys. 59 (1987) 1001

Mitchell J F, Garcia J A and Hinks D G, "Rapid synthesis of 93 K Bi-2212 superconductor from hydroxide precursors", Physica C 245 (1995) 126

Mitzi D B, Lombardo L W, Kapitulnik A, Laderman S S and Jacowitz R D, "Growth and properties of oxygen- and ion-doped $Bi_2Sr_2CaCu_2O_{8+\delta}$ single crystals", Phys. Rev. B 41 (1990) 6564

Motohashi T, Nakayama Y, Fujita T, Kitazawa K, Shimoyama J and Kishio K, "Systematic decrease of resistivity anisotropy in $Bi_2Sr_2CaCu_2O_y$ by Pb doping", Phys. Rev. B 59 (1999) 14080

Motoi Y, Ikeda Y, Uwe H and Sakudo T, "Enhancement of Tc by annealing under reducing conditions on $Bi_2Sr_2CaCu_2O_x$", Physica C 162-164 (1989) 929

Murugakoothan P, Jayavel R, Rao C R V, Subramanian C and Ramasamy P, "Growth and characterization of bulk-textured $Bi_2Sr_2Ca_{1-x}Y_xCu_2O_\delta$ by the float zone technique", Supercond. Sci. Technol. 7 (1994) 367

Nagamatsu J, Nakagawa N, Muranaka T, Zenitani Y and Akimitsu J, "Superconductivity at 39 K in magnesium diboride", Nature 410 (2001) 63

Narsaiah E L, Rao U V S, Pefia O and Perrin C, "Magnetism and superconductivity in the 2 : 2 : 1 : 2 bismuth cuprate by dysprosium substitution $(Bi_2Sr_2Ca_{1-x}Dy_xCu_2O_{8+\Delta})$", Solid State Commun. 83 (1992) 689

Nelson D R and Seung S H, "Theory of melted flux liquids", Phys. Rev. B. 39 (1989) 9153

Noetzel R, Westerhott K, "Vortex pinning by Ni point defects in $Bi_2Sr_2Ca(Cu_{1-x}Ni_x)_2O_{8+\delta}$ single crystals", Phys. Rev. B 58 (1998) 15108

Nomura S, Yoshino H and Ando K, "Enhanced flux pinning in Ag-sheathed $(Bi, Pb)_2Sr_2Ca_2Cu_3O_{10+\delta}$ tapes by post-annealing", Supercond. Sci. Technol. 6 (1993) 858

Nowik I, Felner I and Bauminger E R, "Magnetic order and superconductivity in $Bi_2Sr_2Ca_{1-x}Y_xCu_2O_8$", Phys. Rev. B 45 (1992) 4912

Onnes H K, "The resistance of pure mercury at helium temperatures", Leiden Commn 124 (1911) 1226

Orenstein J, Millis A J, "Advances in the Physics of High-Temperature Superconductivity", Science 288 (2000) 468

Pan S H, Hudson E W, Lang K M, Eisaki H, Uehida S and Davis J C, "Imaging the effects of individual zinc impurity atoms on superconductivity in $Bi_2Sr_2CaCu_2O_{8+\delta}$", Nature 403 (2000) 746

Pearl J, "Current distribution in superconducting films carrying quantized fluxoids", Appl. Phys. Lett. 5 (1964) 65

Phillips P, "Organic materials: From insulator to superconductor", Nature 406 (2000) 687

Poole C P, Farach H A and Creswick R J, Editors, "Superconductivity", Academic Press, California (1995)

Potanina L V, Shikov A K, Vedernikov G P, Vorobieva A E, Pantsyrnyi V I, Gubkin I N, Sylaev A G, Plashkin E I, Dergunova E A and Soudjev S V, "Recent progress of low temperature superconducting materials at Bochvar Institute", Physica C 386 (2003) 390

Prabhakaran D, Subrahmanian C, "Growth and bulk texturing studies of $Bi_xY_{0.1}Sr_{1.9}CaCu_2O_8$ crystals by floating zone technique", Mater. Sci. Engg. B 52 (1998) 169

Pradhan A K, Roy S B, Chaddah P, Chen C and Wanklyn B M, "Magnetic properties of single-crystal $Bi_2Sr_2CaCu_2O_{8+y}$: Experimental evidence for a dimensional crossover", Phys. Rev. B 49 (1994) 12984

Rahier S, Lafort A, Henrist C, Ausloos M, Cloots R and Vertruyen B, "Chemical interactions between $Bi_2Sr_3CaO_7$ (Bi-2310) and $Bi_2Sr_2Ca_{0.8}Dy_{0.2}Cu_2O_8$ [Bi-2212 (Dy)]", Supercond. Sci. Technol. 19 (2006) 39

Raveau B, Michel C and Hervieu M, "Layered cuprates with double and triple copper layers: Structure and superconductivity", J. Solid State Chem. 88 (1990) 140

Rydh A, Rapp O and Andersson M, "Consistent Description of the Vortex Glass Resistivity in High- T_c Superconductors", Phys. Rev. Lett. 83 (1999) 1850

Rydh A, Rapp O and Andersson M, "Magnetic field scaling of the vortex glass resistivity in oxygen deficient $YBa_2Cu_3O_{7-\delta}$ single crystals", Physica B 284-288 (2000) 707

Saito G, Yamochi H, Nakamura T, Komatsu T, Nakashima M, Mori H and Oshima K, "Recent progress in organic superconductors", Physica B 169 (1991) 372

Sager D, Koch M, Hallstedt H, Chen M and Gauckler L J, "Enhanced residual secondary phase dissolution by atmosphere control in Bi-2212 superconductors", Physica C 405 (2004) 103

Salah B A, Mansuori M and Fremy M A, "High-T_c superconductor/silver composites A new direct preparation process", Physica C 262 (1996) 111

Sanderson R J and Hewitt K C, "Stoichiometry control of magnetron sputtered $Bi_2Sr_2Ca_{1-x}Y_xCu_2O_y$ $(0 \leq x \leq 0.5)$ thin film, composition spread libraries: Substrate bias and gas density factors", Physica C 425 (2005) 52

Sarun P M, Aloysius R P and Syamaprasad U, "Preparation of high performance (Bi,Pb)-2223 superconductor using a sol–gel synthesized amorphous precursor through controlled gelation ",   Mater. Lett. 60 (2006) 3797

Sarun P M, Shabna R, Vinu S, Biju A and Syamaprasad U, "Highly enhanced superconducting properties of Bi-2212 by Y and Pb co-doping", Physica B 404 (2009) 1602

Sarun P M, Vinu S, Shabna R, Biju A and Syamaprasad U, "Highly enhanced superconducting properties of Eu-doped (Bi,Pb)-2212 ", Mater. Lett. 62 (2008) 2725

Salpietro E, "Status of the ITER magnets", Supercond. Sci. Technol. 19 (2006) S84

Shabna R, Sarun P M, Vinu S, Biju A, Guruswamy P and Syamaprasad U, "Metal-insulator transition and conduction mechanism in dysprosium doped Bi1.7Pb0.4Sr2Ca1.1Cu2. 1O8+δ system", J. Appl. Phys. 104 (2008) 013919

Shabna R, Sarun P M, Vinu S and Syamaprasad U, "Charge carrier localization and metal to insulator transition in Cerium substituted (Bi, Pb)-2212 superconductor", J. Alloys Compd. 493 (2010) 11

Shantsev D V, Bobyl A V, Galperin Y M and Hohansen T H, "Comparison of two methods for analysis of vortex motion: flux creep versus nonlinear current-voltage curve approach", Physica C 341-348 (2000) 1145

Shigemori M, Okabe T, Uchida S, Sugioka T, Shimoyama J, Horii S and Kisho K, "Enhanced flux pinning properties of Bi(Pb)-2212 single crystals",   Physica C 408-410 (2004) 40

Singh S, "Suppression of superconductivity in Sm and Co substituted $Bi_2Sr_2Ca_1Cu_2O_{8+\delta}$ system", Physica C 294 (1998) 249

Sinha S K, Gadkari S C, Sabharwal S C, Gupta L C and Gupta M K, "Bulk synthesis of $(Bi,Pb)_2Sr_2Ca_2Cu_3O_x$ superconductor", Physica C 185-189 (1991) 499

Su H L, Majewski P and Aldinger F, "Precipitation and pinning in Pb doped Bi-2212 ceramics", Physica C 249 (1995) 241

Sunshine S A, Siegrist T, Schneemeyer L F, Murphy D W, Cava R J, Batlogg B, Dover R B V, Fleming R M, Glarum S H, Nakahara S, Farrow R, Krajewski J J, Zahurak S M, Waszczak J V, Marshall J H, Marsh P, Jr L W R and Peck W F, "Structure and physical properties of single crystals of the 84 K superconductor $Bi_{2.2}Sr_2Ca_{0.8}Cu_2O_{8+\delta}$", Phys. Rev. B 38 (1988) 893

Szabo P, Samuely P, Kamark J, Klein T, Marcus J, Fruchart D, Miraglia S, Marcenat C and Jansen A G M, "Evidence for Two Superconducting Energy Gaps in MgB_2 by Point-Contact Spectroscopy", Phys. Rev. Lett. 87 (2001) 137005

Tarascon J M, Le-page Y, Barboux P, Bagley B G, Greene L H, Mckinnon W R, Hull G W, Giroud M and Hwang D M, "Preparation, structure, and properties of the superconducting compound series $Bi_2Sr_2Ca_{n-1}Cu_nO_y$ with n=1, 2, and 3", Phys. Rev. B 38 (1988) 8885

Tarascon J M, Barboux P, Miceli P F, Greene L H, Hull G W, Eibshutz M and Sunshine S A, "Structural and physical properties of the metal (M) substituted $YBa_2Cu_{3-x}M_xO_{7-y}$ perovskite", Phys. Rev. B 37 (1998) 7458

Tamegai T, Koga K, Suzuki K, Ichihara M, Sakai F and Iye Y, "Metal-Insulator Transition in the $Bi_2Sr_2Ca_{1-x}Y_xCu_2O_{8+y}$ System", Jpn. J. Appl. Phys. 28 (1989) L112

Tarascon J M, Barboux P, Hull G W, Ramesh R, Greene L H, Grioud M, Hedge M S and Mckinnon W R, "Bismuth cuprate high-T_c superconductors using cationic substitution", Phys. Rev. B 39 (1989) 4316

Tarascon J M, Barboux P, Miceli P F, Greene L H, Hull G W, Eibshutz M and Sunshine S A, "Structural and physical properties of the metal (M) substituted $YBa_2Cu_{3-x}M_xO_{7-y}$ perovskite",Phys. Rev. B 37 (1998) 7458

Thamizhavel A, Prabhakaran D, Jayavel R and Subaramanian C, "Growth and characterization of superconducting $Bi_2Sr_2Ca_{1-x}Ce_xCu_2O_{8+\delta}$ single crystals", Physica C 275 (1997) 279

Traholt C, Zandbergen H W, Li T W, Drost R J, Kes P H, Menovsky A A, Hien N T and Franse J J M, "TEM analysis of planar defects induced by Ti doping in Bi-2212 single crystals", Physica C 290 (1997) 239

Uprety K K, Hovart J, Wang X L, Ionescu M, Liu H K and Dou S X, "Enhancement of vortex pinning by Josephson coupling of two-dimensional pancake vortices in heavy lead-doped $Bi_{2-x}Pb_xSr_2CaCu_2O_y$", Supercond. Sci. Technol. 14 (2001) 479

Veenendaal M A V, Schlatmann R, Sawatzky G A and Groen W A, "Doping dependence of the chemical potential in $Bi_2Sr_2Ca_{1-x}Y_xCu_2O_{8+\delta}$", Phys. Rev. B 47 (1993) 446

Villard G, Pelloquin D, Maigan A and Wahl A, "Evidence of enhanced pinning properties in optimally doped $Bi_2Sr_2Ca_{1-x}Y_xCu_2O_{8+\delta}$ single crystals", Appl. Phys. Lett. 69 (1996) 1480

Villard G, Legendre F, Poissonnet S, Regnier P, Bifulco C and Giunchi G, "Enhancement of the critical current density of Bi-2212 electrodeposited tapes through microstructure control", Physica C 341-348 (2000) 2007

Villard G, Legendre F, Poissonnet S, Regnier P, Bifulco C and Giunchi G, "Enhancement in J_C of Bi-2212/Ag tapes", Physica C 355 (2001) 312

Vinu S, Sarun P M, Shabna R, Biju A, Guruswamy P and Syamaprasad U, "Effect of Dy substitution at the Sr-site on the critical current density and flux pinning properties of (Bi, Pb)-2212 ceramics", J. Am. Ceram. Soc. 91 (2008) 3585

Vinu S, Sarun P M, Biju A, Shabna R, Guruswamy P and Syamaprasad U, "The effect of substitution of Eu on the critical current density and flux pinning properties of (Bi, Pb)-2212 superconductor", Supercond. Sci. Technol. 21 (2008) 045001

Vinu S, Sarun P M, Shabna R, Biju A and Syamaprasad U, "The influence of sintering temperature on the microstructure and superconducting properties of $Bi_{1.7}Pb_{0.4}Sr_{1.8}Nd_{0.2}Ca_{1.1}Cu_{2.1}O_{8+\delta}$ superconductor", Supercond. Sci. Technol. 21 (2008) 085010

Vom Hedt B , Liieck W, Westerholt K and Back H, "Superconductivity in $Bi_2Sr_2CaCu_2O_{8+\delta}$ single crystals doped with Fe, Ni, and Zn",   Phys. Rev. B 49 (1994) 9898

Wakimoto S, Zhang H, Yamada K, Swainson I, Kim H and Birgeneau R J, "Direct Relation between the Low-Energy Spin Excitations and Superconductivity of Overdoped High-T_c Superconductors",   Phys. Rev. Lett. 92 (2004) 217004

Watanabe K, Awaji S and Motokawa M, "Cryogenfree superconducting magnets",   Physica B 329-333 (2003) 1487

Wang X L, Muromachi E T, Li A H, Cheng Z X, Keshavarzi S, Qin M J and Dou S X, "Growth, microstructures, and superconductivity of $Bi_{2-x}Pb_xSr_2Ca_{1-y}Gd_yCu_2O_{8+z}$ single crystals",   J. Appl. Phys. 95 (2004) 6699

Wang X L, Liu H K, Dou S X, Horvot J and Giu G D, "The peak effect in Fe-doped Bi-2212 single crystals",   Spercond. Sci. Technol. 15 (2002) 356

Wang X L, Liu H K, Dou S X, Horvat J, Millikon D, Heine G, Lang W, Luo H M and Ding S Y, "Superconductivity and flux pinning in Y and heavily Pb codoped Bi-2212 single crystals", J. Appl. Phys. 89 (2001) 7669

Weijers H W, Trociewitz U P, Marken K, Meinesz M, Miao H and Schwartz J, "The generation of 25.05 T using a 5.11 T $Bi_2Sr_2CaCu_2O_x$ superconducting insert magnet", Supercond. Sci. Technol. 17 (2004) 636

Worthigton T K, Gallagher W J and Dinger T R, "Anisotropic nature of high-temperature superconductivity in single-crystal $Y_1Ba_2Cu_3O_{7-x}$",   Phys. Rev. Lett. 59 (1987) 1160

Wu M K, Ashburn J R, Torng C J, Hor P H, Meng R L, Gao L, Huang Z J, Wang Y Q and Chu C W, "Superconductivity at 93 K in a new mixed-phase Y-Ba-Cu-O compound system at ambient pressure",   Phys. Rev. Lett. 58 (1987) 908

Yamauchi H, Karppinen M, "Application of high-pressure techniques: stabilization and oxidation-state control of novel superconductive and related multi-layered copper oxides",   Supercond. Sci. Technol. 13 (2000) R33

Yamafuji K and Kiss T, "Current-voltage characteristics near the glass-liquid transition in high-T_c superconductors", Physica C 290 (1997) 9

Yorimasa K, Uehara M, Kuramoto T, Inoue H and Kimishima Y, "S-doping effects on pinning property of Bi-2212 single crystals", Physica C 392-396 (2003) 306

Zhang F C, Rice T M, "Effective Hamiltonian for the superconducting Cu oxides", Phys. Rev. B 37 (1988) 3759

Zhao J and Seehra M S, "Dependence of Tc of $Bi_2Sr_2CaCu_2O_{8+x}$ on high temperature cycling and oxygen stoichiometry", Physica C 159 (1989) 639

Zhao B, Song W H, Du J J and Sun Y P, "Study on resistivity anisotropy and flux pinning of $Bi_{2-x}Pb_xSr_2CaCu_2O_y$ single crystals", Physica C 386 (2003) 60